A NEW TIME DOMAIN BOUNDARY ELEMENT FORMULATION FOR RATE-DEPENDENT INELASTICITY WITH APPLICATION TO HOMOGENIZATION

A THESIS SUBMITTED TO
THE GRADUATE SCHOOL OF NATURAL AND APPLIED SCIENCES
OF
MIDDLE EAST TECHNICAL UNIVERSITY

BY

AHMET ARDA AKAY

IN PARTIAL FULFILLMENT OF THE REQUIREMENTS
FOR
THE DEGREE OF DOCTOR OF PHILOSOPHY
IN
AEROSPACE ENGINEERING

AUGUST 2023

Approval of the thesis:

A NEW TIME DOMAIN BOUNDARY ELEMENT FORMULATION FOR RATE-DEPENDENT INELASTICITY WITH APPLICATION TO HOMOGENIZATION

submitted by **AHMET ARDA AKAY** in partial fulfillment of the requirements for the degree of **Doctor of Philosophy in Aerospace Engineering Department, Middle East Technical University** by,

Prof. Dr. Halil Kalıpçılar
Dean, Graduate School of **Natural and Applied Sciences** _____

Prof. Dr. Serkan Özgen
Head of Department, **Aerospace Engineering** _____

Assoc. Prof. Dr. Ercan Gürses
Supervisor, **Aerospace Engineering, METU** _____

Assoc. Prof. Dr. Serdar Göktepe
Co-supervisor, **Civil Engineering, METU** _____

Examining Committee Members:

Prof. Dr. Altan Kayran
Aerospace Engineering, METU _____

Assoc. Prof. Dr. Ercan Gürses
Aerospace Engineering, METU _____

Prof. Dr. Kağan Tuncay
Civil Engineering, METU _____

Prof. Dr. Hakan Argeşo
Aerospace Engineering, Atılım University _____

Assoc. Prof. Dr. İzzet ÖZDEMİR
Civil Engineering, İzmir Institute of Technology _____

Date:21.08.2023

I hereby declare that all information in this document has been obtained and presented in accordance with academic rules and ethical conduct. I also declare that, as required by these rules and conduct, I have fully cited and referenced all material and results that are not original to this work.

Name, Surname: Ahmet Arda Akay

Signature :

ABSTRACT

A NEW TIME DOMAIN BOUNDARY ELEMENT FORMULATION FOR RATE-DEPENDENT INELASTICITY WITH APPLICATION TO HOMOGENIZATION

Akay, Ahmet Arda
Ph.D., Department of Aerospace Engineering
Supervisor: Assoc. Prof. Dr. Ercan Gürses
Co-Supervisor: Assoc. Prof. Dr. Serdar Göktepe

August 2023, 194 pages

Effective determination of the homogenized properties of a heterogeneous medium is crucial in multi-scale analysis. The analysis of a heterogeneous medium, such as polymer nano-composites, using the conventional finite element method requires finite element meshes with much smaller element sizes than the dimensions of nano-reinforcements. The finite element analysis of the macroscopic model with such a mesh would be computationally very expensive. For this purpose, in this thesis study, two- and three-dimensional applications of the boundary element method have been discussed. The implementation of linear elasticity to BEM has been examined with the introduction of homogenization techniques using uniform tractions, linear displacement, and periodic displacement boundary conditions. The accuracy of the developed linear elasticity approach with homogenization has been demonstrated through various numerical examples from the literature. Moreover, in mostly heterogeneous Representative Volume Elements (RVEs) with significant differences in material properties between mediums, a third face, often referred to as an interface (or interphase), is observed. The modeling of these regions with BEM is also discussed

in this study. Viscoelasticity modeling is first introduced by adapting the Dynamic Correspondence Principle to the developed linear elastic BEM methodology. A comparison study of modeling viscoelasticity with this approach is conducted with FEM and examples from the literature. Domain integration appears in many engineering problems, making effective determination of the domain integral crucial. In conventional Boundary Element Method (BEM) analysis, domain integration is mostly done by using a finite number of internal cells and having BEM solutions in each cell to represent overall behavior. In this thesis study, mesh-free domain integration methods are introduced to developed BEM. The methodology of the Cartesian Transformation Method (CTM) with Moving Least Squares (MLS) and Radial Point Integration (RPIM) interpolation methods are discussed. The developed approach is first validated with a parameter study on mathematical examples. Subsequently, applications on physical engineering problems such as elasticity with body forces, thermoelasticity, and steady-state and transient heat conduction are conducted. Moreover, the developed BEM approach is extended to handle inelastic problems, wherein a new non-iterative rate-dependent inelastic formulation is developed and implemented in BEM. In contrast to the scarce existing rate formulations of inelasticity developed within BEM, the proposed non-iterative formulation exploits the hybrid semi-implicit update of strain-like kinematic history variables. The excellent performance of the proposed approach is demonstrated through comparisons with corresponding analytical and fully implicit finite element results for various boundary-value problems of linear and non-linear viscoelasticity. The limitations of the developed approach are also discussed in its applications to viscoplasticity.

Keywords: Boundary element method, homogenization, meshless domain integration, cartesian transformation method, radial point interpolation method, elasticity, linear/non-linear viscoelasticity, non-linear elastoplasticity, semi-implicit time integration

ÖZ

YÜKLEME HIZINA BAĞLI ELASTİK OLMAYAN MALZEMELER İÇİN YENİ BİR ZAMAN ALANI SINIR ELEMAN FORMÜLASYONU VE HOMOJENLEŞTİRME UYGULAMASI

Akay, Ahmet Arda
Doktora, Havacılık ve Uzay Mühendisliği Bölümü
Tez Yöneticisi: Doç. Dr. Ercan Gürses
Ortak Tez Yöneticisi: Doç. Dr. Serdar Göktepe

Ağustos 2023 , 194 sayfa

Heterojen bir ortamın homojenleştirilmiş özelliklerinin etkin bir şekilde belirlenmesi, çok ölçekli analizde önemlidir. Polimer nano-kompozitler gibi heterojen bir ortamın konvansiyonel sonlu eleman yöntemiyle analizi, nano-takviyelerin boyutlarından çok daha küçük eleman boyutlarına sahip sonlu eleman örgülerinin gerekliliğini doğurur. Bu tür bir örgüyle makroskopik modelin sonlu eleman analizi, hesaplama açısından oldukça maliyetli olabilir. Bu amaçla, bu tez çalışmasında, sınır eleman yönteminin iki ve üç boyutlu uygulamaları ele alınmıştır. Sınır eleman yöntemine lineer elastikiyet uygulaması, homojenleştirme tekniklerinin kullanımı ile tartışılmıştır; bunlar arasında düzgün çekmeler, doğrusal yer değiştirme ve periyodik yer değiştirme sınır koşulları bulunmaktadır. Geliştirilen lineer elastikiyet yaklaşımının doğruluğu, literatürdeki çeşitli sayısal örneklerle kanıtlanmıştır. Ayrıca, çoğunlukla heterojen temsili hacim elemanlarında (RVE'lerde) iki farklı ortam arasında büyük bir malzeme özelliği farkı varsa, üçüncü bir yüzey gözlenir. Bu bölgelerin BEM ile modellemesi de bu çalışmada tartışılmıştır. Viskoelastikiyet modellemesi, geliştirilen lineer elastik BEM

yönteminin Dinamik Uygunluk Prensibi'ne adapte edilmesiyle önce tanıtılmıştır. Bu yaklaşımla viskoelastikiyetin modellemesi, sonlu elemanlar yöntemi ile yapılan karşılaştırmalı bir çalışma ile literatürden örneklerle incelenmiştir. Alan integrallerinin birçok mühendislik problemde görülmesi nedeniyle, alan integrallerinin etkin bir şekilde belirlenmesi oldukça önemlidir. Geleneksel sınır eleman yöntemi (BEM) analizinde, alan integrali genellikle sonlu sayıda iç hücre kullanılarak ve her hücredeki BEM çözümleri, genel davranışı temsil etmek için kullanılır. Bu tez çalışmasında, geliştirilen sonlu elemanlar yöntemine bir çözüm ağına ihtiyaç duymayan integrasyon yöntemleri eklenmiştir. Cartesian Transformation Method (CTM) ile Moving Least Squares (MLS) ve Radial Point Integration (RPIM) interpolasyon yöntemleri incelenmiştir. Geliştirilen yaklaşım önce matematiksel örnekler üzerinde parametre çalışması ile doğrulanmıştır. Ardından, elastisite ile vücut kuvvetleri, termoelastisite ve durağan ve geçici ısı transferi gibi fiziksel mühendislik problemlerine uygulanmıştır. Ayrıca, geliştirilen BEM yaklaşımı, inelastik problemlerin çözümüne genişletilmiştir. Yeni bir iterasyon gerektirmeyen inelastik formülasyon BEM'e uygulanmıştır. BEM içinde mevcut olan sınırlı sayıdaki zamana göre türev içeren formülasyonların aksine, ileri sürülen iterasyon gerektirmeyen formülasyon, gerilme benzeri kinematik geçmiş değişkenlerinin hibrit yarı-ıtici güncellemesinden yararlanır. Önerilen yaklaşımın mükemmel performansı, doğrusal ve doğrusal olmayan viskoelastisite için çeşitli sınır değeri problemleri için karşılık gelen analitik ve tamamen iteratif sonlu eleman sonuçlarıyla karşılaştırılarak gösterilmiştir. Geliştirilen yaklaşımın viskoplastisiteye yönelik uygulamalarındaki sınırlamaları da tartışılmıştır.

Anahtar Kelimeler: Sınır eleman yöntemi, homojenleştirme, ağsız bölge entegrasyonu, kartezyen dönüşüm yöntemi, radyal nokta enterpolasyon yöntemi, elastikiyet, doğrusal/doğrusal olmayan viskoelastiklik, doğrusal olmayan elastoplastisite, yarı örtülü zaman entegrasyonu

To my cuk, family and friends

ACKNOWLEDGMENTS

I would like to express my deep appreciation and gratitude to my advisors, Ercan Gürses and Serdar Göktepe, for their unwavering guidance, invaluable insights, and continuous support throughout my doctoral journey. Their mentorship, marked by countless meetings and discussions, has been instrumental in shaping my research and academic growth, and their collaborative efforts have enriched my research experience.

I extend my heartfelt thanks to the esteemed members of my thesis committee, Altan Kayran, Kağan Tuncay, Hakan Argeşo, and İzzet Özdemir, for their valuable feedback and constructive criticism, which significantly enhanced the quality of this work.

I am immensely grateful for my girlfriend, Amandine, who is soon to be my wife. Your unwavering love and support have been my anchor throughout this challenging journey. Your presence has made the highs sweeter and the lows more bearable. I eagerly anticipate our future together as a married couple, knowing that your belief in me and our shared dreams will continue to inspire and strengthen me. Thank you for being not only my partner but also my greatest source of strength and inspiration.

My family, Olcay, and Dinçer, has been my pillar of strength and the driving force behind my academic pursuits. Your investments, both in education and in life for me, have made this achievement possible. Your dedication to my growth and well-being has been the foundation upon which I built my academic journey. Your unwavering support, sacrifices, and belief in my abilities have been my greatest motivation.

I would like to extend my heartfelt appreciation to my housemates, Mesut and Can, over the past six years. Your companionship and support have made my journey through graduate school not only more enjoyable but also more manageable. From late-night study sessions to shared meals and laughter, our time together has been invaluable.

To all my cousins and friends, near and far, your unwavering friendship has been a constant source of strength and joy throughout my academic journey. Your belief in me, your encouragement, and the countless shared moments have been truly remarkable. Thank you for being an essential part of my life's journey.

In addition to expressing my deepest gratitude to my four-legged girls, Nermin and Jacky, who tirelessly shared the long hours of work with me, offering their unwavering support and often providing moments of much-needed levity. Their presence was a source of comfort and inspiration throughout this journey, and I am endlessly thankful for their furry support.

In closing, I want to acknowledge the countless individuals, too numerous to name individually, who have contributed in various ways to my academic and personal growth. Your support, no matter how small, has played a vital role in the realization of this achievement.

Finally, I would like to express my gratitude to The Council of Scientific and Industrial Research (TÜBİTAK) for their financial support through Project ID 218M274, which has been a valuable addition to the success of my research.

TABLE OF CONTENTS

ABSTRACT v

ÖZ vii

ACKNOWLEDGMENTS x

TABLE OF CONTENTS xii

LIST OF TABLES xvii

LIST OF FIGURES xxi

LIST OF ABBREVIATIONS xxx

CHAPTERS

1 INTRODUCTION 1

1.1 Motivation and Problem Definition 1

1.2 The Outline of the Thesis 5

2 APPLICATION OF BOUNDARY ELEMENT METHOD TO HOMOGENIZATION PROBLEMS 7

2.1 2D and 3D Linear Elasticity Boundary Element Method Formulation 7

2.2 Homogenization of Linear Elasticity 12

2.2.1 Implementation of Boundary Conditions to BEM 12

2.2.1.1 Uniform Tractions 13

2.2.1.2 Linear Displacement 16

2.2.1.3 Periodic Displacement 17

2.2.2 Determination of the Tangent Moduli 20

2.2.3 Numerical Examples 21

2.2.3.1 2D RVEs with a Single Centered and a Single Eccentric Hole 22

2.2.3.2 2D RVE Consisting a Single Inclusion with Varying Volume Fractions and Material Properties 30

2.2.3.3 2D RVE Consisting Multi Inclusions with Varying Volume Fractions 34

2.2.3.4 3D RVEs Consisting Single- and Multi-Inclusions . . . 35

2.3 Homogenization of Linear Elasticity with Interface Modeling 39

2.3.1 Interface Models in Literature 39

2.3.2 Incorporating a Cohesive Traction-Separation Interface Model into Boundary Element Method 42

2.3.3 Numerical Examples 47

2.3.3.1 First Model Problem 47

2.3.3.2 Second Model Problem 49

2.4 Homogenization of Viscoelasticity with Dynamic Correspondence Principle 53

2.4.1 Implementation of Dynamic Correspondence Principle in Boundary Element Method 55

2.4.2 Determination of Homogenized Real and Imaginary Material Constants 57

2.4.3 Numerical Examples 59

2.4.3.1 First Application: Comparisons with Numerical Studies 59

2.4.3.2 Second Example: Comparison with Experimental Studies 65

2.5 Homogenization of Nonlinear Viscoelasticity with a Novel Non-iterative Approach 69

3 MESH-FREE INTEGRATION AND INTERPOLATION 71

3.1 Methodology 72

3.1.1 Mesh-free Integration - Cartesian Transformation Method (CTM) 73

3.1.2 Mesh-free Interpolation 76

3.1.2.1 Concept of Support Domain 77

3.1.2.2 Moving Least Squares Method (MLS) 78

3.1.2.3 Radial Point Interpolation Method (RPIM) 81

3.2 Applications of Mesh-Free Integration and Interpolation 83

3.2.1 Introduction of Body Force on Elasticity Problems 84

3.2.2 Steady State Heat Conduction and Thermoelastic Problems . . 85

3.2.2.1 Steady State Heat Conduction 85

3.2.2.2 Thermoelasticity 87

3.2.3 Transient Heat Conduction with Heat Source 90

3.2.3.1 Boundary Element Method Equations 90

3.2.3.2 Numerical Examples 95

4 2D LINEAR AND NONLINEAR VISCOELASTICITY/ELASTOPLASTICITY APPLICATIONS OF BOUNDARY ELEMENT METHOD 103

4.1 Time-Domain Boundary Element Formulation for Generalized Models of Linear Viscoelasticity 107

4.1.1 Theory 107

4.1.1.1 Generic Model of Viscoelasticity 107

4.1.1.2 Boundary Element Formulation 111

4.1.2 Numerical Examples 116
4.1.2.1 BVPs with Uniform Strain Field 117
4.1.2.2 BVPs with Non-Uniform Strain Field 121
4.1.3 Concluding Remarks 129
4.2 Time-Domain BEM Formulation for Nonlinear Power Type Viscoelasticity 131
4.2.1 Theory 131
4.2.1.1 Generic Model of Power Type Viscoelasticity 131
4.2.1.2 Boundary Element Formulation 134
4.2.2 Numerical Example 135
4.2.2.1 Model Problem 1: The Perforated Plate 136
4.2.2.2 Model Problem 2: The Flange 139
4.2.3 Concluding Remarks 143
4.3 Time-Domain BEM Formulation for nonlinear Power Type Viscoplasticity 145
4.3.1 Theory 145
4.3.1.1 Generic Model of Power Type Viscoplasticity 146
4.3.1.2 Boundary Element Formulation 149
4.3.1.3 Identification of Material Parameters by Optimization . 152
4.3.2 Numerical Example 156
4.3.2.1 Model Problem 1 - BVP with Uniform Strain Field . . . 156
4.3.2.2 Model Problem 2 - Flange 159
4.3.3 Concluding Remarks 160
5 CONCLUSION 163

REFERENCES 167

APPENDICES

CURRICULUM VITAE 193

LIST OF TABLES

TABLES

Table 2.1 Homogenized stresses of the uniaxial tension loading under uniform traction boundary condition for the current study and study by Miehe and Koch [1] 23

Table 2.2 Homogenized stress results of the uniaxial tension loading under linear displacement boundary condition for the current study and study by Miehe and Koch [1] 24

Table 2.3 Homogenized stresses of the uniaxial tension loading under periodic displacement boundary condition for the current study and study by Miehe and Koch [1] 26

Table 2.4 Homogenized stresses of the simple shear loading mode under uniform traction boundary condition for the current study and study by Miehe and Koch [1] 28

Table 2.5 Homogenized stresses of the simple shear loading under linear displacement boundary condition for the current study and study by Miehe and Koch [1] 29

Table 2.6 Homogenized stresses of the simple shear loading under periodic displacement boundary condition for the current study and study by Miehe and Koch [1] 29

Table 2.7 Material properties for the matrix and the inclusion phases presented by Fernandes et al. [2] 31

Table 2.8 Homogenized stress components of the an RVE consisting multi inclusions-voids for three types of boundary conditions (all stress components are presented in MPa) 36

Table 2.9 Material properties 36

Table 2.10 Number of elements used for the meshes of BEM and FEM models created for the comparison study 37

Table 2.11 Homogenized material properties obtained with three different mesh for boundary element and finite element methods 38

Table 2.12 Material and interface properties 48

Table 2.13 Solution times of analysis for different iteration stopping criteria . . 52

Table 2.14 Solution times of analysis for varying mesh sizes 52

Table 2.15 Investigated models 52

Table 2.16 Investigated models 52

Table 2.17 Material properties used to represent stiff and soft viscoelastic materials using Pronny series [3] 60

Table 2.18 Solution times of the Model1 and Model2 65

Table 2.19 Normal and effective volume fraction of inclusion, and volume fraction of interphase [4] 66

Table 2.20 Constants used to represent viscoelastic matrix material [4] 67

Table 2.21 Specific sinusoidal functions of the $\bar{\varepsilon}$ macroscopic strain loading along with the accompanying linear displacement boundary conditions . . 69

Table 3.1 Mesh-free interpolation techniques in literature 77

Table 3.2 MLS, RPIM, and analytical results for body force example for three different loadings 85

Table 4.1 Algorithmic box 116

Table 4.2 Model parameters used for the standard linear solids of Maxwell and Kelvin-type (SLS-M & SLS-K) 117

Table 4.3 Specific sinusoidal functions of the axial $u_x(t)$ and shear $u_y(t)$ loadings along with the accompanying boundary conditions in the perpendicular directions applied on the right edge 121

Table 4.4 Model parameters of the standard linear solid of Maxwell-type (SLS-M) in the heterogeneous BVPs 122

Table 4.5 Algorithmic box for the semi-implicit update of the viscoelastic strain 134

Table 4.6 Algorithmic box 136

Table 4.7 Model parameters used for plasticity with hardening 137

Table 4.8 Specific sinusoidal functions of the axial $u_x(t)$ loading along with the accompanying boundary conditions in the perpendicular directions applied on the left and right edges 137

Table 4.9 Four different loadings investigated for the flange problem 141

Table 4.10 Algorithmic box for constitutive law 149

Table 4.11 Algorithmic box 151

Table 4.12 Algorithmic box of nonlinear implicit driver algorithm for uni-axial tension 155

Table 4.13 Model parameters used for power type plasticity with hardening . . 157

Table 4.14 Four different loadings investigated for the flange problem 160

Table A1 Analytical and boundary element method stress results obtained on a simple elasticity problem under linear displacement boundary condition . 182

Table B1 Solution times of stiff and soft RVEs 183

Table C1 Integrands of domain integral $\int_\Omega f h d\Omega$ with source point at (0.25, 0.25) 184

Table C2 Fixed and adaptive monomial order results for MLS interpolation with fine mesh 185

Table C3 Fixed and adaptive monomial order results for RPIM interpolation with fine mesh 186

Table C4 Results for three different integration mesh for MLS interpolation . . 187

Table C5 Results for three different integration mesh for RPIM interpolation . 187

Table C6 Results for three different data point mesh for MLS interpolation . . 188

Table C7 Results for three different data point mesh for RPIM interpolation . 188

Table E1 Parameters of the SLS-Maxwell and Pure Maxwell models 190

Table F1 Boundary element meshes utilized in the mesh convergence study of the perforated plate 191

LIST OF FIGURES

FIGURES

Figure 2.1 Problem domain under the displacement and traction loadings . . 8

Figure 2.2 A typical heterogeneous rectangular RVE consists of a circular inclusion 12

Figure 2.3 Heterogeneous RVEs consisting of a matrix phase and a single centered or eccentric hole 22

Figure 2.4 Deformed shapes presented by Miehe and Koch [1] and current study under strain driven uniaxial tensile loading with uniform traction type boundary condition 24

Figure 2.5 Deformed shapes presented by Miehe and Koch [1] and current study under strain driven uniaxial tensile loading with linear displacement type boundary condition 25

Figure 2.6 Deformed shapes presented by Miehe and Koch [1] and current study under strain driven uniaxial tensile loading with periodic displacement type boundary condition 26

Figure 2.7 Deformed shapes presented by Miehe and Koch [1] and current study under strain driven simple shear loading with uniform traction type boundary condition 27

Figure 2.8 Deformed shapes presented by Miehe and Koch [1] and current study under strain driven simple shear loading with linear displacement type boundary condition 28

Figure 2.9 Deformed shapes presented by Miehe and Koch [1] and current study under strain driven simple shear loading with periodic displacement type boundary condition 30

Figure 2.10 Heterogeneous two-phase RVE with a matrix phase (black) and an inclusion phase (red) 31

Figure 2.11 For macroscopic strain driven loading, effect of change in the volume fraction of the soft inclusion on the homogenized stress results for different solution methods 32

Figure 2.12 For macroscopic strain driven loading, effect of change in the volume fraction of the stiff inclusion on the homogenized stress 33

Figure 2.13 For macroscopic strain driven loading, effect of change in the volume fraction of the void on the homogenized stress 34

Figure 2.14 Heterogeneous two-phase RVE with a matrix phase (black) and an inclusion phase (red) 35

Figure 2.15 Boundary element meshes of three-dimensional RVEs 38

Figure 2.16 Variation of the homogenized shear modulus (μ_H) results obtained by the asymptotic, self-consistent, Mori-Tanaka and the BEM-based homogenization methods presented in this study with the volume ratio of the reinforcing phase 39

Figure 2.17 (a) 8-node linear rectangular interface element defined between 8-node linear rectangular prism (brick) elements, 6-node linear triangle interface element defined between a 4-node linear tetrahedron and 10-node quadratic triangle interface element defined between 10-node quadratic tetrahedron [5], (b) Modeling of separation between reinforcement and interphase/matrix with zero thickness interface element [6] 40

Figure 2.18 Adhesion interface models for the normal stress vector under monotonic loading conditions 40

Figure 2.19 Frictionless adhesive interface models for tangential stress vector 41

Figure 2.20 Adhesion and friction in Tvergaard's interface model [7] 41

Figure 2.21 RCCM model which investigates the interface behavior in normal direction 41

Figure 2.22 Cohesive traction-separation model [8] 42

Figure 2.23 Interface nodes [8] 44

Figure 2.24 Investigated 2-phase representative volume element 47

Figure 2.25 Macroscopic stress-strain and iteration-strain curves of RVEs with same volume fraction but different inclusion diameters. Models involve cohesive interface models and results are obtained for three different boundary conditions. 48

Figure 2.26 Multi inclusion representative volume element 49

Figure 2.27 Macroscopic stress-strain curves of two RVEs consisting single and multi inclusions, involving cohesive interface model with different iteration starting conditions, obtained for periodic displacement boundary condition (PBC) 51

Figure 2.28 Macroscopic stress-strain curves of RVE consisting multi inclusions, involving cohesive interface model with different iteration stopping parameters and with varying mesh sizes, obtained for periodic displacement boundary condition (PBC) 51

Figure 2.29 Three-phase RVE consisting of matrix phase (black), interphase (blue), and inclusion (red) 59

Figure 2.30 BEM meshes of two-phase RVE with $\phi_f = 0.25$ and $\phi_f = 0.36$. 61

Figure 2.31 Storage and loss Young's modulus of viscoelastic stiff inclusion-soft matrix materials defined on a two-phase RVE having $\phi_f = 0.25$ and $\phi_f = 0.36$ 62

Figure 2.32 Storage and loss Young's modulus of viscoelastic soft inclusion-stiff matrix materials defined on a two-phase RVE having $\phi_f = 0.25$ and $\phi_f = 0.36$ 63

Figure 2.33 Boundary element mesh of three phase RVE with 0.3 and 0.1 volume fractions of inclusion and interphase, respectively 64

Figure 2.34 Storage and loss Young's modulus of Model1 and Model2 64

Figure 2.35 Two-phase BEM models for four different volume fractions of nclusions 66

Figure 2.36 Three-phase BEM models for four different volume fractions of inclusions 66

Figure 2.37 Young's modulus of a two-phase composite material with the change of frequency. Experimental results (shown with discrete data points), micromechanics solution (shown with dash lines-only for storage modulus) [4] and BEM results (solid lines) of the proposed method are presented for four different volume fractions of inclusions. 68

Figure 2.38 Young's modulus of a three-phase composite material with the change of frequency. Experimental results (shown with discrete data points) and BEM results (solid lines) of the proposed method are presented for four different volume fractions of inclusions. 68

Figure 2.39 The perforated plate model 69

Figure 2.40 The change in macroscopic stress with the applied macroscopic strain for the perforated plate domain with nonlinear power-type viscoelasticity is defined as material. 70

Figure 3.1 Problem domain Ω and auxiliary domain Ω_R [9] 73

Figure 3.2 Integration points on the triangular domain for two methods [9] . 76

Figure 3.3 Types of support domain around the desired point x_Q [10] 78

Figure 3.4 Boundary condition and integration mesh used for the body force example 84

Figure 3.5 Boundary condition and BEM mesh used for the steady state heat conduction example 87

Figure 3.6 Temperature and flux results for FEM and BEM on the bottom and right edge 87

Figure 3.7 Boundary conditions used for the elasticity and thermal conductivity problems 89

Figure 3.8 Change in displacements in x and y directions on the left edge . . 89

Figure 3.9 Variation of the exponential integral function ($\mathrm{E}_1(x)$) with x . . . 91

Figure 3.10 Problem domain with boundary conditions 96

Figure 3.11 Variation of temperature of the right boundary with time 96

Figure 3.12 Problem domain with boundary conditions 97

Figure 3.13 For three types of initial loading and two solution methods, variation of temperature with respect to x for different paths taken on the problem domain 98

Figure 3.14 For three types of initial loading and two solution methods, variation of temperature with respect to time for different points on the problem domain 99

Figure 3.15 Problem domain with boundary conditions 101

Figure 3.16 Time dependent contour plots for the BEM and ODE solutions of the problem involving internal heat generation 101

Figure 4.1 A generic rheological model of viscoleasticity 108

Figure 4.2 Problem domain under displacement and traction loadings 111

Figure 4.3 The viscoelastic rectangular body subjected to creep and relaxation 117

Figure 4.4 Boundary element mesh with inner points used for interpolation and CTM integration points 118

Figure 4.5 Analytical and BEM results for the creep-type BVP with uniform strain field modeled with (a) SLS-M and (b) SLS-K 119

Figure 4.6 Analytical and BEM results for the relaxation-type BVP with uniform strain field modeled with (a) SLS-M and (b) SLS-K 120

Figure 4.7 The viscoelastic solid body subjected to cyclic (a) axial and (b) shear loadings resulting in uneven strain distributions 121

Figure 4.8 Boundary element mesh with inner points used for interpolation and CTM integration points 123

Figure 4.9 Comparison of global (a) axial force-displacement and (b) axial force-time curves obtained by BEM and FEM for the BVP with non-uniform strain distribution 123

Figure 4.10 Contours of planar stress components σ_{xx} (first row), σ_{xy} (second row), and σ_{yy} (third row) obtained by the proposed BEM (first column) and FEM (second column) analyses of the axial BVP with non-uniform strain at $t = 37$ s. All stress values are in Pascals 124

Figure 4.11 The variation of σ_{xx} at $(x{=}2, y{=}1)$ over time for axially deformed BVP 125

Figure 4.12 Comparison of global (a) shear force-displacement and (b) shear force-time curves obtained by BEM and FEM for the BVP with non-uniform strain 126

Figure 4.13 Variation of ε_{yy} along the path located at $y = 1.5$ m and time $t = 7$ s for shear loading 127

Figure 4.14 Variation of (a) ε_{yy} and (b) σ_{yy} along the path located at $y = 1.5$ m and time $t = 7$ s for shear loading 127

Figure 4.15 Variation of σ_{xx} along the clamped vertical left edge at (a) $t = 7$ s and (b) $t = 32$ s for shear loading 128

Figure 4.16 Contours of planar stress components σ_{xx} (first row), σ_{xy} (second row), and σ_{yy} (third row) obtained by the proposed BEM (first column) and FEM (second column) analyses of the shear loading at $t = 7$ s. All stress values are in Pascals 129

Figure 4.17 A generic rheological model of viscoplasticity 131

Figure 4.18 The square body subjected to displacement type sinusoidal loading 137

Figure 4.19 Boundary element mesh with inner points used for interpolation and CTM integration points 138

Figure 4.20 Comparison of global reaction force-displacement curves obtained by BEM and FEM for the perforated plate model 139

Figure 4.21 Contours of the norm of viscoelastic strain for different δ values of 2, 3, and 4 are shown in three columns obtained by the proposed BEM (first row) and FEM (second row) analyses of the perforated plate problem at the time when the maximum loading is reached. 140

Figure 4.22 The flange body subjected to displacement type sinusoidal loading applied in radial direction 141

Figure 4.23 Boundary element mesh with inner points used for interpolation and CTM integration points 142

Figure 4.24 Change in the reaction force with respect to the applied displacement at the node located on the bottom left corner for the investigated loadings 144

Figure 4.25 Contours of norm of viscoelastic strain for loadings L2 (first column), L3 (second column), and L4 (third column) obtained by the proposed BEM (first row) and FEM (second row) analyses of the flange problem at $t = 25$ s 145

Figure 4.26 A generic rheological model of viscoplasticity 146

Figure 4.27 Change in shear stress with respect to shear strain for different loading rates of XCrNi 18.9 steel [11] 152

Figure 4.28 Change in shear stress with respect to shear strain for different loading rates of XCrNi 18.9 steel presented in [11] and obtained with nonlinear implicit driver algorithm 156

Figure 4.29 The square body subjected to displacement type ramp loading . . 157

Figure 4.30 Boundary element mesh with inner points used for interpolation and CTM integration points 158

Figure 4.31 FEM and BEM result for the uniform strain loading with different rates 158

Figure 4.32 The flange body subjected to displacement type sinusoidal loading applied in radial direction 159

Figure 4.33 Change in the reaction force with respect to the applied displacement at the node located on the bottom left corner for the investigated loadings 161

Figure A1 3D single phase boundary element model 181

Figure B1 Storage and loss Young's Modulus of viscoelastic stiff-stiff material (a)-(b) and soft-soft material (c)-(d) defined on both phases of a two-phase RVE 183

Figure C1 Three different integration domains used for the evaluation of the effect of integration points on the integral result 186

Figure C2 Three domains with different numbers of inner data points used for the evaluation of the effect of data points on the integral result 188

Figure E1 Analytical and BEM results for the relaxation-type BVP with uniform strain field modeled with (a) SLS-M and (b) the Pure Maxwell Model 190

Figure F1 The change in reaction force with respect to the applied axial loading for three models with different discretizations. 192

Figure F2 The change in reaction force with respect to the applied axial loading for different time steps 192

LIST OF ABBREVIATIONS

2D	2 Dimensional
3D	3 Dimensional
BEM	Boundary Element Method
BVP	Boundary Value Problem
CTM	Cartesian Transformation Integration Method
DMA	Dynamic Mechanical Analysis
DFT	Density Functional Theory
DRBEM	Dual Reciprocity Boundary Element Method
EFG	Element-free Galerkin Method
FEM	Finite Element Method
MD	Molecular Dynamics
MLS	Moving Least Square Method
MTHFE	Mathematical Theory of Homogenization Based Finite Element
ODE	Ordinary Differential Equation
PBC	Periodic Boundary Condition
RBF	Radial Basis Function
RPIM	Radial Point Interpolation Method
RVE	Representative Volume Element
TBC	Traction Boundary Condition
UBC	Displacement Boundary Condition

CHAPTER 1

INTRODUCTION

1.1 Motivation and Problem Definition

In the literature, different approaches are proposed for the numerical simulation of materials with heterogeneous microstructures. It is possible to collect these approaches into two large groups, which take into account the discontinuous nature of materials and consider materials as a continuous medium [12, 13]. Molecular dynamics and density functional theory are approaches that take into account the low-scale discontinuous structure of the material. On the other hand, continuum mechanics-based micro-mechanical approaches and Finite Element Method (FEM) are classified as methods that accept materials as continuous media. There are also multi-scale modeling approaches that combine these two approaches to some extent.

Approaches Considering Discontinuous Structure in the Low Scale

In the literature, two approaches are widely used. These are the approaches using Density Functional Theory (DFT) method [14] and Molecular Dynamics (MD) method. There are also coarse-grained models that define a number of atoms, a molecule, or a portion of a molecule as a single particle to accelerate the molecular dynamic method. Since the Density Functional Theory (DFT) has been formulated by Hohenberg and Kohn [14], it was the method commonly used in quantum mechanical calculations of small and medium-sized systems. The density functional theory is especially used in the determination of interaction energies, binding energies [15], and mechanical properties of a single carbon nano-tube in the calculation of mesh constants [16] and in the determination of elastic constants of titanium boride [17].

Unfortunately, while this method is generally effective for very small systems (several hundred atoms), the use of the method to determine the mechanical properties of a macro-scale system is very expensive. The Molecular Dynamics (MD) method is a multi-particulate numerical simulation method used to study the physical movement of atoms, molecules, or sub-units of the system at various scales under external forces and interactions with each other. In its most common description, the path followed by atoms in space is found in the numerical solution of Newton's equations of motion for the system of particles in interaction. In this solution, the forces between the particles and the potential energy are calculated from the intermolecular potentials or the molecular mechanical force fields. The accuracy of the simulations using MD methods is highly dependent on the inter-atomic potential used and the molecular mechanical force field. The selection of the appropriate potential and the determination of the parameters of this potential is of critical importance according to the material being modeled. As the size of the representative volume element (RVE) increases, the MD method becomes quite expensive in terms of calculation. For the RVEs including a large number of nano-reinforcements, the MD method is only possible with the use of computer clusters that will perform parallel calculations [18].

Large Scale Micro-mechanical Approaches

The main purpose of these approaches is to determine the effective properties of heterogeneous microstructures; therefore, these approaches are generally called homogenization methods. The simplest homogenization methods are the rule of mixture proposed by Voigt [19] and the inverse rule of mixtures proposed by Reuss [20]. In the rule of mixtures, it is assumed that the strain is the same everywhere in the microstructure, whereas, in the inverse rule of mixtures, the stress in the microstructure is assumed to be constant. The basic assumptions of these two methods are far from being realistic for materials with heterogeneous microstructures, making them very limited in use. On the other hand, the method of equivalent inclusion, defined by Eshelby, one of the pioneers in the field of homogenization, is still effectively used [21]. Based on the work of Eshelby on the equivalent conversion tensor, analytical solutions of homogenization methods such as Mori-Tanaka are developed [22]. These methods and approaches have long been used to determine the effective properties of

inhomogeneous materials. Additionally, the use of these approaches in calculating the effective properties of materials with heterogeneous microstructures has also increased in the last decades. In these materials, it is known that, in addition to the matrix and the micro-reinforcement, a third phase, the so-called interphase, is formed in the region close to the surface of the secondary phase, which has different properties than both the two phases in the microstructure. The three-phase homogenization methods [23, 24], which are derived from the Mori-Tanaka homogenization method, are also used to calculate the mechanical properties of materials with heterogeneous microstructures in recent years [25, 26, 27]. Unfortunately, these approaches have some limitations. Firstly, the derived analytical expressions apply to situations where both phases are assumed to be linear elastic. Secondly, these relationships are valid only for some ideal shapes, such as ellipsoids, spheres, and platelets.

Multi-scale Approaches

As the reinforcing phase in heterogeneous microstructures violates the homogeneity of the structure, it is a controversial topic to assume materials as a continuous medium when calculating the average properties of such materials. Especially in materials with nano-scale reinforcements, material interactions at the atomic level can control the material's behavior at the micro and macro scales. Under these conditions, computational methods of uniformly created spatial and temporal regimes connected in a multi-scale manner offer a viable solution approach. In this context, multi-scale approaches that combine different scales with different solution methods have been used in the numerical modeling of materials with heterogeneous microstructures, including polymer nano-composites [28, 25, 29, 30, 31].

Determination of the homogenized properties of a heterogeneous medium is very significant for multi-scale analyses. Generally, in multi-scale analysis, a macro-scale finite element model uses the homogenized properties extracted from a heterogeneous representative volume element (RVE) in micro or nano scale. The boundary element method (BEM) is a powerful, semi-analytical numerical technique with high accuracy that has been effectively used in the problems of elasticity, wave propagation, heat conduction, soil-structure interaction, and acoustics, to mention a few [32, 33, 34, 35,

36, 37]. BEM is a strong alternative to the finite element method (FEM), especially in the numerical analysis of boundary-value problems (BVPs) with stress concentrations that require greater precision. Probably, one of the most important advantages of BEM over the other numerical methods is that only the discretization of the boundary is sufficient to solve a BVP for the entire domain rather than discretizing the whole domain [38]. Therefore, in this thesis study, firstly, a boundary element method-based approach is developed to determine the homogenized stress tensor of an RVE.

Modeling of Inelasticity with BEM

In modeling of heterogeneous microstructures, it is common to observe that the matrix phase exhibits inelastic material behavior. Consequently, finding effective ways to model inelasticity using the Boundary Element Method (BEM) becomes a crucial challenge to address in order to determine the homogenized properties of the Representative Volume Element (RVE). While BEM's applicability to linear problems is well-established, its extension to nonlinear, particularly inelastic problems, has been limited. However, researchers have explored BEM's nonlinear solid mechanics applications since the 1970s. Various approaches have been proposed, including Laplace transformation for linear viscoelasticity, displacement discontinuity method for viscoelasticity, and the Dual Reciprocity Boundary Element Method (DRBEM) for inelastic problems. In many methods, it is observed that the treatment of inelastic models are handled mostly with rate formulations in BEM. It has been reported that the time step significantly influences the solution performance, requiring a fine temporal discretization, especially in the initial time steps. Therefore, in this thesis study, a novel algorithmic non-iterative formulation incorporating Cartesian Transformation Method (CTM) and Radial Point Interpolation Method (RPIM) for handling domain integrals is introduced to BEM's application to rate-dependent Boundary Value Problems (BVPs) for viscoelasticity and viscoplasticity models. Moreover, the proposed approach is versatile in a way that allows examination of not only the generalized models of viscoelasticity and viscoplasticity, but also more complex materials by incorporating parallel or serial branches. The success of the developed approach is demonstrated through various examples in which linear/nonlinear viscoelasticity and viscoplasticity material models are used.

1.2 The Outline of the Thesis

In Chapter 2 of the thesis study, a linear elastic BEM formulation for both 2D and 3D is presented. The chapter covers the introduction of uniform tractions, linear displacement, and periodic displacement boundary conditions to BEM for homogenization purposes. The section also includes solutions to various numerical problems involving heterogeneous microstructures. Subsequently, a cohesive traction-separation type interface modeling is implemented into the developed BEM. A comparison of the developed interface model with problems from the literature is presented. Finally, in Chapter 2, viscoelasticity modeling using the Dynamic Correspondence Principle with BEM is introduced, and its verification is conducted on three different examples from the literature, covering both experimental and numerical studies. The last homogenization example discussed in this section briefly follows the methodology for nonlinear inelasticity modeling approach presented in Chapter 4. A homogenization study of macroscopic strain loading on the perforated plate model with power-type viscoelasticity is presented.

In Chapter 3, the effective evaluation of domain integrals with BEM is emphasized as a crucial aspect. The chapter introduces a mesh-free integration method to BEM, to enhance the accuracy and efficiency of domain integral evaluations. A parameter study for the integration method with BEM is conducted to assess its performance and effectiveness. Additionally, the chapter concludes with practical applications of the developed approach on various engineering problems involving domain integrals.

In Chapter 4, a novel non-iterative approach for modeling inelasticity with BEM is introduced. The developed non-iterative BEM is applied to several linear and nonlinear viscoelasticity problems. A comparison is made with an iterative FEM solution, and excellent agreement is found. Additionally, the limitations of the developed approach in handling nonlinear power-type viscoplasticity are also discussed in this chapter. At the end of each section in Chapter 4, some concluding remarks are also presented.

In Chapter 5, a concise conclusion of this thesis study is presented, summarizing the key findings from the thesis study.

CHAPTER 2

APPLICATION OF BOUNDARY ELEMENT METHOD TO HOMOGENIZATION PROBLEMS

The boundary element method is a strong alternative to the finite element method (FEM) for linear problems with stress concentrations which require greater precision. The most important advantage of the boundary element method is that only the discretization of the boundary is sufficient to solve the entire domain, rather than the discretization of the whole volume [38]. In the problems having very small dimensions of inclusions in a matrix phase (i.e., polymer nano-composite materials), FEM analysis of such a structure will be computationally inefficient and expensive. Since the FEM mesh size should be smaller than the size of the filler in the neighborhood of the inclusion and should macroscopically cover all the material, the transition of the mesh from small-scale to macro-scale will be difficult. Hence, the number of finite elements required in such a mesh will be large.

2.1 2D and 3D Linear Elasticity Boundary Element Method Formulation

Consider a solid body Ω with a boundary Γ, as shown in Figure 2.1. The boundary Γ is decomposed into the parts Γ_u and Γ_t, where the displacement (Dirichlet) and traction (Neumann) boundary conditions are prescribed, respectively. Note that these parts fulfill the conditions $\Gamma = \Gamma_u \cup \Gamma_t$ and $\Gamma_u \cap \Gamma_t = \emptyset$.

Within the domain given in Figure 2.1, the balance of linear momentum under quasi-static conditions ($\rho \ddot{u}_i \approx 0$) can be written as

$$\frac{\partial \sigma_{ij}}{\partial x_j} + b_i = 0 \quad \text{in} \quad \Omega \,, \tag{2.1}$$

where the vector b_i denotes the given body forces. The Kelvin fundamental solution for the elastic body is used for weighing Equation 2.1 over the domain Ω.

$$\int_{\Omega} u^*_{ki} \left(\frac{\partial \sigma_{ij}}{\partial x_j} + b_i \right) d\Omega = 0. \tag{2.2}$$

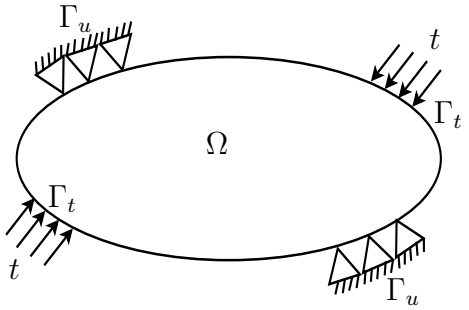


Figure 2.1: Problem domain under the displacement and traction loadings

In Equation 2.2, u^*_{ki} is the Kelvin displacement fundamental solution for an infinite elastic body. The application of the divergence theorem to the stress term appearing in the integral results in

$$\int_{\Gamma} u^*_{ki} \sigma_{ij} n_j d\Gamma - \int_{\Omega} \frac{\partial u^*_{ki}}{\partial x_j} \sigma_{ij} d\Omega + \int_{\Omega} u^*_{ki} b_i d\Omega = 0\,. \tag{2.3}$$

The partial derivative $(\partial u^*_{ki}/\partial x_j)$ appearing in the second integral of Equation 2.3 is the Kelvin strain fundamental solution $(\varepsilon^*_{kij} := \partial u^*_{ki}/\partial x_j)$. The Cauchy stress theorem $(t_i = \sigma_{ij} n_j)$ can be adopted in the first integral to write Equation 2.3 as

$$\int_{\Gamma} u^*_{ki} t_i d\Gamma - \int_{\Omega} \varepsilon^*_{kij} \sigma_{ij} d\Omega + \int_{\Omega} u^*_{ki} b_i d\Omega = 0\,, \tag{2.4}$$

where t_i is the traction vector. The second integral in Equation 2.4 can be recast as

$$\int_{\Omega} \varepsilon^*_{kij} \sigma_{ij} d\Omega = \int_{\Omega} \sigma^*_{kij} \varepsilon_{ij} d\Omega. \tag{2.5}$$

σ^*_{kij} is defined as $\sigma^*_{kij} := \varepsilon^*_{kij} \mathrm{C}_{ijmn}$, where C is the elasticity tensor. Rewriting $(\varepsilon^*_{kij} := \partial u^*_{ki}/\partial x_j)$ and applying the Cauchy's stress theorem, Equation 2.5 can be reduced to a boundary integral as

$$C_{ki} u_i + \int_{\Gamma} t^*_{ki} u_i d\Gamma = \int_{\Gamma} u^*_{ki} t_i d\Gamma + \int_{\Omega} u^*_{ki} b_i d\Omega\,, \tag{2.6}$$

where the term t^*_{ki} stands for the Kelvin's traction solution. The Kelvin solutions introduced in the formulation can be summarized for the 2-D plane strain case as follows

$$u^*_{ij} = \frac{-1}{8\pi(1-\nu)\mu}\Big\{ (3-4\nu)\ln\frac{1}{r}\delta_{ij} - r_{,i}r_{,j}\Big\}\,, \tag{2.7a}$$

$$t^*_{ij} = \frac{-1}{4\pi(1-\nu)r}\Big\{ [(1-2\nu)\delta_{ij} + 2r_{,i}r_{,j}]\,\frac{\partial r}{\partial n} - (1-2\nu)(r_{,i}n_j - r_{,j}n_i)\Big\}\,, \tag{2.7b}$$

and for 3-D cases, they are given as

$$u^*_{ij} = \frac{1}{16\pi\mu(1-\nu)r}\left[(3-4\nu)\delta_{ij} + r_{,i}r_{,j}\right]\,, \tag{2.8a}$$

$$t^*_{ij} = \frac{-1}{8\pi\mu(1-\nu)r^2}\left\{\frac{d}{r}\left[(1-2\nu)\delta_{ij} + 3r_{,i}r_{,j}\right] + (1-2\nu)(r_{,i}n_j + n_i r_{,j})\right\}. \tag{2.8b}$$

In Equations 2.7 and 2.8, $r := \sqrt{r_i r_i}$, $r_i := y_i - x_i$ denotes the distance between the source and the field points of BEM with r_i being the components of $\boldsymbol{r}$ and $\partial r/\partial n := n_i \partial r/\partial y_i$ is the perpendicular distance between the source and the element containing field points. Moreover, $r_{,i}$ is defined as the partial derivative of r with respect to y_i. By setting $\nu \to \nu/(\nu+1)$ in the relations (2.7), the plane stress assumption can be adopted. The way to calculate the matrix C_{ki} is deeply discussed by Mantic [39]. A straightforward way to determine it is by using the concept of rigid body motion.

Logarithmic functions are incorporated into the displacement basic solution for the two-dimensional problems as presented in Figure 2.7. However, these logarithmic terms may introduce non-uniqueness into the boundary element solutions. Typically, this issue can be resolved by normalizing the distance 'r' within the logarithmic term relative to some dimension, such as the maximum distance in the domain. It's important to note that this normalization process does not alter the solution; it simply introduces a rigid body displacement of magnitude into the formulation. Different formulations for the two-dimensional kernel solution is presented in [38, 35]. Moreover, the domain integral appearing in Equation 2.6 is handled by the mesh-free methodology presented in Chapter 3, and the body forces will be assumed as zero for the problems handled in this chapter. Equation 2.6 is solved by discretization of the boundary domain Γ into boundary elements. Note that for 2-D geometries, the boundary elements will be 1-D line elements, and for 3-D domains, the boundary elements will be 2-D surface elements. Linear boundary elements are employed for 2-D BEM solutions, while constant boundary elements are used for 3-D BEM solutions in this study. In

isoparametric element formulation, the nodal coordinates x_j, the displacement fields u_j and the traction fields t_j can be written as follows.

$$\begin{aligned} x_j &= \sum_{\alpha=1}^{m} N_\alpha(\eta) x_j^\alpha \\ u_j &= \sum_{\alpha=1}^{m} N_\alpha(\eta) u_j^\alpha \\ t_j &= \sum_{\alpha=1}^{m} N_\alpha(\eta) t_j^\alpha \end{aligned} \tag{2.9}$$

where N_α is the isoparametric shape functions. These shape functions are defined in terms of non-dimensional coordinates η defined between -1 to 1. For linear elements, the shape functions are defined as

$$N_1 = \frac{1}{2}(1-\eta) \qquad N_2 = \frac{1}{2}(1+\eta). \tag{2.10}$$

After discretizing the integral equation Equation 2.6 into N_e boundary elements with N_n nodes and utilizing the isoparametric shape functions N_α on the boundary Γ, the discretized form of Equation 2.6 can be expressed as

$$C_{ki} u_i + \sum_{n=1}^{N_e} \sum_{\alpha=1}^{N_n} H_{ki}^{n\alpha} u_i^{n\alpha} = \sum_{n=1}^{N_e} \sum_{\alpha=1}^{N_n} G_{ki}^{n\alpha} t_i^{n\alpha}. \tag{2.11}$$

Moreover, by expressing Equation 2.11 for all the boundary nodes, a linear system of equations can be obtained. In the matrix form, the equation system can be represented as

$$\tilde{\mathbf{H}}\mathbf{u} = \mathbf{G}\mathbf{t}\,. \tag{2.12}$$

Components of the matrices in Equation 2.12 can be expressed separately in indicial form as

$$\tilde{H}_{ki} = C_{ki} + \sum_{n=1}^{N_e} \sum_{\alpha=1}^{N_n} H_{ki}^{n\alpha}\,, \tag{2.13a}$$

$$G_{ki} = \sum_{n=1}^{N_e} \sum_{\alpha=1}^{N_n} G_{ki}^{n\alpha}\,. \tag{2.13b}$$

By considering the boundary conditions of the problem, the known and unknown boundary quantities of Equation 2.12 can be combined on each side, and the resultant

system becomes

$$\mathbf{A}\,\mathbf{x} = \mathbf{b}. \tag{2.14}$$

In Equation 2.14, matrix $\mathbf{A}$ is the unsymmetric and densely populated coefficient matrix. The vector $\boldsymbol{x}$ is composed of the unknowns, which include the tractions and displacements of the boundary nodes, while the vector b is known and determined from the boundary conditions. The major drawback of BEM compared to FEM is the unsymmetric and highly populated coefficient matrix. Various numerical methods have been proposed in the literature for efficiently solving Equation 2.14 [36].

In general BEM solutions, depending on the characteristics of the kernel and the collocation point's position concerning the element being integrated, five distinct categories of integral singularities can be observed. These categories include regular, nearly singular, weakly singular, strongly singular, and hypersingular integrals. In the kernel expressions of the boundary element formulation, weak and strong singularities are the most common types of singularities that occur. The *weak singularities* are defined as the singularities when the collocation node are within the integration element, and the singularities of the kernel for two- and three-dimensional problems are of order O($\ln(1/r)$) and O($1/r$), respectively. There are three fundamental methods for dealing with this kind of integral: Weighted Gaussian Integration, Transformation of Variable, and Substraction of Singularity [36]. *Strongly singular* integrals are encountered in the flow, displacement, and stress boundary element integral equations when the integrands become unbounded, preventing standard Riemann integration. In such cases, the result of the integration corresponds to the finite portion of the diverging integral. The conditions for the existence of finite-part integrals are the same as those for principal-value integrals, involving considerations of continuity. In Aliabadi's work [36], methods for addressing strong singular integrals are thoroughly discussed for the three fundamental approaches typically employed to handle weak singularities. This thesis work adopts the methods outlined in the referenced study to address singular integrals.

2.2 Homogenization of Linear Elasticity

Determination of the homogenized properties of a heterogeneous medium is very significant for multi-scale analyses. Generally, in multi-scale analysis, a macro-scale finite element model requires the determination of the homogenized moduli and the stress tensor at each integration point. Therefore, effective and robust determination of homogenized properties of heterogeneous representative volume elments (RVEs) by using numerical solutions is crucial. For this purpose, a boundary element method-based approach is developed to determine the homogenized properties of heterogeneous RVEs. The homogenization with BEM is achieved by the implementation of the three classical types of boundary conditions.

2.2.1 Implementation of Boundary Conditions to BEM

To explain how the uniform traction, linear displacement, and periodic boundary conditions are implemented on the BEM algorithm, a typical rectangular RVE with inclusion, as shown in Figure 2.2, is considered. Domain variables presented in Figure

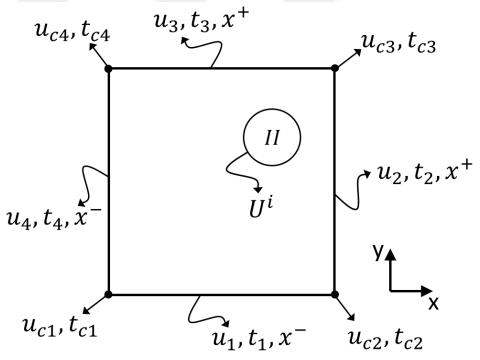


Figure 2.2: A typical heterogeneous rectangular RVE consists of a circular inclusion

2.2 can be introduced as follows.

- Nodes except corners have two displacement ($\mathbf{u}_n^i$) and two traction ($\mathbf{t}_n^i$) components.

$$\mathbf{u}_n^i = [u_{n_x}^i,\ u_{n_y}^i] \qquad \mathbf{t}_n^i = [t_{n_x}^i,\ t_{n_y}^i]$$

  - Superscript i denotes the edge number on the boundary of RVE.

– Subscripts n_x and n_y denote the field variable of the n^{th} node in the x and y directions, respectively.

- $\mathbf{u}^i$ and $\mathbf{t}^i$ are the vectors composed of displacements and tractions at nodes located on the i^{th} edge of the outer boundary except the corner nodes, and it is defined as,

$$\mathbf{u}^i = [u^i_{1_x}\ u^i_{1_y}\ u^i_{2_x}\ u^i_{2_y}\ ...\ u^i_{[(M-4)/4]_x}\ u^i_{[(M-4)/4]_y}]$$

$$\mathbf{t}^i = [t^i_{1_x}\ t^i_{1_y}\ t^i_{2_x}\ t^i_{2_y}\ ...\ t^i_{[(M-4)/4]_x}\ t^i_{[(M-4)/4]_y}],$$

  where M is the total number of nodes on the outer boundary of the RVE ("-4" is for components of the corners).

- Corners have two displacement ($\boldsymbol{u_{ci}}$) and four traction ($\boldsymbol{t_{ci}}$) components.

$$\mathbf{u}_{ci} = [u_{ci_x}\ u_{ci_y}] \qquad \mathbf{t}_{ci} = [t^{before}_{ci_x}\ t^{before}_{ci_y}\ t^{after}_{ci_x}\ t^{after}_{ci_y}]$$

  – Subscripts ci_x and ci_y denote the field variable of the i^{th} corner in the x and y directions, respectively.

  – The superscripts $before$ and $after$ in $\mathbf{t}_{ci}$ represent the tractions before and after the corner node in global coordinates, considering a counter-clockwise rotation of the outer domain.

- $\mathbf{U}^i$ are the displacements of the nodes located on the interior boundary i. Tractions at those nodes are calculated at the post-process.

2.2.1.1 Uniform Tractions

This type of boundary condition ensures a constant stress state on every element located on the boundary of the RVE. Firstly, to ensure this condition, Equation 2.12 is written in the following form

$$\mathbf{G}\mathbf{t}_n - \mathbf{H}\mathbf{u}_n = \mathbf{0}. \tag{2.15}$$

In Equation 2.17, a set of linear equations for the uniform traction-type boundary condition is given. The presented system has the first ten rows for the set of relations with each consisting of more than one equation. The relations used to implement the uniform traction boundary condition are summarized as follows.

- The 1^{st} lines of the equation system is the classical BEM equation (Equation 2.15).
- Between the 2^{nd} and 9^{th} lines of the equation system, a constant stress state ($\bar{\boldsymbol{\sigma}}$) is governed in each element on the outer boundary of RVE using Cauchy's stress principle ($\boldsymbol{t} = \boldsymbol{\sigma n}$).
- The 10^{th} and the last line of the equation system ensures that the volumetric average of the total strain on the boundary of the RVE equals the applied macroscopic strain $\bar{\boldsymbol{\varepsilon}}$ [40].

$$\bar{\boldsymbol{\varepsilon}} := \frac{1}{|V|} \int_{\partial V} \text{sym}[\boldsymbol{u} \otimes \boldsymbol{n}] dA \tag{2.16}$$

$$\begin{bmatrix} \mathbf{G}_1 & \bar{\mathbf{H}}_1 & \cdots & \mathbf{G}_4 & \bar{\mathbf{H}}_4 & \widetilde{\mathbf{H}}_i & \mathbf{G}_c^1 & \bar{\mathbf{H}}_c^1 & \cdots & \mathbf{G}_c^4 & \bar{\mathbf{H}}_c^4 & 0 \\ \mathbf{I} & 0 & \cdots & 0 & 0 & 0 & 0 & 0 & \cdots & 0 & 0 & \tilde{\mathbf{N}}_1 \\ \vdots & \vdots & \ddots & \vdots & \vdots & \vdots & \vdots & \vdots & \ddots & \vdots & \vdots & \vdots \\ 0 & 0 & \cdots & \mathbf{I} & 0 & 0 & 0 & 0 & \cdots & 0 & 0 & \tilde{\mathbf{N}}_4 \\ 0 & 0 & \cdots & 0 & 0 & 0 & \mathbf{I} & 0 & \cdots & 0 & 0 & \tilde{\mathbf{N}}_c^1 \\ \vdots & \vdots & \ddots & \vdots & \vdots & \vdots & \vdots & \vdots & \ddots & \vdots & \vdots & \vdots \\ 0 & 0 & \cdots & 0 & 0 & 0 & 0 & 0 & \cdots & \mathbf{I} & 0 & \tilde{\mathbf{N}}_c^4 \\ 0 & \mathbf{S}_1 & \cdots & 0 & \mathbf{S}_4 & 0 & 0 & \mathbf{S}_c^1 & \cdots & 0 & \mathbf{S}_c^4 & 0 \end{bmatrix} \begin{bmatrix} \mathbf{t}_1 \\ \mathbf{u}_1 \\ \vdots \\ \mathbf{t}_4 \\ \mathbf{u}_4 \\ \mathbf{U}^i \\ \mathbf{t}_{c1} \\ \mathbf{u}_{c1} \\ \vdots \\ \mathbf{t}_{c4} \\ \mathbf{u}_{c4} \\ \bar{\boldsymbol{\sigma}} \end{bmatrix} = \begin{bmatrix} \bar{\mathbf{H}}_c^4 \\ \bar{\mathbf{H}}_1 \\ \vdots \\ \tilde{\mathbf{N}}_1 \\ \bar{\mathbf{H}}_1 \\ \vdots \\ \tilde{\mathbf{N}}_c^4 \\ \bar{\boldsymbol{\varepsilon}} \end{bmatrix} \tag{2.17}$$

Variables used in Equation 2.17 can be summarized as follows.

- $\bar{\boldsymbol{\sigma}}$ is the homogenized stress tensor and defined as $\bar{\boldsymbol{\sigma}} = [\bar{\sigma}_{xx}\ \bar{\sigma}_{xy}\ \bar{\sigma}_{yy}]$.
- Matrices $\widetilde{\mathbf{H}}_i$ and $\bar{\mathbf{H}}_i$ are defined as,

$$\widetilde{\mathbf{H}}_i = -\mathbf{H}_i - \mathbf{G}_i(\mathbf{G}^{II})^{-1}\mathbf{H}^{II} \qquad \bar{\mathbf{H}}_i = -\mathbf{H}_i.$$

- $\mathbf{G}^{II}$ and $\mathbf{H}^{II}$ are the matrices obtained from the BEM equations written for the inclusion phase "II".
- $\mathbf{I}$ is the identity matrix with size of $size(\mathbf{t}_i) \times size(\mathbf{t}_i)$.

- $\tilde{\mathbf{N}}_i$ consists of elemental unit vectors for intermediate nodes on the boundary of the RVE, and it is defined as,

$$\tilde{\mathbf{N}}_i = [\mathbf{n}^1\ \mathbf{n}^2\ ...\ \mathbf{n}^{(M-4)/4}]^T,$$

where

$$\mathbf{n}^i = \begin{bmatrix} -n_1 & -n_2 & 0 \\ 0 & -n_1 & -n_2 \end{bmatrix}$$

is the matrix defined in terms of components of the resultant unit normal n_1 and n_2 of elements containing node i, and M is number of nodes on edges of the RVE (-4 in equation is for corners). n_1 and n_2 are the components of the unit vector on the corresponding element.

- $\tilde{\mathbf{N}}_c^n$ consists of elemental unit vectors for corners nodes on the boundary of the RVE, and it is defined as,

$$\tilde{\mathbf{N}}_c^n = \begin{bmatrix} -n_1^b & -n_2^b & 0 \\ 0 & -n_1^b & -n_2^b \\ -n_1^a & -n_2^a & 0 \\ 0 & -n_1^a & -n_2^a \end{bmatrix},$$

where superscript n denotes the n^{th} corner. Superscripts b and a are for the elements before and after the corner node.

- Integral in Equation 2.16 can be approximated with a discrete sum as follows.

$$\bar{\boldsymbol{\varepsilon}} := \frac{1}{|V|}\int_{\partial V} \text{sym}[\mathbf{u}\otimes\mathbf{n}]dA \ \Rightarrow\ \bar{\boldsymbol{\varepsilon}} = \frac{1}{V}\sum_{q=1}^{M}\text{sym}[\mathbf{u}_q\otimes\mathbf{a}_q] \ \Rightarrow\ \bar{\boldsymbol{\varepsilon}} = \sum_{q=1}^{M}\mathbf{S}_q\mathbf{u}_q,$$

where $\mathbf{S}_n = [\mathbf{S}_n^1\ \mathbf{S}_n^2\ ...\ \mathbf{S}_n^{(M-4)/4}]$.

- $\mathbf{S}_n^q$ is a matrix consists of the area vector $\mathbf{a}_q$ of the q^{th} node on the n^{th} boundary,

$$\mathbf{S}_n^q = \frac{1}{2V}\begin{bmatrix} 2a_1 & 0 \\ 0 & 2a_2 \\ a_2 & a_1 \end{bmatrix},$$

where a_1 and a_2 are the components of the nodal area vector, which is defined as $\mathbf{a}_q = \frac{1}{2}[\mathbf{x}_{q+1} - \mathbf{x}_{q-1}] \times \mathbf{e}_3$. The vector $\mathbf{e}_3$ is the unit vector in the out of plane direction.

2.2.1.2 Linear Displacement

This type of boundary condition ensures a linear deformation state at nodes located on the boundary ∂V of the RVE, as depicted in Equation 2.18.

$$\mathbf{u} = \bar{\boldsymbol{\varepsilon}}\mathbf{x} \quad \text{on } \mathbf{x} \in \partial V \tag{2.18}$$

where $\bar{\boldsymbol{\varepsilon}}$ is the macroscopic strain tensor. Equation 2.19 provides a set of linear equations for implementing the linear displacement type boundary condition. The system presented consists of five lines, each line representing a set of relations comprising multiple equations. The summary of the relations utilized to implement the linear displacement boundary condition is as follows.

- The 1^{st} line of the equation system is the classical BEM equation (Equation 2.14) written in the form of $\mathbf{Gt}_n = \mathbf{Hu}_n$.
- Between the 2^{nd} and 5^{th} lines of the equation system, continuity of the tractions at the corner nodes is achieved. This procedure is further explained in detail.

$$\begin{bmatrix} \mathbf{G}_1 & \mathbf{G}_2 & \mathbf{G}_3 & \mathbf{G}_4 & \widetilde{\mathbf{H}}_i & \mathbf{G}_c^1 & \mathbf{G}_c^2 & \mathbf{G}_c^3 & \mathbf{G}_c^4 \\ 0 & 0 & 0 & 0 & 0 & \mathbf{D}_1 & 0 & 0 & 0 \\ 0 & 0 & 0 & 0 & 0 & 0 & \mathbf{D}_2 & 0 & 0 \\ 0 & 0 & 0 & 0 & 0 & 0 & 0 & \mathbf{D}_3 & 0 \\ 0 & 0 & 0 & 0 & 0 & 0 & 0 & 0 & \mathbf{D}_4 \end{bmatrix} \begin{bmatrix} \mathbf{t}_1 \\ \mathbf{t}_2 \\ \mathbf{t}_3 \\ \mathbf{t}_4 \\ \mathbf{U}^i \\ \mathbf{t}_{c1} \\ \mathbf{t}_{c2} \\ \mathbf{t}_{c3} \\ \mathbf{t}_{c4} \end{bmatrix} = \begin{bmatrix} \mathbf{H} & 0 & 0 & 0 & 0 \\ 0 & \mathbf{I} & 0 & 0 & 0 \\ 0 & 0 & \mathbf{I} & 0 & 0 \\ 0 & 0 & 0 & \mathbf{I} & 0 \\ 0 & 0 & 0 & 0 & \mathbf{I} \end{bmatrix} \begin{bmatrix} \mathbf{u} \\ \mathbf{e}^1 \\ \mathbf{e}^2 \\ \mathbf{e}^3 \\ \mathbf{e}^4 \end{bmatrix} \tag{2.19}$$

Variables and relations used in Equation 2.19 can be summarized as follows.

- The equation $\mathbf{u} = \bar{\boldsymbol{\varepsilon}}\mathbf{x}$ describes the relationship between the nodal coordinates $\mathbf{x}$, macroscopic strain $\bar{\boldsymbol{\varepsilon}}$, and displacements $\mathbf{u}$ of the nodes located on the boundary of the RVE.
- $\mathbf{I}$ is a identity matrix.
- Matrix $\widetilde{\mathbf{H}}_i$ is defined as,

$$\widetilde{\mathbf{H}}_i = -\mathbf{H}_i - \mathbf{G}_i(\mathbf{G}^{II})^{-1}\mathbf{H}^{II}$$

- $\mathbf{G}^{II}$ and $\mathbf{H}^{II}$ are the matrices obtained from the BEM equations written for inclusion phase "II".

- Last four lines of the above equation satisfy the traction continuity at the corners. For corner i,

$$\mathbf{D}_i = \begin{bmatrix} -f_1(b) & f_2(b) & f_1(a) & -f_2(a) \\ -f_3(b) & f_4(b) & f_3(a) & -f_4(a) \end{bmatrix},$$

  where b and a are the elements before and after corner i. Functions f_1, f_2, f_3 and f_4 are defined as,

$$f_1(x) = 2s_x^2 c_x + \left(s_x^2 c_x \frac{\nu}{1-\nu} + c_x^3 \right), \; f_2(x) = 2s_x c_x^2 - \left(s_x^3 \frac{\nu}{1-\nu} + c_x^2 s_x \right)$$

$$f_3(x) = 2s_x^2 c_x - \left(s_x^2 c_x + c_x^3 \frac{\nu}{1-\nu} \right), \; f_4(x) = 2s_x c_x^2 + \left(s_x^3 + c_x^2 s_x \frac{\nu}{1-\nu} \right),$$

  where ν is the Poisson's ratio, and the normal vector of an element "e" is defined as $\vec{\mathbf{n}_e} = c_x \vec{i} + s_x \vec{j}$.

- On the right-hand side of the equation, everything is known. For corners, $\mathbf{e}^c$ is defined as

$$\mathbf{e}^c = \begin{bmatrix} s_b^2 \varepsilon_b \dfrac{E}{1-v}^2 - s_a^2 \varepsilon_a \dfrac{E}{1-v}^2 \\ c_a^2 \varepsilon_a \dfrac{E}{1-v}^2 - c_b^2 \varepsilon_b \dfrac{E}{1-v}^2 \end{bmatrix},$$

  where ε_b and ε_a are the normal strains in the element direction (ε_{11}) of elements before and after the corner node, calculated by using the derivatives of the shape functions and the prescribed displacements at the nodes on ∂V, respectively.

After the determination of the unknown vector, using the traction values on the nodes located at the boundary of RVE, macroscopic stress tensor $\bar{\boldsymbol{\sigma}}$ is evaluated using Equation 2.20.

$$\bar{\boldsymbol{\sigma}} := \frac{1}{|V|} \int_{\partial V} \text{sym}[\mathbf{t} \otimes \mathbf{x}] dA \tag{2.20}$$

2.2.1.3 Periodic Displacement

This type of boundary condition guarantees periodic deformations and anti-periodic traction states at the nodes situated on the boundary ∂V of the RVE, as illustrated in

Equation 2.21.

$$\mathbf{t}(x^+) + \mathbf{t}(x^-) = \mathbf{0} \quad \text{and} \quad \mathbf{u}(x^+) - \mathbf{u}(x^-) = \bar{\boldsymbol{\varepsilon}}(x^+ - x^-) \tag{2.21}$$

Here, the boundary ∂V is decomposed into two parts the upper (∂V^+) and lower (∂V^-) boundaries. Nodes located on these upper and lower boundaries are coupled. In Figure 2.2, edges shown with subscripts $1-3$ and $2-4$ are coupled, and Equation 2.21 is written for the nodes located on these coupled edges. In Equation 2.22, a linear set of equations for periodic displacement-type boundary condition is given. The presented system comprises 11 lines of relations, with each line containing multiple equations. The relations used to implement the periodic displacement boundary condition are summarized as follows.

- The 1^{st} line of equation system is the classical BEM equation (Equation 2.14) written in the form of $\mathbf{Gt}_n - \mathbf{Hu}_n = \mathbf{0}$.
- Edges 1-3 and 2-4, shown in Figure 2.2, are coupled for periodicity.
  - Lines 2 and 4 are the relations of tractions written for intermediate nodes located on edges 1-3 and 2-4:

    $$\mathbf{t}(x^+) + \mathbf{t}(x^-) = \mathbf{0}$$

  - Lines 3 and 5 are the relations of displacements written for intermediate nodes located on edges 1-3 and 2-4:

    $$\mathbf{u}(x^+) - \mathbf{u}(x^-) = \bar{\boldsymbol{\varepsilon}}(x^+ - x^-)$$

- Between the 6^{th} and 9^{th} line of the equation system, displacements of the corner nodes are fixed using

  $$\mathbf{u}_{cn} = \bar{\boldsymbol{\varepsilon}} x_{cn}.$$

  The relation is written for an arbitrary corner cn.
- The 10^{th} line of the equation system involves four equations.
  - First two equations equate the addition of tractions before corner-1 and after corner-2 to zero.

    $$\mathbf{t}_{c1}^{before} + \mathbf{t}_{c2}^{after} = \mathbf{0}$$

– Last two equations equate the addition of tractions after corner-1 and before corner-4 to zero.

$$\mathbf{t}_{c1}^{after} + \mathbf{t}_{c4}^{before} = \mathbf{0}$$

- The 11^{th} line of equation system involves four equations.

  – First two equations equate the addition of tractions before corner-3 and after corner-4 to zero.

$$\mathbf{t}_{c3}^{before} + \mathbf{t}_{c4}^{after} = \mathbf{0}$$

  – Last two equations equate the addition of tractions after corner-3 and before corner-2 to zero.

$$\mathbf{t}_{c3}^{after} + \mathbf{t}_{c2}^{before} = \mathbf{0}$$

- Upper-lower and left-right boundaries of Figure 2.2 are coupled for periodicity

$$\mathbf{u}^{ij} = \bar{\boldsymbol{\varepsilon}}(\mathbf{x}_i - \mathbf{x}_j),$$

  where $\mathbf{x}_i$ are coordinates of the nodes located on boundary i except the corner nodes.

$$\begin{bmatrix}
[\mathbf{G}_1\ \bar{\mathbf{H}}_1] & [\mathbf{G}_2\ \bar{\mathbf{H}}_2] & [\mathbf{G}_3\ \bar{\mathbf{H}}_3] & [\mathbf{G}_4\ \bar{\mathbf{H}}_4\ \widetilde{\mathbf{H}}_i] & [\mathbf{G}_c^1\ \mathbf{H}_c^1\ \mathbf{G}_c^2\ \mathbf{H}_c^2\ \mathbf{G}_c^3\ \mathbf{H}_c^3\ \mathbf{G}_c^4\ \mathbf{H}_c^4] \\
[0\ \ 0] & [\mathbf{I}\ \ 0] & [0\ \ 0] & [\mathbf{I}_s\ \ 0\ \ 0] & [0\ \ 0\ \ 0\ \ 0\ \ 0\ \ 0\ \ 0\ \ 0] \\
[0\ \ 0] & [0\ \ \mathbf{I}] & [0\ \ 0] & [0\ \ \text{-}\mathbf{I}_s\ \ 0] & [0\ \ 0\ \ 0\ \ 0\ \ 0\ \ 0\ \ 0\ \ 0] \\
[\mathbf{I}_s\ \ 0] & [0\ \ 0] & [\mathbf{I}\ \ 0] & [0\ \ 0\ \ 0] & [0\ \ 0\ \ 0\ \ 0\ \ 0\ \ 0\ \ 0\ \ 0] \\
[0\ \ \text{-}\mathbf{I}_s] & [0\ \ 0] & [0\ \ \mathbf{I}] & [0\ \ 0\ \ 0] & [0\ \ 0\ \ 0\ \ 0\ \ 0\ \ 0\ \ 0\ \ 0] \\
[0\ \ 0] & [0\ \ 0] & [0\ \ 0] & [0\ \ 0\ \ 0] & [0\ \ \mathbf{I}_2\ \ 0\ \ 0\ \ 0\ \ 0\ \ 0\ \ 0] \\
[0\ \ 0] & [0\ \ 0] & [0\ \ 0] & [0\ \ 0\ \ 0] & [0\ \ 0\ \ 0\ \ \mathbf{I}_2\ \ 0\ \ 0\ \ 0\ \ 0] \\
[0\ \ 0] & [0\ \ 0] & [0\ \ 0] & [0\ \ 0\ \ 0] & [0\ \ 0\ \ 0\ \ 0\ \ 0\ \ \mathbf{I}_2\ \ 0\ \ 0] \\
[0\ \ 0] & [0\ \ 0] & [0\ \ 0] & [0\ \ 0\ \ 0] & [0\ \ 0\ \ 0\ \ 0\ \ 0\ \ 0\ \ 0\ \ \mathbf{I}_2] \\
[0\ \ 0] & [0\ \ 0] & [0\ \ 0] & [0\ \ 0\ \ 0] & [\mathbf{I}_4\ \ 0\ \ \mathbf{A}\ \ 0\ \ 0\ \ 0\ \ \mathbf{B}\ \ 0] \\
[0\ \ 0] & [0\ \ 0] & [0\ \ 0] & [0\ \ 0\ \ 0] & [0\ \ 0\ \ \mathbf{B}\ \ 0\ \ \mathbf{I}_4\ \ 0\ \ \mathbf{A}\ \ 0]
\end{bmatrix}
\begin{bmatrix}
\mathbf{t}_1 \\ \mathbf{u}_1 \\ \mathbf{t}_2 \\ \mathbf{u}_2 \\ \mathbf{t}_3 \\ \mathbf{u}_3 \\ \mathbf{t}_4 \\ \mathbf{u}_4 \\ \mathbf{U}^i \\ \mathbf{t}_{c1} \\ \mathbf{u}_{c1} \\ \mathbf{t}_{c2} \\ \mathbf{u}_{c2} \\ \mathbf{t}_{c3} \\ \mathbf{u}_{c3} \\ \mathbf{t}_{c4} \\ \mathbf{u}_{c4}
\end{bmatrix}
=
\begin{bmatrix}
0 \\ 0 \\ \mathbf{u}^{24} \\ 0 \\ \mathbf{u}^{31} \\ \mathbf{u}_{c1} \\ \mathbf{u}_{c2} \\ \mathbf{u}_{c3} \\ \mathbf{u}_{c4} \\ 0 \\ 0
\end{bmatrix} \tag{2.22}$$

Variables and relations used in Equation 2.22 can be summarized as follows.

- Matrices $\widetilde{\mathbf{H}}_i$ and $\bar{\mathbf{H}}_i$ are defined as,

$$\widetilde{\mathbf{H}}_i = -\mathbf{H}_i - \mathbf{G}_i(\mathbf{G}^{II})^{-1}\mathbf{H}^{II} \qquad \bar{\mathbf{H}}_i = -\mathbf{H}_i.$$

- $\mathbf{G}^{II}$ and $\mathbf{H}^{II}$ are the matrices obtained from the BEM equations written for the inclusion phase "II".

- $\mathbf{I}$ and $\mathbf{I}_n$ are identity matrices with sizes of $size(\mathbf{t}_i) \times size(\mathbf{t}_i)$ and $n \times n$, respectively. Matrix $\mathbf{I}_s$ has also a size of $size(\mathbf{t}_i) \times size(\mathbf{t}_i)$. Matrices $\mathbf{I}_s$, $\mathbf{A}$ and $\mathbf{B}$ are defined as,

$$\mathbf{I}_s = \begin{bmatrix} \mathbf{0} & \mathbf{0} & \cdots & \mathbf{0} & \mathbf{1} \\ \mathbf{0} & \mathbf{0} & \cdots & \mathbf{1} & \mathbf{0} \\ \vdots & \vdots & \ddots & \vdots & \vdots \\ \mathbf{0} & \mathbf{1} & \cdots & \mathbf{0} & \mathbf{0} \\ \mathbf{1} & \mathbf{0} & \cdots & \mathbf{0} & \mathbf{0} \end{bmatrix}, \mathbf{A} = \begin{bmatrix} \mathbf{0} & \mathbf{1} \\ \mathbf{0} & \mathbf{0} \end{bmatrix}, \mathbf{B} = \begin{bmatrix} \mathbf{0} & \mathbf{0} \\ \mathbf{1} & \mathbf{0} \end{bmatrix}, \text{ where } \mathbf{1} = \begin{bmatrix} 1 & 0 \\ 0 & 1 \end{bmatrix}.$$

- Displacement of a corner node "cn" is fixed and equals to

$$\mathbf{u}_{cn} = \bar{\boldsymbol{\varepsilon}} x_{cn}.$$

After the determination of the unknown vector, using the traction values on the nodes located at the boundary of RVE, macroscopic stress tensor $\bar{\boldsymbol{\sigma}}$ is evaluated using Equation 2.20.

2.2.2 Determination of the Tangent Moduli

The developed algorithm is capable of determining the homogenized tangent moduli of the RVE through solving the heterogeneous domain for three distinct loading scenarios: two uniaxial tensile loadings and one simple shear loading with an arbitrary loading value denoted as α. The resultant macroscopic stress outcomes are subsequently divided by α in order to evaluate the specific column of the tangent moduli matrix. For a 2-D problem, a typical tangent moduli consist of 9 components as shown in Equation 2.23.

$$\bar{\boldsymbol{C}} = \begin{bmatrix} C_{11} & C_{12} & C_{13} \\ C_{21} & C_{22} & C_{23} \\ C_{31} & C_{32} & C_{33} \end{bmatrix} \tag{2.23}$$

To get the first column of the tangent moduli, the procedure shown in Equation 2.24 is followed. The red components of the moduli in Equation 2.24 determined by applying a macroscopic strain given with $\boldsymbol{\varepsilon_1}$.

$$\boldsymbol{\varepsilon_1} = \begin{bmatrix} \alpha \\ 0 \\ 0 \end{bmatrix} \xrightarrow{\text{Using BEM}} \boldsymbol{\sigma}(\boldsymbol{\varepsilon_1}) \Rightarrow \boldsymbol{\sigma}(\boldsymbol{\varepsilon_1}) = \begin{bmatrix} C_{11} & C_{12} & C_{13} \\ C_{21} & C_{22} & C_{23} \\ C_{31} & C_{32} & C_{33} \end{bmatrix} \begin{bmatrix} \alpha \\ 0 \\ 0 \end{bmatrix} \tag{2.24}$$

To get the second column of the tangent moduli, the procedure shown in Equation 2.25 is followed.

$$\boldsymbol{\varepsilon_2} = \begin{bmatrix} 0 \\ \alpha \\ 0 \end{bmatrix} \xrightarrow{\text{Using BEM}} \boldsymbol{\sigma}(\boldsymbol{\varepsilon_2}) \Rightarrow \boldsymbol{\sigma}(\boldsymbol{\varepsilon_2}) = \begin{bmatrix} C_{11} & C_{12} & C_{13} \\ C_{21} & C_{22} & C_{23} \\ C_{31} & C_{32} & C_{33} \end{bmatrix} \begin{bmatrix} 0 \\ \alpha \\ 0 \end{bmatrix} \tag{2.25}$$

To get the third column of the tangent moduli, the procedure shown in Equation 2.26 is followed.

$$\boldsymbol{\varepsilon_3} = \begin{bmatrix} 0 \\ 0 \\ \alpha \end{bmatrix} \xrightarrow{\text{Using BEM}} \boldsymbol{\sigma}(\boldsymbol{\varepsilon_3}) \Rightarrow \boldsymbol{\sigma}(\boldsymbol{\varepsilon_3}) = \begin{bmatrix} C_{11} & C_{12} & C_{13} \\ C_{21} & C_{22} & C_{23} \\ C_{31} & C_{32} & C_{33} \end{bmatrix} \begin{bmatrix} 0 \\ 0 \\ \alpha \end{bmatrix} \tag{2.26}$$

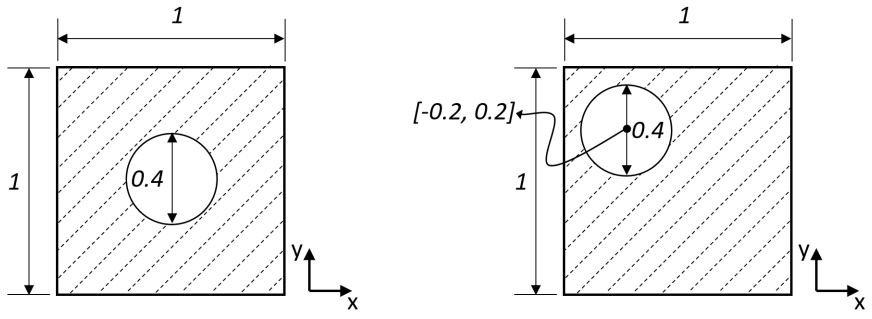
2.2.3 Numerical Examples

A MATLAB code is developed for the solution of the 2D and 3D linear elasticity problems together with the explained homogenization process. The developed algorithm can solve problems including single and multi-inclusion. In this section, the developed algorithm is first applied to two homogenization problems presented in the literature by Miehe and Koch [1] and by Fernandes et al. [2]. Problems include both single inclusion-void and multi-inclusion-void cases. The effect of the three classical types of boundary conditions is investigated under macroscopic strain-driven loading. Homogenized stress tensors of the RVEs are compared with the results presented in the literature. Secondly, a preliminary multi-scale analysis is done. Homogenized

tangent moduli of the RVE are obtained using the procedure given in Section 2.2.2.

2.2.3.1 2D RVEs with a Single Centered and a Single Eccentric Hole

Investigated problem is taken from the work conducted by Miehe and Koch, and the model is given in Figure 2.3. In the reference study, the homogenized stress tensor of an RVE is calculated by using FEM [1]. Two square RVEs with an edge length of 1 are used. The circular holes have diameters of 0.4, and they are located at the center and at an eccentric position of [-0.2, 0.2] from the center of the RVE, as shown in Figure 2.3. The bulk modulus κ_m and shear modulus μ_m of the matrix material are defined as 17.5 and 8, respectively. The ratio between the material properties of the inclusion and the matrix k is defined as a small value (10^{-5}) to model the inclusion as a hole. Two types of macroscopic strain-driven loadings, a uniform tensile loading $\bar{\varepsilon} = [0.4\ 0\ 0]^T$ and a simple shear loading $\bar{\varepsilon} = [0\ 0\ 0.4]^T$, are applied to both RVEs under uniform traction, linear displacement, and periodic displacement boundary conditions discussed in Section 2.2.1. The 4-point Gauss Quadrature formula is used for the numerical evaluation of the integral expressions. Both a single edge of the RVE and the boundary of the hole are divided into 40 boundary elements. Plane strain assumption is used.



(a) Centered hole (b) Eccentric hole

Figure 2.3: Heterogeneous RVEs consisting of a matrix phase and a single centered or eccentric hole

Tensile Loading

In the first example, we focus on the simple uniaxial, extension mode of the RVEs with a macroscopic strain of $\bar{\boldsymbol{\varepsilon}} = [0.4\ 0\ 0]^T$ under three classical types of boundary conditions. In the following subsections, the deformed shapes and the macroscopic stress tensors obtained for three boundary conditions are presented with the results given by Miehe and Koch (M&K) in [1].

Uniform Traction

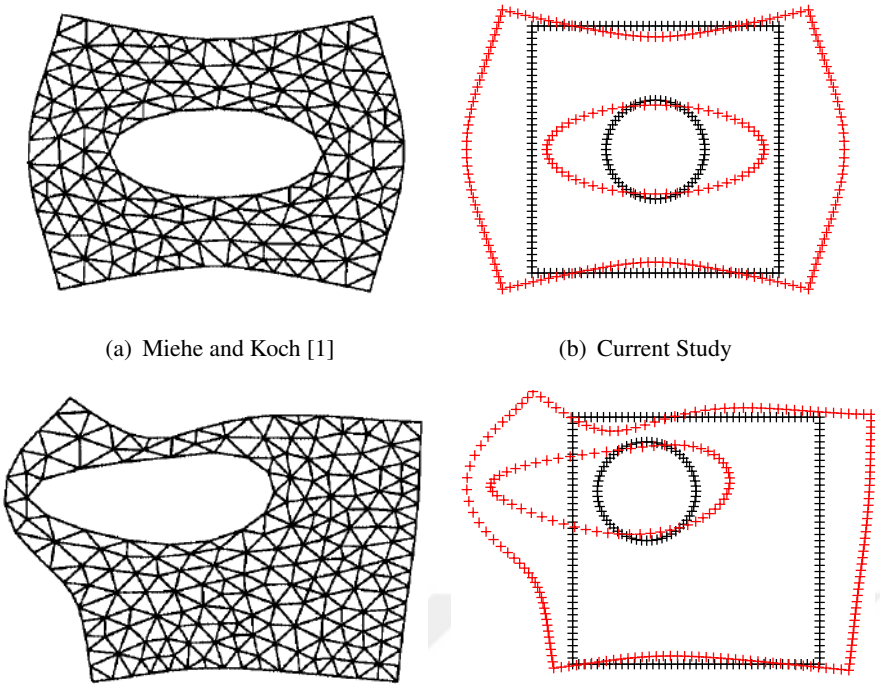
In Figures 2.4(b) and 2.4(d), deformed shapes of the current study under macroscopic strain-driven uniaxial tensile loading for RVE with a centered and an eccentric hole are presented. Red and black curves on the figure show the deformed and the undeformed shapes, respectively. In Figures 2.4(a) and 2.4(c), deformed shapes obtained by Miehe and Koch [1] are presented. As it is observed from the figures, the deformed shapes are consistent with each other. Table 2.1 summarizes the homogenized stress results for both studies. The letters (a), (b), (c), and (d) used in Table 2.1 correspond to the letters of the models presented in Figure 2.4. Similar to the deformed shapes, the homogenized stress results of both studies agree well.

Table 2.1: Homogenized stresses of the uniaxial tension loading under uniform traction boundary condition for the current study and study by Miehe and Koch [1]

	M&K (a)	**Current (b)**		**M&K (c)**	**Current (d)**
σ_{xx}	7.451	7.3	σ_{xx}	6.792	6.546
σ_{yy}	3.4	3.431	σ_{yy}	3.191	3.234
σ_{xy}	-0.002	0	σ_{xy}	-0.059	-0.075

Linear Displacement

Figures 2.5(b) and 2.5(d) present the deformed shapes of the current study under macroscopic strain-driven uniaxial tensile loading for RVEs with a centered and eccentric hole. Red and black curves on the figure show the deformed and the undeformed shapes, respectively. In Figures 2.5(a) and 2.5(c), deformed shapes obtained by Miehe and Koch [1] are presented. As is observed from the figures, the deformed



(a) Miehe and Koch [1]

(b) Current Study

(c) Miehe and Koch [1]

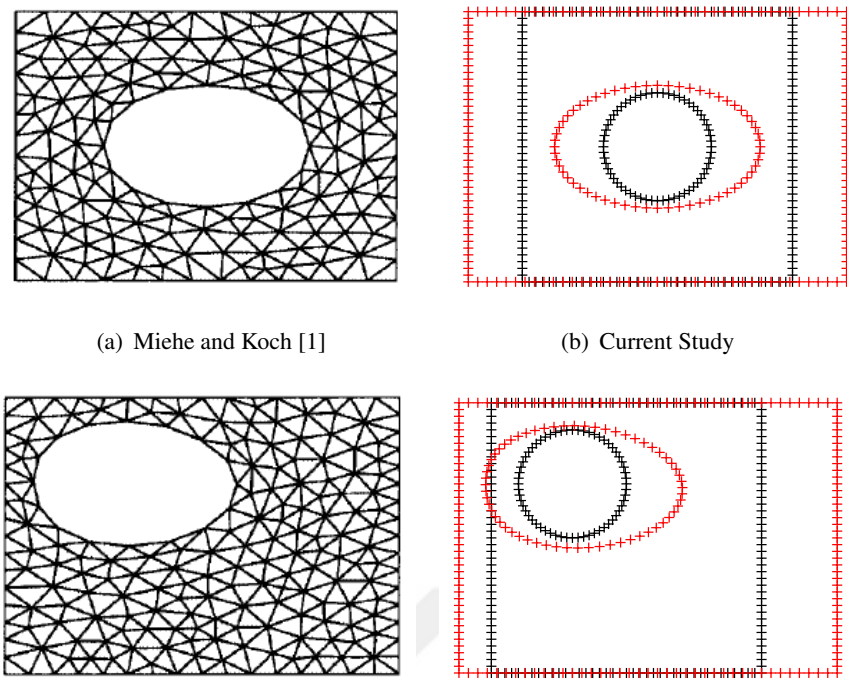
(d) Current Study

Figure 2.4: Deformed shapes presented by Miehe and Koch [1] and current study under strain driven uniaxial tensile loading with uniform traction type boundary condition

shapes agree well. Table 2.2 summarizes the homogenized stress results obtained in [1] and the current study. The letters (a), (b), (c), and (d) used in Table 2.2 are consistent with the letters of the models presented in Figure 2.5. Similar to the deformed shapes, there is a good agreement on the homogenized stress results of both studies.

Table 2.2: Homogenized stress results of the uniaxial tension loading under linear displacement boundary condition for the current study and study by Miehe and Koch [1]

	M&K (a)	**Current (b)**		**M&K (c)**	**Current (d)**
σ_{xx}	7.953	7.844	σ_{xx}	8.222	8.124
σ_{yy}	3.029	2.991	σ_{yy}	3.166	3.138
σ_{xy}	-0.002	0	σ_{xy}	0.053	0.056



(a) Miehe and Koch [1]

(b) Current Study

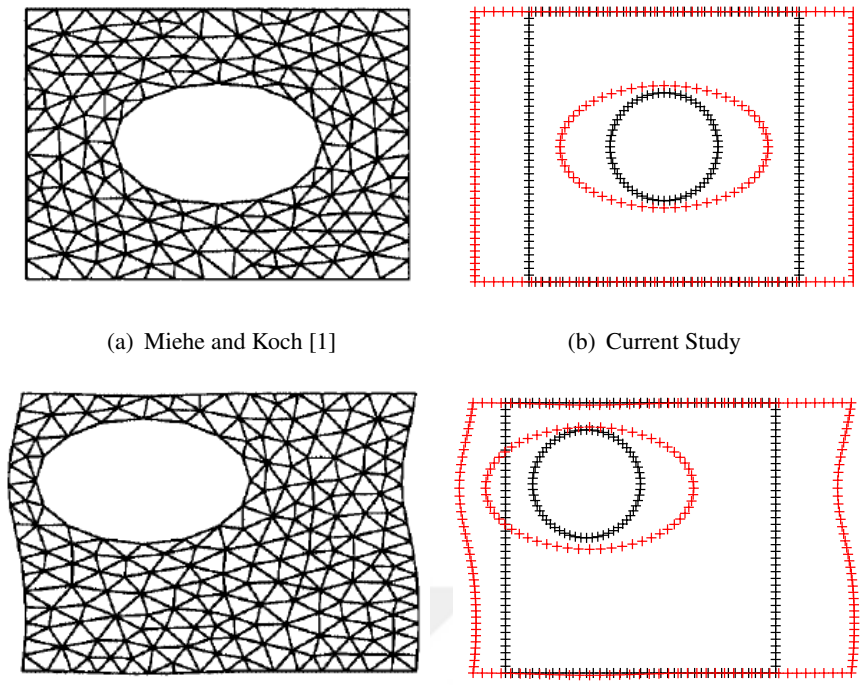
(c) Miehe and Koch [1]

(d) Current Study

Figure 2.5: Deformed shapes presented by Miehe and Koch [1] and current study under strain driven uniaxial tensile loading with linear displacement type boundary condition

Periodic Displacement

In Figures 2.6(b) and 2.6(d), deformed shapes of the current study under macroscopic strain-driven tensile loading for RVE with a centered and an eccentric hole are presented. Red and black curves on the figure show the deformed and the undeformed shapes, respectively. In Figures 2.6(a) and 2.6(c), deformed shapes from [1] are presented. Table 2.3 compares the homogenized stress results of [1] and the current study. The deformed shapes and the homogenized stress results of the current study exhibit good agreement with [1].



(a) Miehe and Koch [1] (b) Current Study

(c) Miehe and Koch [1] (d) Current Study

Figure 2.6: Deformed shapes presented by Miehe and Koch [1] and current study under strain driven uniaxial tensile loading with periodic displacement type boundary condition

Table 2.3: Homogenized stresses of the uniaxial tension loading under periodic displacement boundary condition for the current study and study by Miehe and Koch [1]

	M&K (a)	**Current (b)**		**M&K (c)**	**Current (d)**
σ_{xx}	7.898	7.786	σ_{xx}	7.9	7.787
σ_{yy}	3.019	2.982	σ_{yy}	3.017	2.982
σ_{xy}	-0.001	0	σ_{xy}	0.001	0

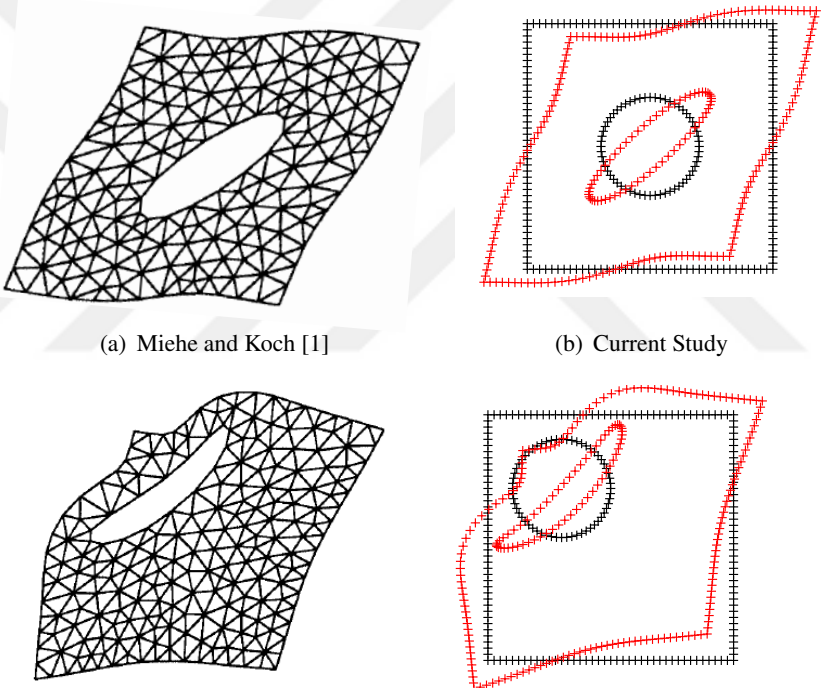
Shear Loading

As the second type of loading, we focus on the simple shear mode of the RVEs with a macroscopic strain of $\bar{\varepsilon} = [0\ 0\ 0.4]^T$ under three classical types of boundary conditions. In the following subsections, the deformed shapes and the macroscopic stress tensors obtained for three types of boundary conditions are compared with the results

given by Miehe and Koch (M&K) [1].

Uniform Traction

In Figures 2.7(b) and 2.7(d), deformed shapes of the current study under macroscopic strain-driven simple shear loading for RVEs with a centered and an eccentric hole are presented. Red and black curves on the figure show the deformed and the undeformed shapes, respectively. Figures 2.7(a) and 2.7(c) present the deformed shapes from Miehe and Koch [1]. As is observed from the figures, the deformed shapes of both studies are consistent. Table 2.4 summarizes the homogenized stress results from [1] and in the current study. There is a notable agreement in the homogenized stress results of both studies.



(a) Miehe and Koch [1] (b) Current Study

(c) Miehe and Koch [1] (d) Current Study

Figure 2.7: Deformed shapes presented by Miehe and Koch [1] and current study under strain driven simple shear loading with uniform traction type boundary condition

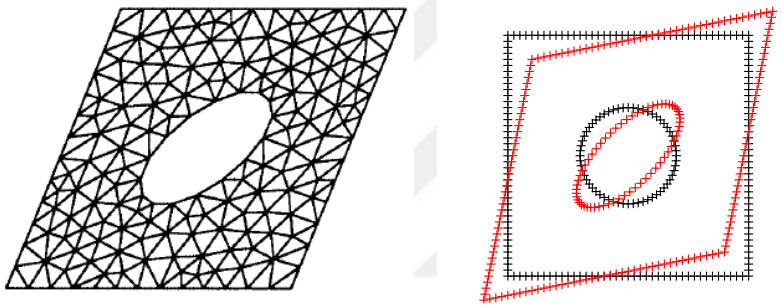
Linear Displacement

Figures 2.8(b) and 2.8(d) show deformed shapes from the current study for RVE with a centered and eccentric hole. Red and black curves on the figure show the deformed

Table 2.4: Homogenized stresses of the simple shear loading mode under uniform traction boundary condition for the current study and study by Miehe and Koch [1]

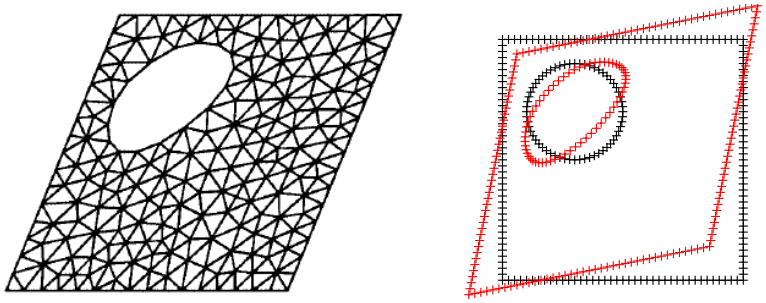
	M&K (a)	**Current (b)**		**M&K (c)**	**Current (d)**
σ_{xx}	-0.002	0	σ_{xx}	-0.059	-0.075
σ_{yy}	0.002	0	σ_{yy}	-0.061	-0.075
σ_{xy}	2.113	2.02	σ_{xy}	1.845	1.714

and the undeformed shapes, respectively. Deformed shapes from Miehe and Koch [1] are depicted in Figures 2.8(a) and 2.8(c). Table 2.5 compares the current study's homogenized stress values to [1]. The current study's deformed shapes, Figure 2.8, and homogenized stress results, Table 2.5, are in good accord with [1].



(a) Miehe and Koch [1]

(b) Current Study



(c) Miehe and Koch [1]

(d) Current Study

Figure 2.8: Deformed shapes presented by Miehe and Koch [1] and current study under strain driven simple shear loading with linear displacement type boundary condition

Periodic Displacement

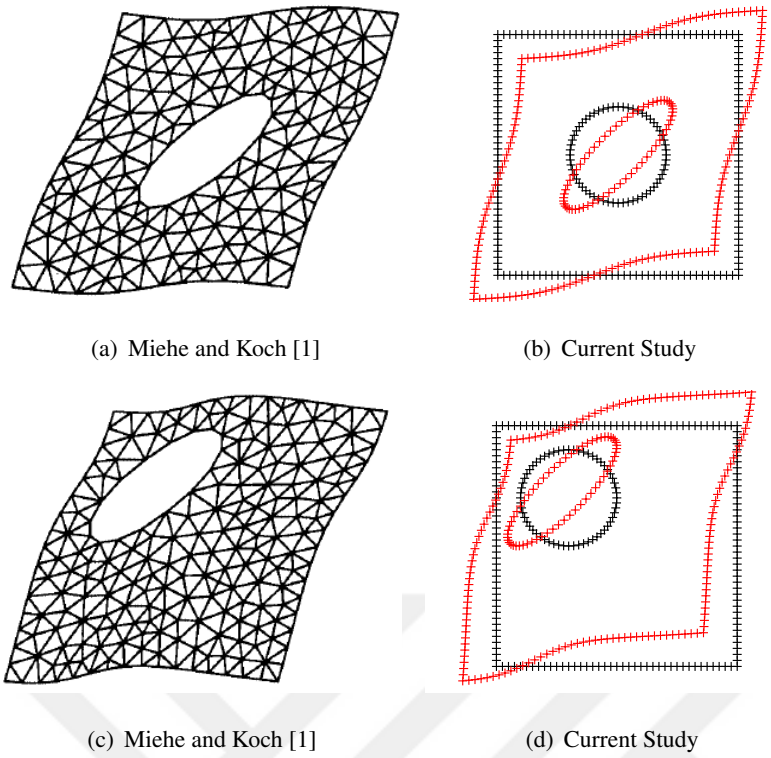
Table 2.5: Homogenized stresses of the simple shear loading under linear displacement boundary condition for the current study and study by Miehe and Koch [1]

	M&K (a)	**Current (b)**		**M&K (c)**	**Current (d)**
σ_{xx}	-0.001	0	σ_{xx}	0.053	0.056
σ_{yy}	0.001	0	σ_{yy}	0.052	0.056
σ_{xy}	2.435	2.387	σ_{xy}	2.521	2.486

Deformed shapes under simple shear loading obtained by the proposed BEM-based homogenization approach for RVEs with a centered and with eccentric hole are presented in Figures 2.9(b) and 2.9(d), respectively. The red curve corresponds to the deformed RVE, while the black curve the undeformed RVE. In Figures 2.9(a) and 2.9(c), deformed shapes obtained using FEM given by Miehe and Koch [1] are presented. The results of homogenized stress in [1] and the current study are compared in Table 2.6. Similar to the deformed shapes, the homogenized stress results of both studies are in good agreement.

Table 2.6: Homogenized stresses of the simple shear loading under periodic displacement boundary condition for the current study and study by Miehe and Koch [1]

	M&K (a)	**Current (b)**		**M&K (c)**	**Current (d)**
σ_{xx}	-0.001	0	σ_{xx}	0.001	0
σ_{yy}	0.001	0	σ_{yy}	-0.001	0
σ_{xy}	2.222	2.145	σ_{xy}	2.213	2.145



(a) Miehe and Koch [1] (b) Current Study

(c) Miehe and Koch [1] (d) Current Study

Figure 2.9: Deformed shapes presented by Miehe and Koch [1] and current study under strain driven simple shear loading with periodic displacement type boundary condition

2.2.3.2 2D RVE Consisting a Single Inclusion with Varying Volume Fractions and Material Properties

A second application of the developed BEM code is performed on a problem consisting of two distinct regions, as shown in Figure 2.10, with colors red and black. The problem model is taken from the work conducted by Fernandes et al. [2]. The model consists of two regions with two different material properties. The diameter of the inclusion changes with the volume fraction of the inclusion. The effect of the volume fraction of the inclusion phase on the homogenized stress tensor is presented. Soft and stiff inclusion cases and void cases are investigated in this study. Material properties used for the matrix and the inclusion phases are tabulated in Table 2.7. Two types of macroscopic strain-driven loadings, for soft and stiff inclusion cases $\bar{\boldsymbol{\varepsilon}} = [-0.00099\ 0.0032\ 0]^T$ and for the void case $\bar{\boldsymbol{\varepsilon}} = [-0.00045\ 0.0015\ 0.0002]^T$, are applied to the RVEs under three classical type of boundary conditions. The 4-

point Gauss Quadrature formula is used for the numerical evaluation of the integral expressions. Plane stress assumption is employed.

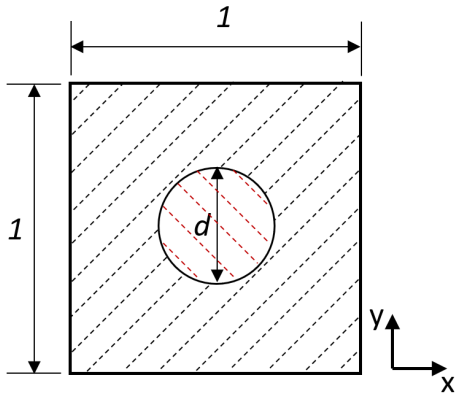


Figure 2.10: Heterogeneous two-phase RVE with a matrix phase (black) and an inclusion phase (red)

Table 2.7: Material properties for the matrix and the inclusion phases presented by Fernandes et al. [2]

Matrix		**Soft Inclusion**		**Stiff Inclusion**	
E [GPa]	ν [-]	E [GPa]	ν [-]	E [GPa]	ν [-]
70	0.3	25	0.2	200	0.2

RVE with a Soft Inclusion

Volume fractions (ν_f) of 0, 0.1, 0.3, and 0.37 are investigated for uniform traction, linear displacement, and periodic displacement boundary conditions. Inclusion is located at the center of the RVE. A macroscopic strain of $\bar{\varepsilon} = [-0.00099\ 0.0032\ 0]^T$ is applied. In Figure 2.11, the change in the σ_{xx} and σ_{yy} components of the homogenized stress tensor with the variation in the volume fraction of the inclusion under three classical boundary conditions are given for both studies. Fernandes et al. [2] presented both FEM and BEM results under periodic displacement boundary conditions. The acronyms PBC, UBC, and TBC used in the legends of the figures are periodic displacement, linear displacement, and uniform traction boundary conditions, respectively. (C) and (F) are the results of the current study and the study of

Fernandes et al. [2], respectively. It is observed from the results that that, except for the uniform traction boundary condition, all the other results are very similar. In the main loading direction "yy", periodic displacement and linear displacement boundary conditions give close results to the FEM result. Another observation is that the uniform traction boundary condition gives, as expected, the softest response. Moreover, as the volume fraction of the soft inclusion increases, the stiffness of the RVE decreases.

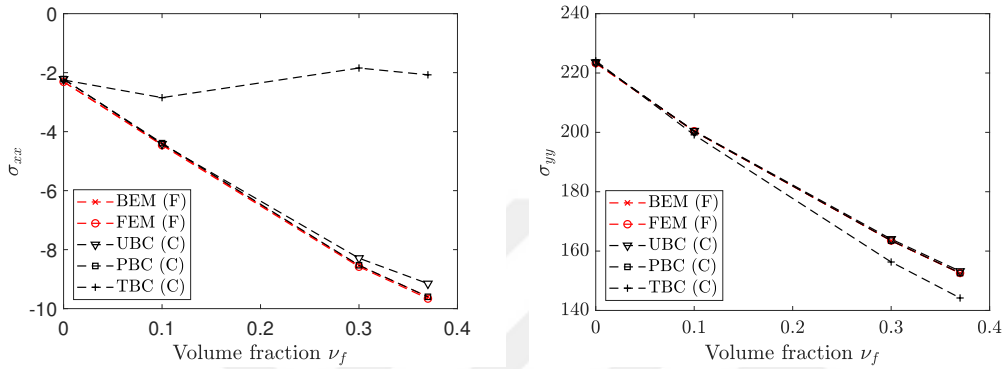


Figure 2.11: For macroscopic strain driven loading, effect of change in the volume fraction of the soft inclusion on the homogenized stress results for different solution methods

RVE with a Stiff Inclusion

Volume fractions (ν_f) of 0, 0.1, 0.3, and 0.37 are studied for uniform traction, linear displacement, and periodic displacement boundary conditions. A macroscopic strain of $\bar{\boldsymbol{\varepsilon}} = [-0.00099\ 0.0032\ 0]^T$ is applied. Figure 2.12 depicts the change in the σ_{xx} and σ_{yy} components of the homogenized stress tensor with inclusion volume fraction for three classical boundary conditions. The acronyms PBC, UBC, and TBC used in the legends of the figures are periodic displacement, linear displacement, and uniform traction boundary conditions, respectively. (C) and (F) correspond to the current study and the study of Fernandes et al. [2], respectively. Once again, uniform traction boundary condition gives the softest response compared to the other boundary conditions. It is also seen that as the volume fraction of the stiff inclusion increases , the stiffness of the RVE increases. In the main loading direction "yy", periodic displace-

ment and linear displacement boundary conditions give close results to the FEM and BEM results given by Fernandes et al. [2].

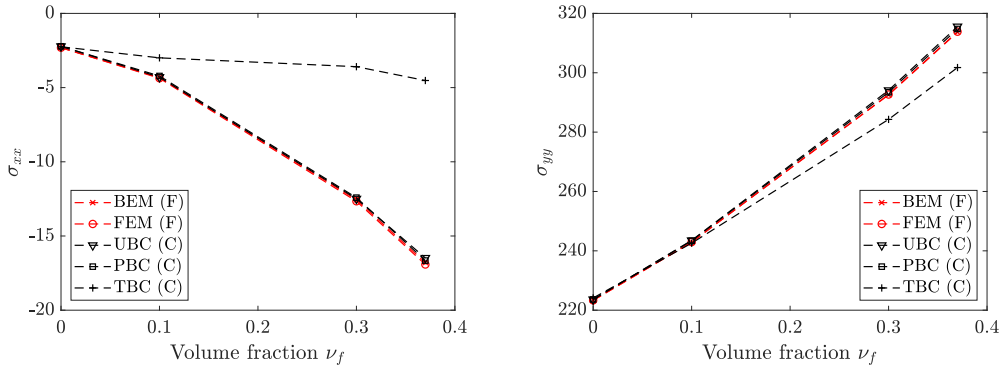


Figure 2.12: For macroscopic strain driven loading, effect of change in the volume fraction of the stiff inclusion on the homogenized stress

RVE with a Void

Similar to the previous two examples, void volume fractions (ν_f) of 0, 0.1, 0.3, and 0.37 are analyzed for uniform traction, linear displacement, and periodic displacement boundary conditions. A macroscopic strain of $\bar{\boldsymbol{\varepsilon}} = [-0.00045\ 0.0015\ 0.0002]^T$ is applied to the RVE. Figure 2.13 presents the variation of σ_{xx}, σ_{yy}, and σ_{xy} with the volume fraction of the void under three classical boundary conditions. Only periodic boundary conditions are applied in the FEM result [2]. In the main loading direction "yy", periodic displacement and linear displacement boundary conditions give close results to the FEM and BEM results given by Fernandes et al. [2]. As expected, in the direction perpendicular to the main loading direction, the best agreement between FEM and BEM results is seen for the periodic boundary condition. Once again, uniform traction boundary condition gives the softest result. Moreover, as the volume content of the void increases, the stiffness of the RVE significantly decreases.

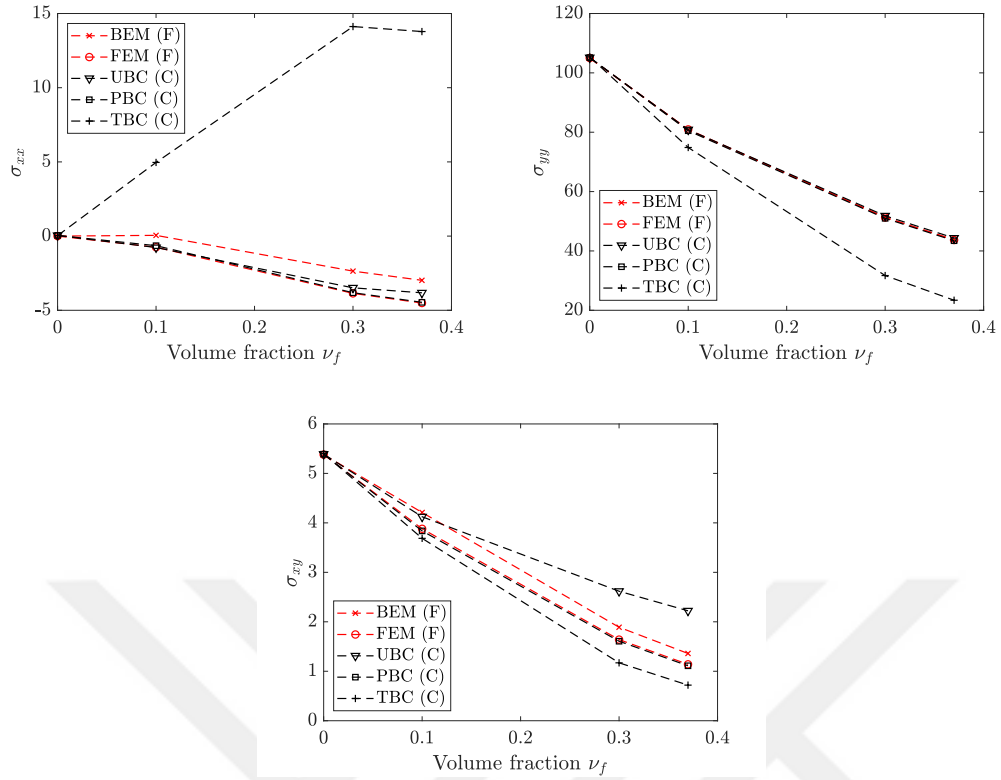


Figure 2.13: For macroscopic strain driven loading, effect of change in the volume fraction of the void on the homogenized stress

2.2.3.3 2D RVE Consisting Multi Inclusions with Varying Volume Fractions

Figure 2.14 depicts a third application of the developed BEM algorithm to a problem containing a matrix and several inclusions. The problem model is again taken from Fernandes et al. [2].The model consists of two phases, a matrix, and several inclusions, with different material properties. RVE consists of five inclusions with a total volume fraction of 0.37. Stiff inclusion cases and void cases are analyzed in this study. Stiff inclusion properties are given in Table 2.7. Two types of macroscopic strain-driven loadings, for inclusion case $\bar{\boldsymbol{\varepsilon}} = [-0.00099\ 0.0032\ 0]^T$ and for the void case $\bar{\boldsymbol{\varepsilon}} = [-0.00045\ 0.0015\ 0.0002]^T$, are considered. The effects of three types of boundary conditions are studied. The integral expressions are numerically evaluated using the 4-point Gauss Quadrature formula. The assumption of plane stress is employed.

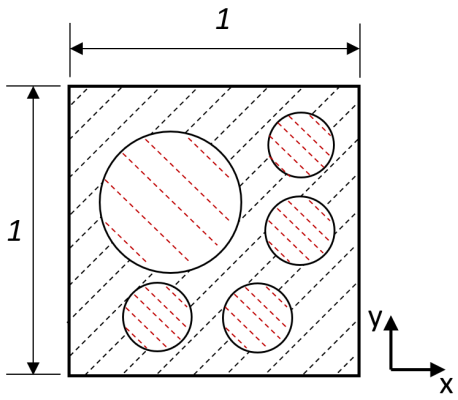


Figure 2.14: Heterogeneous two-phase RVE with a matrix phase (black) and an inclusion phase (red)

The homogenized stress components of the RVE with multi inclusion-voids for the uniform traction (TBC), linear displacement (UBC), and periodic displacement (PBC) boundary conditions are presented in Table 2.8. The results of Fernandes et al. [2] and the present study agree for all three types of boundary conditions. Another observation is that the uniform traction boundary condition gives, as expected, the softest response. Linear displacement and periodic displacement type boundary conditions give close responses, whereas a difference exists in homogenized stress results of uniform traction boundary conditions.

2.2.3.4 3D RVEs Consisting Single- and Multi-Inclusions

In Appendix A, homogenization of a 3D homogeneous RVE is presented. Next, a homogenization study is performed on the three-dimensional heterogeneous representative volume element presented by Penta and Gerisch [41]. In the related study, the effects of different reinforcement types and the volumetric ratio of each reinforcement geometry on the macroscopic material properties are investigated. Penta and Gerisch [41] use the Asymptotic Homogenization, Voigt, Reuss, Mori-Tanaka, and Self-consistent homogenization methods. In this work, models with both single and multi-spherical inclusion phases are investigated. The material parameters used in the analyses are given in Table 2.9. Before making a comparison with the literature, a mesh convergence study is carried out for both the finite element model (FEM) and

Table 2.8: Homogenized stress components of the an RVE consisting multi inclusions-voids for three types of boundary conditions (all stress components are presented in MPa)

Void				**Inclusion**			
	UBC (F)	**FEM (F)**	**UBC (C)**		**UBC (F)**	**FEM (F)**	**UBC (C)**
σ_{xx}	0.59	-2.07	-1.67	σ_{xx}	-15.3	-15.87	-14.60
σ_{yy}	43.76	44.12	43.89	σ_{yy}	314.74	315.63	312.73
σ_{xy}	3.48	2.66	2.66	σ_{xy}	0.76	0.79	0.69
	PBC (F)	**FEM (F)**	**PBC (C)**		**PBC (F)**	**FEM (F)**	**PBC (C)**
σ_{xx}	0.84	-1.86	-1.42	σ_{xx}	-14.95	-15.46	-14.22
σ_{yy}	41.86	42.21	41.94	σ_{yy}	313.29	314.05	311.32
σ_{xy}	2.63	1.82	1.82	σ_{xy}	0.37	0.39	0.35
	TBC (F)	**FEM (F)**	**TBC (C)**		**TBC (F)**	**FEM (F)**	**TBC (C)**
σ_{xx}	9.17	6.73	7.38	σ_{xx}	-9.02	-9.37	-8.45
σ_{yy}	32.65	33.24	33.07	σ_{yy}	306.80	306.80	305.70
σ_{xy}	2.59	1.38	1.41	σ_{xy}	0.44	0.45	0.40

the boundary element model (BEM). During this study, a comparison of the solution times of both methods is also given. In the finite element analysis, 8-node trilinear brick elements are used, and in the boundary element analysis, constant triangular elements are used.

Table 2.9: Material properties

Matrix		Inclusion	
μ_0 [GPa]	ν_0 [-]	μ_1 [GPa]	ν_0 [-]
1.92	0.3	42.97	0.28

For mesh convergence study, coarsely, intermediately, and finely meshed representative volume elements containing %15 spherical reinforcement are created. The number of elements in these models is given in Table 2.10.

After creating the coarse, medium, and fine mesh models for each method, the con-

Table 2.10: Number of elements used for the meshes of BEM and FEM models created for the comparison study

	Coarse Model		Medium Model		Fine Model	
Method	**Matrix**	**Inclusion**	**Matrix**	**Inclusion**	**Matrix**	**Inclusion**
FEM	320	224	1600	896	3696	1600
BEM	96	80	384	320	1536	1280

vergence study is carried out. With the uniaxial tensile load given below, it is possible to determine the first column of the macroscopic homogenized tangent modulus (C).

$$\varepsilon = [\alpha \ 0 \ 0 \ 0 \ 0 \ 0]^T \tag{2.27}$$

With the assumption of isotropic linear elasticity and using the coefficients in this column, it is possible to determine the homogenized material properties of the heterogeneous representative volume element, as shown in Equation 2.28.

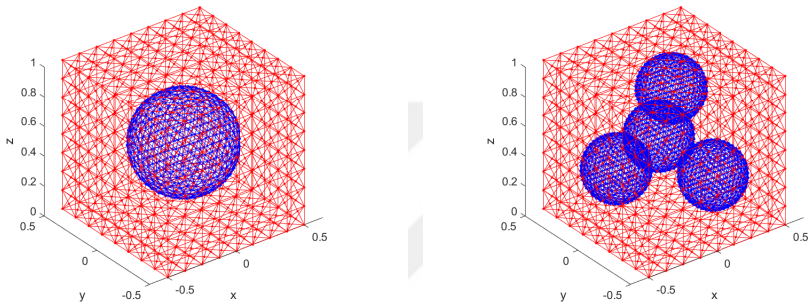
$$\begin{aligned} E_H &= \frac{C_{11}(C_{11}+C_{12}) - 2C_{12}^2}{C_{11}+C_{12}} \\ \nu_H &= \frac{C_{12}}{C_{11}+C_{12}} \end{aligned} \tag{2.28}$$

The results obtained with FEM and BEM for the three types of meshes are given in Table 2.11. For both methods, it is observed that there is a convergence between coarse-medium and medium-fine models. Another observation is that, as expected, the finite element method gives much higher solution times compared to the boundary element method. It has been concluded that fine mesh networks for the boundary elements and finite element method can be used in this problem.

After comparing the developed boundary element method with the finite element method, another comparison study is made with the results of the different homogenization methods presented by Penta and Gerisch. Heterogeneous RVEs given in Figure 2.15 are investigated in a comparison study. The results of the current study and Penta and Gerisch [41] are given in Figure 2.16. It is seen that the boundary element method model with a single inclusion phase gives very consistent results with

Table 2.11: Homogenized material properties obtained with three different mesh for boundary element and finite element methods

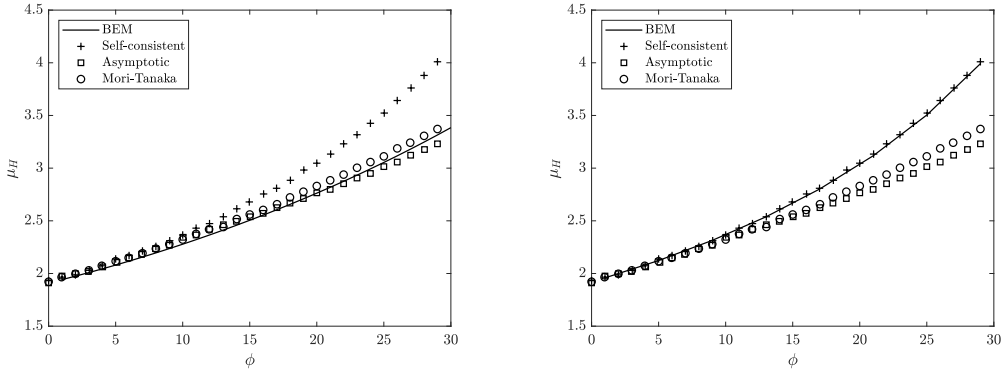
Method	Coarse		Medium		Fine	
	E_H [GPa]	Time [s]	E_H [GPa]	Time [s]	E_H [GPa]	Time [s]
FEM	7.122	5.69	7.045	523.79	7.025	4576.42
BEM	6.781	3.64	7.015	39.85	7.027	729.93



(a) Single-inclusion (b) Multi-inclusion

Figure 2.15: Boundary element meshes of three-dimensional RVEs

the Mori-Tanaka and asymptotic methods, see Figure 2.16(a), whereas the results of the boundary element method model with a multi-inclusion phase are closer to the self-consistent method results, see Figure 2.16(b) .



(a) Single inclusion

(b) Multi inclusion

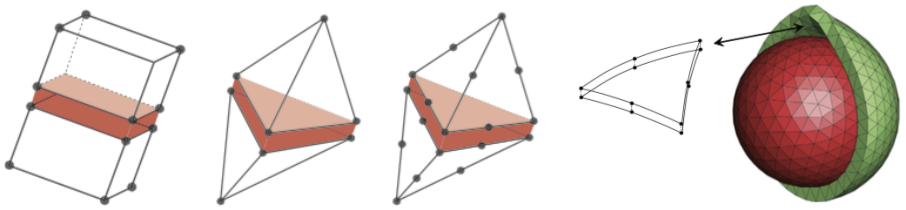
Figure 2.16: Variation of the homogenized shear modulus (μ_H) results obtained by the asymptotic, self-consistent, Mori-Tanaka and the BEM-based homogenization methods presented in this study with the volume ratio of the reinforcing phase

2.3 Homogenization of Linear Elasticity with Interface Modeling

2.3.1 Interface Models in Literature

One of the most important parameters determining the strength of heterogeneous domains is the strength of the reinforcement-matrix interface. Interface modeling plays a crucial role in the mathematical modeling of RVEs with reinforcing phases. The boundary elements where the matrix and the reinforcement material at the interface intersect should be defined in a way that separation is allowed. Unlike the continuous medium of finite elements, the mechanical behavior of these elements can be described not by a constitutive equation between the stress tensor-strain tensor, but by linear or nonlinear constitutive equations between the stress vector-displacement jump (traction-displacement jump). In the finite element method, as shown in Figure 2.17, traditional interface elements in three-dimensional problems are two-dimensional surface elements. Similarly, between two-dimensional finite elements, one-dimensional interface elements with zero thickness are defined. In the boundary element method, since the elements are already defined in the boundary regions, a separate element definition is not required as in the finite element method.

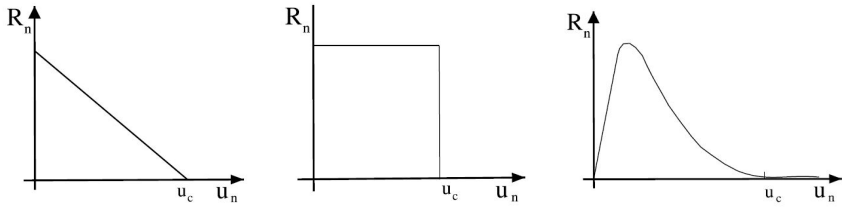
Classical interface models have been presented in many different studies in the litera-



(a) (b)

Figure 2.17: (a) 8-node linear rectangular interface element defined between 8-node linear rectangular prism (brick) elements, 6-node linear triangle interface element defined between a 4-node linear tetrahedron and 10-node quadratic triangle interface element defined between 10-node quadratic tetrahedron [5], (b) Modeling of separation between reinforcement and interphase/matrix with zero thickness interface element [6]

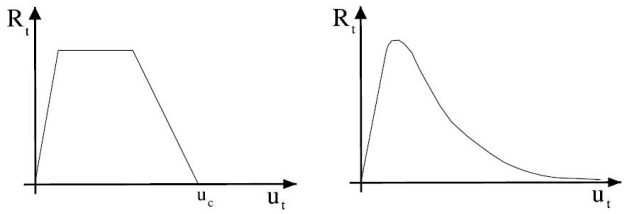
ture. To address the relationship between nodes on two different faces of an interface, we first need to define the relative displacement (**u**) and the stress vector (**R**) between these nodes. The normal and tangential components of these variables are defined as ($\mathbf{u}_n$, $\mathbf{u}_t$) and ($\mathbf{R}_n$, $\mathbf{R}_t$), respectively. In the literature, various laws are used to represent the relationship between the stress vector **R** and the relative displacement **u**. Some of these models are presented in Figures 2.18 and 2.19.



(a) Barenblatt [42] (b) Dugdale [43] (c) Needleman [44]

Figure 2.18: Adhesion interface models for the normal stress vector under monotonic loading conditions

Adhesive interface models for the normal stress vector under monotonic loading conditions are mainly used for the numerical simulation of the propagation of cracks in Mode-I fracture, and therefore only displacements in the normal direction are taken into account. The models of Barenblatt [42], Dugdale [43], and Needleman [44],



(a) Tvergaard [45] (b) Xu-Needleman [46]

Figure 2.19: Frictionless adhesive interface models for tangential stress vector

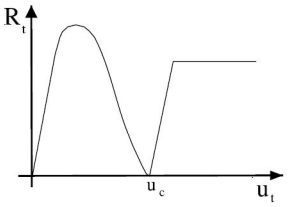
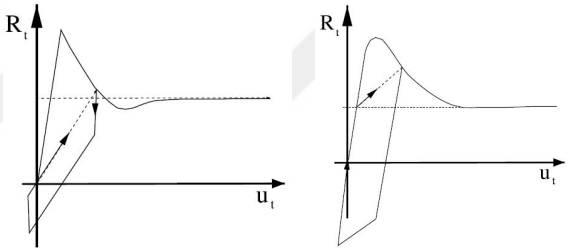


Figure 2.20: Adhesion and friction in Tvergaard's interface model [7]



(a) RCMM [47] (b) Chaboche [48]

Figure 2.21: RCCM model which investigates the interface behavior in normal direction

which are presented in Figure 2.18, can be considered as representative examples of such numerical methods. The interface models that take the friction/adhesion effects into account were first introduced in 1970 (Palmer and Rice [49]). In the 1980s, Frémond introduced the concept of the intensity of adhesion [50]. As shown in Figure 2.19, some authors in the literature have not taken friction into account while modeling the interface (Tvergaard and Hutchinson [45] and Xu and Needleman [46]). In the 1990s, the first representation of an interface, in which adhesion and friction were modeled sequentially, as shown in Figure 2.20, was presented by Tvergaard [7]. Fi-

nally, in the early 2000s, models that combined adhesion and friction behavior with a smooth transition were presented, see Figure 2.21 for the two examples of such models.

2.3.2 Incorporating a Cohesive Traction-Separation Interface Model into Boundary Element Method

In this study, a bilinear cohesive traction-separation interface model based on experimental results presented by Tan et al. [51] is used. The model allows the separation of the reinforcing particle from the matrix. In this model, the traction between nodes on either side of the interface is continuous, while the separation displacement vector is the difference in displacement values of nodes. As shown in Figure 2.22, the model consists of three phases: the linear elastic phase ($|OA|$), the softening phase ($|AC|$), and the dissociation phase ($|CD|$). Here, it should be noted that this model accounts only for the behavior in the normal direction of the interface.

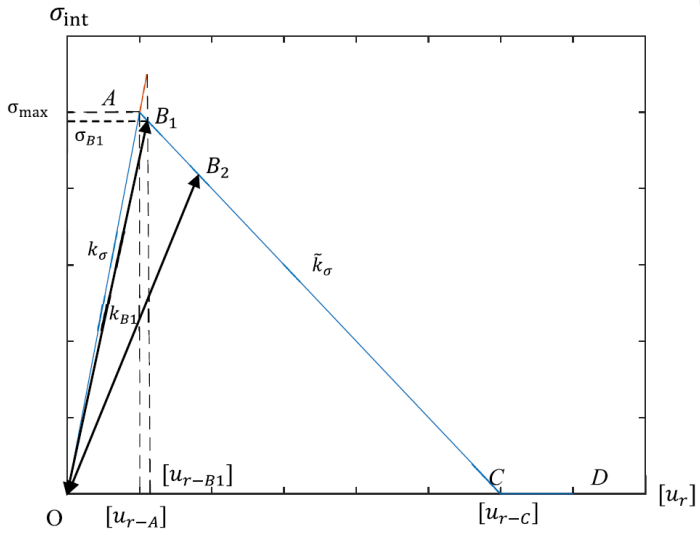


Figure 2.22: Cohesive traction-separation model [8]

The relationship between opening displacement and traction is given in Equation 2.29.

$$\sigma^{int} = \begin{cases} k_\sigma[u_r], & [u_r] < [u_{r-A}] \\ \left(1 + \dfrac{k_\sigma}{\tilde{k}_\sigma}\right)\sigma_{max} - \tilde{k}_\sigma[u_r], & [u_{r-A}] < [u_r] < [u_{r-C}] \\ 0, & [u_{r-C}] < [u_r] \end{cases} \tag{2.29}$$

In Equation 2.29, σ^{int} is the interface stress in the normal direction, σ_{max} is the maximum allowable interface stress, $[u_r]$ is the opening displacement in the normal direction, k_σ and $\tilde{k}_\sigma$ are the elastic and softening elastic moduli of the interface, respectively. The interface conditions in each section of the bilinear interface behavior can be summarized as follows:

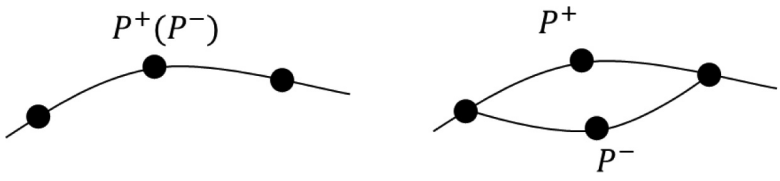
- $[u_r] < [u_{r-A}]$: The interface is in linear elastic phase ($|OA|$), where k_σ denotes the interface modulus. The loading and unloading are on the line $|OA|$.

- $[u_{r-A}] < [u_r]$: This interface is in the linear softening phase. The point which corresponds to the value of $[u_r]$ is determined. For example, it is point B_1 in Figure 2.22. Afterward, the stress corresponding to this point, σ_{B1}, is calculated by using Equation 2.29. The value of the modulus is updated as k_{B1}. For the new interface modulus, the problem is solved again by an iterative solution method in the relevant load step until the equilibrium is reached.

- $[u_r] < [u_{r-B_1}]$: Loading and unloading of the interface are done on the line by using modulus k_{B1} (this is the case once $[u_r] = [u_{r-B_1}]$ previously in the loading history).

- $[u_{r-C}] < [u_r]$: The interface is in the dissociation phase. The interface modulus k_σ is taken as zero, resultantly, the stress on the interface is zero.

In the boundary element analysis of a two-phase composite without interface modeling, an equation system is created based on the assumption that the nodes in the matrix and those on the reinforcing side of the interface move together, as shown in Figure 2.23(a). Between the nodes indicated by P^+ and P^-, the displacement and traction relations given in Equation 2.30 are used.



(a) Sticky (b) Separation

Figure 2.23: Interface nodes [8]

$$\begin{cases} u_\alpha(P^+) = u_\alpha(P^-) \\ t_\alpha(P^+) = -t_\alpha(P^-) \end{cases} \quad \alpha = 1, 2 \text{ for 2-D problems} \tag{2.30}$$

To model the separation of the interface as shown in Figure 2.23(b), an interface law between the nodes P^+ ve P^- should be inserted into the equation system. The displacements of P^+ and P^- are discontinuous, while tractions are continuous. In addition, the displacements and stresses on either side of the interface must satisfy a certain interface condition, as shown in Equation 2.31.

$$\begin{cases} f([u_\alpha]) = g\left(t_\alpha(P^+)\right) \\ t_\alpha(P^+) = -t_\alpha(P^-) \end{cases} \quad \alpha = 1, 2 \text{ for 2-D problems} \tag{2.31}$$

The $f(\cdot)$ and $g(\cdot)$ functions in the above equation express the interface relationship between displacement and traction. $[u_\alpha]$ is defined as the difference in the normal displacements of the P^+ and P^- nodes on both sides of the interface, i.e., $[u_\alpha] = u_\alpha(P^+) - u_\alpha(P^-)$.

To adapt the interface relationship presented in Equation 2.29 by Tan et al. [51] to the boundary element method, the functions $f(\cdot)$ and $g(\cdot)$ given in Equation 2.31 must be selected to represent this interface model. Interface behavior is expressed by defining the relationship between displacement and traction on either side of the interface. The relationship between traction and displacement for this interface is given in Equation 2.32.

$$\begin{cases} T_{Ik}^0 = S_k(U_{Ik}^0 - U_I^k) \\ T_{Ik}^0 + T_I^k = 0 \end{cases} \tag{2.32}$$

In Equation 2.32, T_{Ik}^0 ve U_{Ik}^0 are defined as the tractions and the displacements of the nodes on the matrix side for the k^{th} interface. Additionally, T_I^k and U_I^k are the tractions and the displacements of the nodes on the inclusion side for the k^{th} interface. The S_k matrix is a diagonal matrix consisting of sub-matrices containing the elastic modulus k_b of size 2×2. For the interface model adopted in this study, these submatrices are defined as in Equation 2.33.

$$S_{2\times 2} = \begin{bmatrix} k_b & 0 \\ 0 & k_b \end{bmatrix} \tag{2.33}$$

Inserting Equation 2.32 in the BEM equation system and making the simplifications, the equation system is obtained as given below.

$$\begin{bmatrix} -G^0 & H^0 & G_{I1}^0 S_1 - H_{I1}^0 & -G_{I1}^0 S_1 & \cdots & G_{In}^0 S_n - H_{In}^0 & -G_{In}^0 S_n \\ & & -G^1 S_1 & G_1 S_1 - H^1 & & & \\ & & & & \ddots & & \\ & & & & & -G^n S_n & G_n S_n - H^n \end{bmatrix} \begin{bmatrix} U^0 \\ T^0 \\ U_{I1}^0 \\ U_I^1 \\ \vdots \\ U_{In}^0 \\ U_I^n \end{bmatrix} = 0 \tag{2.34}$$

The variables U^0 and T^0 given in the above equation are the displacement and the stress vectors of the nodes on the outer boundary of the matrix domain. The matrices G and H are the coefficient matrices obtained by the boundary element equations. After defining the classical boundary element equation in this way, the system of equations is finalized using the homogenization method developed for three classical boundary conditions, as discussed in previous sections.

Since the modulus (k_{int}) of each node pair may change during the softening phase

of the cohesive interface model, the coefficient matrix S given in Equation 2.34 that describes the relationship between the traction and the opening displacement will also change. Thus, the new S matrix may not satisfy the equilibrium condition in that load step. Therefore, an iterative procedure is needed to reach an equilibrium solution for a given loading. The steps that are used to reach equilibrium can be described as follows.

- **STEP 1**: Initially, the relationship between the interface node pairs is defined as $k_{int} = k_\sigma$ and $u_{r\text{-}hist} = 0$. The maximum number of iterations and the tolerance value are set to N and e_0, respectively.
- **STEP 2**: The next incremental step of macroscopic strain-driven loading is applied.
- **STEP 3**: The boundary element equations containing the $k_{int} = k_\sigma$ interface modulus values specified for the relevant load step are solved. Then, the difference in the normal displacements between the interface node pairs $[u_r]$ is calculated.
- **STEP 4**: Using the opening displacements $[u_r]$ calculated in STEP 3, the current interface condition of each interface node pair is determined.
  - **STEP 4.1**: Depending on the condition of the node pair determined in STEP 4, the interface stress σ_{int} and moduli $k_{int} = \sigma_{int}/[u_r]$ are calculated.
  - **STEP 4.2**: For each node pair at the interface, the check for equilibrium state is achieved by using the relation given below.

$$e = \frac{[u_r] - [u_{r\text{-}hist}]}{[u_r]} > e_0, \tag{2.35}$$

    where e_0 and $u_{r\text{-}hist}$ are defined as the reference error for iterations to stop and the difference of normal displacements in the previous iteration, respectively.
  - **STEP 4.3**: Even if the equilibrium conditions given in Equation 2.35 are satisfied for one single node pair, the solution returns to STEP 3. If none of the interface node pairs satisfies Equation 2.35 or the number of iterations

reaches the designated number of maximum iterations N, the solution will continue with STEP 2.

2.3.3 Numerical Examples

The boundary element method-based homogenization of a heterogeneous RVE with a bilinear interface model is considered for two studies from the literature. The results of the proposed BEM-based homogenization approach are compared with the literature in the following subsections.

2.3.3.1 First Model Problem

The study presented by Wu et al. [8] is a boundary element method-based study, in which the interface model presented in Figure 2.22 is used. Investigated RVE is given in Figure 2.24. Three models having inclusion diameters (d) of 40 μm, 60 μm, and 80 μm are analyzed. For all the models, the volume fraction of the inclusions (ϕ_f) is kept constant at 0.2, so the edge length (a) of square RVE changes for each model. Each edge of the square boundary of the RVE is divided into ten elements and the interface is divided into 60 boundary elements. The material and the interface properties used in the study are given in Table 2.12.

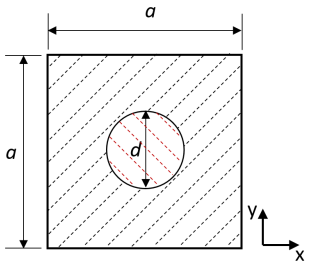


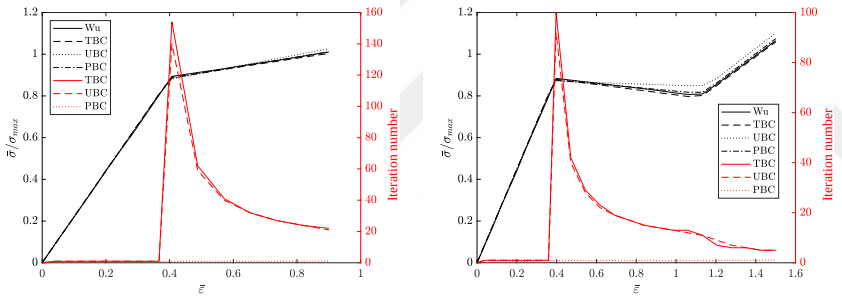
Figure 2.24: Investigated 2-phase representative volume element

In this study, the representative volume element given in Figure 2.24 is investigated under equibiaxial macroscopic strain loading for three different diameters of inclusions specified above. The effects of three classical boundary conditions (uniform traction (TBC), linear displacement (UBC), and periodic displacement (PBC)) on the

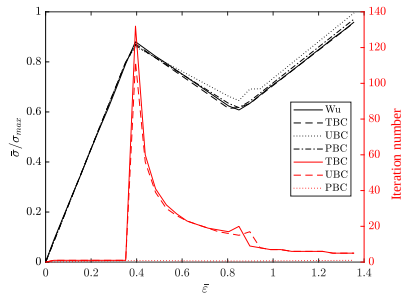
Table 2.12: Material and interface properties

Matrix		Inclusion		Interface		
E_0 [MPa]	ν_0 [-]	E_1 [MPa]	ν_1 [-]	σ_{max} [MPa]	k_σ [MPa/μm]	$\tilde{k}_\sigma$ [MPa/μm]
1	0.4	150	0.3	0.02	1	0.02

homogenized stress response are studied. In Figure 2.25, the macroscopic stress versus macroscopic strain (black curves and y-axis on the left) and the iteration number versus macroscopic strain (red curves and y-axis on the right) curves obtained for the three different diameters of a representative volume element are presented. As seen in the figures, the results of three different boundary conditions obtained in this study are consistent with the results presented in the literature in which only the periodic boundary condition (PBC) is considered. It is also observed that the highest iteration number is reached at the load step in which the softening of the interface starts.



(a) d= 40μm (b) d= 60μm



(c) d= 80μm

Figure 2.25: Macroscopic stress-strain and iteration-strain curves of RVEs with same volume fraction but different inclusion diameters. Models involve cohesive interface models and results are obtained for three different boundary conditions.

2.3.3.2 Second Model Problem

The second study is conducted by Inglis et al. [52], which examines the behavior of representative volume elements with a cohesive interface containing one or more reinforcing phases under macroscopic strain loading. The interface model presented in Equation 2.22 is used. A periodic displacement boundary condition (PBC) is defined on the boundaries of the representative volume elements. In the study of Inglis et al. [52], the problem was solved with the classical Mori-Tanaka approach and micromechanics-based finite elements solution called the Mathematical Theory of Homogenization based Finite Element (MTHFE) approach. Two RVEs with including one centered circular inclusion (Figure 2.24) and 18 randomly circular inclusions (Figure 2.26) are used in the study. The diameter of the inclusions used in both single and multi-inclusion representative volume elements is 60 μm and the volume fraction of inclusions is 0.32. The material and the interface parameters are given in Table 2.12. An equibiaxial macroscopic strain-driven loading, with strain increment ($\Delta\varepsilon$) of 0.02, is applied to the RVEs.

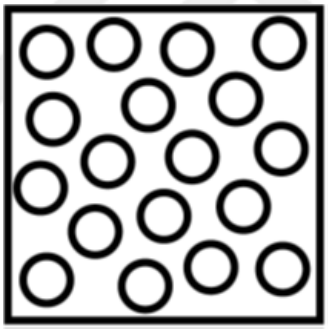


Figure 2.26: Multi inclusion representative volume element

In this study, the effects of a few interface parameters on the results were investigated. The parameters studied are summarized below.

- Comparison study of interface algorithm in which, at each load increment, the initial or the last interface.
- Comparison study of interface algorithm in which different maximum iteration and maximum error criteria are used.
- Mesh convergence study.

Comparison study of interface algorithm in which, at each load increment, the initial or the last interface condition is used.

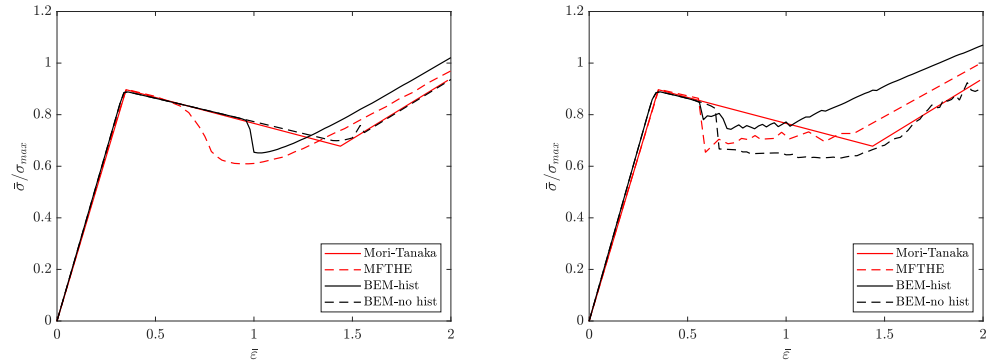
In this study, at each loading step $\Delta\varepsilon$, two cases where the opening displacement of interface node pairs is taken from the state where it remained in the previous loading step (BEM-hist) and from the first state, which is zero opening (BEM-no hist) in the interface equilibrium iterations are examined. This comparison study is conducted for two RVEs including one centered inclusion, and 18 randomly distributed inclusions. Each inclusion is divided in to 30 elements and outer edges of the RVE is discretized into 50 elements. The maximum error and iteration number for the stopping criteria of the interface equilibrium iterations are taken as 10^{-5} and 400, respectively.

The results obtained for both models are presented in Figure 2.27. The red-colored curves are the results obtained with the MFTHE and Mori-Tanaka approaches presented by Inglis et al. [52]. The black colored curves are the results obtained in this study. It is observed that the results, where the interface condition starts from the first loading state (BEM-no hist), give similar results to the Mori-Tanaka approach. It should be noted that Mori-Tanaka approach is not accounting the difference in the case whether single or multi inclusions are used. The consistent result with the MFTHE approach is obtained with the model in which the interface is renewed in each load step (BEM-hist).

Comparison study of interface algorithm in which different maximum iteration and maximum error criteria are used

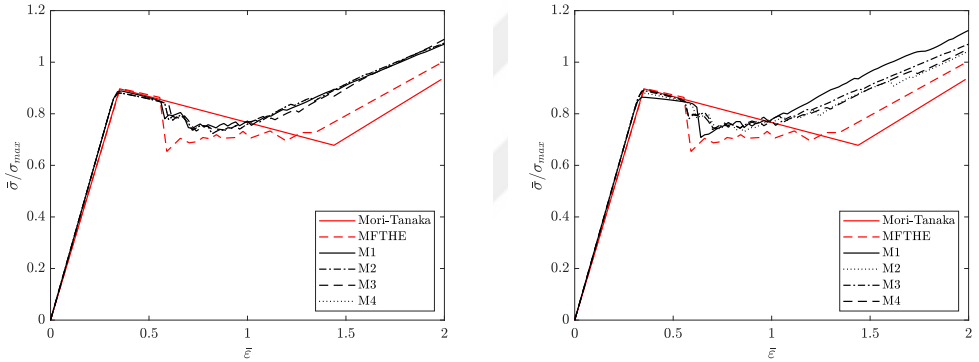
This study examines the situation where the interface starts from the condition in the previous loading step (BEM-hist) in the interface equilibrium iterations. The effect of the change of maximum error and a maximum number of iterations, presented in Equation 2.35, on the macroscopic behavior of the multi-inclusion RVE given in Figure 2.28(a) is compared. Each inclusion is divided in to 30 elements and outer edges of the RVE is discretized in to 50 elements. Four different models given in Table 2.15 are investigated.

In Figure 2.28(a), the results obtained for all models are presented. The red-colored curves are the results obtained with the MFTHE and Mori-Tanaka approaches pre-



(a) Single inclusion (b) Multi inclusion

Figure 2.27: Macroscopic stress-strain curves of two RVEs consisting single and multi inclusions, involving cohesive interface model with different iteration starting conditions, obtained for periodic displacement boundary condition (PBC)



(a) Results for different iteration stopping parameters (b) Results for varying mesh sizes

Figure 2.28: Macroscopic stress-strain curves of RVE consisting multi inclusions, involving cohesive interface model with different iteration stopping parameters and with varying mesh sizes, obtained for periodic displacement boundary condition (PBC)

sented in the literature. The black-colored curves are the results obtained with the boundary element method in this study. No major differences are observed between our boundary element models. As expected, the M3 model displays a slightly different behavior than the other models, in which the tolerances are low. The solution times of each model are given in Table 2.13.

Models	Solution Time [s]
M1	11166
M2	15345
M3	9047
M4	20629

Table 2.13: Solution times of analysis for different iteration stopping criteria

Models	Solution Time [s]
M1	3664
M2	9700
M3	32149
M4	125108

Table 2.14: Solution times of analysis for varying mesh sizes

Table 2.15: Investigated models

Models	Maximum Error	Maximum Iteration
M1	10^{-5}	400
M2	10^{-7}	800
M3	10^{-3}	200
M4	10^{-9}	1600

Mesh convergence study

In this study, the situation where the interface starts from the condition in the previous loading step (BEM-hist) is examined in the interface equilibrium iterations. The effect of the number of boundary elements on the macroscopic behavior is investigated in the representative volume element containing more than one reinforcing phase. Four different boundary element meshes presented in Table 2.16 are considered. The number in Table 2.16 refers to the discretization of a single circular inclusion. The outer edges of the RVEs are always divided into 50 boundary elements.

Table 2.16: Investigated models

Models	Number of Elements
M1	15
M2	30
M3	60
M4	120

In Figure 2.28(b), the results obtained for all models are also presented. The red-colored curves are the results obtained with the MFTHE and Mori-Tanaka approaches presented in the literature. The black-colored curves are the results obtained with the boundary element method in this study. No major differences are observed between our boundary element models. As expected, the biggest variance between the results is seen in the M1 model, which corresponds to the coarsest. The solution times of each model are given in Table 2.14.

2.4 Homogenization of Viscoelasticity with Dynamic Correspondence Principle

Various solution methodology of viscoelastic material modeling with BEM is reported in the literature. Dynamic Correspondence Principle is a well-studied modeling approach for viscoelastic materials. The Dynamic Correspondence Principle transforms the problem from the time domain to the frequency domain and requires time-dependent material properties. The BEM application of this methodology is straightforward and applicable by extending elasticity formulation to a succession of different frequencies. In the literature, various methods are presented for constitutive modeling of viscoelastic materials. Kelvin, Maxwell, and Burger's models use combinations of linear springs and dissipation elements to represent the mechanical behavior of viscoelastic materials. Hereditary integral expressions are different approaches that calculate the stress at the current time step using the prescribed strain history over time $[-\infty,\ t]$. It is an iterative method that uses integral equations and Stieltjes convolution to represent the time-dependent behavior of viscoelastic material. Detailed discussions on hereditary integrals are given in [53] and will not be discussed in this study. Assuming each phase in the heterogeneous RVE as isotropic and linear viscoelastic material, constitutive law can be written as shown in Equation 2.36.

$$\begin{aligned} s_{ij}(t) &= \int_{-\infty}^{t} 2G(t-\xi)\frac{de_{ij}}{d\xi}d\xi \\ \sigma_{kk}(t) &= \int_{-\infty}^{t} 3K(t-\xi)\frac{d\varepsilon_{kk}}{d\xi}d\xi \end{aligned} \tag{2.36}$$

In Equation 2.36, s_{ij} and σ_{kk} are the time-dependent deviatoric and volumetric com-

ponents of the stress tensor, e_{ij} and ε_{kk} are the time-dependent deviatoric and volumetric components of the strain tensor, and $G(t)$ and $K(t)$ are the time-dependent shear and bulk moduli, respectively. The major problem in heredity integral expressions of viscoelastic materials is that the solution of long periods is computationally intensive. Dynamic Correspondence Principle is a commonly used tool that allows reformulating the problem in the time domain to the frequency domain [54, 55]. Time-dependent harmonic deformation history can be expressed in the frequency domain as given in Equation 2.37.

$$\varepsilon_{ij}(t) = \overline{\varepsilon}_{ij}(\omega)e^{i\omega t} \tag{2.37}$$

Using Equation 2.37, Equation 2.36 reduces to

$$\begin{aligned} \overline{s}_{ij}(\omega) &= 2i\omega\overline{G}(\omega)\overline{e}_{ij}(\omega) \\ \overline{\sigma}_{kk}(\omega) &= 3i\omega\overline{K}(\omega)\overline{\varepsilon}_{kk}(\omega). \end{aligned} \tag{2.38}$$

In Equation 2.38, $\overline{G}$ and $\overline{K}$ can be expressed as follows.

$$\begin{aligned} \overline{G} &= \int_0^\infty G(t)e^{-i\omega t}dt \\ \overline{K} &= \int_0^\infty K(t)e^{-i\omega t}dt \end{aligned} \tag{2.39}$$

The real part of the moduli is called the storage moduli, which defines the elastic behavior of the material, while the viscoelastic character is defined by the loss moduli, which is the imaginary part of the complex moduli. Complex bulk and shear moduli are expressed in Equation 2.40.

$$\begin{aligned} i\omega\overline{G}(\omega) &\equiv G^*(\omega) = G'(\omega) + iG''(\omega) \\ i\omega\overline{K}(\omega) &\equiv K^*(\omega) = K'(\omega) + iK''(\omega) \end{aligned} \tag{2.40}$$

As can be observed from the above equations, the hereditary integrals of viscoelasticity in the frequency domain are similar to the elasticity representation of the material. However, it should be noted that with the transformation to the frequency domain, all

the field variables are transformed into complex quantities which are frequency dependent. The power of the transformation is that it is possible to solve a viscoelastic problem with solution methods developed for elasticity problems, such as the proposed method in this study.

2.4.1 Implementation of Dynamic Correspondence Principle in Boundary Element Method

Implementation of the Dynamic Correspondence Principle to the boundary element method is pretty straightforward. As discussed in the previous subsection, the field variables are now complex quantities. Tractions and displacements can be expressed as given in Equation 2.41.

$$\mathbf{u} = \begin{bmatrix} u'_x + iu''_x \\ u'_y + iu''_y \end{bmatrix}, \ \mathbf{t} = \begin{bmatrix} t'_x + it''_x \\ t'_y + it''_y \end{bmatrix} \tag{2.41}$$

Any variable given with superscripts (') and (") denotes the real and the imaginary parts of that variable, respectively. Moreover, complex numbers can be expressed in matrix form as follows.

$$a + ib = \begin{bmatrix} a & -b \\ b & a \end{bmatrix} \tag{2.42}$$

In Section 2.1, a detailed formulation of the boundary element method is discussed. The classical boundary element equation system is given below.

$$\mathbf{Hu} = \mathbf{Gt}\,. \tag{2.43}$$

In Section 2.2.1, the implementation of the classical boundary conditions to BEM is presented. For this purpose, additional relations are added to the equation system. These relations are discussed in detail for uniform traction (TBC), linear displacement (UBC), and periodic displacement (PBC) boundary conditions. After the addition of

these relations to the classical boundary element equation system given in Equation 2.43, the below system is obtained.

$$\begin{bmatrix} \mathbf{A}_{BEM} \\ \mathbf{A}_{BC} \end{bmatrix} \begin{bmatrix} \mathbf{x} \end{bmatrix} = \begin{bmatrix} \mathbf{0} \\ \mathbf{b}_{BC} \end{bmatrix} \tag{2.44}$$

In the above equation, $\mathbf{A}_{BEM}$ consists of matrices **G** and **H**, and **x** is the unknown vector composed of nodal tractions and displacements. $\mathbf{A}_{BC}$ is the boundary condition matrix, which is formed differently for each boundary condition as discussed in Section 2.2.1. When the viscoelastic material formulation is introduced, the coefficient matrices **G** and **H** become matrices involving complex variables as well. Following the property of complex numbers highlighted in Equation 2.42, Equation 2.43 can be rewritten as follows.

$$\begin{bmatrix} \mathbf{G}' & -\mathbf{G}'' \\ \mathbf{G}'' & \mathbf{G}' \end{bmatrix} \begin{bmatrix} \mathbf{t}' \\ \mathbf{t}'' \end{bmatrix} - \begin{bmatrix} \mathbf{H}' & -\mathbf{H}'' \\ \mathbf{H}'' & \mathbf{H}' \end{bmatrix} \begin{bmatrix} \mathbf{u}' \\ \mathbf{u}'' \end{bmatrix} = \begin{bmatrix} \mathbf{0} \\ \mathbf{0} \end{bmatrix} \tag{2.45}$$

Employing the viscoelastic material property description discussed, the matrices $\mathbf{A}_{BEM}$ and **x** in Equation 2.44 will be complex. Following the analogy discussed in Equations 2.42 and 2.45, the boundary element equation system obtained for the elasticity can be rewritten as shown in Equation 2.46 for viscoelastic modeling using the Dynamic Correspondence Principle. It should also be noted that the relations used to implement the classical boundary conditions of elasticity ($\mathbf{A}_{BC}$) are used to satisfy boundary conditions for both real and imaginary field variables, as shown below.

$$\left[\begin{array}{c|c} \mathbf{A}'_{BEM} & -\mathbf{A}''_{BEM} \\ \mathbf{A}_{BC} & \mathbf{0} \\ \hline \mathbf{A}''_{BEM} & -\mathbf{A}'_{BEM} \\ \mathbf{0} & \mathbf{A}_{BC} \end{array}\right] \left[\begin{array}{c} \mathbf{x}' \\ \hline \mathbf{x}'' \end{array}\right] = \left[\begin{array}{c} \mathbf{0} \\ \mathbf{b}'_{BC} \\ \hline \mathbf{0} \\ \mathbf{b}''_{BC} \end{array}\right] \tag{2.46}$$

The solution of Equation 2.46 will give real ($\boldsymbol{\sigma}'$) and imaginary ($\boldsymbol{\sigma}''$) homogenized stresses for the applied macroscopic strain.

2.4.2 Determination of Homogenized Real and Imaginary Material Constants

Following the discussion in Section 2.4.1, the proposed boundary element method can solve a heterogeneous RVE, in which elastic/viscoelastic material properties are used. Under macroscopic strain loading, the proposed method gives real ($\boldsymbol{\sigma}^{'}$) and imaginary ($\boldsymbol{\sigma}^{''}$) homogenized stresses. For a 2-D problem, both real ($\bar{\boldsymbol{C}}'$) and imaginary ($\bar{\boldsymbol{C}}''$) parts of tangent moduli consist of in total nine entities, as shown in Equation 2.47.

$$\bar{\boldsymbol{C}}' = \begin{bmatrix} C'_{11} & C'_{12} & C'_{13} \\ C'_{21} & C'_{22} & C'_{23} \\ C'_{31} & C'_{32} & C'_{33} \end{bmatrix}, \; \bar{\boldsymbol{C}}'' = \begin{bmatrix} C''_{11} & C''_{12} & C''_{13} \\ C''_{21} & C''_{22} & C''_{23} \\ C''_{31} & C''_{32} & C''_{33} \end{bmatrix} \tag{2.47}$$

Following the approach proposed in Section 2.2.2, it is possible to evaluate the homogenized material parameters using two macroscopic strain loadings, as discussed below.

The procedure shown in Equation 2.48 gives the first column of both real and imaginary tangent moduli.

$$\boldsymbol{\varepsilon_1} = \begin{bmatrix} \alpha \\ 0 \\ 0 \\ 0 \\ 0 \\ 0 \end{bmatrix} \xrightarrow{\text{Evaluate using BEM}} \begin{bmatrix} \boldsymbol{\sigma}^{'}(\boldsymbol{\varepsilon_1}) \\ \boldsymbol{\sigma}^{''}(\boldsymbol{\varepsilon_1}) \end{bmatrix} = \begin{bmatrix} \sigma'_{11} \\ \sigma'_{22} \\ \sigma'_{12} \\ \sigma''_{11} \\ \sigma''_{22} \\ \sigma''_{12} \end{bmatrix}$$

$$\begin{bmatrix} \boldsymbol{\sigma}^{'}(\boldsymbol{\varepsilon_1}) \\ \boldsymbol{\sigma}^{''}(\boldsymbol{\varepsilon_1}) \end{bmatrix} = \left[\begin{array}{ccc|ccc} C'_{11} & C'_{12} & C'_{13} & -C''_{11} & -C''_{12} & -C''_{13} \\ C'_{21} & C'_{22} & C'_{23} & -C''_{21} & -C''_{22} & -C''_{23} \\ C'_{31} & C'_{32} & C'_{33} & -C''_{31} & -C''_{32} & -C''_{33} \\ -- & -- & -- & -- & -- & -- \\ C''_{11} & C''_{12} & C''_{13} & C'_{11} & C'_{12} & C'_{13} \\ C''_{21} & C''_{22} & C''_{23} & C'_{21} & C'_{22} & C'_{23} \\ C''_{31} & C''_{32} & C''_{33} & C'_{31} & C'_{32} & C'_{33} \end{array}\right] \begin{bmatrix} \alpha \\ 0 \\ 0 \\ 0 \\ 0 \\ 0 \end{bmatrix} \tag{2.48}$$

The third column of both real and imaginary tangent moduli is determined by follow-

ing the procedure shown in Equation 2.49.

$$\boldsymbol{\varepsilon_2} = \begin{bmatrix} 0 \\ 0 \\ \alpha \\ 0 \\ 0 \\ 0 \end{bmatrix} \xrightarrow{\text{BEM}} \begin{bmatrix} \boldsymbol{\sigma}^{'}(\boldsymbol{\varepsilon_2}) \\ \boldsymbol{\sigma}^{''}(\boldsymbol{\varepsilon_2}) \end{bmatrix}$$

$$\begin{bmatrix} \boldsymbol{\sigma}^{'}(\boldsymbol{\varepsilon_2}) \\ \boldsymbol{\sigma}^{''}(\boldsymbol{\varepsilon_2}) \end{bmatrix} = \left[\begin{array}{ccc|ccc} C^{'}_{11} & C^{'}_{12} & C^{'}_{13} & -C^{''}_{11} & -C^{''}_{12} & -C^{''}_{13} \\ C^{'}_{21} & C^{'}_{22} & C^{'}_{23} & -C^{''}_{21} & -C^{''}_{22} & -C^{''}_{23} \\ C^{'}_{31} & C^{'}_{32} & C^{'}_{33} & -C^{''}_{31} & -C^{''}_{32} & -C^{''}_{33} \\ -- & -- & -- & -- & -- & -- \\ C^{''}_{11} & C^{''}_{12} & C^{''}_{13} & C^{'}_{11} & C^{'}_{12} & C^{'}_{13} \\ C^{''}_{21} & C^{''}_{22} & C^{''}_{23} & C^{'}_{21} & C^{'}_{22} & C^{'}_{23} \\ C^{''}_{31} & C^{''}_{32} & C^{''}_{33} & C^{'}_{31} & C^{'}_{32} & C^{'}_{33} \end{array}\right] \begin{bmatrix} 0 \\ 0 \\ \alpha \\ 0 \\ 0 \\ 0 \end{bmatrix} \tag{2.49}$$

Using $C^{'}_{33}$ and $C^{''}_{33}$ evaluated using Equation 2.49, it is possible to determine real and imaginary parts of the shear moduli as follows.

$$\mu = \mu^{'} + i\mu^{''} \Rightarrow \mu^{'} = C^{'}_{33},\ \mu^{''} = C^{''}_{33} \tag{2.50}$$

By solving $C^{'}_{11}$ and $C^{''}_{11}$ using Equation 2.48 and the evaluated value of μ, it is possible to calculate real and imaginary parts of the bulk moduli as follows.

$$K = K^{'} + iK^{''} \Rightarrow K^{'} = C^{'}_{11} - \frac{4}{3}\mu^{'},\ K^{''} = C^{''}_{11} - \frac{4}{3}\mu^{''} \tag{2.51}$$

After determining the shear and the bulk modulus, it is possible to determine other material parameters using the relationship between elastic constants.

2.4.3 Numerical Examples

The developed boundary element method-based homogenization of a heterogeneous RVE involving elastic/viscoelastic materials is applied to three examples from the literature, and a comparison study is conducted in this section. In some of the comparison studies in this section, a third region called "*interphase*", which has the material properties of neither matrix nor inclusion, is presented. A representative volume element involving interphase is given in Figure 2.29.

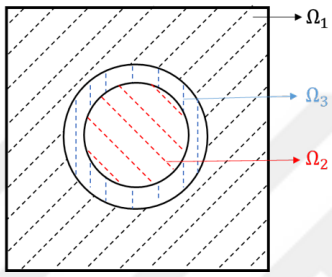


Figure 2.29: Three-phase RVE consisting of matrix phase (black), interphase (blue), and inclusion (red)

2.4.3.1 First Application: Comparisons with Numerical Studies

The developed methodology is applied to various RVEs having different sets of materials defined for matrix, interphase, and inclusion phases. The comparison studies conducted in this section involve two hypothetical viscoelastic materials proposed by Brinson et al. [3]. These materials are called *stiff* and *soft* materials. In Table 2.17, the material constants that are used to represent these materials as a Prony series expansion are presented. The formulation presented in Equation 2.52 can be used to determine both shear and bulk modulus at a desired frequency using the material constants.

$$G'(\omega) = G_\infty + \sum_{i=1}^{n} \frac{G_i \omega^2}{\frac{1}{\xi_i^2} + \omega^2}$$
$$G''(\omega) = \sum_{i=1}^{n} \frac{\frac{G_i}{\xi_i}\omega}{\frac{1}{\xi_i^2} + \omega^2}, \tag{2.52}$$

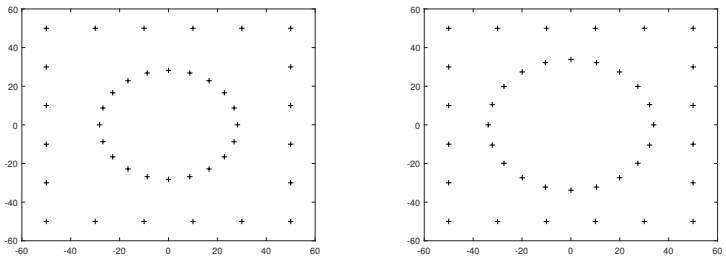
Table 2.17: Material properties used to represent stiff and soft viscoelastic materials using Pronny series [3]

Stiff material		Soft material		asymptotic mod.
τ_i^1 [s]	G_i^1 [bar]	τ_i^2 [s]	G_i^2 [bar]	
3	3.162	0.032	2.512	$G_\infty^1 = 100.00$ bar
10	17.783	0.100	10.000	$G_\infty^2 = 3.162$ bar
32	100.000	0.316	56.234	
100	316.228	1.000	316.228	
316	1000.000	3.162	1000.000	$K_\infty^1 = 8000$ bar
1000	5623.413	10.000	199.526	$\tau_1^1 = 10000$ s
3162	10000.000	31.623	50.119	$K_1^1 = 40000$ bar
10000	562.341	100.000	19.953	
31623	141.254	316.228	12.589	$K_\infty^2 = 200$ bar
100000	56.234	1000.000	2.512	$\tau_1^2 = 100$ s
316228	17.783	3162.278	1.698	$\tau_2^2 = 316.228$ s
1000000	5.623	10000.000	1.202	$K_1^2 = 3000$ bar
3162278	3.162	31622.777	1.148	$K_2^2 = 100$ bar
10000000	1.778	100000.000	1.096	

where ξ_i is defined as the inverse of the time constant (τ_i) given Table 2.17. In the following subsections, the results obtained using the proposed method are compared with the FEM results presented by Brinson et al. [54]. The reference study investigates a square RVE consisting of a single inclusion. A uni-axial displacement of $\bar{u}_y = u_0 + 0i$ is applied to the single edge of the RVE. Moreover, accuracy and time comparison studies with FEM results presented by Guzel [56] are also conducted in the following subsections.

Two-Phase Heterogeneous Viscoelastic RVE

In Appendix B, the results of a two-phase RVE with identical viscoelastic material properties on phases are presented for the verification of the defined material properties. After verifying the frequency response of Young's modulus for stiff and soft materials with the developed boundary element method-based method, investigation of the RVEs containing 0.25 and 0.36 volume fraction (ϕ_f) of circular inclusion is done. Each edge at the outer boundary is divided into 5 elements, and the inclusion boundary is divided into 20 elements. Boundary element meshes are presented in Figure 2.30. For each RVE, soft inclusion-stiff matrix and stiff inclusion-soft matrix cases are investigated. In Figure 2.31, the frequency response of storage and loss Young's modulus of the viscoelastic stiff inclusion-soft matrix for the volume fraction of 0.25 and 0.36 are presented. In Figure 2.32, the frequency response of storage and loss Young's modulus of the viscoelastic soft inclusion-stiff matrix for the volume fraction of 0.25 is presented. In all results, it is seen that the general trend of the material behavior is captured for all boundary conditions [54]. Moreover, it is also observed that the displacement boundary condition (UBC) shows the closest response to the results presented in the literature in which a displacement controlled boundary condition is used as well.

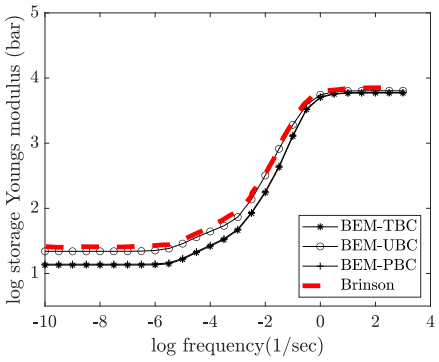


(a) $\phi_f = 0.25$ (b) $\phi_f = 0.36$

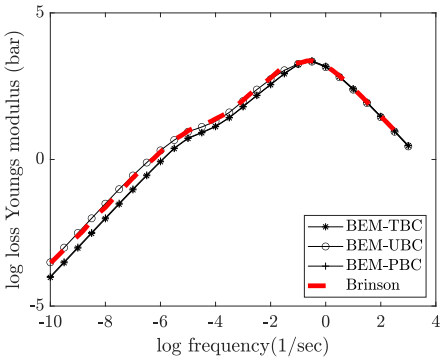
Figure 2.30: BEM meshes of two-phase RVE with $\phi_f = 0.25$ and $\phi_f = 0.36$

Three-Phase RVE with Elastic Inclusion, Viscoelastic Interphase, and Matrix

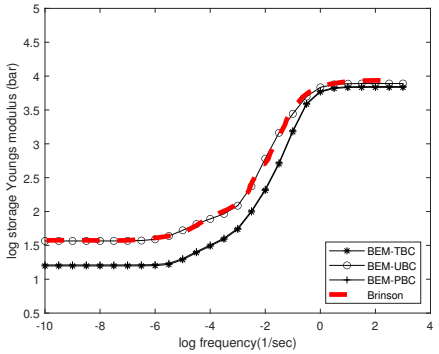
It is a common practice to assume the inclusion to be elastic in modeling heterogeneous materials in which the stiffness of the inclusion is significantly greater than the matrix. Furthermore, an interphase region is frequently formed in nanocomposites



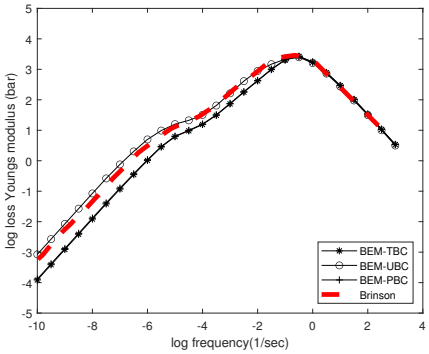
(a) Storage Young's Modulus ($\phi_f = 0.25$)



(b) Loss Young's Modulus ($\phi_f = 0.25$)



(c) Storage Young's Modulus ($\phi_f = 0.36$)

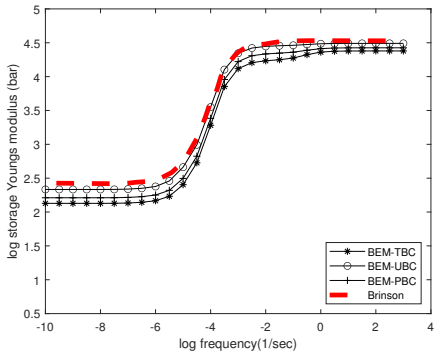


(d) Loss Young's Modulus ($\phi_f = 0.36$)

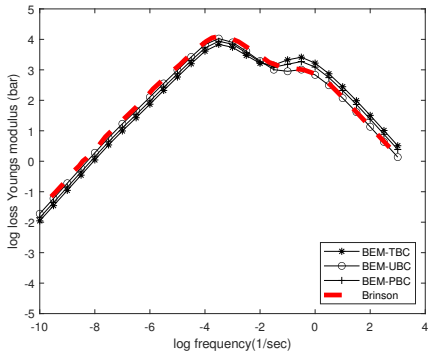
Figure 2.31: Storage and loss Young's modulus of viscoelastic stiff inclusion-soft matrix materials defined on a two-phase RVE having $\phi_f = 0.25$ and $\phi_f = 0.36$

around the nano-inclusion in the form of a coating. For this reason, in this part of the study, a three-phase RVE is , as shown in Figure 2.33. Volume fractions of inclusion and interphase are taken as 0.3 and 0.1, respectively. Each edge at the outer boundary is divided into 10 elements, and the inclusion boundary is divided into 20 elements. The boundary between interphase and matrix is divided consistently with the diameter ratio of interphase and inclusion. For the elastic inclusion, bulk modulus (K) and shear modulus (μ) are taken as 100000 and 40000, as given by Fisher and Brinson [57]. Units are not specified, but they are consistent with the hypothetical viscoelastic stiff and soft materials proposed by Brinson et al. [54]. The following models are investigated:

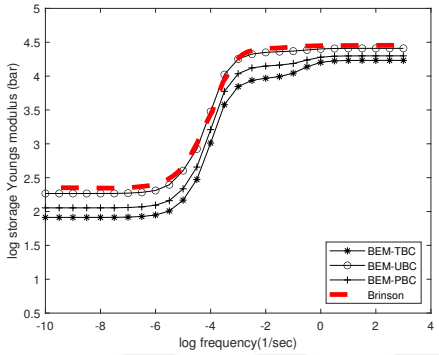
- Model1: Elastic inclusion, viscoelastic stiff interphase, and viscoelastic soft



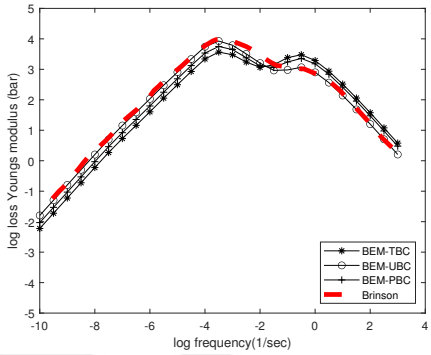
(a) Storage Young's Modulus ($\phi_f = 0.25$)



(b) Loss Young's Modulus ($\phi_f = 0.25$)



(c) Storage Young's Modulus ($\phi_f = 0.36$)



(d) Loss Young's Modulus ($\phi_f = 0.36$)

Figure 2.32: Storage and loss Young's modulus of viscoelastic soft inclusion-stiff matrix materials defined on a two-phase RVE having $\phi_f = 0.25$ and $\phi_f = 0.36$

matrix

- Model2: Elastic inclusion, viscoelastic soft interphase, and viscoelastic stiff matrix

Homogenized storage and loss of Young's Modulus concerning change in frequency are given in Figure 2.34 for Model1 and Model2. The results are presented with the finite element solution (FEM) of the same problem presented in [56]. In Table 2.18, the solution times of FEM and BEM are presented. The outcomes from the developed BEM approach exhibit a notable correspondence with the FEM results, and importantly, they are achieved at a speed nearly six times faster. Notably, in Model1, where the displacement boundary condition is applied, there is a tendency to overpredict the behavior. Nevertheless, for the other models, there is a strong alignment with the

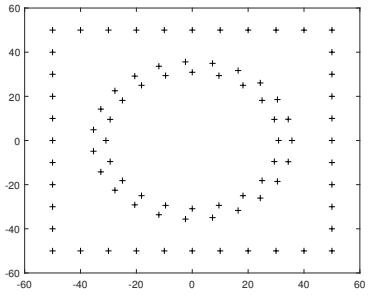
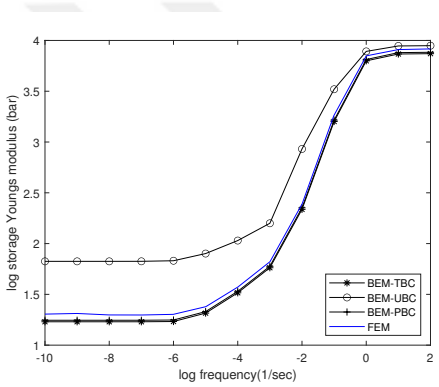
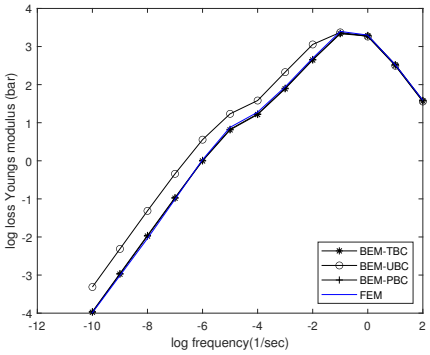


Figure 2.33: Boundary element mesh of three phase RVE with 0.3 and 0.1 volume fractions of inclusion and interphase, respectively

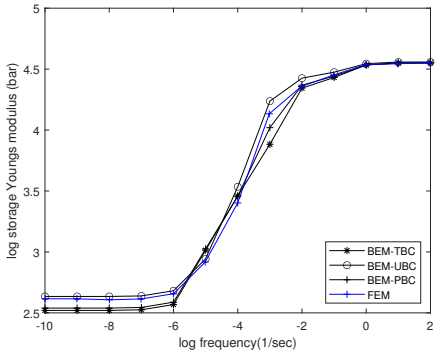
FEM results, confirming the accuracy and efficiency of the proposed approach.



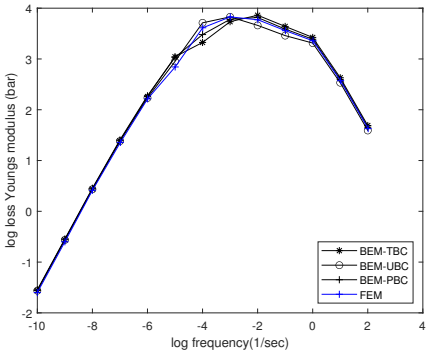
(a) Model1 - Storage Young's Modulus



(b) Model1 - Loss Young's Modulus



(c) Model2 - Storage Young's Modulus



(d) Model2 - Loss Young's Modulus

Figure 2.34: Storage and loss Young's modulus of Model1 and Model2

Table 2.18: Solution times of the Model1 and Model2

Models	Solution Time of Model1 [s]	Solution Time of Model2 [s]
TBC	12.23	12.22
UBC	11.75	11.71
PBC	12.03	12.11
FEM	73.1	73.1

2.4.3.2 Second Example: Comparison with Experimental Studies

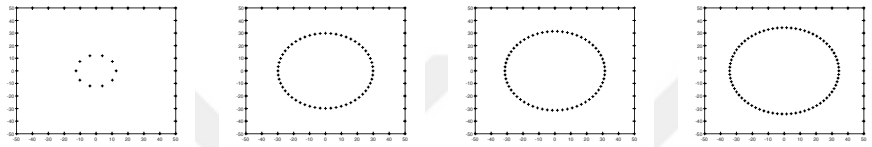
The results of the developed Dynamical Correspondence Principle-based viscoelasticity modeling approach is compared with an experimental and micromechanics-based study in the literature. In the experimental work presented by Diani et al. [4], six sets of specimens with 0%, 2.4%, 13%, 16.7%, and 20% volume fractions of coated carbon-black filled styrene-butadiene rubbers (SBR) in a random copolymer matrix with 15%-mole fraction of styrene, a molecular mass of 120 g/mol and a density of 0.94 g/cm^3 are created. Dynamic mechanical analysis (DMA) is used to determine the frequency response of the manufactured samples. Tests were done at 0.1% strain for frequencies ranging from 0.01 to 10 Hz. In the same study, a micromechanics modeling approach for heterogeneous RVEs is introduced and a comparison with the experimental study is conducted. Details of the numerical approach are presented in the related study. Moreover, a discussion on the effective volume fraction of inclusion is made in the study of Diani et al. [4]. It is proposed that because of the presence of rubber gum trapped between fillers, reinforcing rigid phase is significantly underestimated when accounting for the filler volume fraction only. Hence, this rubber gum phase acts as rigid and increases the volume fraction of the inclusion phase. Actual and effective volume fractions of the inclusion phase for each model are given in Table 2.19.

Two-phase and three-phase models are investigated by the proposed method. In the two-phase model, the effective volume fractions of inclusions (ϕ_{eff}) presented in Table 2.19 are used. In three-phase model, the volume fractions of inclusions (ϕ) and interphase (ϕ_{int}) presented in Table 2.19 are defined. Boundary element meshes used in two-phase and three-phase models are presented in Figures 2.35 and 2.36, respec-

tively.

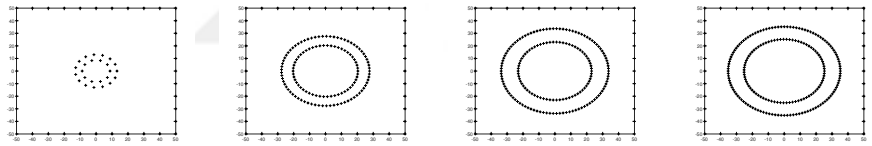
Table 2.19: Normal and effective volume fraction of inclusion, and volume fraction of interphase [4]

Material	M0	M5	M30	M40	M50
ϕ	0	2.4	13.0	16.7	20.0
ϕ_{eff}	0	5.0	28.0	31.0	37.0
ϕ_{int}	0	3.0	11.0	19.0	19.0



(a) M5 (b) M30 (c) M40 (d) M50

Figure 2.35: Two-phase BEM models for four different volume fractions of nclusions



(a) M5 (b) M30 (c) M40 (d) M50

Figure 2.36: Three-phase BEM models for four different volume fractions of inclusions

In BEM analyses, two-phase and three-phase models are used to obtain homogenized material properties of the given microstructure. The inclusion phase is assumed to be linear elastic with Young's modulus of 70 GPa and Poisson's ratio of 0.5. For the viscoelastic matrix phase, Prony series constants presented in Table 2.20 are used with Equation 2.54 to calculate Young's modulus at a desired frequency. The bulk modulus of the matrix (K_m) is kept constant at 3500 MPa for all frequencies. To model the interface, Diani et al. [4] proposed a simple method to model the interphase behavior. They have assumed that the material properties of interphase will neither be the same

as the inclusion nor the matrix, but a value in between. For this purpose, a variable parameter χ is defined which is between 0 and 1. Using this variable, it is possible to define the interphase Young's modulus ($E_i^*(\omega)$) as shown in Equation 2.53.

$$E_i^*(\omega) = E_{mg}^* + \chi \left(E_m^*(\omega) - E_{mg}^* \right) \tag{2.53}$$

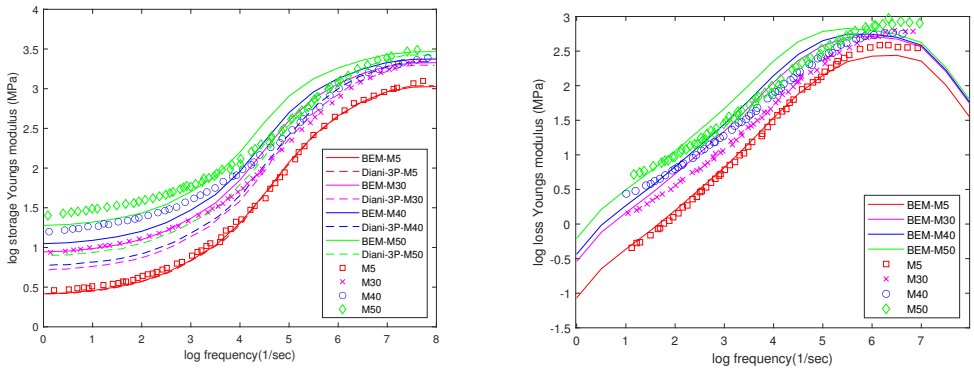
In the above equation, E_{mg}^* and E_m^* are the complex Young's modulus of matrix and inclusion, respectively. The interface modeling approach presented by Diani et al. [4], which is formulated in Equation 2.53, is used with a χ value of 0.95.

$$\begin{aligned} E'(\omega) &= E_e + E_i \sum_{i=1}^{n} \frac{(2\omega\tau_i)^2}{1 + (2\omega\tau_i)^2} \\ E''(\omega) &= E_i \sum_{i=1}^{n} \frac{2\omega\tau_i}{1 + (2\omega\tau_i)^2} \end{aligned} \tag{2.54}$$

Table 2.20: Constants used to represent viscoelastic matrix material [4]

$\tau_i(s)$	1.852×10^{-8}	8.993×10^{-8}	4.368×10^{-7}	2.121×10^{-6}
$E_i(\mathrm{MPa})$	320.3	293.7	235.3	86.88
$\tau_i(\mathrm{\ s})$	1.030×10^{-5}	5.004×10^{-5}	2.431×10^{-4}	1.181×10^{-3}
$E_i(\mathrm{MPa})$	18.79	4.283	2.488	0.8908
$\tau_i(s)$	5.734×10^{-3}	2.785×10^{-2}	0.1353	0.6570
$E_i(\mathrm{MPa})$	0.3943	0.2369	0.8696×10^{-2}	0.2707×10^{-3}

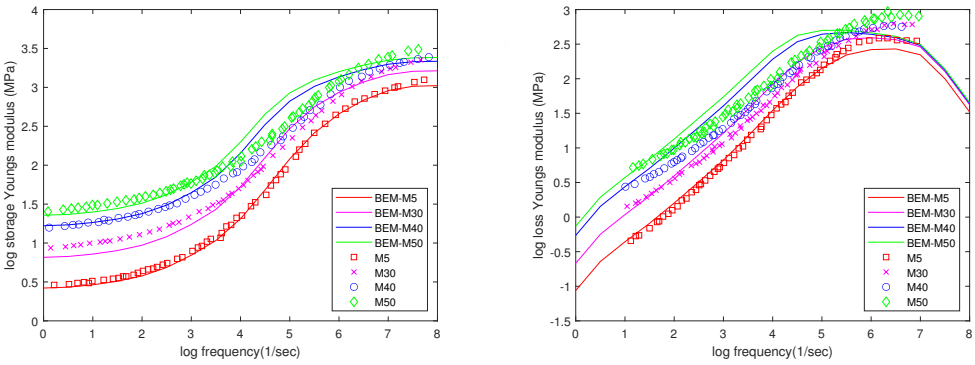
Two-phase and three-phase BEM results under displacement boundary condition (UBC) for four different RVEs are presented in Figures 2.37 and 2.38 with experimental and micromechanics results presented by Diani et al. [4]. Only storage Young's modulus results of the two-phase model are presented for the micromechanics solution. The performance of the proposed two-phase model is considerably better compared to the micromechanics solution of the literature, especially for lower volume fractions of inclusion. Furthermore, inclusion of the third phase (interphase) improves the agreement between the proposed model and the experimental results [4], see Figure 2.38. The consistency between experimental and BEM results is significantly better for the three-phase model, especially at low frequencies.



(a) Storage Young's Modulus

(b) Loss Young's Modulus

Figure 2.37: Young's modulus of a two-phase composite material with the change of frequency. Experimental results (shown with discrete data points), micromechanics solution (shown with dash lines-only for storage modulus) [4] and BEM results (solid lines) of the proposed method are presented for four different volume fractions of inclusions.



(a) Storage Young's Modulus

(b) Loss Young's Modulus

Figure 2.38: Young's modulus of a three-phase composite material with the change of frequency. Experimental results (shown with discrete data points) and BEM results (solid lines) of the proposed method are presented for four different volume fractions of inclusions.

2.5 Homogenization of Nonlinear Viscoelasticity with a Novel Non-iterative Approach

In this section, the homogenization capability of the developed approach on the formulation of time domain BEM for rate-dependent inelasticity, as discussed in detail in Chapter 4, is demonstrated through a nonlinear viscoelasticity example. The solution methodology specifically follows the formulation presented in Section 4.2. The numerical model's geometry and dimensions are shown in Figure 2.39. The rheological model used to represent viscoelasticity is depicted in Figure 4.17, and the nonlinear viscoelasticity model parameters utilized in the analyses of the perforated plate are provided in Table 4.7. The power term used for the evolution of viscoelastic strain δ (see Equation 4.33) is selected as 3.

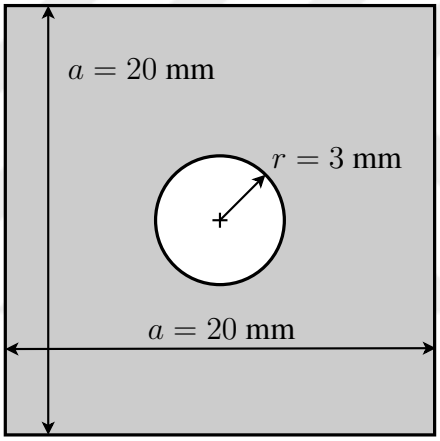


Figure 2.39: The perforated plate model

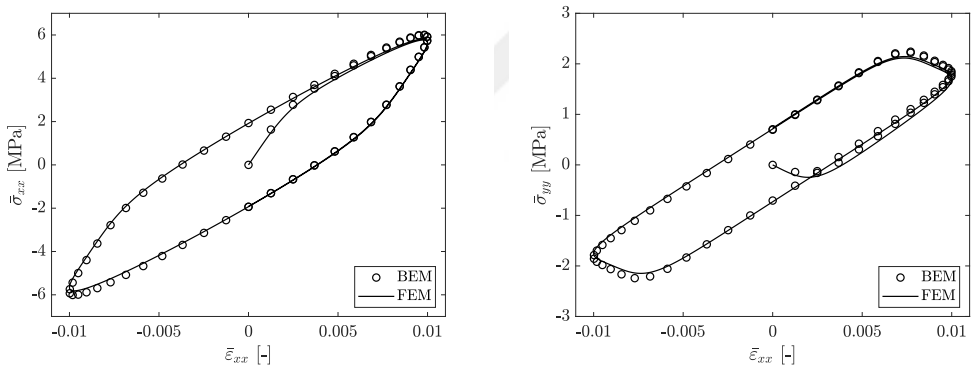
Cyclic loading is applied to the perforated plate using prescribed macroscopic strains $\bar{\boldsymbol{\varepsilon}}$, and the linear displacement boundary condition (UBC) is employed for homogenization purposes. The specific sinusoidal function used to define the axial loading function $\bar{\boldsymbol{\varepsilon}}$ is given in Table 2.21. The time-step is selected as 0.1s.

Table 2.21: Specific sinusoidal functions of the $\bar{\boldsymbol{\varepsilon}}$ macroscopic strain loading along with the accompanying linear displacement boundary conditions

$\bar{\varepsilon}_{xx} = 0.01 \sin(2\pi\, t/100)$	$\bar{\varepsilon}_{yy} = -\dfrac{0.01}{3} \sin(2\pi\, t/100)$	$\bar{\varepsilon}_{xy} = 0$

Figure 4.19 depicts the spatial discretization scheme utilized in the BEM model. A total of 80 linear boundary elements are employed to model both the outer and hole boundaries. The Cartesian Transformation Method (CTM) and the Radial Point Interpolation Method (RPIM), discussed in 3, use 5956 integration points and 1208 data points, denoted by red crosses ($\times$). On the figure, CTM and RPIM points are represented by blue circles ($\bigcirc$) and red crosses ($\times$), respectively. For comparative study, a fully-implicit FEM solution of the problem is also solved with a FEM mesh of the quarter model for the perforated plate is created. 4800 quadrilateral elements are used for the discretization of the quarter perforated plate domain for the FEM analyses.

The change in the components of the macroscopic stress with the applied macroscopic strain in x-direction is presented in Figure 2.40 for both the FEM and BEM solutions. The BEM formulation for viscoelasticity has effectively captured the dissipative nature of viscoelastic behavior on the macroscopic stress results. Moreover, a perfect consistency is observed between the results of two numerical approaches.



(a) Storage Young's Modulus

(b) Loss Young's Modulus

Figure 2.40: The change in macroscopic stress with the applied macroscopic strain for the perforated plate domain with nonlinear power-type viscoelasticity is defined as material.

CHAPTER 3

MESH-FREE INTEGRATION AND INTERPOLATION

Even though the Finite Element Method (FEM) and Boundary Element Method (BEM) are useful tools to solve applied mechanics problems, the desired accuracy of the solution is always a problem that is open for improvement. For the Finite Element Method (FEM), the problems involving large deformations and crack propagation, the strength of the solution strongly depends on the use of a suitable mesh [58]. In the conventional Boundary Element Method (BEM), the domain integration, when needed, brings extra computational workload due to the requirement of discretizing the problem domain into a finite number of cells; therefore, it creates a bigger problem domain involving boundary equations written for all cells. For this reason, the necessity of employing an efficient mesh-free integration method had raised to solve this problem.

The need for a mesh-free method evolves from reducing the necessity of elements or mesh in the equation system. In mesh-free methods, the numerical integration is a subject studied by researchers extensively to eliminate the requirement of a background mesh on the solution domain [59, 60, 61]. These methods can be referred to as truly mesh-free methods. The nodal integration technique is used in some of these truly mesh-free methods. The domain integral is evaluated as the summation of products of weights and the values of the integrand at these nodes. Some drawbacks of the nodal integration technique have been reported as the oscillation in the solution of the Element-free Galerkin (EFG) method [62]. To eliminate these oscillations in integrals, the shape functions used before the nodal integration have been modified, and these stabilized techniques are called robust Galerkin mesh-free methods [9]. However, after modifications, this method requires the construction of a Voronoi diagram

and can not be called a truly mesh-free method. In summary, a price is paid to have a truly mesh-free method [58]. In this study, a truly mesh-free method called the Cartesian Transformation Method (CTM) is used to evaluate domain integrals with good accuracy and low computational cost. The domain integral, is transformed into a double integral which is composed of a boundary integral over a boundary of the problem domain and a 1D integral to model the inner domain. Radial Point Interpolation Method (RPIM) and Moving Least Squares Method (MLS) are introduced to interpolate the values of integrands on the desired points using a finite number of scattered data in the problem domain.

The domain integral in the boundary element method needs to be evaluated numerically. The conventional integration methods used in the boundary element method on integrating domain integrals include the discretization of the inner domain into a finite number of cells. However, recently introduced mesh-free methods are more efficient in terms of computational power to deal with domain integration in the boundary element method. In Section 3.1, mesh-free methods are discussed. The formulation and interpolation of the mesh-free integration method, which is called the Cartesian Transformation Method (CTM), is presented in this section. For the determination of the value of the integrand at the integration points of CTM, two interpolation methods, which are called Moving Least Squares (MLS) and Radial Point Integration (RPIM), are used. Validation of the developed method with mathematical examples is presented in Appendix C. Finally, the application on real engineering problems are given in Section 3.2.

3.1 Methodology

The Cartesian Transformation Method (CTM) has been used in cooperation with BEM to evaluate of domain integrals in the literature [63, 64] for the solution of thermal diffusion problems. The domain integral is decomposed into two sub-integrals: a boundary integral over the boundary of the problem domain and a 1-D integral to model the inner domain. The Radial Point Interpolation Method (RPIM) and Moving Least Square Method (MLS) [10] are introduced to interpolate the values of integrands at the desired points using a finite number of scattered data in the problem

domain. The details of the implementation of the method are discussed in detail in the following subsections.

3.1.1 Mesh-free Integration - Cartesian Transformation Method (CTM)

The formulation proposed in this study mostly follows the work on Cartesian Transformation Method (CTM) proposed by Khosravifard and Hematiyan [58]. Suppose the integral to be evaluated is in the form given in Equation 3.1:

$$I = \int_{\Omega} f(x,y) d\Omega, \tag{3.1}$$

where f is the function to be integrated, and Ω is the solution domain. An arbitrarily shaped secondary domain Ω_R covering the problem domain is defined and it is called the auxiliary domain. A new function g can be defined, in this domain as given in Equation 3.2.

$$g(x,y) = \begin{cases} f(x,y) & (x,y) \in \Omega \\ 0 & (x,y) \notin \Omega \end{cases} \tag{3.2}$$

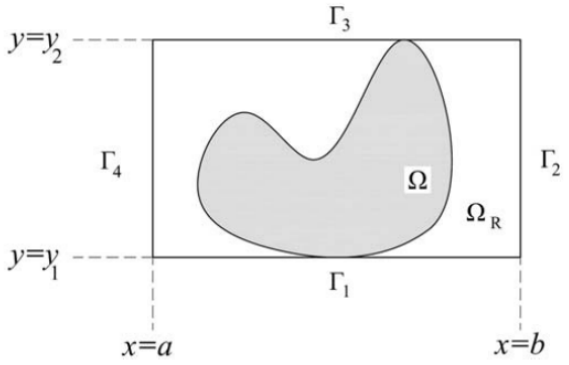


Figure 3.1: Problem domain Ω and auxiliary domain Ω_R [9]

Equation 3.2 can be rewritten as shown in Equation 3.3.

$$I = \int_{\Omega} f(x,y) d\Omega = \int_{\Omega_R} g(x,y) d\Omega \tag{3.3}$$

For Equation 3.3, Green's theorem can be applied to write the domain integral as a boundary integral and a 1D integral. Green's theorem is defined as follows:

$$\int_{\Omega} \frac{\partial u(x,y)}{\partial x} d\Omega = \int_{\Gamma} u(x,y) dy, \tag{3.4}$$

where Γ is the boundary of the problem domain Ω. The newly introduced function u in the above equation can be defined as:

$$u(x,y) = \int_{c}^{x} g(\xi, y) d\xi, \tag{3.5}$$

where c is selected as an arbitrary constant. Substitution of the above relation into Equation 3.4 gives:

$$\int_{\Omega_R} \frac{\partial u(x,y)}{\partial x} d\Omega = \int_{\Omega_R} g(x,y) d\Omega = \int_{\Gamma_R} \left(\int_{c}^{x} g(\xi, y) d\xi \right) dy. \tag{3.6}$$

It is seen that the domain integral in Equation 3.3 is transformed into two line integrals, as shown in Equation 3.6. For easiness, the auxiliary domain Ω_R is considered as a rectangular domain, as shown in Figure 3.1. Consequently, the boundary Γ_R includes four sections as follows:

$$\Gamma_1 : y = y_1, \Gamma_2 : x = b, \Gamma_3 : y = y_2, \Gamma_4 : x = a. \tag{3.7}$$

For the evaluation of the outer integral, the Gauss quadrature integration method is used in this study. When the constant c in Equation 3.5 is set to a, the outer integral Γ_R will reduce to Γ_2. The upper and lower bounds of Γ_4 will be the same after setting $c = a$; therefore, the integral will be zero. Γ_1 and Γ_3 vanish because the integral is evaluated with respect to the y-coordinate and these boundaries are parallel to x-coordinate. Therefore, integral in Equation 3.6 becomes:

$$I = \int_{y_1}^{y_2} \left(\int_{a}^{b} g(x,y) dx \right) dy. \tag{3.8}$$

The above integral is evaluated numerically by using the Gauss quadrature method. Considering L integration intervals in the x-direction and employing the Gauss quadrature method, the integral in Equation 3.8 becomes:

$$I = \sum_{k=1}^{K} J_k \sum_{i=1}^{N} w_i \sum_{l=1}^{L} J_l \sum_{j=1}^{J} w_j g(x(\xi_j), y(\xi_i)), \tag{3.9}$$

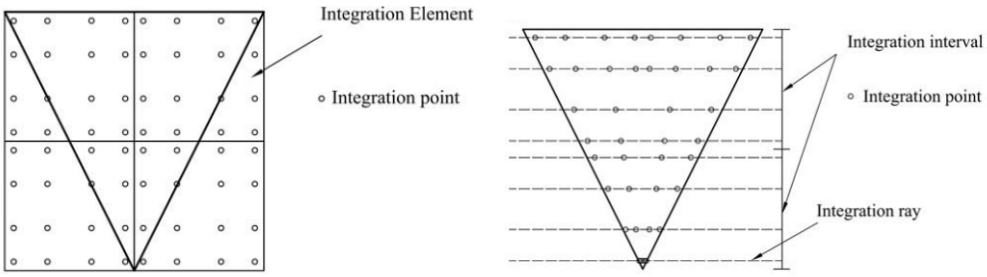
where

- J_k, N: Jacobian of the transformation and the number of Gaussian integration points for the outer integral
- J_l, J: Jacobian of the transformation and the number of Gaussian integration points for the integration over the l^{th} interval of the inner integral
- w_i, w_j: Weights for the 1D Gauss points ξ_i and ξ_j.

When function g is defined as an irregularly distributed set of data on the problem domain, evaluation of the value of g in Gauss integration nodes requires the implementation of mesh-free interpolation techniques. In this study, the Moving Least Squares (MLS) method and Radial Point Integration (RPIM) method are used, and details are presented in the following subsections.

The following observations are stated on CTM in the literature [65, 9, 10].

- No integration points fall outside of the problem domain, therefore, the necessity of using weight functions for equating functions value outside the problem domain is not required. Hence, the performance of CTM in irregular boundaries and multiply connected domains is much better than the conventional Gauss quadrature method with a background mesh.
- Since the CTM considers the points of intersection of each section with the boundary, sharp corners and irregular shapes are covered better. Hence, no section in the problem domain is missed compared to the conventional Gauss quadrature method. As can be observed in Figure 3.2, the conventional Gauss quadrature method is not able to capture the sharp corners, while, CTM captures that corner, and the integral is evaluated perfectly.



(a) Conventional Gauss quadrature (b) CTM

Figure 3.2: Integration points on the triangular domain for two methods [9]

- In conventional methods with background mesh, each Gauss quadrature point is checked to determine whether they are located in the problem domain or not, while in CTM, there is no possibility of having an integration point outside of the domain.

3.1.2 Mesh-free Interpolation

For the mesh-free integration methodology introduced in this study, the functional values of the integrand at the integration points of CTM need to be evaluated using a set of discrete numbers of field data. In order to approximate a value of a function or solution to a problem, it is necessary to determine the unknown field value at the integration points using shape functions. These shape functions are supported in small local domains and treated as zero outside the local domain. These local domains are referred to as the support, smoothing, or influence domains in the literature [10]. In these local domains, the determination of mesh-free shape functions is a hot topic that has been discussed intensively in the last two-three decades. A shape function is considered sufficient if it satisfies the following requirements.

- If it is robust enough for the reasonable amount of data points in the local domain.
- If it is numerically stable.
- If it is consistent after increasing the order of shape function.

- If it is bounded in the local support domain and is zero outside the domain.
- It is ideal if the shape function has a Kronecker delta property by itself, i.e., the value of the shape function will be one at the desired node and zero at the rest of the nodes in the support domain.
- If it is efficient computationally.

Categories of mesh-free interpolation techniques are presented in three main groups, as presented in Table 3.1. In this study, Moving Least Squares (MLS) and Radial Point Interpolation (RPIM) methods are used.

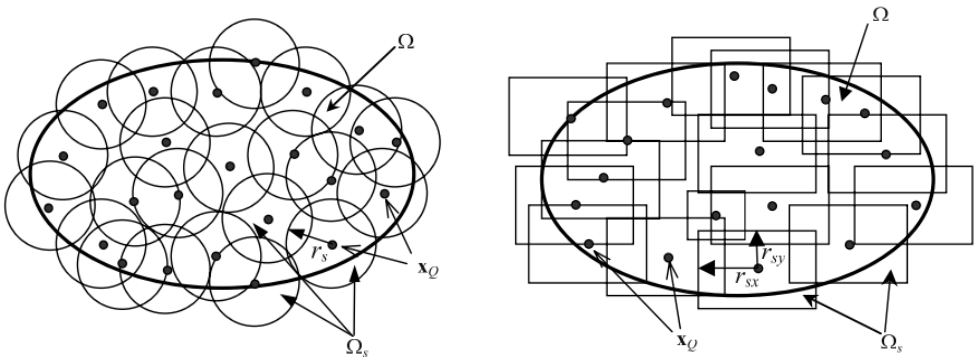
Table 3.1: Mesh-free interpolation techniques in literature

Categories	**Mesh-free approximation techniques**
Integral representation	Smoothed Particle Hydrodynamics (SPH)
	Reproducing Kernel Particle Method (RKPM)
Series representation	Moving Least Squares (MLS)
	Point Interpolation Methods (PIM, RPIM)
	Partition of Unity (PU)
Differential representation	General Finite difference method (GFDM)

3.1.2.1 Concept of Support Domain

As stated previously, in mesh-free methods, a set of arbitrarily distributed data points represents the problem. The data points in the local support domain are used for approximation to evaluate the value of the field variable at an arbitrary location in the problem domain. Therefore, the accuracy of the interpolation at the desired point is directly dependent on the data points in the support domain. Resultantly, the determination of the size of the support domain has great importance. In Figure 3.3, two types of support domains are presented around desired point x_Q. In this study, rectangular support domains are used.

The procedure for the determination of the size of the rectangular domain is presented by Lui and Gu [10] as follows:



(a) Circular support domain (b) Rectangular support domain

Figure 3.3: Types of support domain around the desired point x_Q [10]

- Estimate the dimensions of the support domain in x and y directions (d_{sx} and d_{sy}).
- Calculate the area of the estimated support domain (A_s) by using estimated d_{sx} and d_{sy}.
- Calculate the average nodal spacing in x and y directions using the relation given as:

$$d_c = \frac{\sqrt{A_s}}{\sqrt{n_{A_s}} - 1}, \tag{3.10}$$

  where n_{A_s} is the number of nodes in the support domain.

- Calculate the true size of the support domain by using

$$d_{sx} = \alpha_{sx} d_{cx} \quad \text{and} \quad d_{sy} = \alpha_{sy} d_{cy}, \tag{3.11}$$

  where α_{sx} and α_{sy} are arbitrary constants, and they are taken as 2.0 as suggested by Lui and Gu [10].

3.1.2.2 Moving Least Squares Method (MLS)

The moving least squares (MLS) method has been introduced into literature by Lancaster and Salkausdas [66] and Cleaveland [67]. A summarized version of the derivation of MLS equations is presented here. A detailed derivation of shape functions is presented by Lui and Gu [10]. Suppose a scalar function $u(x)$ in domain Ω,

$$u(x) \approx u^h(x) = \sum_{i=1}^{n} \phi_i(x) u_i = \boldsymbol{\phi}^{\boldsymbol{T}}(\mathbf{x}) \mathbf{U_s}, \tag{3.12}$$

where $\mathbf{U_s}$ is the vector of nodal values of the function in the support domain, and $\boldsymbol{\phi}^{\boldsymbol{T}}$ is the vector consisting of the MLS shape functions in the support domain of point of interest x. For n number of nodes in the support domain, the shape functions matrix can be written as

$$\boldsymbol{\phi}^{\boldsymbol{T}}(\mathbf{x}) = \{\phi_1(\mathbf{x}) \quad \phi_2(\mathbf{x}) \quad \cdots \quad \phi_n(\mathbf{x})\}_{1\times n} = \mathbf{p}^T(\mathbf{x}) \mathbf{A}^{-1}(\mathbf{x}) \mathbf{B}(\mathbf{x}), \tag{3.13}$$

where $\mathbf{p}(\mathbf{x})$ is the basis function of spatial coordinates with the size of $(m \times 1)$. The basis function is formed mostly by using the Pascal triangle. For $m = 3$, it is defined as

$$\mathbf{p}(\mathbf{x}) = [1 \quad x \quad y]. \tag{3.14}$$

For $m = 3$, the matrices $\mathbf{A}(\mathbf{x})$ and $\mathbf{B}(\mathbf{x})$ given in Equation 3.13 are defined as presented in Equations 3.15 and 3.16.

$$\begin{aligned}
\mathbf{A}_{3\times3}(\mathbf{x}) = \sum_{i=1}^{n} W_i(\mathbf{x}) \mathbf{p}(\mathbf{x}_i) \mathbf{p}^T(\mathbf{x}_i) &= W_i(\mathbf{x}-\mathbf{x}_1) \begin{bmatrix} 1 & x_1 & y_1 \\ x_1 & x_1^2 & x_1 y_1 \\ y_1 & x_1 y_1 & y_1^2 \end{bmatrix} \\
&+ W_i(\mathbf{x}-\mathbf{x}_2) \begin{bmatrix} 1 & x_2 & y_2 \\ x_2 & x_2^2 & x_2 y_2 \\ y_2 & x_2 y_2 & y_2^2 \end{bmatrix} + \cdots + W_i(\mathbf{x}-\mathbf{x}_n) \begin{bmatrix} 1 & x_n & y_3 \\ x_n & x_n^2 & x_n y_n \\ y_n & x_n y_n & y_n^2 \end{bmatrix} \\
&= \sum_{i=1}^{n} \begin{bmatrix} W_i & x_i W_i & y_i W_i \\ x_i W_i & x_i^2 W_i & x_i y_i W_i \\ y_i W_i & x_i y_i W_i & y_i^2 W_i \end{bmatrix}_{3\times3}
\end{aligned} \tag{3.15}$$

$$\begin{aligned}\mathbf{B}_{3\times n}(\mathbf{x}) &= [W_1(\mathbf{x})\mathbf{p}(\mathbf{x_1}) \quad W_2(\mathbf{x})\mathbf{p}(\mathbf{x_2}) \quad \cdots \quad W_n(\mathbf{x})\mathbf{p}(\mathbf{x_n})] \\ &= \begin{bmatrix} W_1 & W_2 & \cdots & W_n \\ x_1W_1 & x_2W_2 & \cdots & x_nW_n \\ y_1W_1 & y_2W_2 & \cdots & y_nW_n \end{bmatrix}_{3\times n}\end{aligned} \tag{3.16}$$

For the weight functions W_i given in Equations 3.15 and 3.16, the functions presented by Liu and Liu [68] are used, as shown in Equation 3.17.

$$W_i(\mathbf{x}) = \begin{cases} 2/3 - 4\bar{r}_i^2 + 4\bar{r}_i^3 & \bar{r}_i \leq 0.5 \\ 4/3 - 4\bar{r}_i + 4\bar{r}_i^2 - 4/3\bar{r}_i^3 & 0.5 < \bar{r}_i \leq 1 \\ 0 & \bar{r}_i > 1 \end{cases} \tag{3.17}$$

In the above equation $\bar{r}_i$ is defined as,

$$\bar{r}_i = \frac{d_i}{r_w} = \frac{|\mathbf{x} - \mathbf{x}_i|}{r_w}, \tag{3.18}$$

where d_i is the distance from the point of interest x and x_i, which is the i^{th} node in the support domain, and r_w is the radius of the support domain for a circular support domain.

The procedure of MLS implemented in this study can be summarized as follows:

- An adaptive monomial order decision algorithm is introduced in this study. Depending on the number of nodes (N_s) in the support domain of x, the order of monomial (m) is selected:

$$m = \begin{cases} 1 & 1 < N_s \leq 3 \\ 3 & 3 < N_s \leq 6 \\ 6 & 6 < N_s \leq 10 \\ 10 & 10 < N_s \end{cases} \tag{3.19}$$

- Weight functions are calculated between the nodes in the support domain and point of interest x using Equation 3.17.

- After calculating weight functions, matrices $\mathbf{A}(\mathbf{x})$ and $\mathbf{B}(\mathbf{x})$ are formed using Equations 3.15 and 3.16, respectively.

- The vector consisting of the MLS shape functions ($\boldsymbol{\phi}^{\boldsymbol{T}}(\mathbf{x})$) are calculated by using Equation 3.13.

- The value of the function at the point of interest ($u^h(x)$) is then calculated using Equation 3.12.

3.1.2.3 Radial Point Interpolation Method (RPIM)

The radial point interpolation (RPIM) method has been introduced by Liu and Gu [69] and Wang and Liu [70]. A detailed derivation of the RPIM method is explained in Lui and Gu [10]. In this subsection, the functions used and the procedure are presented. Suppose a scalar function $u(x)$ in domain Ω,

$$u(x) \approx u^h(x) = \sum_{i=1}^{n} \phi_i(x) u_i = \boldsymbol{\phi}^{\boldsymbol{T}}(\mathbf{x}) \mathbf{U_s}, \tag{3.20}$$

where $\mathbf{U_s}$ is the vector of nodal values of the function in the support domain, and $\boldsymbol{\phi}^{\boldsymbol{T}}$ is the vector consisting of the RPIM shape functions in the support domain of point of interest x. For n number of nodes in the support domain, the shape functions matrix can be written as

$$\boldsymbol{\phi}^{\boldsymbol{T}}(\mathbf{x}) = \{\phi_1(\mathbf{x}) \quad \phi_2(\mathbf{x}) \quad \cdots \quad \phi_n(\mathbf{x})\}_{1\times n} = \mathbf{R}^T(\mathbf{x}) \mathbf{p}^T(\mathbf{x}) \mathbf{G}^{-1}, \tag{3.21}$$

where $\mathbf{p}(\mathbf{x})$ is the basis function of spatial coordinates with the size of $(m \times 1)$. The basis function is formed mostly by using the Pascal triangle. For $m = 3$, it is defined as in Equation 3.14.

The vector $\mathbf{R}^T(\mathbf{x})$ in Equation 3.21 is the radial basis function (RBF) matrix. In this study, the Gaussian type of radial basis function is used. To sum up, the vector $\mathbf{R}^T(\mathbf{x})$ is determined as

$$\mathbf{R}^T(\mathbf{x}) = [R_1(\mathbf{x}) \quad R_2(\mathbf{x}) \quad \cdots \quad R_n(\mathbf{x})]_{1\times n} \quad \text{and} \quad R(x) = exp\left[-\alpha_c(\frac{r}{d_c})^2\right], \tag{3.22}$$

where α_c is a constant and is taken as 2.0, r is the distance between the point of interest x and the data point in the support domain, and d_c is the size of the support domain. The column vector $\mathbf{R}^T(\mathbf{x})$ is formed by writing the RBF for n number of nodes in the support domain. The vector $\mathbf{G}$ in Equation 3.21 is defined as

$$\mathbf{G} = \begin{bmatrix} \mathbf{R}_0 & \mathbf{P}_m \\ \mathbf{P}_m^T & 0 \end{bmatrix}, \tag{3.23}$$

where $\mathbf{R}_0$ is formed by writing Equation 3.22 between n number of nodes in the support domain. Similarly, $\mathbf{P}_m^T$ is formed by writing the monomials for n number of nodes in the support domain. Both matrices can be represented as,

$$\begin{aligned} \mathbf{R}_0 &= \begin{bmatrix} R_1(r_1) & R_2(r_1) & \cdots & R_n(r_1) \\ R_1(r_2) & R_2(r_2) & \cdots & R_n(r_2) \\ \vdots & \vdots & \ddots & \vdots \\ R_1(r_n) & R_2(r_n) & \cdots & R_n(r_n) \end{bmatrix}_{n\times n} \\ \mathbf{P}_m^T &= \begin{bmatrix} 1 & 1 & \cdots & 1 \\ x_1 & x_2 & \cdots & x_n \\ y_1 & y_2 & \cdots & y_n \\ \vdots & \vdots & \ddots & \vdots \\ p_m(\mathbf{x}_1) & p_m(\mathbf{x}_2) & \cdots & p_m(\mathbf{x}_m) \end{bmatrix}_{m\times n} \end{aligned} \tag{3.24}$$

The procedure of RPIM implemented in this study can be summarized as follows:

- An adaptive monomial order decision algorithm is introduced in this study. Depending on the number of nodes (N_s) in the support domain of x, the order

of monomial (m) is selected:

$$m = \begin{cases} 1 & 1 < N_s \leq 3 \\ 3 & 3 < N_s \leq 6 \\ 6 & 6 < N_s \leq 10 \\ 10 & 10 < N_s \end{cases}$$

- Using the RBF given in Equation 3.22, $\mathbf{R}_0$ in Equation 3.24 is determined for n number of nodes in the support domain.

- $\mathbf{P}_m$ in Equation 3.24 is calculated for n number of nodes in the support domain, and the G matrix is formed.

- The vector consisting of the RPIM shape functions ($\boldsymbol{\phi}^{\boldsymbol{T}}(\mathbf{x})$) are calculated by using Equation 3.21.

- The value of the function at the point of interest $u^h(x)$ is then calculated using Equation 3.20.

3.2 Applications of Mesh-Free Integration and Interpolation

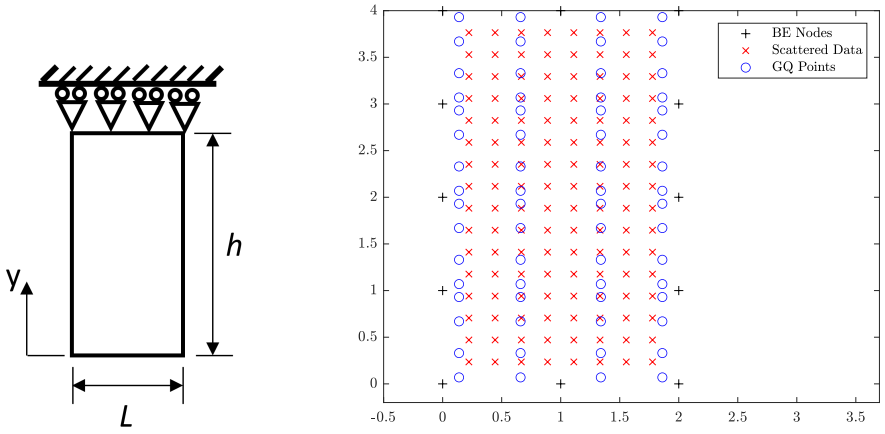
The validation of the developed approach on the mathematical problems with a parameter study is presented in Appendix C. In this section, the implementation of the mesh-free integration method presented in Section 3.1 to developed boundary element method is discussed with the physical examples. The solution of an elasticity problem under the effect of a distributed body force is given in Section 3.2.1. Afterward, in Section 3.2.2, the solution of steady-state heat conduction problems with the boundary element method is discussed, and it is extended to thermoelastic problems, which require the domain integration of thermal forces. Lastly, the transient heat conduction problem, which is subjected to heat sources presenting in the domain, is solved in Section 3.2.3.

3.2.1 Introduction of Body Force on Elasticity Problems

For isotropic elasticity problems, including body forces, the boundary integral equations are given as:

$$C_{ij}(x_f)u_i(x_f) + \int_\Gamma H_{ij}(x_f, x_s)u_j(x_s)d\Gamma = \int_\Gamma G_{ij}(x_f, x_s)t_j(x_s)d\Gamma + \\ + \int_\Omega G_{ij}(x_f, x_s)b_i(x_s)d\Omega, \tag{3.25}$$

where u_i and t_i are the displacements and the tractions at the boundary nodes, G_{ij} and H_{ij} are the kernel solutions of the elasticity problem, and b_i is the body force term. The solution of the elasticity problem without the integral including body forces, is discussed in detail in Section 2.1. The domain integral in Equation 3.25 is computed by using the mesh-free integration methodology discussed in Section 3.1. The boundary conditions of the problem are presented in Figure 3.4(a). The CTM mesh with the interpolation data points are given in Figure 3.4. 64 integration points indicated by blue circles (◯) are used for CTM, and 128 inner data points shown by red crosses (×) are used for interpolation. The dimensions L and h are taken as 1 and 4 meters, respectively. The plane stress problem is analyzed.



(a) Boundary conditions

(b) Integration mesh

Figure 3.4: Boundary condition and integration mesh used for the body force example

Three different body force loading is applied to the problem:

- Loading 1: $b(y) = -g\rho_0$
- Loading 2: $b(y) = -g\rho_0 \dfrac{y}{h}$
- Loading 3: $b(y) = -g\rho_0 \left(\dfrac{y^3}{h^3} + 3\dfrac{y^2}{h^2} - \dfrac{y}{h} - 1 \right)$

where $\rho_0 = 1440kg/m^3$, $g = 9.81m/s^2$ and Poisson's ratio ν is taken as zero. The total reaction force on the upper boundary and the displacements on the lower boundary are compared for the analytical and BEM solutions of the problem.

Table 3.2: MLS, RPIM, and analytical results for body force example for three different loadings

	MLS		**RPIM**		**Exact**	
	F [N]	**u [m]**	**F [N]**	**u [m]**	**F [N]**	**u [m]**
Loading 1	1.1301120	-1.129	1.1304879	-1.128	1.1301120	-1.130
Loading 2	0.5652306	-0.3751	0.5652240	-0.3755	0.5650560	-0.377
Loading 3	-0.2785583	0.8188	-0.2800287	0.819	-0.2825280	0.829

Table 3.2 displays the results obtained through MLS, RPIM, and analytical methods for three distinct applied loadings. The agreement between the results obtained from MLS, RPIM, and the analytical approach is deemed satisfactory, even with a coarse discretization, for all loadings employed within the domain.

3.2.2 Steady State Heat Conduction and Thermoelastic Problems

This subsection first discusses an overview of the methodology employed for solving the steady-state heat conduction problem using BEM. Subsequently, we discuss the coupling of the steady-state heat conduction solution with the elasticity solution of BEM to obtain the thermoelastic solution. Then, the mesh-free integration method is applied to the domain integrals appearing in these problems.

3.2.2.1 Steady State Heat Conduction

This section focuses on implementing the BEM to solve the steady-state heat conduction problem. The formulation proposed by Aliabadi [36] is adopted, and a summary

of the method is presented. The steady-state heat conduction equation is derived by first considering the Laplace equation, as given in Equation 3.26.

$$\theta_{,ii}(x) = 0 \quad \text{for} \quad x \in V \tag{3.26}$$

Steady-state heat conduction problems involve temperature (θ) boundary conditions on Γ_θ and flux (q) boundary conditions on Γ_q. The boundary integral formulation for the steady-state conduction problem is expressed as follows

$$C(x_f)\theta(x_f) - \int_\Gamma q^*(x_f, x_s)\theta(x_s)d\Gamma = -\int_\Gamma \theta^*(x_f, x_s)q(x_s)d\Gamma, \tag{3.27}$$

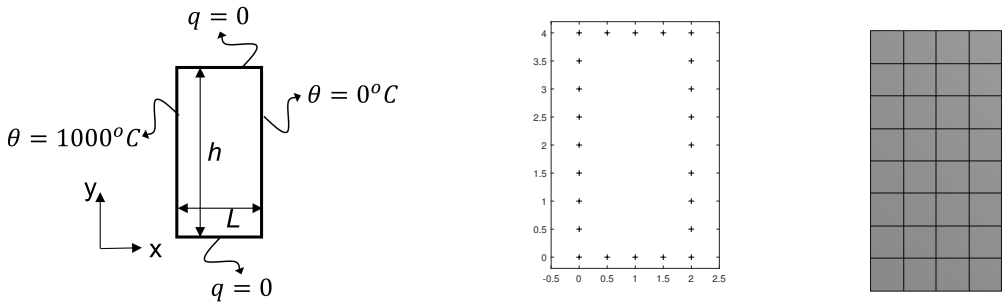
where $C(x_f)$ is calculated in the same way as the elasticity boundary integral equation. For 2D problem, kernel solutions $q^*(x_f, x_s)$ and $\theta^*(x_f, x_s)$ are defined as:

$$\begin{aligned} \theta^*(x_f, x_s) &= \frac{1}{2\pi k}\ln\frac{1}{r} \\ q^*(x_f, x_s) &= \frac{r_{,i}n_i}{2\pi r} \qquad i = 1, 2. \end{aligned} \tag{3.28}$$

The numerical discretization and the solution methodology of BEM for the steady-state heat conduction problem is just the extension of the elasticity case presented in Section 2.1 for the scalar field variables.

The developed algorithm is verified through a thermal problem, which is solved using the developed BEM algorithm as well as the finite element method (FEM) by using the commercially available program ANSYS. The boundary conditions of the problem are depicted in Figure 3.5(a). The dimensions of the domain are set to $L = 2$m and $h = 4$m, respectively. The thermal conductivity k is taken as 1.0 W/m^{o}C. The same discretization is used at the boundaries of both BEM and FEM models. The BEM and FEM meshes are shown in Figures 3.5(b) and 3.5(c), respectively.

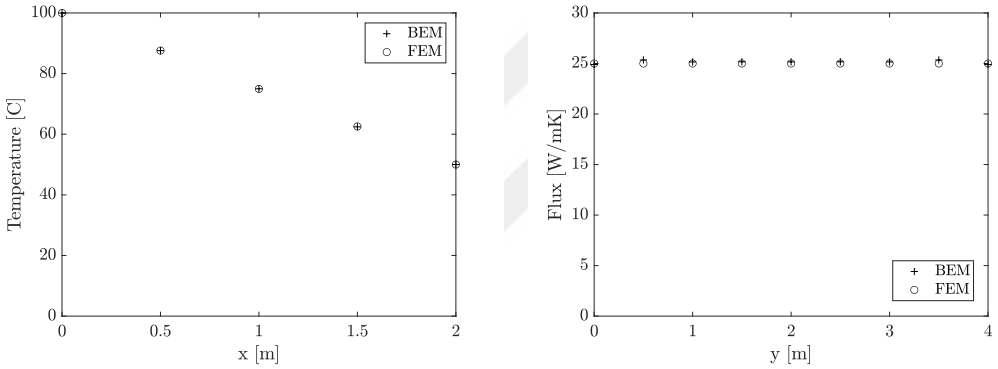
Figure 3.6 illustrates the temperature and flux variations along the bottom edge ($y = 0$m) and right edge ($x = 2$m). The results obtained from the developed BEM algorithm show good agreement with the FEM results. This confirms the accuracy and reliability of the developed BEM algorithm for solving steady-state heat conduction



(a) Boundary conditions (b) BEM mesh (c) FEM mesh

Figure 3.5: Boundary condition and BEM mesh used for the steady state heat conduction example

problems.



(a) Temperature (b) Flux

Figure 3.6: Temperature and flux results for FEM and BEM on the bottom and right edge

3.2.2.2 Thermoelasticity

By using the methodology presented for the solutions of the steady state heat conduction and the elasticity problems with BEM, presented in Sections 3.2.2 and 2.1, respectively, a coupled thermoelastic problem solution can be obtained. This can be achieved by introducing the conductivity equation into the elasticity solution as the thermal body force term, as defined in Equation 3.25. Detailed derivation and numer-

ical discretization of the thermoelastic problem solution using BEM are presented by Aliabadi [36]. The numerical discretization and solution methodology for the thermoelasticity problem using the boundary element method (BEM) is an extension of the approach presented in Section 2.1 for elasticity problems. The same principles and techniques used for the discretization and solution of the elasticity problem can be directly applied to the thermoelasticity problem. The governing integral equation reads

$$\begin{aligned} &C_{ij}(x_f)u_i(x_f) + \int_\Gamma H_{ij}(x_f, x_s)u_j(x_s)d\Gamma - \int_\Gamma P_i(x_f, x_s)\theta(x_s)d\Gamma = \\ &\int_\Gamma G_{ij}(x_f, x_s)t_j(x_s)d\Gamma + \int_\Omega G_{ij}(x_f, x_s)b_i(x_s)d\Omega - \int_\Gamma Q_i(x_f, x_s)q(x_s)d\Gamma, \end{aligned} \tag{3.29}$$

where G_{ij} and H_{ij} are the kernel solutions of the elasticity problem, and P_i and Q_i are defined as follows:

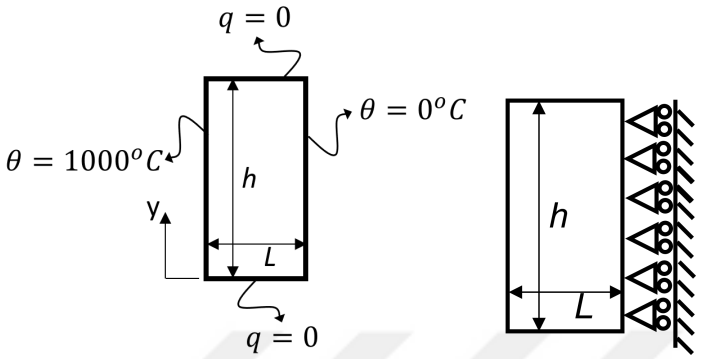
$$\begin{aligned} P_i(x_f, x_s) &= \frac{(1+\nu)h}{4\pi(1-\nu)}\left[\left(\ln\frac{1}{r} - \frac{1}{2}\right)n_i - r_{,i}r_{,k}n_k\right] \\ Q_i(x_f, x_s) &= \frac{(1+\nu)}{4\pi k(1-\nu)}hrr_{,i}\left[\ln\frac{1}{r} - \frac{1}{2}\right]. \end{aligned} \tag{3.30}$$

In Equation 3.30, h is defined as the thermal expansion coefficient. The solution is carried out in two sequential steps:

- The steady state heat conduction problem, given in Equation 3.27, is firstly solved. The temperature and flux values on the boundary nodes are determined.
- Field variables determined in steady state heat conduction problem are used as input to Equation 3.29, and unknown elasticity boundary values are determined.
- The solution can be done either sequentially or simultaneously by combining the first two items in a single set of systems of equations and solving for all the elasticity and thermal field variables.

A model problem of a rectangular domain is created to observe the effectiveness and accuracy of the BEM solution. The boundary conditions of the model problem are

depicted in Figure 3.7. The dimensions L and h are taken as 2m and 4m, respectively. The thermal conductivity k and thermal expansion coefficient h are taken as 10W/m^{o}C and 1.67×10^{-5} 1/^{o}C, respectively. BEM and FEM meshes presented in Figures 3.5(b) and 3.5(c) are used for the solution of the thermoelasticity problem as well.

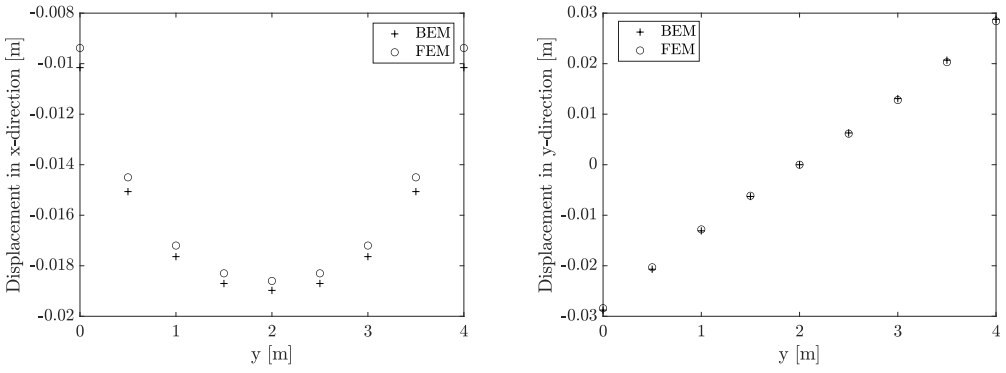


(a) Thermal boundary conditions

(b) Elasticity boundary conditions

Figure 3.7: Boundary conditions used for the elasticity and thermal conductivity problems

The model problem is again solved by using FEM and BEM. ANSYS is used for the FEM solution. In Figure 3.8, the variation of components of the displacement vector on the left boundary is presented. A good match is observed between the results of the two methodologies.



(a) u_x

(b) u_y

Figure 3.8: Change in displacements in x and y directions on the left edge

3.2.3 Transient Heat Conduction with Heat Source

3.2.3.1 Boundary Element Method Equations

The transient heat conduction equation in a medium with a heat source can be written as

$$\bigtriangledown^2\theta(\mathbf{x},t)+\frac{1}{K}g(\mathbf{x},t)=\frac{1}{k}\frac{\partial}{\partial t}\theta(\mathbf{x},t), \tag{3.31}$$

where K and k are the thermal diffusivity and conductivity, g is the heat source function, and t is the solution time. Recall that the thermal diffusivity can be expressed as $k = K/\rho c$, where ρ is the density and c is the specific heat. Brebbia [71] has presented the boundary integral equation of Equation 3.31 as

$$\begin{aligned}
&C(\mathbf{x_s})\theta(\mathbf{x_s},t_{n+1})+k\int_\Gamma\int_{t_n}^{t_{n+1}}\theta(\mathbf{x_s},\tau)q^*(\mathbf{x_s},t_{n+1};\mathbf{x_f},\tau)d\tau d\Gamma\\
&=k\int_\Gamma\int_{t_n}^{t_{n+1}}q(\mathbf{x_f},\tau)\theta^*(\mathbf{x_s},t_{n+1};\mathbf{x_f},\tau)d\tau d\Gamma+\int_\Omega\theta(\mathbf{x_f},t_n)\theta^*(\mathbf{x_s},t_{n+1};\mathbf{x_f},t_n)d\Omega\\
&+\frac{k}{K}\int_\Omega\int_{t_n}^{t_{n+1}}g(\mathbf{x_f},\tau)\theta^*(\mathbf{x_s},t_{n+1};\mathbf{x_f},\tau)d\tau d\Omega,
\end{aligned} \tag{3.32}$$

where $\mathbf{x_s}$ and $\mathbf{x_f}$ are the source and the field points, respectively. The fundamental solutions (θ^*, q^*) for the transient heat conduction problem are given as [72]

$$\begin{aligned}
\theta^*(\mathbf{x_s},t_{n+1};\mathbf{x_f},\tau)&=\frac{1}{4\pi k(t-\tau)}\exp\left[\frac{-r^2}{4k(t-\tau)}\right]H(t-\tau)\\
q^*(\mathbf{x_s},t_{n+1};\mathbf{x_f},\tau)&=\frac{\partial}{\partial n}\theta^*(x_s,t_{n+1};x_f,\tau)\\
&=\frac{-r}{8\pi[k(t-\tau)]^2}\exp\left[\frac{-r^2}{4k(t-\tau)}\right]H(t-\tau)\frac{\partial r}{\partial n}.
\end{aligned} \tag{3.33}$$

In the above equation, r is the distance between the source and the field points, and $H(x)$ is the Heaviside function. Assuming the field variables θ and q in Equation 3.32 change slower concerning time compared to the singular functions θ^* and q^*, those terms can be taken out of the time integrals. Hence, for the constant time integration,

inner integrals can be expressed as follows

$$\begin{aligned}\int_{t_n}^{t_{n+1}} \theta^*(x_s, t_{n+1}; x_f, \tau) &= \frac{1}{4\pi k}\mathrm{E}_1\left(\frac{r^2}{4k \triangle t}\right), \\ \int_{t_n}^{t_{n+1}} q^*(x_s, t_{n+1}; x_f, \tau) &= \frac{-1}{2\pi k r}\exp\left(\frac{r^2}{4k \triangle t}\right)\frac{\partial r}{\partial n}.\end{aligned} \tag{3.34}$$

In the above equation, E_1 (see Figure 3.35) is the exponential integral function [73], defined as

$$\mathrm{E}_1(x) = \int_x^\infty \frac{e^{-u}}{u}du = -0.57721566 + \sum_{n=1}^{\infty}\left[(-1)^{n-1}\frac{x^n}{n(n!)}\right] - \ln(x) \tag{3.35}$$

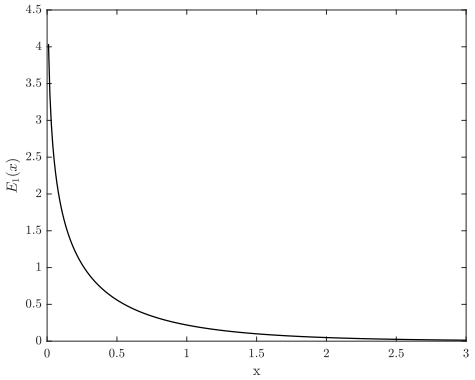


Figure 3.9: Variation of the exponential integral function ($\mathrm{E}_1(x)$) with x

After performing an analytical evaluation of the time integrals, the boundary integrals of the first two integrals in Equation 3.32 can be computed using the Gauss Quadrature method. The third integral takes into account the influence of temperatures from the previous time step. The calculation of domain integrals is efficiently carried out using the Cartesian Transform Method (CTM) with RPIM interpolation.

The last integral in Equation 3.32, which involves the heat source term, is evaluated using the midpoint integration rule. This integration rule is utilized by Hematiyan [74] for the evaluation of the time integral of the source term. Consequently, the last domain integral can be expressed as follows

$$\begin{aligned}&\int_{\Omega}\int_{t_n}^{t_{n+1}} g(x_f,\tau)\theta^*(x_s,t_{n+1};x_f,\tau)d\tau d\Omega \\ &= \int_{\Omega} g(x_f,t_{n+\frac{1}{2}})\int_{t_n}^{t_{n+1}} \theta^*(x_s,t_{n+1};x_f,\tau)d\tau d\Omega\end{aligned} \tag{3.36}$$

Moreover, the time integral of the kernel in Equation 3.36 can be determined analytically, as given in Equation 3.34.

Due to the nature of the Kernel expressions given in Equation 3.33, when the source point ($\mathbf{x_s}$) and the field point ($\mathbf{x_f}$) are located on the same coordinate, the distance r between these two points becomes zero. Consequently, the first relation in Equation 3.34 will be infinity ($\mathrm{E}_1(0) \to \infty$). Therefore, a special treatment is necessary for the diagonal elements of the $\mathbf{G}$ matrix of BEM. Brebbia [71] offers a way to analytically integrate the boundary integral for constant elements in which the source and field points are located at the same point. The extension to the linear elements is presented in this section. The integral to be evaluated is,

$$\begin{aligned}G_{ii} &= \int_{\Gamma}\int_{t_n}^{t_{n+1}} q(\mathbf{x_f},\tau)\theta^*(\mathbf{x_s},t_{n+1};\mathbf{x_f},\tau)d\tau d\Gamma \\ &= \int_{\Gamma} q(\mathbf{x_f},\tau)\frac{1}{4\pi k}\mathrm{E}_1\left(\frac{r^2}{4k\triangle t}\right)d\Gamma.\end{aligned} \tag{3.37}$$

Insertion of $\alpha = \dfrac{l^2}{16k\triangle t}$ and $d\Gamma = \dfrac{l(1+\eta)}{4}$ into Equation 3.37 gives

$$G_{ii} = \frac{l}{16\pi k}q_{ii}\int_{-1}^{1}\mathrm{E}_1\left(\alpha(1-\eta)^2\right)(1+\eta)d\eta, \tag{3.38}$$

using Equation 3.35, we can express the exponential integral function as follows

$$\mathrm{E}_1(x) = \overline{\mathrm{E}}_1(x) - \ln(x). \tag{3.39}$$

Insertion of Equation 3.39 into the integral expression in Equation 3.38 gives

$$
\begin{aligned}
I &= \int_{-1}^{1} \mathrm{E}_1\left(\alpha(1-\eta)^2\right)(1+\eta)d\eta \\
&= \int_{-1}^{1} \overline{\mathrm{E}}_1\left(\alpha(1-\eta)^2\right)(1+\eta)d\eta - \int_{-1}^{1} \ln\left(\alpha(1-\eta)^2\right)(1+\eta)d\eta
\end{aligned}
\tag{3.40}
$$

Writing the series sum for $\overline{\mathrm{E}}_1$ and applying integration by parts on both integrals, the final form of the integral is as follows

$$
I = 2(0.57721566) - 2\ln\alpha - 2\ln 16 - \sum_{n=1}^{\infty}(-1)^{n-1}\frac{\alpha^n 2^{2n+2}}{n(2n+1)(2n+2)(n!)}. \tag{3.41}
$$

According to Aliabadi [36], when using constant time interpolation, the results show a variation of 5-10% compared to the results obtained through linear time integration. Moreover, it is seen that the results are insensitive to different time steps while using linear time interpolation. Therefore, linear time interpolation is introduced to the developed BEM for the solution of the transient heat conduction problem. The formulation mostly follows the linear time interpolation methodology proposed by Brebbia et al. [71]. Recall the boundary element equation is,

$$
\begin{aligned}
C(x_s)\theta(x_s,t_{n+1}) + k\sum_{j=1}^{N}\left(\int_{\Gamma_j}\phi^T\int_{t_n}^{t_{n+1}} q^*\psi dt d\Gamma\right)\theta^n &= \int_{\Omega}\theta(x_f,t_n)\theta^* d\Omega \\
&+ k\sum_{j=1}^{N}\left(\int_{\Gamma_j}\phi^T\int_{t_n}^{t_{n+1}} \theta^*\psi d\tau d\Gamma\right)q^n \\
&+ \frac{k}{K}\int_{\Omega} g(x_f,t_{n+\frac{1}{2}})\int_{t_n}^{t_{n+1}}\theta^*(x_s,t_{n+1};x_f,\tau)d\tau d\Omega,
\end{aligned}
\tag{3.42}
$$

where ψ and ϕ are the temporal and spatial shape functions, respectively. The subscripts n and $n+1$ are the values expressed at the previous and current time steps, respectively. The temporal shape functions are defined as follows.

$$
\psi = \begin{bmatrix} \dfrac{t_{n+1}-t}{\triangle t_{n+1}} & \dfrac{t-t_n}{\triangle t_{n+1}} \end{bmatrix} \qquad \text{and} \qquad \triangle\, t_{n+1} = t_{n+1} - t_n \tag{3.43}
$$

Inserting both shape functions into Equation 3.42 and extending it for all boundary nodes, the resulting system of equations can be obtained as

$$H^1U_n + H^2U_{n+1} = G^1Q_n + G^2Q_{n+1} + b_n + b_G, \tag{3.44}$$

where G and H are the BEM matrices, U and Q represent the field variables, and the superscripts 1 and 2 denote the BEM matrices formed with the first and second time interpolation function given in Equation 3.43. The vectors b_n and b_G are created with the third and fifth expressions in Equation 3.42, which introduce the effects of temperature field from the previous time step and the effect of heat source loading, respectively. Each elemental sub-matrices of H^1, H^2, G^1, and G^2 are determined by using the following relations.

$$\begin{aligned}
h_{ij}^1 &= \frac{k}{\triangle t_{n+1}} \int_{\Gamma_i} \phi_j \int_{t_n}^{t_{n+1}} (t_{n+1} - t) q^* dt d\Gamma \\
h_{ij}^2 &= \frac{k}{\triangle t_{n+1}} \int_{\Gamma_i} \phi_j \int_{t_n}^{t_{n+1}} (t - t_n) q^* dt d\Gamma \\
g_{ij}^1 &= \frac{k}{\triangle t_{n+1}} \int_{\Gamma_i} \phi_j \int_{t_n}^{t_{n+1}} (t_{n+1} - t) \theta^* dt d\Gamma \\
g_{ij}^2 &= \frac{k}{\triangle t_{n+1}} \int_{\Gamma_i} \phi_j \int_{t_n}^{t_{n+1}} (t - t_n) \theta^* dt d\Gamma
\end{aligned} \tag{3.45}$$

Each time integral expression in the above equations can be split into two equations. Evaluation of the integrals involving t_{n+1} or t_n constants is straightforward, and the procedure is the same as the constant time interpolation, as explained previously. Meanwhile, for the integrals involving variable t, new expressions should be derived as follows.

$$\begin{aligned}
\int_{t_n}^{t_{n+1}} t q^* dt &= \frac{d}{2\pi k} \int_{t_n}^{t_{n+1}} \frac{t}{4k\tau^2} \exp\left(-\frac{r^2}{4k\tau}\right) dt \\
&= \frac{d}{2\pi k} \left[\frac{t_{n+1}}{r^2} \int_{a_n}^{a_{n+1}} \exp(-x) dx - \frac{1}{4k} \int_{a_n}^{a_{n+1}} \frac{\exp(-x)}{x} dx \right]
\end{aligned} \tag{3.46}$$

$$\begin{aligned}
\int_{t_n}^{t_{n+1}} t u^* dt &= \frac{1}{4\pi k} \int_{t_n}^{t_{n+1}} \frac{t}{\tau} \exp\left(-\frac{r^2}{4k\tau}\right) dt \\
&= \frac{1}{4\pi k} \left[t_{n+1} \int_{a_n}^{a_{n+1}} \frac{\exp(-x)}{x} dx - \frac{r^2}{4k} \int_{a_n}^{a_{n+1}} \frac{\exp(-x)}{x^2} dx \right]
\end{aligned} \tag{3.47}$$

In Equations 3.46 and 3.47, τ and a_x are defined, as given in Equation 3.48.

$$\tau = t_{n+1} - t \quad \text{and} \quad a_x = \frac{r^2}{4k(t_F - t_x)}, \tag{3.48}$$

where t_F is the final time. The integrals involving exponential functions are determined as

$$\begin{aligned}
&\int_{a_n}^{a_{n+1}} \exp(-x)dx = -\exp(-a_{n+1}) + \exp(-a_n) = \exp(-a_n) \\
&\int_{a_n}^{a_{n+1}} \frac{\exp(-x)}{x}dx = E_1(a_n) - E_1(a_{n+1}) = E_1(a_n) \\
&\int_{a_n}^{a_{n+1}} \frac{\exp(-x)}{x^2}dx = \Gamma_1(-1, a_n) - \Gamma(-1, a_{n+1}) = \Gamma(-1, a_n).
\end{aligned} \tag{3.49}$$

In above equation, the terms $\exp(-a_{n+1})$, $E_1(a_{n+1})$ and $\Gamma(-1, a_{n+1})$ equal to zero. $\Gamma(-n, a)$ can be defined by using the series sum given below.

$$\Gamma(-n, a) = \frac{(-1)^n}{n!}\left[E_1(a) - \exp(-a)\sum_{i=0}^{n-1}\frac{(-1)^i i!}{a^{i+1}}\right], \qquad n = 1, 2, ... \tag{3.50}$$

3.2.3.2 Numerical Examples

Effect of Linear Time Interpolation

The example problem offered by Aliabadi [36] is reproduced to show the effectiveness of linear time interpolation on the results. The rectangular domain presented in Figure 3.10 is used for the comparison study. The conductivity, specific heat, and thermal diffusivity values are set to 1. In the reference study, results of the flux and the temperature type boundary element method formulations are presented. In the current study, only the temperature formulation is used. The mesh used in the reference study is composed of 12 quadratic boundary elements, and domain integration is carried out using internal cells. In the current study, a mesh consisting of 80 linear boundary elements is used, and the domain integrals are computed by using CTM with RPIM as the adopted interpolation method. The initial temperature of the domain is set to zero.

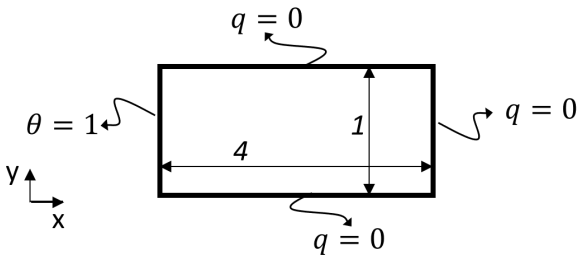


Figure 3.10: Problem domain with boundary conditions

In Figure 3.11, the results presented by Aliabadi [36] and the results of the current study are presented with their initial letters A and C, respectively. The temperature of the right edge with respect to time is given. The flux and temperature types of boundary element formulations are denoted as "Temp." and "Flux", respectively. The time step is shown with the abbreviation "dt". "Constant" and "Linear" are used for the two types of time interpolation methods. The consistency between the two studies is remarkable for linear time interpolation. For both studies, it is clearly seen that the constant time interpolation gives inaccurate results compared to the linear time interpolation.

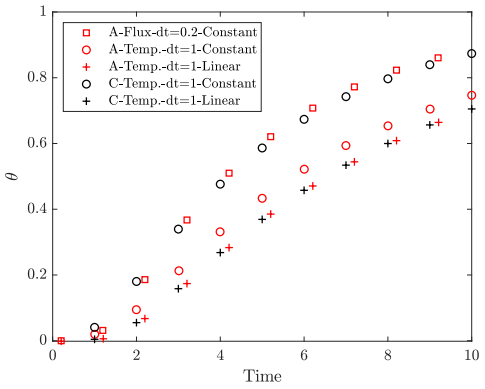


Figure 3.11: Variation of temperature of the right boundary with time

Effect of Abrupt and Gradual Loading

The problem domain given in Figure 3.12 is created to investigate the effect of the way loading is applied. The conductivity, specific heat, and thermal diffusivity values are taken as 1 in the analysis. The mesh involves 40 linear boundary elements, and

the domain integration is computed by using CTM incorporation with RPIM. The time step after reaching the final loading value is taken as 0.01, and the final time is 0.5. The initial temperature of the domain is set to zero. The final temperature of the left edge is set to 1. For comparison, the same analyses are carried out by using the commercially available finite element software ANSYS.

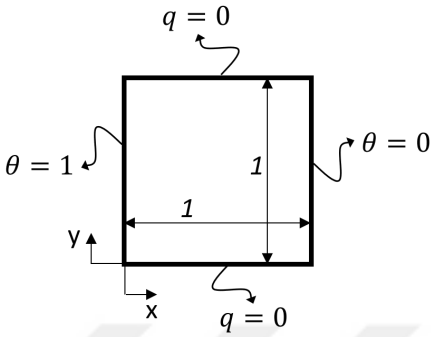


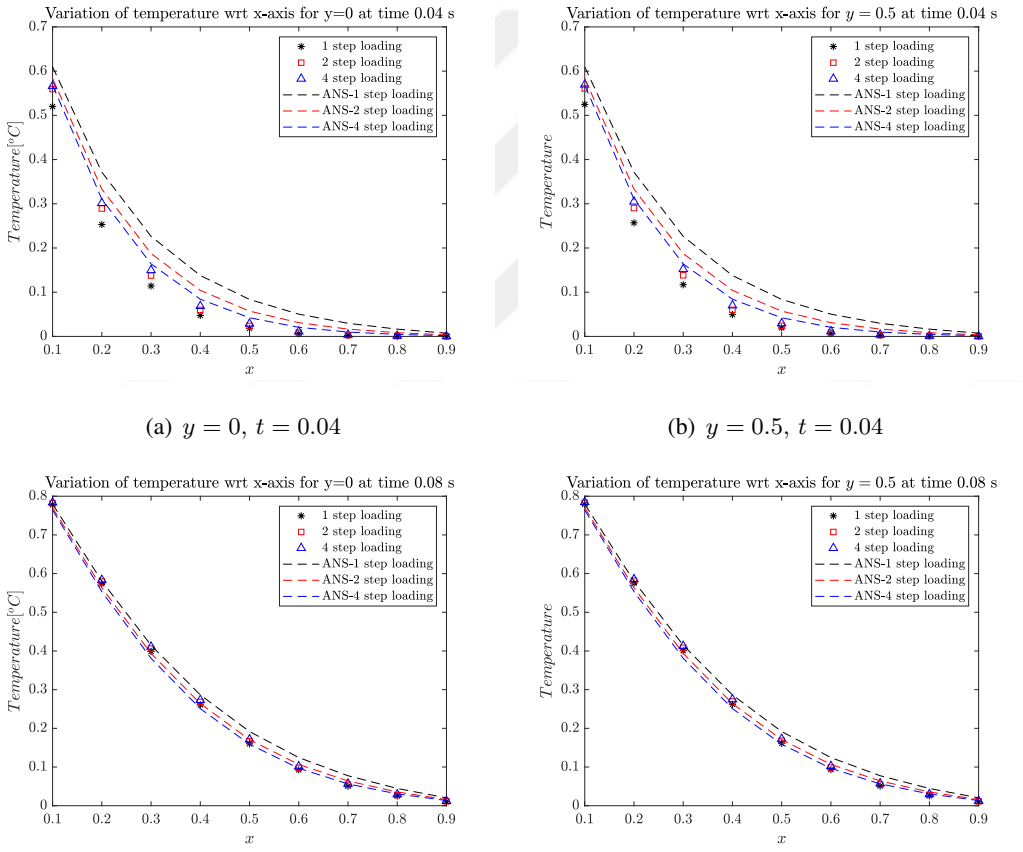
Figure 3.12: Problem domain with boundary conditions

Three different analyses considering the different ways of temperature loadings are discussed.

- 1-step loading: The loading is applied in one step with a time step 0.04.
- 2-step loading: The loading is applied in two steps with time steps 0.02.
  - Step 1: θ_{left} =0.5
  - Step 2: θ_{left} =1
- 4-step loading: The loading is applied in four steps with time steps 0.01.
  - Step 1: θ_{left} =0.25
  - Step 2: θ_{left} =0.5
  - Step 3: θ_{left} =0.75
  - Step 4: θ_{left} =1

It should be noted that after reaching the final temperature on the left edge, the time steps are set to 0.01 for all types of loading. In Figure 3.14, the change of temperature with time for points located at different coordinates on the problem domain is

presented for different loading types. The ANSYS results are abbreviated as "ANS" for brevity. The consistency between the results is deemed satisfactory. Observing the improvement in results with gradual loading is not easily discernible based on these findings. However, upon examining the results presented in Figure 3.13, it becomes evident that the consistency between the gradual loading results of both the Finite Element Method (FEM) and the Boundary Element Method (BEM) is superior compared to the results obtained with the abrupt 1-step loading approach. Moreover, after the first loading step for the abrupt loading, the agreement between the results of FEM and BEM is much better.



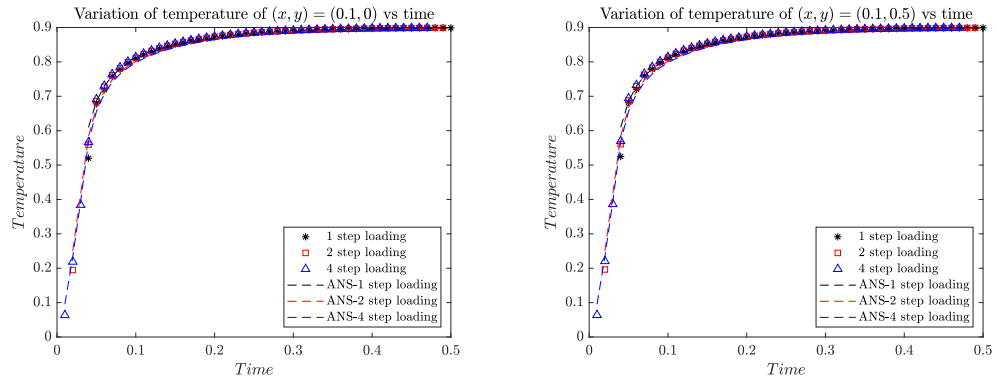
(a) $y = 0$, $t = 0.04$

(b) $y = 0.5$, $t = 0.04$

(c) $y = 0$, $t = 0.08$

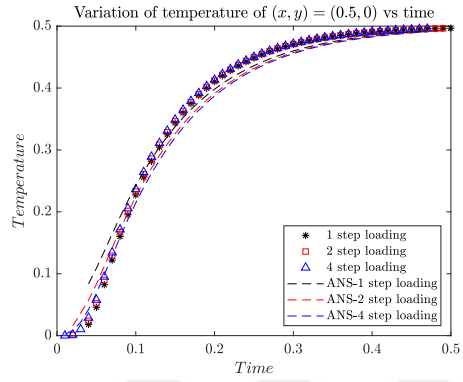
(d) $y = 0.5$, $t = 0.08$

Figure 3.13: For three types of initial loading and two solution methods, variation of temperature with respect to x for different paths taken on the problem domain

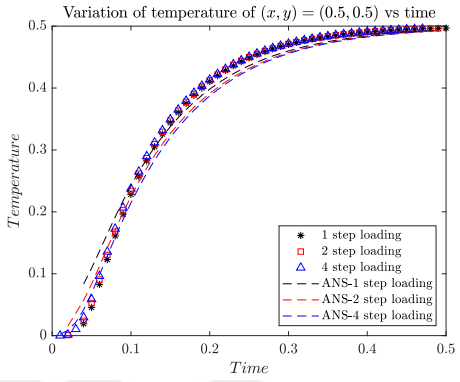


(a) $(x, y) = (0.1, 0)$

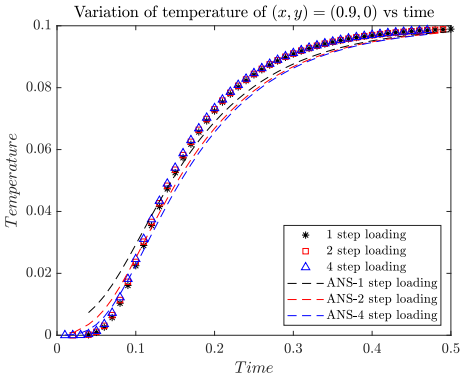
(b) $(x, y) = (0.1, 0.5)$



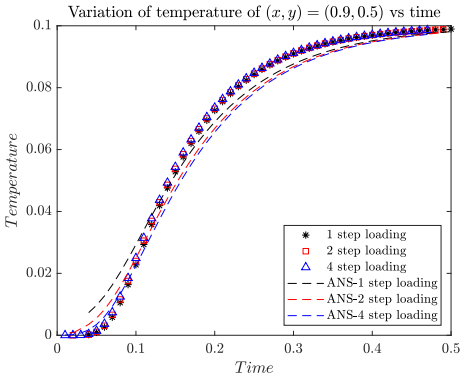
(c) $(x, y) = (0.5, 0)$



(d) $(x, y) = (0.5, 0.5)$



(e) $(x, y) = (0.9, 0)$



(f) $(x, y) = (0.9, 0.5)$

Figure 3.14: For three types of initial loading and two solution methods, variation of temperature with respect to time for different points on the problem domain

Capturing the ODE Solution of a Thermal Conductivity Problem Involving Non-linear Heat Source with BEM

The differential equation for the transient heat conduction problem can be expressed as

$$\bigtriangledown^2\theta(\mathbf{x},t)+\frac{1}{K}g(\mathbf{x},t)=\frac{1}{k}\frac{\partial}{\partial t}\theta(\mathbf{x},t), \tag{3.51}$$

where K is the thermal conductivity, k is the thermal diffusivity, g is the heat source function, and t is the solution time. Recall that the thermal diffusivity can be expressed as $k = K/\rho c$, where ρ is the density and c is the specific heat. Multiplication of both sides of Equation 3.51 with k will result in Equation 3.52.

$$\frac{\partial}{\partial t}\theta(\mathbf{x},t)=k\bigtriangledown^2\theta(\mathbf{x},t)+\frac{k}{K}g(\mathbf{x},t) \tag{3.52}$$

In the above relation, taking a low value for thermal diffusivity (k) without increasing ρc will cause the constant in front of the last expression (k/K) to be significantly bigger than k. Consequently, the gradient expression can be omitted, and the remaining ordinary differential equation (ODE) will be,

$$\frac{\partial}{\partial t}\theta(\mathbf{x},t)=\frac{k}{K}g(\mathbf{x},t) \quad \Rightarrow \quad \theta(\mathbf{x},t_n)=\theta(\mathbf{x},0)+\frac{k}{K}\int_0^{t_n} g(\mathbf{x},t)dt. \tag{3.53}$$

In the boundary element method, by introducing the nonlinear heat source as a domain field and setting very low values for the thermal diffusivity, the ODE solution of the problem is aimed to be captured. For this purpose, a problem domain, as illustrated in Figure 3.15, is established. All boundaries of the domain are flux-free. A boundary element mesh with 80 linear elements is utilized for the domain, and the domain integration is performed using the CTM with the RPIM. The number of inner points for RPIM interpolation is selected as 217. The conductivity, the specific heat and the density are taken as 0.001, 1 and 1, respectively. The time step is selected as 0.5. The initial temperature of the domain is zero. The heat source function is selected as given in Equation 3.54.

$$g(x,y,t)=\left(10-(x-2.5)^2\right)\left(5-(y-0.5)^2\right)t, \tag{3.54}$$

where origin is located at the bottom left corner of the domain.

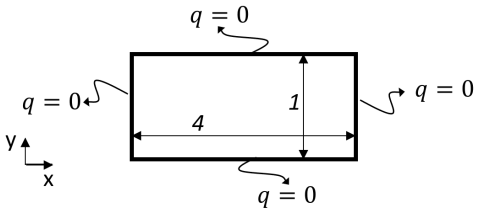
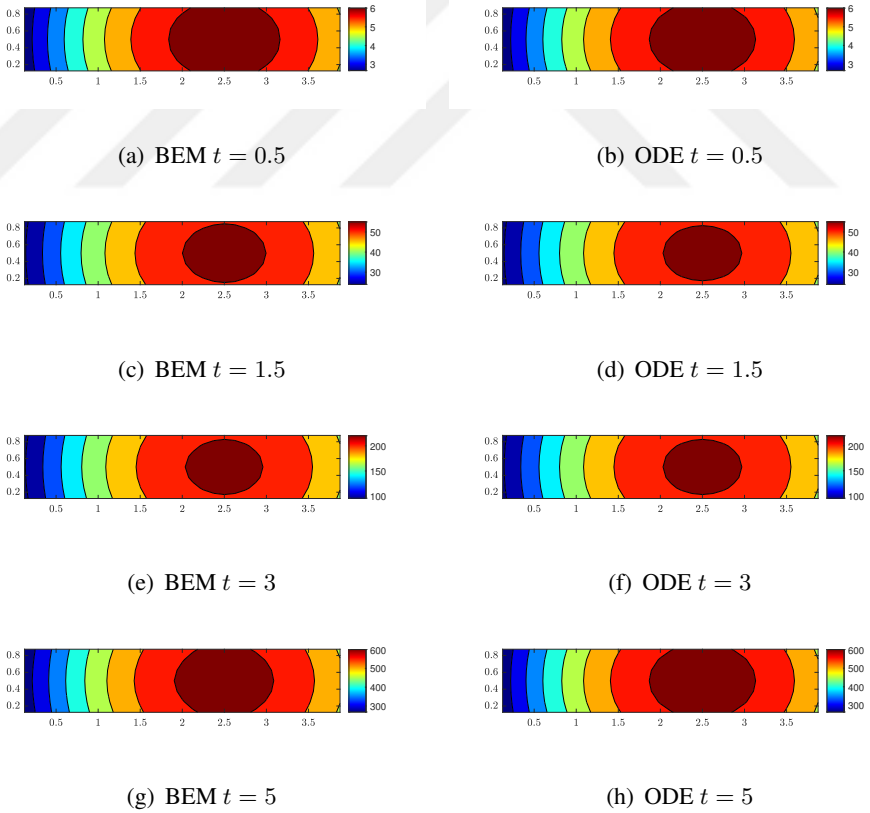


Figure 3.15: Problem domain with boundary conditions

Figure 3.16 displays the results obtained through the BEM alongside the analytical solutions obtained by solving the ODE at various time steps. It is clearly seen that, when the thermal conductivity and specific heat are set to 0.001 and 1, respectively, the results are consistent with the ODE solution of the problem. Based on this specific configuration, it can be inferred that solving an ODE using the BEM is achievable. Hence, considering the potential of representing ODEs using BEM, extending this approach to viscoelasticity is possible.



(a) BEM $t = 0.5$ (b) ODE $t = 0.5$

(c) BEM $t = 1.5$ (d) ODE $t = 1.5$

(e) BEM $t = 3$ (f) ODE $t = 3$

(g) BEM $t = 5$ (h) ODE $t = 5$

Figure 3.16: Time dependent contour plots for the BEM and ODE solutions of the problem involving internal heat generation

CHAPTER 4

2D LINEAR AND NONLINEAR VISCOELASTICITY/ELASTOPLASTICITY APPLICATIONS OF BOUNDARY ELEMENT METHOD

In this section, different methods to model viscoelasticity and elastoplasticity by using BEM are presented. As opposed to FEM, the applicability of BEM, however, to nonlinear, in particular, inelastic problems is scarce. The origins of the BEM's nonlinear solid mechanics applications date back to the 1970s. One of the first successful implementations of the BEM is done on modeling anisotropic viscoplastic materials with hardening by Swedlow and Cruse [75]. It is followed by a viscoplastic analysis of planar problems and time-dependent inelastic deformation of metallic bodies under thermal and mechanical loading by Riccardella [76] and Kumar et al. [77], respectively. Brebbia et al. [34, 78] presented ways to solve inelastic problems using BEM. Telles [79] proposed a guidebook for the solution of time-dependent inelastic solid mechanics problems with the BEM and considered a wide range of numerical examples. A Galerkin-based approach to model viscoplasticity in BEM is proposed by Maier [80]. Leitao [81] is given an improved way to formulate nonlinear fracture mechanics in BEM. Okada et al. [82, 83] conducted comprehensive studies on the application of BEM to different nonlinear problems. Creep and plasticity applications of time-dependent problems are presented by Chandenduang [84], Aliabadi [35], and Leon et al. [85]. In many rate formulations, it has been reported that the time step has a strong effect on the solution performance. Especially in the very first time steps, a fine temporal discretization is proven necessary.

Alternative to the rate formulations in the time domain, the use of the Laplace transformation in modeling linear viscoelastic materials with BEM was adopted in early

works [86, 87, 88, 89]. Using the Laplace transform, and the elastic-viscoelastic correspondence principle, linear viscoelasticity equations can be transformed into elastic equations. Once the solution for the elastic equations is obtained, the inversion from the Laplace domain to the time domain is carried out. Perez-Gavilan and Aliabadi [90] conducted a viscoelastic frequency domain solution by using Galerkin BEM. In the time domain, a quasi-static viscoelastic BEM solution was offered by Birgisson et al. [91], in which a new BEM, the so-called displacement discontinuity method, is used along with an explicit time integration. A boundary element formulation of viscoelastic solids directly in the time domain has been presented in [92] and [93], where only the fundamental solutions of the Laplace domain were used. Later, [94] developed the convolution quadrature boundary element method for quasi-static viscoelastic and poroelastic solids in the Laplace domain. Furthermore, Mesquita and Coda [95, 96] presented an approach to the Kelvin and Boltzmann models of linear viscoelasticity for two-dimensional isotropic solids. A linear time integration scheme is adopted in the BEM formulation for the rate of displacements appearing in the viscoelastic term. The domain integral is tackled by implementing two different methods: the internal cell approach and the conversion of domain integrals to boundary integrals. Since the proposed approach is highly dependent upon the particular rheological model considered, it necessitates the reconstruction of the BEM formulation for different models of viscoelasticity.

The BEM formulations of inelastic materials in the time domain often involve domain integrals, and thus their numerical calculation is inevitable. For this purpose, various studies have been presented in the literature. The most conventional domain integration method that has been widely used in classical inelastic applications of BEM is the internal cell technique. The latter method brings about an extra computational workload due to the requirement of domain discretization into a finite number of cells. Therefore, it leads to a larger equation system involving boundary equations written for all domain cells. In order to overcome the necessity of having internal cells, the Dual Reciprocity Boundary Element (DRBEM) formulation was proposed for the elastodynamics problems by Nardini and Brebbia [97]. Later, an extension of the method to more general problems has been presented in the literature by different authors. Nonlinear mechanics applications of DRBEM were first discussed in

[98, 99, 100]. An intensive study of the thermo-viscoelasticity application of DRBEM was presented by Baranoglu and Mengi [101], where coupled, uncoupled, stationary, quasi-static, and transient problems were investigated. For the simulation of viscoelastic properties, the correspondence principle is used.

The viscoplastic applications of the BEM have also been presented with sensitivity analysis of nonlinear (both geometric and material) problems. In sensitivity analysis, the effects of design parameters (shape parameters, boundary conditions, material parameters, etc.) on the response (displacements and stresses) are investigated. Both geometrically and materially nonlinear sensitivity analyses using explicit BEM have been proposed by Zhang et al. [102, 103], Leu and Mukherjee [104], and Wei et al. [105]. Rate-dependent BEM formulation was used with explicit time integration. Implicit time integration is first used in BEM by Jin et al. [106] and Telles and Carrer [107, 108].

The consistent tangent operator (CTO) is proposed for FEM analysis of rate-independent viscoplasticity by Simo and Taylor [109]. The first implementation of CTO into the implicit BEM is done by Bonnet and Mukherjee [110] for the solution of 1-D inelastic problems and then extended to multi-dimensions by Poon et al. [111]. CTO-based inelastic applications of the BEM are further used by researchers in solid mechanics applications, to mention a few [112, 113, 114].

In some viscoplasticity applications of the BEM, classical bending theories have been used. Kirchoff's bending theory is iteratively employed with BEM by various authors on different applications, to cite a few [115, 116, 117, 118]. The works following Reissner's theory can be found in [119, 120, 121, 122, 123].

A key novelty of the proposed approach is the incorporation of Cartesian Transformation Method (CTM) supplemented by Radial Point Interpolation Method (RPIM) into the framework of BEM for the solution of rate-dependent BVPs. To this end, a novel algorithmic formulation for generalized models of viscoelasticity and viscoplasticity within the framework of the boundary element method (BEM) is developed. The rheological model is chosen in such a way that it can be easily extended to the conventional generalized models of viscoelasticity and/or viscoplasticity by the addition of parallel or serial branches. On the other hand, the rheology can be readily reduced to

the fundamental Kelvin and Maxwell models. Furthermore, as opposed to the scarce existing rate formulations of inelasticity developed within BEM, the suggested non-iterative approach exploits the hybrid semi-implicit update of strain-like kinematic history variables. This allows one to adopt the existing well-established update algorithms of inelastic models, originally developed for FEM, with minor modifications to the BEM setting. As mentioned in the first place, the challenge arising from the indispensable domain integrals is overcome through the mesh-free CTM, complemented by the RPIM technique presented in Section 3 of the thesis study.

In Section 4.1, the fundamental equations of BEM are derived for a generic rheological model of viscoelasticity (Figure 4.1) along with the associated constitutive equations in the continuous and algorithmic settings. Furthermore, the details of the numerical calculation of domain integrals using CTM are outlined. Afterward, for linear viscoelasticity, the illustrative numerical examples include BVPs with both uniform and non-uniform strain fields. In the BVPs with non-uniform strain fields, creep and relaxation tests for the standard linear solids of Maxwell and Kelvin-type are considered. The displacement-controlled axial- and shear-type deformations are incorporated in the BVPs with uneven strain fields using the standard linear solid of Maxwell-type. The temporal variation of the prescribed transient displacements is described through the sinusoidal functions. It is shown that the results generated by the proposed BEM formulation of viscoelasticity agree well with the analytical and FEM solutions generated with ANSYS® [124] obtained for BVPs with uniform and non-uniform strain fields, respectively.

In Section 4.2, the approach presented in Section 4.1 is extended for the nonlinear applications of power-type viscoelasticity. Linearization of internal variables is adopted for the non-iterative update of viscous strains. Two model problems of commonly used mechanical elements are investigated to check the performance of the developed approach on nonlinear viscoelastic problems. Sinusoidal loadings are considered for the selected perforated plate and flange models, and a relaxation type of loading is specifically considered for the flange model. The investigation includes varying the loading period, the power term for the evolution of internal variables, and different loading types. The approach's performance is compared to an iterative FEM solution obtained with FEAP [125], and a good consistency between the results is observed

for the investigated models.

In Section 4.3, the extension of the nonlinear viscoelastic approach accompanied by BEM to nonlinear power-type viscoplasticity is presented. Firstly, the semi-implicit model for power type viscoplasticity is introduced. Subsequently, a brief explanation of the implementation of viscoplasticity in the BEM formulation is provided. Then, an optimization study on the determination of the material model parameters of a highly nonlinear viscoplastic material, as offered in the literature, is presented. The application of the proposed method to boundary value problems (BVPs) with uniform strain fields is demonstrated. Comparison studies are given with a fully implicit FEM solution. The limitations of the proposed approach in applying nonlinear viscoplasticity are discussed.

4.1 Time-Domain Boundary Element Formulation for Generalized Models of Linear Viscoelasticity

4.1.1 Theory

In this section, firstly, the generic model of viscoelasticity, presented in Figure 4.1, is introduced along with its constitutive equations in one-dimensional (1-D) and three-dimensional (3-D) settings. Furthermore, a semi-implicit integration scheme is introduced for the temporal update of strain-like internal variables (viscous strains). Then the BEM equations for the generic viscoelastic model are derived, where the incorporation of the algorithmic update scheme is elucidated. Furthermore, the details of the mesh-free CTM, along with RPIM, are given for the numerical calculation of the domain integrals.

4.1.1.1 Generic Model of Viscoelasticity

Description of Viscoelastic Model in 1-D Setting

The generic rheological model of viscoelasticity is composed of a spring with the modulus E_e representing *ground elasticity* connected in parallel to a viscous branch

that is comprised of a Kelvin element (the spring with E_1 and the dashpot with viscosity η_1 in parallel) and a spring with E_v in series to the Kelvin body as depicted in Figure 4.1. It should be noted that the generic model is capable of reproducing both the standard linear solid of Kelvin-type (SLS-K) and the standard linear solid of Maxwell-type (SLS-M) by setting $E_e = 0$ and $E_1 = 0$, respectively. Undoubtedly, the latter can be further extended to the generalized models of Maxwell and Kelvin. In this aspect, the viscoelastic model is general enough to cover the structures of most models of linear viscoelasticity. Hereafter, the latter (lower) branch is referred to as the viscoelastic branch.

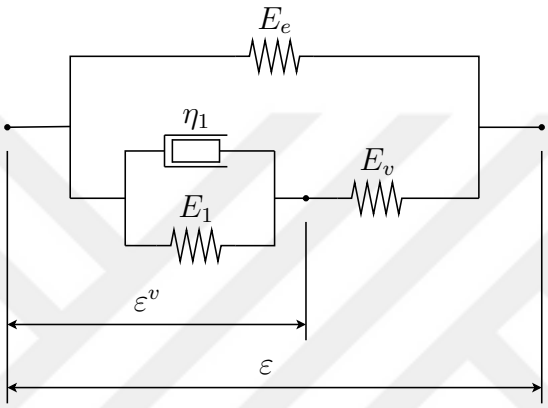


Figure 4.1: A generic rheological model of viscoleasticity

At this stage, it is important to note that the generic structure of the viscoelastic model allows us to develop a new algorithmic BEM formulation that is model-independent to a great extent, as opposed to the other approaches to viscoelasticity within BEM [95, 96, 126]. Furthermore, the upper elastic branch of the model has an additional function other than being used to model ground elastic response. Specifically, this fully elastic branch serves to provide an additional set of equations through which the total strain can be post-processed. Within the framework of the proposed algorithmic approach, this is particularly useful when the model is reduced to describe a fluid-like response through a Maxwell-type model and it is furthered to model nonlinear viscoelasticity and rate-dependent elastoplasticity using a power-type evolution equation. The latter extension is addressed in Sections 4.2 and 4.3.

In the 1-D setting, the total stress σ can be expressed as the summation of the elastic stress σ^e in the upper branch and the viscoelastic stress σ^v in the lower branch, as

given below.

$$\sigma = \sigma^e + \sigma^v \tag{4.1}$$

The elastic stress can further be expressed as follows

$$\sigma^e = E_e \varepsilon \,. \tag{4.2}$$

Similarly, the viscous stress σ^v can be expressed in two alternative ways by using either the Kelvin model or the individual spring element in the viscoelastic branch, as given in Equation 4.3a and Equation 4.3b, respectively.

$$\sigma^v = \eta_1 \dot{\varepsilon}^v + E_1 \varepsilon^v \tag{4.3a}$$

$$\sigma^v = E_v \left(\varepsilon - \varepsilon^v\right) \tag{4.3b}$$

The kinematic variables ε and ε^v are defined as the total strain and the viscous strain, respectively. The evolution of the viscous strain ε^v can be obtained by equating Equation 4.3a and Equation 4.3b, and solving the resultant identity for $\dot{\varepsilon}^v$ as given in Equation 4.4

$$\dot{\varepsilon}^v := \frac{d\varepsilon^v}{dt} = \eta_1^{-1} \left[E_v \left(\varepsilon - \varepsilon^v\right) - E_1 \varepsilon^v\right] \,. \tag{4.4}$$

In the algorithmic time-discrete setting, it is aimed to advance the solution from the preceding time step t_n to the current time step t_{n+1} within a typical time interval $[t_n, t_{n+1}]$ of step size $\Delta t := t_{n+1} - t_n$. For the update of the current viscous strain ε^v_{n+1}, a semi-implicit time integration scheme is adopted. To this end, the rate of viscous strain $\dot{\varepsilon}^v$ is integrated through the implicit (backward) Euler scheme

$$\varepsilon^v_{n+1} = \varepsilon^v_n + \Delta t \dot{\varepsilon}^v_{n+1} \,. \tag{4.5}$$

Substituting the evolution rule in 4.4 evaluated at t_{n+1} for $\dot{\varepsilon}^v_{n+1}$ and solving the consequent expression for the current viscous strain ε^v_{n+1}, the following relation is obtained.

$$\varepsilon^v_{n+1} = \left(1 + \Delta t \, \frac{E_1 + E_v}{\eta_1}\right)^{-1} \left[\varepsilon^v_n + \frac{\Delta t}{\eta_1} E_v \tilde{\varepsilon}_{n+1}\right] \,, \tag{4.6}$$

where the total strain is updated using the explicit (forward) scheme as follows

$$\tilde{\varepsilon}_{n+1} = \varepsilon_n + \Delta t \dot{\varepsilon}_n \,. \tag{4.7}$$

It is important to notice that the rate of the total strain appearing in Equation 4.7 is updated through the implicit corrector operation

$$\dot{\varepsilon}_{n+1} = \frac{\varepsilon_{n+1} - \varepsilon_n}{\Delta t}\,, \tag{4.8}$$

where the current value of the total strain ε_{n+1} is obtained by post-processing of the BEM solution at time t_{n+1}.

Extension of Model to 3-D Setting

In the 3-D setting, the scalar elastic moduli introduced in the 1-D formulation must be expressed as fourth-order tensors. We recall that the elasticity tensor of a linear elastic isotropic material can be expressed as follows

$$C_{ijkl} = \lambda\,\delta_{ij}\delta_{kl} + \mu\left(\delta_{ik}\delta_{jl} + \delta_{il}\delta_{jk}\right)\,, \tag{4.9}$$

where λ and μ denote the Lamé constants and δ stands for the Kronecker's Delta. In this study, a non-dimensional form of the elasticity tensor concerning a modulus of elasticity $E = \mu(3\lambda + 2\mu)/(\lambda + \mu)$ is used as introduced in Equation 4.10.

$$\tilde{C}_{ijkl} := E^{-1}\,C_{ijkl} \tag{4.10}$$

Similarly, the fourth-order viscosity tensor is defined as

$$\eta_{ijkl} = \eta_1^{\lambda}\lambda_v\,\delta_{ij}\delta_{kl} + \eta_1^{\mu}\mu_v\,\left(\delta_{ik}\delta_{jl} + \delta_{il}\delta_{jk}\right)\,, \tag{4.11}$$

where η_1^{λ} and η_1^{μ} are the Lamé-type viscosity constants. In the 3-D notation, the relations presented in the previous subsection can be rewritten as given in Equation 4.12.

$$\sigma_{ij}^{e} = E_e\tilde{C}_{ijkl}\varepsilon_{kl} \tag{4.12a}$$

$$\sigma_{ij}^{v} = \eta_{ijkl}\dot{\varepsilon}_{kl}^{v} + E_1\tilde{C}_{ijkl}\varepsilon_{kl}^{v} \tag{4.12b}$$

$$\sigma_{ij}^{v} = E_v\tilde{C}_{ijkl}\left(\varepsilon_{kl} - \varepsilon_{kl}^{v}\right) \tag{4.12c}$$

$$\begin{aligned}(\varepsilon_{ij}^{v})_{n+1} = &\left[\mathbb{I}_{ijkl} + \Delta t(E_1 + E_v)\eta_{ijtv}^{-1}\tilde{C}_{tvkl}\right]^{-1} \\ &\cdot\ \left[(\varepsilon_{kl}^{v})_n + \Delta t\eta_{klmn}^{-1}E_v\tilde{C}_{mnop}(\tilde{\varepsilon}_{op})_{n+1}\right]\end{aligned} \tag{4.12d}$$

Note that $\mathbb{I}_{ijkl}$ is the fourth-order symmetric identity tensor.

It is well-known that most materials exhibit distinct behavior under volumetric and deviatoric deformations, such as polymers and metals, where the volumetric response is often elastic, while the volume-preserving response is inelastic. The viscoelastic constitutive formulation outlined above can be readily recast to a form, where this distinction is straightforwardly incorporated.

4.1.1.2 Boundary Element Formulation

Boundary Integral Equations

Consider a solid body Ω with boundary Γ, as shown in Figure 4.2. The boundary Γ is decomposed into the parts Γ_u and Γ_t where the displacement (Dirichlet) and traction (Neumann) boundary conditions are prescribed, respectively. Note that these parts fulfill the conditions $\Gamma = \Gamma_u \cup \Gamma_t$ and $\Gamma_u \cap \Gamma_t = \emptyset$.

Within the domain given in Figure 4.2, the balance of linear momentum under quasi-static conditions ($\rho \ddot{u}_i \approx 0$), can be written as

$$\frac{\partial \sigma_{ij}}{\partial x_j} + b_i = 0 \quad \text{in} \quad \Omega\,, \tag{4.13}$$

where the vector b_i denotes the given body forces. The Kelvin fundamental solution for the elastic body is used for weighing Equation 4.13 over the domain Ω.

$$\int_\Omega u^*_{ki} \left(\frac{\partial \sigma_{ij}}{\partial x_j} + b_i \right) d\Omega = 0 \tag{4.14}$$

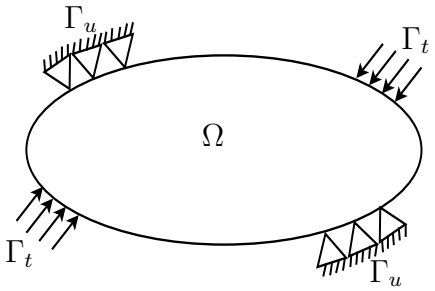


Figure 4.2: Problem domain under displacement and traction loadings

In Equation 4.14, u^*_{ki} is Kelvin's displacement fundamental solution for an infinite elastic body. The application of the divergence theorem to the stress term appearing

in the integral results in

$$\int_{\Gamma} u^*_{ki}\sigma_{ij}n_j d\Gamma - \int_{\Omega} \frac{\partial u^*_{ki}}{\partial x_j}\sigma_{ij} d\Omega + \int_{\Omega} u^*_{ki} b_i d\Omega = 0\,. \tag{4.15}$$

The partial derivative $(\partial u^*_{ki}/\partial x_j)$ appearing in the second integral of Equation 4.15 is Kelvin's strain fundamental solution ($\varepsilon^*_{kij} := \partial u^*_{ki}/\partial x_j$). The Cauchy stress theorem ($t_i = \sigma_{ij}n_j$) can be adopted in the first integral to write Equation 4.15 as

$$\int_{\Gamma} u^*_{ki} t_i d\Gamma - \int_{\Omega} \varepsilon^*_{kij}\sigma_{ij} d\Omega + \int_{\Omega} u^*_{ki} b_i d\Omega = 0\,, \tag{4.16}$$

where t_i is the traction vector. Insertion of the tensorial counterpart of Equation 4.1 into Equation 4.16 leads us to

$$\int_{\Gamma} u^*_{ki} t_i d\Gamma - \int_{\Omega} \varepsilon^*_{kij}\left(\sigma^e_{ij} + \sigma^v_{ij}\right) d\Omega + \int_{\Omega} u^*_{ki} b_i d\Omega = 0\,. \tag{4.17}$$

Using relations introduced for the elastic and viscous stresses in Equation 4.12a and Equation 4.12c, the integrand of the second integral in Equation 4.17 can be rewritten as

$$\begin{aligned}
\varepsilon^*_{kij}\left(\sigma^e_{ij} + \sigma^v_{ij}\right) &= \varepsilon^*_{kij} E_e \tilde{\mathbf{C}}_{ijmn}\varepsilon_{mn} + \varepsilon^*_{kij} E_v \tilde{\mathbf{C}}_{ijmn}\left(\varepsilon_{mn} - \varepsilon^v_{mn}\right) \\
&= \varepsilon^*_{kij}\left(E_e + E_v\right)\tilde{\mathbf{C}}_{ijmn}\varepsilon_{mn} - \varepsilon^*_{kij} E_v \tilde{\mathbf{C}}_{ijmn}\varepsilon^v_{mn} \\
&= \sigma^*_{kmn}\varepsilon_{mn} - \varepsilon^*_{kij}\bar{\sigma}^v_{ij}\,,
\end{aligned} \tag{4.18}$$

with $\sigma^*_{kmn} := \varepsilon^*_{kij}\left(E_e + E_v\right)\tilde{\mathbf{C}}_{ijmn}$ and the new field variable $\bar{\sigma}^v$ is introduced as

$$\bar{\sigma}^v_{ij} := E_v \tilde{\mathbf{C}}_{ijmn}\varepsilon^v_{mn}\,, \tag{4.19}$$

where the update scheme given in Equation 4.12d is used to calculate the current value of the viscous strain tensor ε^v_{mn}. Insertion of Equation 4.18 into Equation 4.17 gives the following representation

$$\begin{aligned}
\int_{\Gamma} u^*_{ki} t_i d\Gamma - \int_{\Omega} \sigma^*_{kij}\varepsilon_{ij} d\Omega + \int_{\Omega} \varepsilon^*_{kij}\bar{\sigma}^v_{ij} d\Omega \\
+ \int_{\Omega} u^*_{ki} b_i d\Omega = 0\,.
\end{aligned} \tag{4.20}$$

Following [71, 33, 35], the second integral expression in Equation 4.20 can be reduced to a boundary integral to recast Equation 4.20 into

$$\begin{aligned}
C_{ki}u_i + \int_{\Gamma} t^*_{ki} u_i d\Gamma = \int_{\Gamma} u^*_{ki} t_i d\Gamma + \int_{\Omega} \varepsilon^*_{kij}\bar{\sigma}^v_{ij} d\Omega \\
+ \int_{\Omega} u^*_{ki} b_i d\Omega\,,
\end{aligned} \tag{4.21}$$

where the term t^*_{ki} stands for Kelvin's traction solution. The way that it can be utilized to calculate the matrix C_{ki} is discussed by Mantic [39]. Moreover, the domain integrals appearing in Equation 4.21 are handled by the mesh-free method presented in the Chapter 3.

Numerical Discretization and Post-processing

Discretizing the integral equation Equation 4.21 into N_e boundary elements with N_n nodes and the isoparametric shape functions N_α on the boundary Γ and utilizing CTM Equation 3.9 with N_G integration points for calculating the domain integrals under a single summation, the discretized form of Equation 4.21 can be expressed as

$$\begin{aligned} C_{ki}u_i + \sum_{n=1}^{N_e}\sum_{\alpha=1}^{N_n} H^{n\alpha}_{ki}u^{n\alpha}_i\Gamma_n = \sum_{n=1}^{N_e}\sum_{\alpha=1}^{N_n} G^{n\alpha}_{ki}t^{n\alpha}_i\Gamma_n \\ + \sum_{m=1}^{N_G}\left[\left(\varepsilon^*_{kij}\right)^m\left(\bar{\sigma}^v_{ij}\right)^m + \left(u^*_{ki}\right)^m\left(b_i\right)^m\right] , \end{aligned} \tag{4.22}$$

where Γ_n denotes the elemental length. Moreover, by expressing Equation 4.22 for all the boundary nodes, a linear system of equations can be obtained. In matrix form, the equation system can be represented as

$$\tilde{\mathbf{H}}\mathbf{u} = \mathbf{G}\mathbf{t} + \mathbf{b}_\sigma + \mathbf{b}_\Omega \, , \tag{4.23}$$

where the vectors $\mathbf{b}_\sigma$ and $\mathbf{b}_\Omega$ are the contributions of the viscous strain and the body forces, respectively. It should be noted that matrices $\mathbf{G}$ and $\tilde{\mathbf{H}}$ are calculated once and for all time steps. Similarly, ε^*_{kij} and u^*_{ki} in Equation 4.22 are also determined once for each boundary node-integration point pair. Components of the matrices in Equation 4.23 can be expressed separately in indicial form as

$$\tilde{H}_{ki} = C_{ki} + \sum_{n=1}^{N_e}\sum_{\alpha=1}^{N_n} H^{n\alpha}_{ki} \, , \tag{4.24a}$$

$$G_{ki} = \sum_{n=1}^{N_e}\sum_{\alpha=1}^{N_n} G^{n\alpha}_{ki} \, , \tag{4.24b}$$

$$\left(b_\sigma\right)_k = \sum_{m=1}^{\text{NGQP}} \left(\varepsilon^*_{kij}\right)^m\left(\bar{\sigma}^v_{ij}\right)^m \, , \tag{4.24c}$$

$$\left(b_\Omega\right)_k = \sum_{m=1}^{\text{NGQP}} \left(u^*_{ki}\right)^m\left(b_i\right)^m \, . \tag{4.24d}$$

By incorporating the boundary conditions into Equation 4.23, the equation system can be solved for unknown boundary quantities.

Once the system of BEM equations in Equation 4.23 is solved at time t_n, the unknown field variables are determined. For the semi-implicit update of viscous strain presented in Equation 4.12d, the total strain tensor ε_{ij} and its rate $\dot{\varepsilon}_{ij}$ at time step t_n must be determined. The auxiliary (upper) branch in Figure 4.1 is used for post-processing purposes in this study. With the displacement field at the boundary nodes is at hand (by using Equation 4.23), it can be applied directly to the auxiliary branch elastically, and the strain field in the problem domain can be readily obtained. As can be observed in Figure 4.1, the strain field solved by using the auxiliary branch is equal to the total strain ε_{ij} field of the complete model. The total strain can be determined by using the the kinematical relation between strain and displacement. Hence, the insertion of Equation 4.21 into kinematical relation gives

$$\varepsilon_{ij} = \int_{\Gamma} \varepsilon^*_{ikj} t_k d\Gamma - \int_{\Gamma} \tilde{t}^*_{ikj} u_k d\Gamma + \int_{\Omega} \varepsilon^*_{ikj} b_k d\Omega \,. \tag{4.25}$$

The Kelvin solutions introduced in the formulation can be summarized for the plane strain case as follows [71]

$$u^*_{ij} = \frac{-1}{8\pi(1-\nu)\mu} \Big\{ (3-4\nu)\ln(r)\delta_{ij} - r_{,i}r_{,j} \Big\} \,, \tag{4.26a}$$

$$\begin{aligned} t^*_{ij} = \frac{-1}{4\pi(1-\nu)r} \Big\{ & [(1-2\nu)\delta_{ij} + 2r_{,i}r_{,j}] \frac{\partial r}{\partial n} \\ & - (1-2\nu)(r_{,i}n_j - r_{,j}n_i) \Big\} \,, \end{aligned} \tag{4.26b}$$

$$\begin{aligned} \varepsilon^*_{ikj} = \frac{-1}{8\pi(1-\nu)\mu r} \Big\{ & (1-2\nu)(r_{,k}\delta_{ji} + r_{,i}\delta_{jk}) \\ & - r_{,j}\delta_{ik} + 2r_{,i}r_{,j}r_{,k} \Big\} \,, \end{aligned} \tag{4.26c}$$

$$\begin{aligned} \tilde{t}^*_{ikj} = \frac{1}{4\pi(1-\nu)r^2} \Big\{ & (1-2\nu)(\delta_{ik}n_j + \delta_{kj}n_i - \delta_{ij}n_k \\ & + 2r_{,i}r_{,j}n_k) + 2\nu(r_{,k}r_{,j}n_i + r_{,i}r_{,k}n_j) \\ & + [2\nu(\delta_{ik}r_{,j} + \delta_{jk}r_{,i}) + 2\delta_{ji}r_{,k} - r_{,i}r_{,k}r_{,j}] \frac{\partial r}{\partial n} \Big\} \,, \end{aligned} \tag{4.26d}$$

where $r := \sqrt{r_i r_i}$, $r_i := y_i - x_i$ denotes the distance between the source and the field points of BEM with r_i being the components of $\boldsymbol{r}$ and $\partial r/\partial n := n_i \partial r/\partial y_i$ is the perpendicular distance between the source and the element containing field points.

By setting $\nu \rightarrow \nu/(\nu+1)$ in the relations Equation 4.26, the plane stress assumption can be adopted into the proposed method.

It is important to note that the kernel expression ε^*_{ikj} introduced in Equation 4.26c, which is used in the domain integrals of Equation 4.21, introduces a weak singularity when the field point (integration point) is close to the boundary node. Therefore, as the Euclidean distance (r) between the two points reduces considerably, the accuracy of the mesh-free integral solution reduces. To deal with this problem, the weakly singular domain integral can be treated as suggested by Hematiyan et al. [127]. Suppose the integral to be evaluated is in the following form.

$$I = \int_{\Omega} \bar{\sigma}^v_{ij}(\mathbf{Q})\, \varepsilon^*_{kij}(\mathrm{P}, \mathbf{Q})\, d\Omega \tag{4.27}$$

In Equation 4.27, $\bar{\sigma}^v_{ij}$ is the function of non-singular field values and ε^*_{kij} is the weakly singular mathematical expression. Moreover, P and $\mathbf{Q}$ are the boundary node and the vector of integration points, respectively. The integral expression in Equation 4.27 can be rewritten as

$$\begin{aligned} I = &\int_{\Omega} [\bar{\sigma}^v_{ij}(\mathbf{Q}) - \bar{\sigma}^v_{ij}(\mathrm{P})] \varepsilon^*_{kij}(\mathrm{P}, \mathbf{Q}) d\Omega \\ &+ \bar{\sigma}^v_{ij}(\mathrm{P}) \int_{\Omega} \varepsilon^*_{kij}(\mathrm{P}, \mathbf{Q}) d\Omega \,. \end{aligned} \tag{4.28}$$

The first integral in Equation 4.28 is regular and can be evaluated with the introduced mesh-free methodology. The second integral can be transformed into a boundary integral by using the radial integration method as follows

$$\begin{aligned} I' &= \bar{\sigma}^v_{ij}(\mathrm{P}) \int_{\Omega} \varepsilon^*_{kij}(\mathrm{P}, \mathbf{Q}) d\Omega \\ &= \bar{\sigma}^v_{ij}(\mathrm{P}) \int_{\Gamma} \frac{1}{r} \frac{\partial r}{\partial n} \left[\int_0^r \varepsilon^*_{kij} r dr \right] d\Gamma \,. \end{aligned} \tag{4.29}$$

The boundary integral in Equation 4.29 can now be evaluated by using numerical integration methods.

The solution procedure for calculating the field variables at time step t_{n+1} is summarized in Table 4.1.

Table 4.1: Algorithmic box

1. Given the history variables $\{(\varepsilon_{ij})_n, (\dot{\varepsilon}_{ij})_n, (\varepsilon^v_{ij})_n\}$

2. Update the total strain through Equation 4.7.

3. Compute $(\varepsilon^v_{ij})_{n+1}$ at time step t_{n+1} by using the implicit update in (4.12d).

4. Calculate the field variable $(\bar{\sigma}^v_{ij})_{n+1}$ by using Equation 4.65.

5. Solve the BEM equation given in Equation 4.22 for the current time step t_{n+1}.

6. Apply the displacement field found in Step 5 to a BEM problem considering only the auxiliary branch (upper branch) presented in Figure 4.1. Again, use Equation 4.22 for the solution by setting $\bar{\sigma}^v_{ij} = 0$.

7. Calculate the total strain $(\varepsilon_{ij})_{n+1}$ by using Equation 4.25 and update the strain rate $(\dot{\varepsilon}_{ij})_{n+1}$ through Equation 4.8.

8. Calculate the stresses at the upper and lower branches by using Equations 4.12a and 4.12c, respectively.

4.1.2 Numerical Examples

In this section, the performance of the proposed model is assessed and demonstrated through representative numerical examples that cover BVPs with uniform and non-uniform strain fields. The BVPs with uniform strain, considered in Section 4.1.2.1, are concerned with axial creep and relaxation analyses using the standard linear solids of Maxwell and Kelvin-type (SLS-M & SLS-K). The comparison of the results generated through the proposed novel BEM approach with the ones obtained analytically indicates excellent matches. In Section 4.1.2.2, the displacement-controlled cyclic axial and shear deformations are addressed using BVPs with non-uniform strain distribution using the standard linear solid of Maxwell-type (SLS-M). It is shown that the results generated by the proposed BEM formulation of viscoelasticity are in perfect accord with the corresponding FEM solutions.

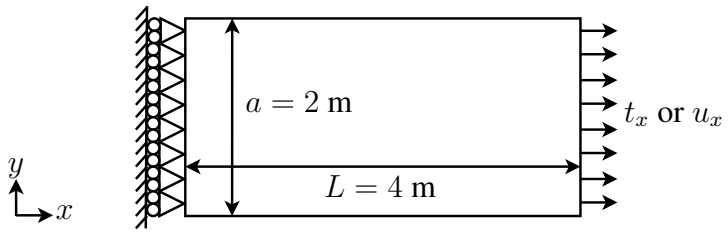


Figure 4.3: The viscoelastic rectangular body subjected to creep and relaxation

4.1.2.1 BVPs with Uniform Strain Field

The geometry, dimensions, and boundary conditions of the BVPs with uniform strain distribution are given in Figure 4.3. While the displacement degrees of freedom on the left boundary is restrained only in the x-direction, the load (displacement/traction) is applied in the x-direction on the right boundary. Therefore, the body is free to deform in the y-direction, which reduces the state of stress to uniaxial. Note that the plane strain conditions are adopted for 2-D modeling purposes.

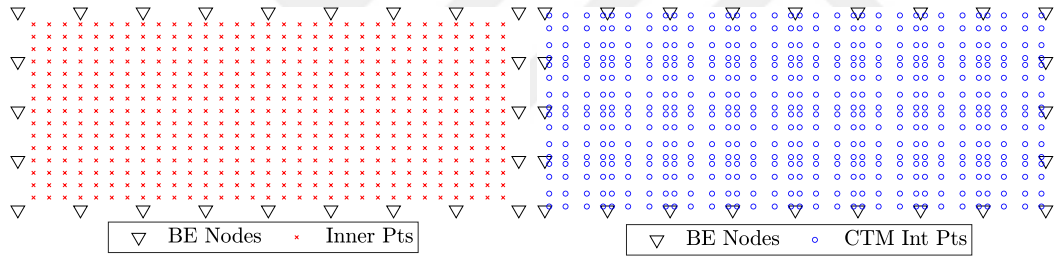
Table 4.2: Model parameters used for the standard linear solids of Maxwell and Kelvin-type (SLS-M & SLS-K)

	E_e [Pa]	E_v [Pa]	E_1 [Pa]	$\eta_1^\lambda = \eta_1^\mu$ [1/s]	ν [−]
SLS-M	15	5	0	10	0
SLS-K	10^{-5}	5	2.5	10	0

Recall that the proposed hybrid model, see Figure 4.1, can be simplified to reproduce the standard linear solids of Maxwell and Kelvin-type through an appropriate selection of the model parameters. The values of the model parameters used in the analyses of BVPs with uniform strain field are given in Table 4.7. Poisson's ratios for all the elasticity elements are set to the same values. As mentioned in Section 4.1.1.1, the upper elastic branch of the model has an auxiliary function of providing an additional set of equations for post-processing the total strain that plays a central role in the proposed algorithmic framework. For this the reason, the value of the elastic modulus E_e has not been set exactly to zero but to a negligibly small value for SLS-

K. A numerical study, presented in Appendix E, conducted to represent the Maxwell model by setting $E_1 = 0\,\text{Pa}$ and varying the ratio E_e/E_v from $2 \cdot 10^{-3}$ to $2 \cdot 10^{-12}$ indicates that the analytical solution for the relaxation response of the Maxwell model is successfully captured by the proposed approach, and no stability issue is caused by the smallest ratio $E_e/E_v = 2 \cdot 10^{-12}$ considered.

Creep and relaxation-type axial loadings are considered for both SLS-K and SLS-M. In both cases, an abrupt (Heaviside) loading is applied. The values of relaxation and creep-type loadings are selected to be $u_x = 0.1$ m and $t_x = 0.375$ Pa, respectively. The time step is set to $\Delta t = 0.1$ s for the BVPs with uniform strain. Furthermore, the spatial discretization used for the BVPs with an even strain field is presented in Figure 4.4. The boundary is discretized with linear boundary elements of 0.5 m length whose nodes are indicated by downward triangles ($\triangledown$). Moreover, 512 integration points indicated by blue circles ($\bigcirc$) are used for CTM, and the post-processing is conducted through 465 inner data points shown by red crosses ($\times$) in Figure 4.4.



(a) Inner data points

(b) CTM integration points

Figure 4.4: Boundary element mesh with inner points used for interpolation and CTM integration points

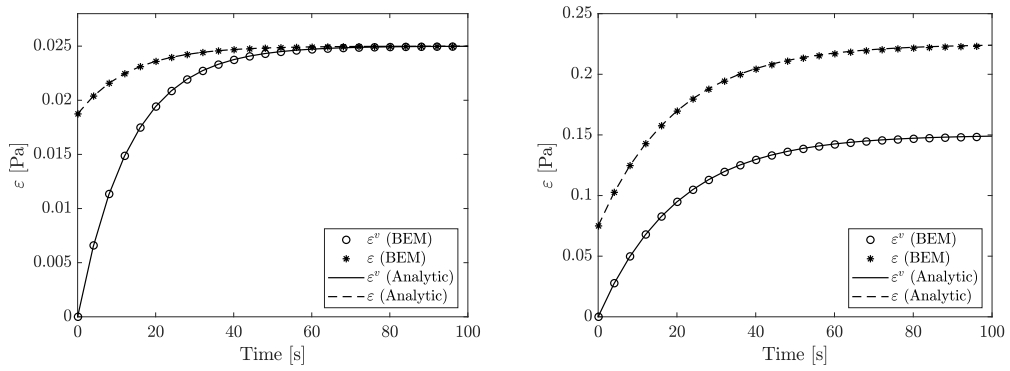
Creep-Type Axial Loading

Under the constant axial traction of $\sigma_x = 0.375$ Pa, the total axial strain vs. time (ε-t) and the viscoelastic axial strain vs. time (ε^v-t) curves generated for SLS-M and SLS-K models are presented in Figures 4.5(a) and 4.5(b), respectively. The BEM results are compared with the corresponding analytical solutions. The analytical solutions of both models are adapted from Tschoegl [128], and given in Equation D1

and Equation D3 in Appendix D. For a clearer illustration, even though BEM analyses are conducted with $\Delta t = 0.1$ s, the BEM results are depicted through discrete points (asterisks, circles) at every certain number of data points. This convention of illustration is adopted in all the numerical examples presented hereafter.

As expected, in both SLS-M and SLS-K, the dashpot initially behaves rigidly and locks the viscous strain ϵ^v upon the initial application of the creep stress. Under the sustained constant stress, ϵ^v evolves by approaching a certain finite value in the limit $t \to \infty$ where either the stress on the dashpot fully vanishes and is transferred to the spring in the upper branch in SLS-M or it is taken over by the spring parallel to the dashpot in SLS-K, as favorably shown in Figures 4.5(a) and 4.5(b), respectively.

The comparison of the results generated through the proposed BEM approach with those obtained by the analytical solution indicates an excellent agreement, as depicted in Figure 4.5. Here, it is important to note that the hybrid semi-implicit integration scheme has been pivotal in obtaining initially non-oscillatory and accurate strain values that would otherwise be unattainable through an entirely explicit scheme under the sudden Heaviside step loading.



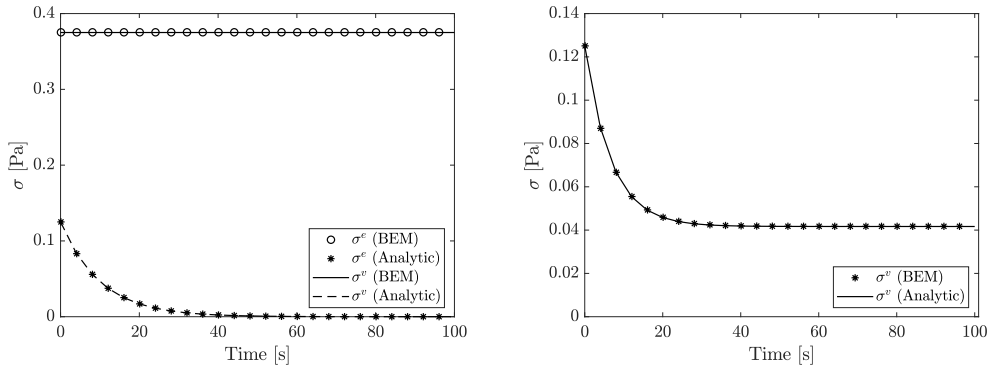
(a) Standard Linear Solid of Maxwell-Type (SLS-M) (b) Standard Linear Solid of Kelvin-Type (SLS-K)

Figure 4.5: Analytical and BEM results for the creep-type BVP with uniform strain field modeled with (a) SLS-M and (b) SLS-K

Relaxation-Type Axial Loading

Analogous to the creep response considered in the preceding subsection, the transients of the elastic stress in the upper elastic branch $(\sigma^e\text{-}t)$, which exists only for SLS-M, and of the viscous stress in the lower branch $(\sigma^v\text{-}t)$ under the constant elongation $u_x = 0.1$ m ($\varepsilon = 0.025$) are presented for SLS-M and SLS-K models in Figures 4.6(a) and 4.6(b), respectively. The results generated through the proposed BEM approach are compared with the analytical counterparts given in Equation D2 and Equation D4 in Appendix D.

The dashpot in both SLS-M and SLS-K behaves rigidly as the relaxation strain is initially applied, as it would be the case for any dashpot belonging to a rheological model of viscoelasticity. Under the constant strain/deformation, the stress in the dashpot relaxes completely in the limit $t \to \infty$. This results in transformations of SLS-M to an elastic model only with the upper branch and SLS-K to an elastic model with the two springs in the lower branch connected serially. These transformations in the models are favorably manifested in the form of stress relaxations, as quantitatively depicted in Figures 4.6(a) and 4.6(b). Note that, as clearly depicted in Figure 4.6, the results produced using the proposed BEM approach agree excellently with the analytical counterparts.



(a) Standard Linear Solid of Maxwell-Type (SLS-M) (b) Standard Linear Solid of Kelvin-Type (SLS-K)

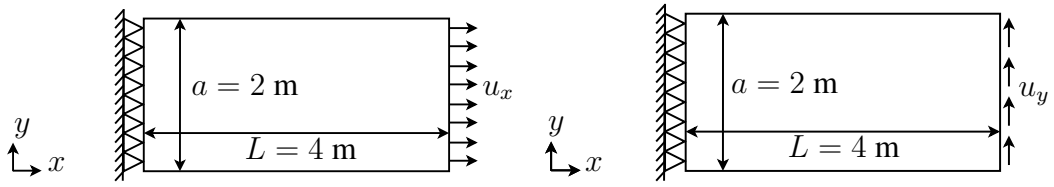
Figure 4.6: Analytical and BEM results for the relaxation-type BVP with uniform strain field modeled with (a) SLS-M and (b) SLS-K

Table 4.3: Specific sinusoidal functions of the axial $u_x(t)$ and shear $u_y(t)$ loadings along with the accompanying boundary conditions in the perpendicular directions applied on the right edge

Axial	$u_x(t) = 0.1\sin(2\pi t/30),$	$t_y(t) = 0$
Shear	$u_x(t) = 0,$	$u_y(t) = 0.1\sin(2\pi t/30)$

4.1.2.2 BVPs with Non-Uniform Strain Field

Besides the BVPs with uniform strain distribution presented in the preceding section, the capabilities of the proposed approach are further assessed based on BVPs where the strain-field is non-uniform. For this purpose, we consider again the viscoelastic rectangular body with the clamped left edge, as shown in Figure 4.7. This body is then subjected to cyclic axial and shear-type loadings through the prescribed displacements $u_x(t)$ and $u_y(t)$ on its right edge, as shown in Figures 4.7(a) and 4.7(b), respectively. The specific sinusoidal functions used to define the axial loading $u_x(t)$ and the shear loading $u_y(t)$ are given in Table 4.3, along with the accompanying boundary conditions in the perpendicular directions. Note that both displacement-controlled loadings have an amplitude of 0.1 m and a period of 30 s. The constant time increment $\Delta t = 1$ s is used in the analyses of the BVPs with non-uniform strain distribution.



(a) Axial Loading (b) Shear Loading

Figure 4.7: The viscoelastic solid body subjected to cyclic (a) axial and (b) shear loadings resulting in uneven strain distributions

Note that the analyses of BVP with non-uniform strain are conducted only for the

standard linear solid of Maxwell-type (SLS-M) with the model parameters given in Table 4.4. Similar to the uniform-strain BVPs of Section 4.1.2.1, the plane strain assumption is adopted in the BVPs with a non-uniform strain field, whereas the Poisson ratios for all the elasticity elements are set to $\nu = 0.3$.

Table 4.4: Model parameters of the standard linear solid of Maxwell-type (SLS-M) in the heterogeneous BVPs

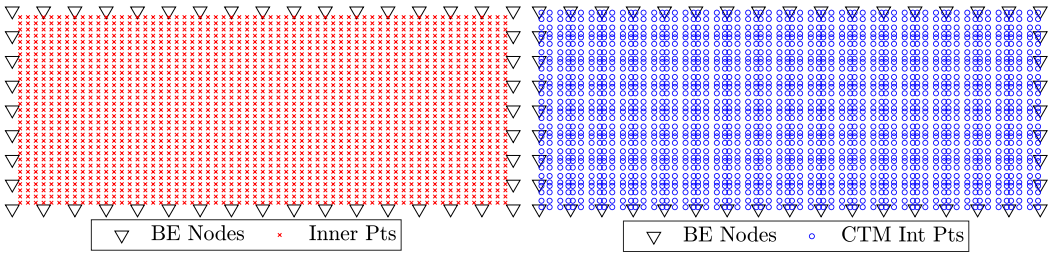
	E_e [Pa]	E_v [Pa]	E_1 [Pa]	$\eta_1^\lambda = \eta_1^\mu$ [1/s]	ν [−]
SLS-M	15	5	0	10	0.3

Axial Loading

In the discretization of the axially loaded BVP with non-uniform strain, see Figure 4.8, 48 boundary elements $(\triangledown)$ of uniform length along with 2048 integration points $(\bigcirc)$ and 1953 inner data points $(\times)$ are used to carry out the BEM analysis of the cyclic axial loading. For the validation of the results, the corresponding Finite Element Method (FEM) analysis is conducted by using the commercial software ANSYS® [124]. In the FEM analysis, the converged results have been obtained for the structured mesh with $64 \times 32 = 2048$ four-node quadrilateral elements. A full integration scheme is used.

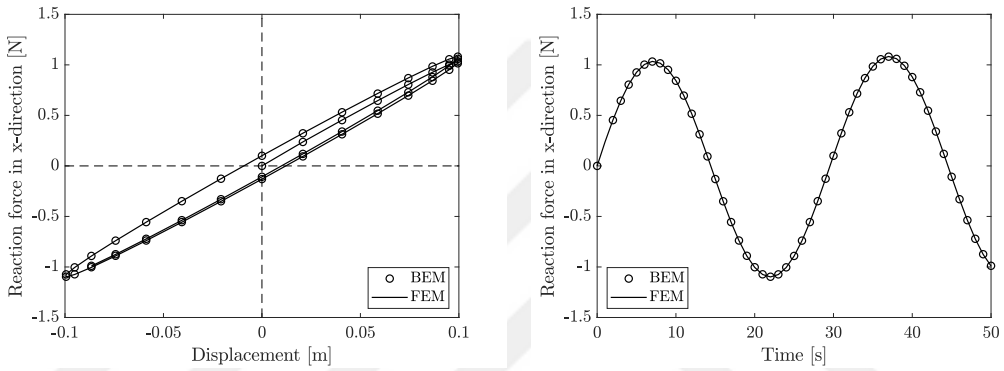
Firstly comparison of the overall force-displacement and force-time curves obtained through the proposed BEM approach and FEM is made in Figures 4.9(a) and 4.9(b), respectively. It is observed that the force-displacement and force-time curves generated by BEM and FEM agree excellently without any deviation from one another. Furthermore, the dissipative nature of the SLS-M has been successfully captured by the proposed non-iterative algorithmic BEM formulation for viscoelasticity, as clearly demonstrated by the hysteretic nature of the force-displacement curve.

The highly non-uniform nature of the axial BVP is clearly illustrated through the contour plots of in-plane components $(\sigma_{xx}, \sigma_{xy}, \sigma_{yy})$ of the stress tensor generated using the proposed BEM and FEM analyses of the axial BVP in the first and second



(a) Inner data points (b) CTM integration nodes

Figure 4.8: Boundary element mesh with inner points used for interpolation and CTM integration points

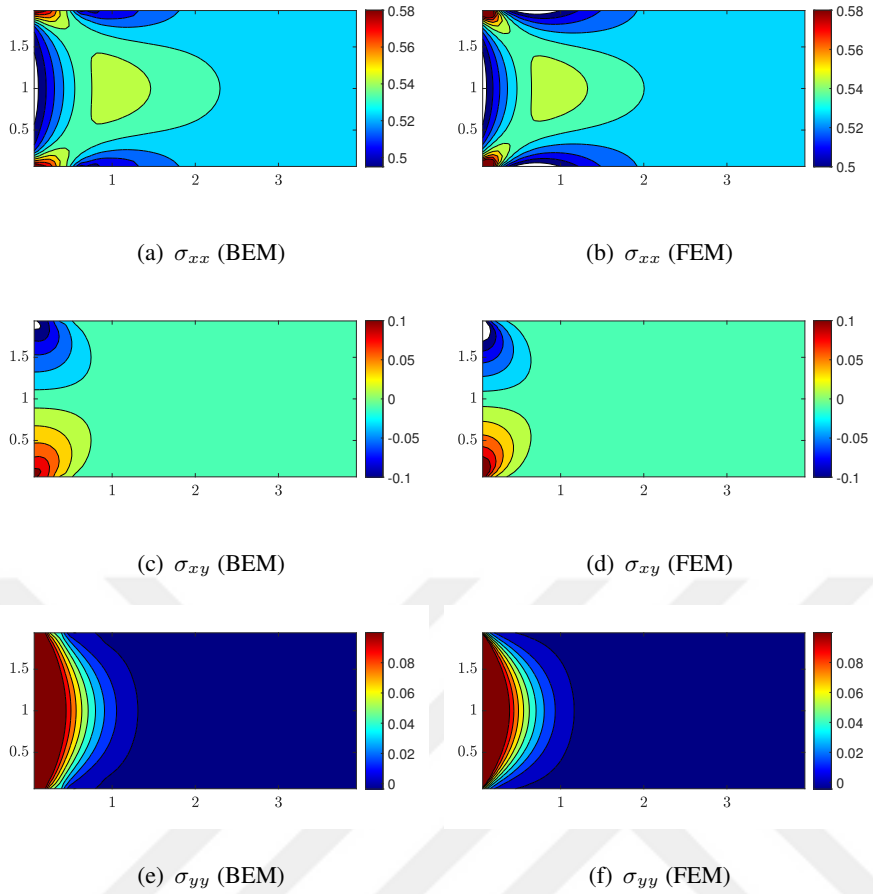


(a) Force-displacement diagram for axial loading (b) Force-time diagram for axial loading

Figure 4.9: Comparison of global (a) axial force-displacement and (b) axial force-time curves obtained by BEM and FEM for the BVP with non-uniform strain distribution

columns of Figure 4.10, respectively. The time point $t = 37$ s at which the stress contours are captured is intentionally chosen to be close to the state where the magnitude of the axial force is maximum, see Figure 4.9(b) so that the uneven distribution of the stress field within the solid body is more pronounced. To make a more objective comparison, the FEM results are exported from ANSYS®, and the contour plots are recreated consistently using the same procedure and formatting as used to craft the BEM contour plots.

Based on the comparison of stress contours, depicted in Figure 4.10, it should be noted that the accuracy of the proposed BEM formulation for viscoelastic materials is



(a) σ_{xx} (BEM)

(b) σ_{xx} (FEM)

(c) σ_{xy} (BEM)

(d) σ_{xy} (FEM)

(e) σ_{yy} (BEM)

(f) σ_{yy} (FEM)

Figure 4.10: Contours of planar stress components σ_{xx} (first row), σ_{xy} (second row), and σ_{yy} (third row) obtained by the proposed BEM (first column) and FEM (second column) analyses of the axial BVP with non-uniform strain at $t = 37$ s. All stress values are in Pascals

not limited only to the global force-displacement or force-time diagrams obtained for the overall body, as shown in Figure 4.9, but also holds for the spatial variation of the planar stress fields. Observe that the contour plots generated by the proposed BEM approach closely resemble the ones obtained through FEM. In particular, the overall spatial distribution of stress components is successfully captured by the proposed BEM. Nevertheless, a careful examination of the contour plots in Figure 4.10 indicates some minor differences near the regions of stress concentrations. Clearly, these minor differences can be eliminated by using a finer BEM mesh and a higher number of integration points locally, and possibly adaptively, refined in the regions of stress concentrations. This aspect is believed to be crucial in the efficient BEM analysis of

inelastic solids where strain localizations such as plastic shear bands occur.

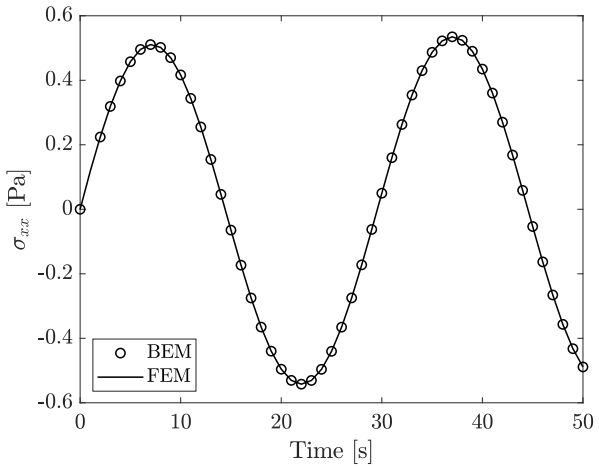


Figure 4.11: The variation of σ_{xx} at $(x{=}2, y{=}1)$ over time for axially deformed BVP

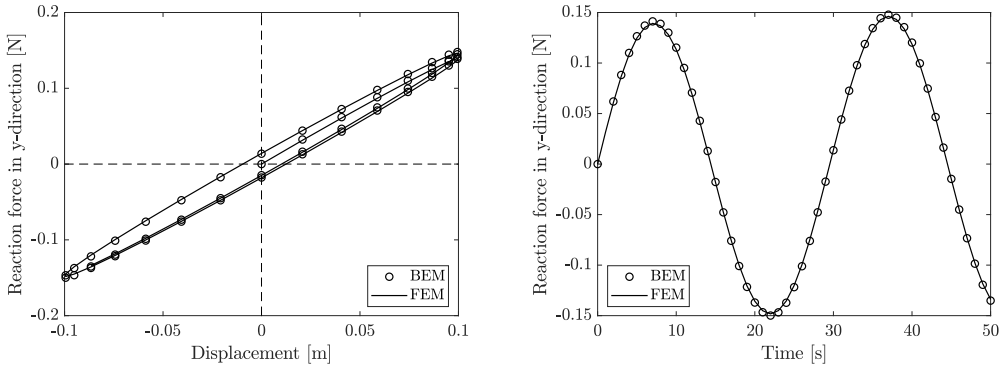
In the last quantitative comparison, given in Figure 4.11, for the axially deformed BVP, the temporal variation of the axial stress σ_{xx} at the center of the body $(x{=}2, y{=}1)$ is depicted for both FEM and BEM analyses. It should again be noted that the results obtained by the proposed BEM approach are favorably consistent with those generated by FEM.

Shear Loading

Similar to the preceding axially loaded BVP with uneven strain/stress distribution, ANSYS® is used to validate the results obtained using the proposed BEM formulation. The converged structured FEM mesh for axial loading with $64 \times 32 = 2048$ four-node quadrilateral elements with full integration is also used for the shear loading.

Analogous to the preceding BVP, the global force-displacement and force-time curves obtained through the proposed BEM approach and FEM are compared in Figures 4.12(a) and 4.12(b), respectively. It is seen that the force-displacement and force-time curves obtained using both methods agree well. Notably, akin to the axial BVP, the hysteresis in the force-displacement curve favorably reflects the intrinsically dissipative character of SLS-M that has been incorporated into the BEM framework through

the proposed non-iterative algorithmic formulation for viscoelasticity.



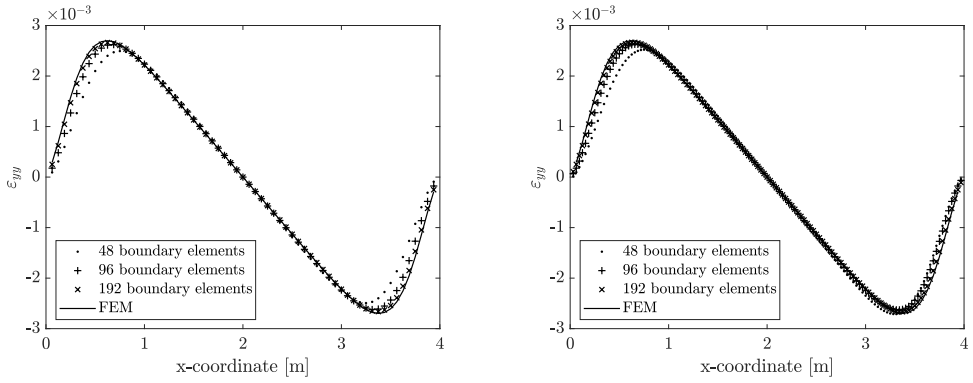
(a) Force-displacement diagram for shear loading

(b) Force-time diagram for shear loading

Figure 4.12: Comparison of global (a) shear force-displacement and (b) shear force-time curves obtained by BEM and FEM for the BVP with non-uniform strain

In order to assess the accuracy of the proposed BEM formulation with respect to the prediction of local stress/strain fields, the variation of ε_{yy} along the horizontal path situated at $y = 1.5$ m, i.e., 0.5 m below the upper horizontal edge, at $t = 7$ s is plotted in Figure 4.13. Since the selected path crosses the points close to the locations of stress/strain concentrations, see Figure 4.16, a uniform refinement in both BEM mesh and CTM integration points is conducted to evaluate the convergence behavior of the proposed BEM formulation. It is observed that the increase in the number of boundary elements, consequently the number of CTM integration points, has a greater effect on the accuracy of the solutions around the stress/strain concentrations than the number of inner data points used. Therefore, 96 boundary elements ($\triangledown$) of uniform length, along with 8192 integration points ($\bigcirc$) and 1953 inner data points ($\times$), are used to carry out the BEM analysis of the cyclic shear loading.

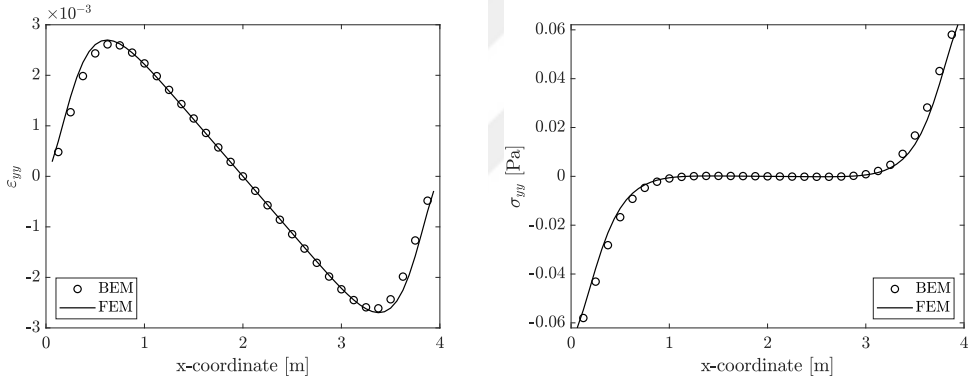
The variation of ε_{yy} and σ_{yy} along the chosen horizontal path at $t = 7$ s, close to the time when the sinusoidal loading function reaches the maximum amplitude, is depicted in Figure 4.14. Moreover, the variation of σ_{xx} along the clamped vertical left edge is given in Figures 4.15(a) and 4.15(b) at $t = 7$ s and $t = 32$ s, respectively. Similar patterns of variation are observed for both methods for selected strain and stress fields. Along the fixed boundary, a more pronounced corner effect is observed in both FEM and BEM results in Figure 4.15. Apart from the corners, the proposed



(a) 1953 inner data points (b) 8001 inner data points

Figure 4.13: Variation of ε_{yy} along the path located at $y = 1.5$ m and time $t = 7$ s for shear loading

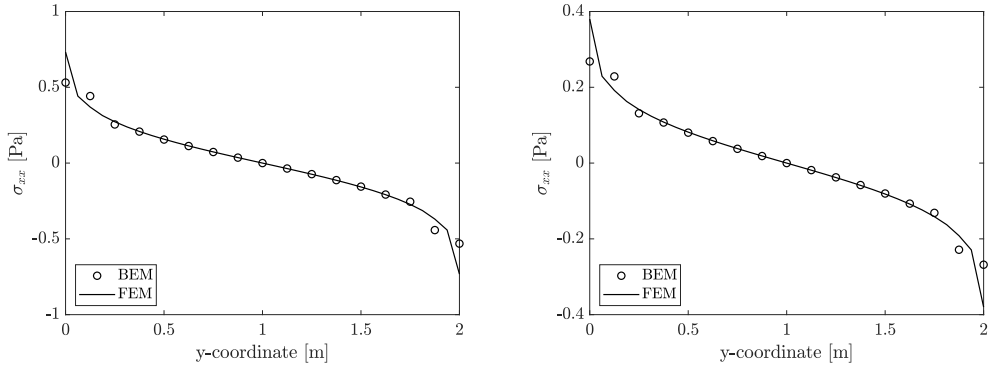
BEM formulation yields results that are consistent with that of FEM.



(a) Variation of ε_{yy} along the path at $y = 1.5$ m (b) Variation of σ_{yy} along the path at $y = 1.5$ m

Figure 4.14: Variation of (a) ε_{yy} and (b) σ_{yy} along the path located at $y = 1.5$ m and time $t = 7$ s for shear loading

A final comparison between the proposed BEM formulation and FEM is made through the contour plots of in-plane components $(\sigma_{xx}, \sigma_{xy}, \sigma_{yy})$ of the stress tensor generated for the shear loading at $t = 7$ s in the first and second columns of Figure 4.16. As explained above, the contour plots corresponding to the solutions by FEM are regenerated using the same procedure as the one used to plot the BEM results. The comparison of stress contours, depicted in Figure 4.16, indicates that the proposed BEM formulation for viscoelastic materials is capable of accurately capturing the spatial

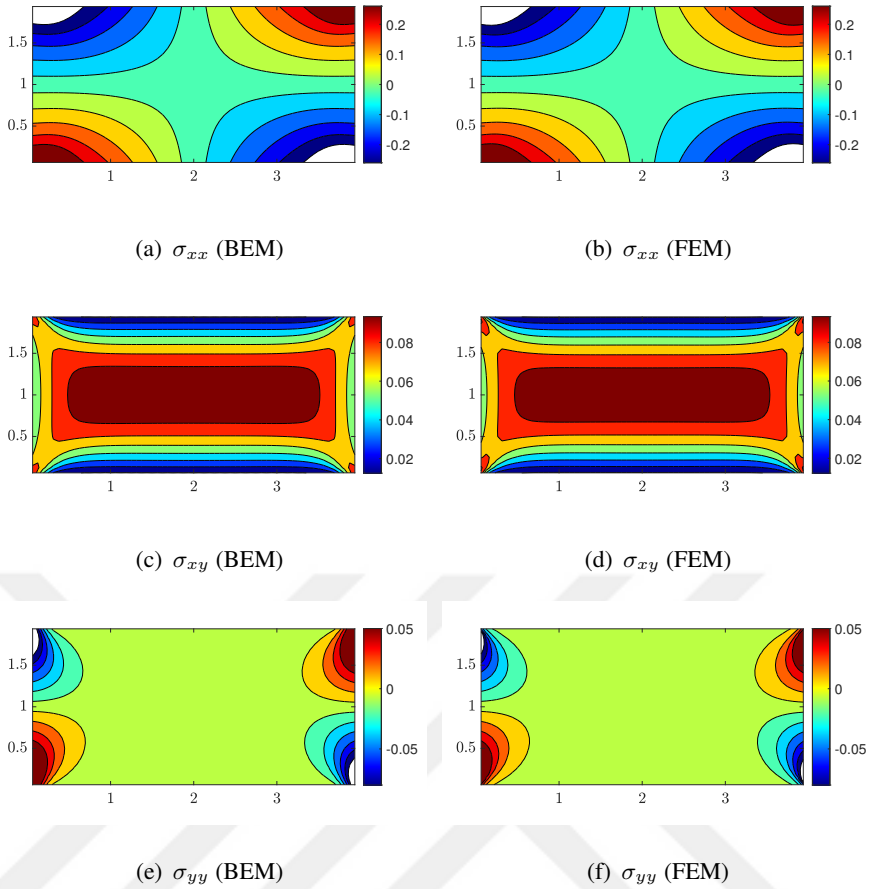


(a) Variation of σ_{xx} along the path at $x = 0$ m at $t = 7$ s

(b) Variation of σ_{xx} along the path at $x = 0$ m at $t = 32$ s

Figure 4.15: Variation of σ_{xx} along the clamped vertical left edge at (a) $t = 7$ s and (b) $t = 32$ s for shear loading

variation of the stress fields. Furthermore, it should be noted that the contour plots generated by the proposed BEM approach favorably agree with the ones obtained through FEM. Similar to the axial loading case, minor differences near the corners and edges are observed in Figure 4.16. As mentioned above, these differences can be circumvented by using a finer BEM mesh and a higher number of integration points in the regions of stress concentrations.



(a) σ_{xx} (BEM) (b) σ_{xx} (FEM)

(c) σ_{xy} (BEM) (d) σ_{xy} (FEM)

(e) σ_{yy} (BEM) (f) σ_{yy} (FEM)

Figure 4.16: Contours of planar stress components σ_{xx} (first row), σ_{xy} (second row), and σ_{yy} (third row) obtained by the proposed BEM (first column) and FEM (second column) analyses of the shear loading at $t = 7$ s. All stress values are in Pascals

4.1.3 Concluding Remarks

In Section 4.1, a novel non-iterative algorithmic formulation for generalized models of viscoelasticity within the framework of BEM in the time domain is developed. The rheological representation of viscoelasticity has been chosen to be generic enough not only for possible extension towards conventional generalized models of viscoelasticity but also for straightforward reduction to more fundamental models demonstrated in the numerical examples. The inherent challenges associated with the domain integrals have been dealt with through mesh-free CTM complemented by RPIM technique. Moreover, the semi-implicit non-iterative scheme developed for the update of internal variables has led to a robust time-stepping procedure without any oscil-

lations, even under abrupt Heaviside loadings that would otherwise be unreachable with explicit integration methods. The non-iterative feature of the suggested algorithm hinges crucially on the availability of the total strains at inner data points. This is guaranteed by the presence of the purely elastic branch that serves as an auxiliary component when such a branch is not needed in the physical model such as SLS-K.

The capabilities of the proposed BEM formulation of viscoelasticity have been assessed by means of BVPs with uniform and non-uniform strain fields, where the quantitative comparisons have been made with the analytical methods and FEM, respectively. The results generated using the proposed BEM approach for creep and relaxation experiments in the uniform-strain BVPs indicate a perfect agreement with the analytical results and the robustness of the semi-implicit integration scheme. Moreover, the BVPs with non-uniform strain field involving higher strain/stress evolution in the neighborhood of corners or edges under cyclic axial and shear loadings have also been considered. The comparisons made with FEM on the basis of global force-displacement diagrams indicate excellent agreement. When the local strain or stress fields are contrasted through the variations along a path or in the form of contour plots, some minor deviations in the regions close to the corners have been observed. It has been shown that these deviations can be overcome through a finer BEM mesh supplemented by a higher number of CTM integration points.

It is worth noting that the proposed modular framework of BEM for linear viscoelasticity has the versatility of being readily extended towards nonlinear evolution equations of viscoelasticity and rate-dependent plasticity through the concurrent linearization of evolution equations as presented in Sections 4.2 and 4.3, respectively. This extension is relatively straightforward and, more importantly, does not require major modifications in the equations of BEM. This aspect will be elaborated on in the follow-up sections.

It should be noted that the proposed approach aims to present a new non-iterative BEM formulation in the time domain where the computational cost is not considered as a primary criterion at this stage. However, regarding this aspect, BEM formulations based on the Laplace transform could be computationally more efficient than the time-domain counterparts for the *linear viscoelasticity* models presented.

4.2 Time-Domain BEM Formulation for Nonlinear Power Type Viscoelasticity

4.2.1 Theory

This section introduces the generic model of power-type viscoelasticity, including its constitutive equations in both one-dimensional (1-D) and three-dimensional (3-D) configurations. Additionally, the semi-implicit update scheme from Section 4.3.1 is expanded to handle nonlinear viscoelasticity. The application of this approach to the BEM formulation is also provided.

4.2.1.1 Generic Model of Power Type Viscoelasticity

Description of Semi-Implicit Model

The rheological model of nonlinear viscoelasticity employed in this study is composed of a spring with the bulk and shear modulus κ_0, μ_0 representing *ground elasticity* connected in parallel to a viscoelastic branch that is comprised of a nonlinear viscosity element and a fully deviatoric spring element with shear modulus μ_v in series, as depicted in Figure 4.17. We note that the generic model is capable of extending complex material models by adding new branches in parallel to the model.

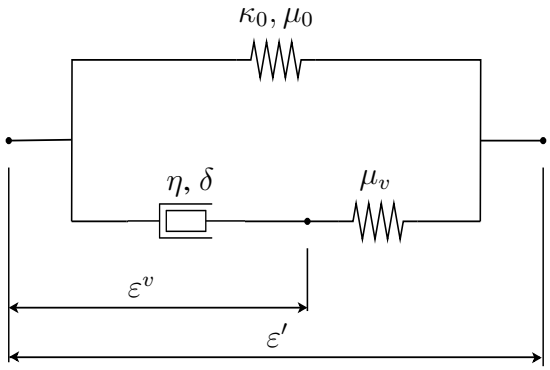


Figure 4.17: A generic rheological model of viscoplasticity

In the 3-D setting, the total stress σ can be expressed as the summation of the elastic stress $\boldsymbol{\sigma}^{\mathrm{e}}$ in the upper branch and the viscoelastic stress $\boldsymbol{\sigma}^{\mathrm{v}}$ in the lower branch, as

given below.

$$\boldsymbol{\sigma} = \boldsymbol{\sigma}^{\mathrm{e}} + \boldsymbol{\sigma}^{\mathrm{v}}. \tag{4.30}$$

The elastic stress can further be decomposed in the volumetric and deviatoric parts as follows

$$\boldsymbol{\sigma}^{\mathrm{e}} = \kappa_0 \mathrm{tr}(\boldsymbol{\varepsilon})\mathbf{1} + 2\mu_0 \boldsymbol{\varepsilon}^{'}, \tag{4.31}$$

where κ_0 and μ_0 are the bulk and shear modulus of the spring element in the upper branch and $\boldsymbol{\varepsilon}$ is the total strain. e and $\boldsymbol{\varepsilon}^{'}$ are defined as the trace and deviatoric part of the total strain, respectively. The viscoelastic stress $\boldsymbol{\sigma}^{\mathrm{v}}$ can be expressed by using the individual spring element in the viscoelastic branch and assuming a fully deviatoric viscoelastic strain

$$\boldsymbol{\sigma}^{\mathrm{v}} = 2\mu_v(\boldsymbol{\varepsilon}^{'} - \boldsymbol{\varepsilon}^{v}), \tag{4.32}$$

where μ_v is the shear modulus of the individual spring element in the viscoelastic branch. The symbol $\boldsymbol{\varepsilon}^{v}$ represents the viscoelastic strain.

The elasticity tensor C in indicial form is introduced in Equation 4.9. The evolution equation for the viscoelastic strain is given in Equation 4.33.

$$\dot{\boldsymbol{\varepsilon}}^{v} := \boldsymbol{f}(\boldsymbol{\sigma}^{v}) = \frac{1}{\eta}\frac{||\boldsymbol{\sigma}^{v}||^{\delta}}{\beta_0^{\delta}}\mathbf{n}, \text{ with } \quad \mathbf{n} := \frac{\boldsymbol{\sigma}^{v}}{||\boldsymbol{\sigma}^{v}||}. \tag{4.33}$$

In Equation 4.33, η is the viscosity parameter governing the speed of evolution of viscoelastic strain. $\boldsymbol{\sigma}^{v}$ is the viscoelastic stress tensor explained previously. $||\cdot||$ is the L2-norm operator. The power term δ governs the order of nonlinearity of the evolution equation. The parameter β_0 is a stress-like constant introduced to normalize the viscoelastic stress.

The semi-implicit model proposed in this study begins by linearizing $\dot{\boldsymbol{\varepsilon}}^{v}$ around the variables $\boldsymbol{\varepsilon}_n^{'}$ and $\boldsymbol{\varepsilon}_n^{v}$ at time step (n), as follows

$$\mathrm{Lin}\,\dot{\boldsymbol{\varepsilon}}^{v}\,|_{\boldsymbol{\varepsilon}_n^{'},\boldsymbol{\varepsilon}_n^{v}} = \dot{\boldsymbol{\varepsilon}}_n^{v} + \left(\frac{\partial \boldsymbol{f}(\boldsymbol{\sigma}^{v})}{\partial \boldsymbol{\varepsilon}^{'}}\right)_n : \Delta\boldsymbol{\varepsilon}^{'} + \left(\frac{\partial \boldsymbol{f}(\boldsymbol{\sigma}^{v})}{\partial \boldsymbol{\varepsilon}^{v}}\right)_n : \Delta\boldsymbol{\varepsilon}^{v}. \tag{4.34}$$

The fourth-order tensors in the second and third expressions between brackets "$(\cdot)$" on the right side of Equation 4.34 are referred as $\mathbb{C}_1$ and $\mathbb{C}_2$, respectively. $\Delta\boldsymbol{\varepsilon}^{'}$ and $\Delta\boldsymbol{\varepsilon}^{v}$ can further be expressed as

$$\Delta\boldsymbol{\varepsilon}^{'} = \boldsymbol{\varepsilon}_{n+1}^{'} - \boldsymbol{\varepsilon}_n^{'} \quad \text{and} \quad \Delta\boldsymbol{\varepsilon}^{v} = \boldsymbol{\varepsilon}_{n+1}^{v} - \boldsymbol{\varepsilon}_n^{v}. \tag{4.35}$$

The procedure to determine of the fourth-order tensors $\mathbb{c}_1$ and $\mathbb{c}_2$ is outlined below.

$$\begin{aligned}\mathbb{c}_1 &= \frac{\partial \boldsymbol{f}(\boldsymbol{\sigma}^v)}{\partial \boldsymbol{\sigma}^v} : \frac{\partial \boldsymbol{\sigma}^v}{\partial \boldsymbol{\varepsilon}^{'}} = \mathbb{b}_n : 2\mu_v \mathbb{I} = 2\mu_v \mathbb{b}_n \\ \mathbb{c}_2 &= \frac{\partial \boldsymbol{f}(\boldsymbol{\sigma}^v)}{\partial \boldsymbol{\sigma}^v} : \frac{\partial \boldsymbol{\sigma}^v}{\partial \boldsymbol{\varepsilon}^v} = -\mathbb{b}_n : 2\mu_v \mathbb{I} = -2\mu_v \mathbb{b}_n\end{aligned} \tag{4.36}$$

Thus, $\mathbb{b}_n$ can be expressed by taking the derivative of nonlinear function $\boldsymbol{f}(\boldsymbol{\sigma}^v)$ with respect to $\boldsymbol{\sigma}^v$ as follows

$$\mathbb{b}_n = \frac{\partial \boldsymbol{f}(\boldsymbol{\sigma}^v)}{\partial \boldsymbol{\sigma}^v} = \frac{||\boldsymbol{\sigma}_n^v||^{\delta-1}}{\eta \beta_0^\delta} \left[(\delta - 1)\mathbf{n}_n \otimes \mathbf{n}_n + \mathbb{I}\right]. \tag{4.37}$$

By introducing the newly evaluated expressions for the variables in Equation 4.34, it can be recast into

$$\begin{aligned}\text{Lin}\, \dot{\boldsymbol{\varepsilon}}^v \,|_{\boldsymbol{\varepsilon}_n^{'}, \boldsymbol{\varepsilon}_n^v} = &\left(\dot{\boldsymbol{\varepsilon}}_n^v + \mathbb{c}_1 : \boldsymbol{\varepsilon}_{n+1}^{'} - \mathbb{c}_1 : \boldsymbol{\varepsilon}_n^{'} - \mathbb{c}_2 : \boldsymbol{\varepsilon}_n^v\right) \\ &+ \mathbb{c}_2 : \boldsymbol{\varepsilon}_{n+1}^v,\end{aligned} \tag{4.38}$$

where an explicit update is used for the deviatoric part of the total strain as given in Equation 4.39.

$$\boldsymbol{\varepsilon}_{n+1}^{'} = \boldsymbol{\varepsilon}_n^{'} + \Delta t \dot{\boldsymbol{\varepsilon}}_n^{'} \tag{4.39}$$

Moreover, the first term within the brackets "$(\cdot)$" on the right side of Equation 4.38 can be represented by a single vector, denoted as

$$\dot{\bar{\boldsymbol{\varepsilon}}}_n^v = \dot{\boldsymbol{\varepsilon}}_n^v + \mathbb{c}_1 : \boldsymbol{\varepsilon}_{n+1}^{'} - \mathbb{c}_1 : \boldsymbol{\varepsilon}_n^{'} - \mathbb{c}_2 : \boldsymbol{\varepsilon}_n^v. \tag{4.40}$$

Then, the viscoelastic strain $\boldsymbol{\varepsilon}^v$ in time step $n+1$ can be evaluated by using the linearized rate of total strain evaluated in Equation 4.38.

$$\boldsymbol{\varepsilon}_{n+1}^v = \boldsymbol{\varepsilon}_n^v + \Delta t \text{Lin}\, \dot{\boldsymbol{\varepsilon}}^v = \boldsymbol{\varepsilon}_n^v + \Delta t \left[\dot{\bar{\boldsymbol{\varepsilon}}}_n^v + \mathbb{c}_2 : \boldsymbol{\varepsilon}_{n+1}^v\right]. \tag{4.41}$$

Equation 4.41 can be written as a system of equations for the determination of unknown viscoelastic strains as follows.

$$\boldsymbol{\varepsilon}_{n+1}^v = \left[\mathbb{I} - \Delta t \mathbb{c}_2\right]^{-1} : \left[\boldsymbol{\varepsilon}_n^v + \Delta t \dot{\bar{\boldsymbol{\varepsilon}}}_n^v\right] \tag{4.42}$$

The semi-implicit update law for the evolution of viscoelastic strain is summarized in Table 4.5.

Table 4.5: Algorithmic box for the semi-implicit update of the viscoelastic strain

1. Given the history variables $\{\boldsymbol{\varepsilon}_n, \dot{\boldsymbol{\varepsilon}}_n, \boldsymbol{\varepsilon}^v\}$.
2. Update the corrected strain through Equation 4.39.
3. Compute $\dot{\boldsymbol{\varepsilon}}^v_n$ at time step t_n by using Equation 4.33.
4. Evaluate $\mathbb{o}_1$, $\mathbb{o}_2$, $\mathbb{b}_n$ and $\dot{\bar{\boldsymbol{\varepsilon}}}^v_n$ by using Equations 4.36, 4.37 and 4.33.
5. Calculate the viscoelastic strain $\boldsymbol{\varepsilon}^v_{n+1}$ at time step t_{n+1} using Equation 4.42.

4.2.1.2 Boundary Element Formulation

Boundary Integral Equations

Recall the BEM equilibrium relation, given in Equation 4.17 of Section 4.1.1.1, as follows:

$$\int_\Gamma u^*_{ki} t_i d\Gamma - \int_\Omega \varepsilon^*_{kij} \left(\sigma^e_{ij} + \sigma^v_{ij}\right) d\Omega + \int_\Omega u^*_{ki} b_i d\Omega = 0\,. \tag{4.43}$$

Using relations introduced for the elastic and viscoelastic stresses in Equations 4.31 and 4.32, the integrand of the second integral in Equation 4.43 can be re-written as

$$\boldsymbol{\varepsilon}^*_{kij} \left(\sigma^e_{ij} + \sigma^v_{ij}\right) = \boldsymbol{\varepsilon}^*_{kij} \left[\kappa_0 \boldsymbol{\varepsilon}_{mm}\delta_{ij} + 2\mu_0 \boldsymbol{\varepsilon}^{'}_{ij} + 2\mu_v(\boldsymbol{\varepsilon}^{'}_{ij} - \boldsymbol{\varepsilon}^v_{ij})\right] \tag{4.44}$$

where δ is the Kronecker's delta operator. In Equation 4.44, because the lower branch is fully deviatoric, to maintain consistency with the BEM formulation, it is necessary to add and subtract $\kappa_1 \text{tr}(\boldsymbol{\varepsilon})\mathbf{1}$ from the expression within the brackets $([\cdot])$. So the equation can be recast into

$$\begin{aligned} \boldsymbol{\varepsilon}^*_{kij} \left(\sigma^e_{ij} + \sigma^v_{ij}\right) &= \boldsymbol{\varepsilon}^*_{kij} \left[(\kappa_0 + \kappa_1)\boldsymbol{\varepsilon}_{mm}\delta_{ij} + 2(\mu_0 + \mu_v)\boldsymbol{\varepsilon}^{'}_{ij}\right] \\ &\quad - \boldsymbol{\varepsilon}^*_{kij} \left[2\mu_v \boldsymbol{\varepsilon}^v_{ij} + \kappa_1 \boldsymbol{\varepsilon}_{mm}\delta_{ij}\right] \\ &= \boldsymbol{\varepsilon}^*_{kij} \mathbb{C}_{ijmn} \boldsymbol{\varepsilon}_{mn} - \boldsymbol{\varepsilon}^*_{kij} \bar{\sigma}^v_{ij}, \end{aligned} \tag{4.45}$$

with $\sigma^*_{kij} := \boldsymbol{\varepsilon}^*_{kmn} \mathbb{C}_{mnij}$ and the new field variable $\bar{\boldsymbol{\sigma}}$ is introduced as

$$\bar{\boldsymbol{\sigma}}^v := 2\mu_v \boldsymbol{\varepsilon}^v + \kappa_1 \text{tr}(\boldsymbol{\varepsilon})\mathbf{1}, \tag{4.46}$$

where the update scheme given in Table 4.5 is used to calculate the current value of the viscoelastic strain tensor ε^v_{ij}. Insertion of Equation 4.45 into Equation 4.43 yields

the following representation

$$\int_{\Gamma} u_{ki}^{*} t_i d\Gamma - \int_{\Omega} \sigma_{kij}^{*} \varepsilon_{ij} d\Omega + \int_{\Omega} \varepsilon_{kij}^{*} \bar{\sigma}_{ij}^{v} d\Omega + \int_{\Omega} u_{ki}^{*} b_i d\Omega = 0\,. \tag{4.47}$$

Following [71, 33, 35], the second integral expression in Equation 4.47 can be reduced to a boundary integral to recast Equation 4.47 into

$$C_{ki} u_i + \int_{\Gamma} t_{ki}^{*} u_i d\Gamma = \int_{\Gamma} u_{ki}^{*} t_i d\Gamma + \int_{\Omega} \varepsilon_{kij}^{*} \bar{\sigma}_{ij}^{v} d\Omega + \int_{\Omega} u_{ki}^{*} b_i d\Omega\,, \tag{4.48}$$

where term t_{ki}^{*} stands for the Kelvin's traction solution. Mantic [39] discusses in detail the way to calculate the matrix C_{ki}. The Cartesian Transformation Method, a completely mesh-free technique, is employed in this work to assess domain integrals. For the assessment of domain integrals in the literature [63, 64, 129], the Cartesian Transformation Method (CTM) has been utilized in conjunction with BEM. A boundary integral covering the problem domain's perimeter and a 1-D integral modeling the inside domain are created from the domain integral. In order to interpolate the values of integrands at the required places using a finite number of dispersed data in the problem domain, the Radial Point Interpolation Method (RPIM) [10] is introduced. Using the approach outlined by Akay et al. [129] and Section 4.1.1.2, the domain integrals are computed.

Numerical Discretization and Post-processing

This sub-section follows completely the expressions used for the linear viscoelasticity in Section 4.1.1.2. The same formulation and methodology can be repeated for nonlinear viscoelasticity. To summarize, the procedure for computing the field variables at the time step t_{n+1} is presented in Table 4.6.

4.2.2 Numerical Example

This section examines the effectiveness of the suggested semi-implicit power-type viscoelasticity model implemented in BEM through two different Boundary Value Problems (BVPs). The BVPs are investigated using the generic model of power-type viscoelasticity. In Section 4.2.2.1, a perforated plate geometry under uniaxial sinusoidal displacement loading is studied. The effects of the power term (δ) of the

Table 4.6: Algorithmic box

1. Given the history variables $\{(\varepsilon_{ij})_n, (\dot{\varepsilon}_{ij})_n, (\varepsilon^v_{ij})_n\}$

2. Update the total strain through Equation 4.35.

3. Compute $(\varepsilon^v_{ij})_{n+1}$ at time step t_{n+1} by using the semi-implicit update methodology in Table 4.5.

4. Calculate the field variable $(\bar{\sigma}^v_{ij})_{n+1}$ by using Equation 4.46.

5. Solve the BEM equation given in Equation 4.22 for the current time step t_{n+1}.

6. Apply the displacement field found in Step 5 to a BEM problem considering only the upper branch presented in Figure 4.17. Again, use Equation 4.22 for the solution by setting $\bar{\sigma}^v_{ij} = 0$.

7. Calculate the total strain $(\varepsilon_{ij})_{n+1}$ by using Equation 4.25 and update the strain rate $(\dot{\varepsilon}_{ij})_{n+1}$.

8. Calculate the stresses at the upper and lower branches by using Equations 4.31 and 4.32, respectively.

power-type viscoelasticity and the period of sinusoidal loading are investigated. In Section 4.2.2.2, four types of radial inward loading on a flange geometry are analyzed. The investigated loadings can be summarized as one relaxation and three sinusoidal-type loadings.

4.2.2.1 Model Problem 1: The Perforated Plate

The numerical model's geometry, dimensions, and boundary conditions are shown in Figure 4.18. For the purpose of 2-D modeling, the plane strain conditions are used. The rheological model used for the representation of viscoelasticity is given in Figure 4.17. The nonlinear viscoelasticity model parameters used in the analyses of perforated plate are given in Table 4.7.

The perforated plate is subjected to a cyclic axial-type loading through the prescribed

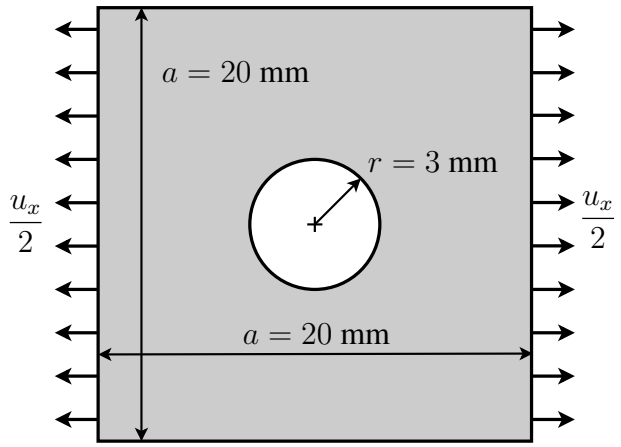


Figure 4.18: The square body subjected to displacement type sinusoidal loading

Table 4.7: Model parameters used for plasticity with hardening

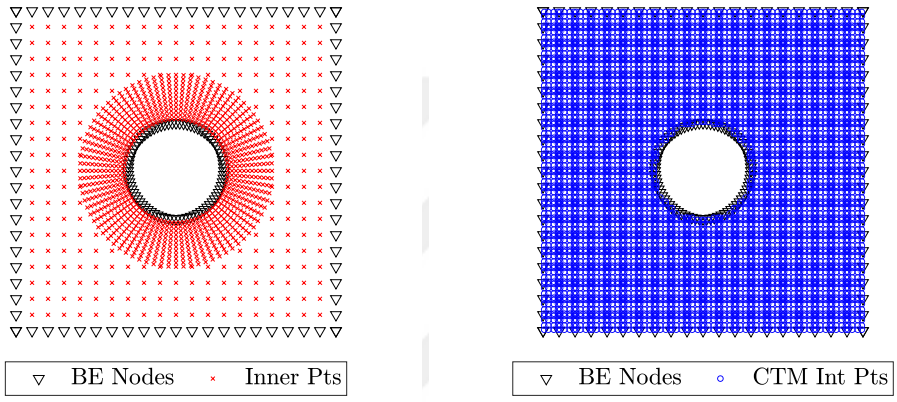
κ_0 [GPa]	μ_0 [MPa]	κ_v [MPa]	μ_v [MPa]	η [s]	β_0 [MPa]
660	100	3300	500	2×10^6	0.2

displacements $\frac{u_x(t)}{2}$ on its left and right edges, as shown in Figure 4.18. The specific sinusoidal function used to define the axial loading function $u_x(t)$ is given in Table 4.8. Note that different loading periods (T) are investigated. Additionally, to avoid rigid body displacement, only the nodes positioned at the midpoints of the left and right boundaries are also constrained in the y-direction. A new parameter (np), which governs the time-step (Δt) to be used in simulations, is introduced. It is defined as the number of steps to reach the period T. The convergence study for the parameter np and mesh is presented in Appendix F.

Table 4.8: Specific sinusoidal functions of the axial $u_x(t)$ loading along with the accompanying boundary conditions in the perpendicular directions applied on the left and right edges

Axial	$u_x(t) = 0.2\sin(2\pi\, t/T)$ mm, $\quad t_y(t) = 0$

The special discretization scheme used in the model is illustrated in Figure 4.19. Both the outer and hole boundaries are modeled using 80 linear boundary elements. The boundary nodes are highlighted with downward triangles ($\triangledown$). The Cartesian Transformation Method (CTM) uses 5956 integration points, which are represented by blue circles ($\bigcirc$). Moreover, 1208 data points, denoted by red crosses ($\times$), are inspected during the post-processing analysis. In the FEM analysis, due to both the horizontal and vertical symmetry, a quarter model for the perforated plate is used. 4800 quadrilateral elements are used for the discretization of the quarter perforated plate domain for the FEM analyses.

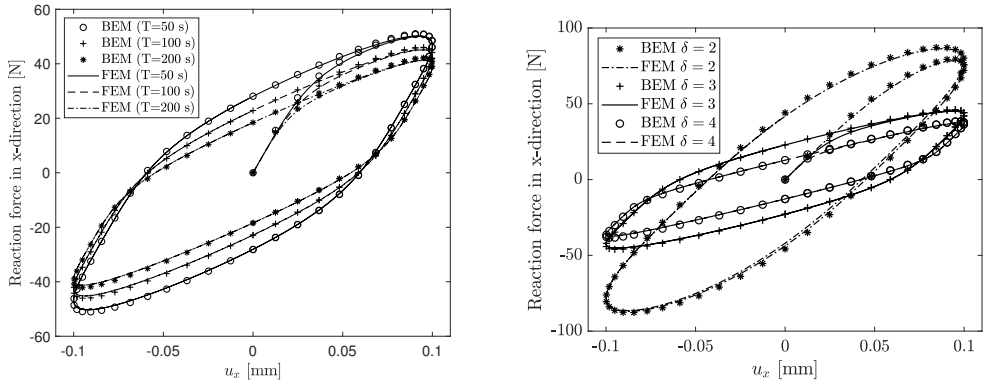


(a) Inner data points (b) CTM integration points

Figure 4.19: Boundary element mesh with inner points used for interpolation and CTM integration points

First, we compare the total force-displacement curve produced by the suggested BEM approach and FEM solution, respectively, in Figure 4.20. For the sinusoidal loading, three distinct periods (50 s, 100 s, and 200 s) are examined in Figure 4.20(a) by setting the np parameter to 10^3 for both BEM and FEM and the power term δ used for the evolution of viscoelastic strain to 3. In Figure 4.20(b), the effect of δ is presented for sinusoidal loading with a period of 100 s and the same np parameter set introduced previously. The BEM outcomes are presented as discrete points (asterisks, circles) at specific intervals of data points to provide a clearer visualization. It is noted that there is no apparent difference between the force-displacement curves produced by BEM and FEM. The hysteric nature of the force-displacement curve further demonstrates

that the suggested non-iterative algorithmic BEM formulation for viscoelasticity has successfully captured the dissipative nature of viscoelasticity. Furthermore, a greater δ value results in softer and less-dissipative response.



(a) Force-displacement diagram for different sinusoidal periods

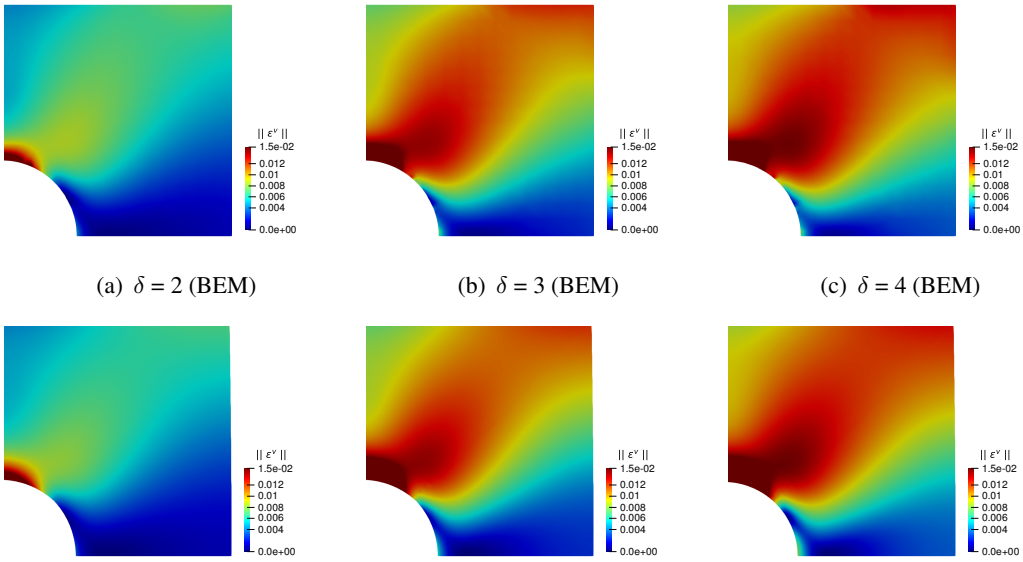
(b) Force-displacement diagram for different power terms (δ)

Figure 4.20: Comparison of global reaction force-displacement curves obtained by BEM and FEM for the perforated plate model

The contour plots of the norm of viscoelastic strain for three different power terms (δ) at the instant when the applied displacement reaches its maximum are given in Figure 4.21. As FEM utilizes a very fine mesh compared to BEM, a BEM analysis with a finer mesh is performed to achieve contours in similar resolution. Remarkable consistency is observed between the contour plots generated by the FEM and BEM approaches. As expected, the increase in δ leads to higher viscoelastic strains evolving in the material.

4.2.2.2 Model Problem 2: The Flange

Figure 4.22 depicts the geometry, dimensions, and boundary conditions of the next model problem. The model represents the quarter shape of a well-known mechanical element called the flange. To ensure symmetry in the quarter model, the displacements of the bottom and right edges are constrained to move in normal directions to the edges. The plane strain assumption is employed for the purpose of 2-D modeling. The rheological model given in Figure 4.17 is utilized in the analysis. The nonlinear



(a) δ = 2 (BEM) (b) δ = 3 (BEM) (c) δ = 4 (BEM)

(d) δ = 2 (FEM) (e) δ = 3 (FEM) (f) δ = 4 (FEM)

Figure 4.21: Contours of the norm of viscoelastic strain for different δ values of 2, 3, and 4 are shown in three columns obtained by the proposed BEM (first row) and FEM (second row) analyses of the perforated plate problem at the time when the maximum loading is reached.

viscoelasticity model parameters given in Table 4.7 are used in the analyses of flange.

The flange is subjected to a radial-type loading, with the prescribed displacements $u_r(t)$ applied at the inner circular edge in the radial inward direction. The radial loading function $u_r(t)$ is defined using three specific sinusoidal functions and one relaxation type loading, as given in Table 4.9. The first loading type, L1, is a relaxation-type loading, while the remaining loadings are sinusoidal in nature. The angle α in L3 and L4 is defined as the angle between the line connecting the nodal point on the inner surface of the flange to the origin and the horizontal x-axis. In both FEM and BEM analyses for sinusoidal loadings, the np parameter, which is discussed in Section 4.2.2.1, is set to 1000. The time step for the relaxation type L1 loading is set to 10^{-3} s, and the initial maximum load is reached in 10 substeps in both FEM and BEM analyses.

The spatial discretization scheme employed in the BEM model is depicted in Fig-

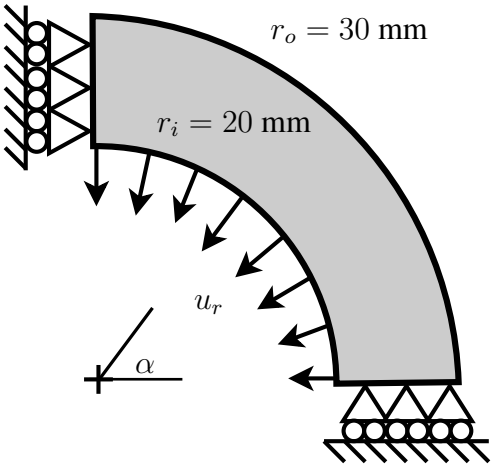


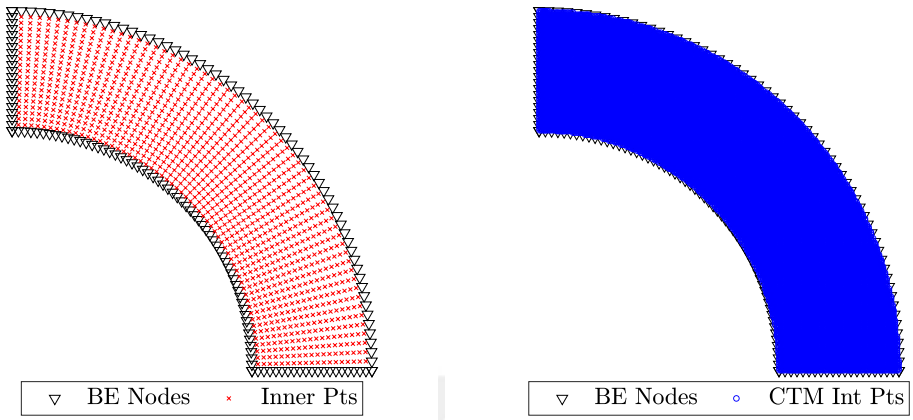
Figure 4.22: The flange body subjected to displacement type sinusoidal loading applied in radial direction

Table 4.9: Four different loadings investigated for the flange problem

Loading	$u_r(t)$
L1	$0.2\, r_i$
L2	$0.2\, r_i \sin(2\pi \frac{t}{T})$
L3	$(1+\alpha)\ 0.2\, r_i \sin(2\pi \frac{t}{T})$
L4	$\left[1+3\left(\cos(\alpha-\frac{\pi}{4})-\cos(\frac{\pi}{4})\right)\right]\ 0.2\, r_i \sin(2\pi \frac{t}{T})$

ure 4.23, where the boundary is represented using 160 linear boundary elements by dividing each the outer square and circular domains into 80 elements. The boundary nodes are denoted by downward triangles ($\triangledown$). The Cartesian Transformation Method (CTM) employs 25119 integration points, represented by blue circles ($\bigcirc$). Subsequently, 1121 data points, indicated by red crosses ($\times$), are examined during

the post-processing analysis. In the FEM analysis, a convergence study revealed that discretizing the radial and circumferential directions into 30 and 120 elements, respectively, is sufficient.



(a) Inner data points (b) CTM integration points

Figure 4.23: Boundary element mesh with inner points used for interpolation and CTM integration points

In Figure 4.24(a), the change in the reaction force with respect to time is presented for the L1 loading. The maximum reaction forces evaluated by FEM and BEM are recorded as 101 N and 109 N, respectively. This difference can be explained by the non-iterative nature of the developed approach. Nevertheless, the relaxation behavior of the BEM solution is in perfect agreement with the iterative FEM solution.

In Figure 4.24(b), the change in the reaction force with respect to the applied displacement at the bottom left corner is presented for the L2 loading. The capital letters "B" and "L" used in the legend of the figure represent the reaction forces on the bottom and left edges, respectively. Both reaction forces are shown in the same figure. As the L2 loading is applied symmetrically through the inner boundary of the flange, the reaction forces obtained on both edges are identical. The agreement between the FEM and BEM results is remarkable.

Figure 4.24(c) illustrates the variation of reaction force on the bottom and left edges in response to the applied radial displacement at the bottom left corner for the L3

loading case. The legend of the figure employs capital letters "B" and "L" to denote the reaction forces on the bottom and left edges, respectively. Both reaction forces are presented in a single figure. Due to the asymmetry of the applied radial displacement on the inner boundary of the flange, the left boundary exhibits higher reaction forces compared to the bottom boundary. Moreover, the global viscoelastic responses obtained by FEM and BEM match perfectly.

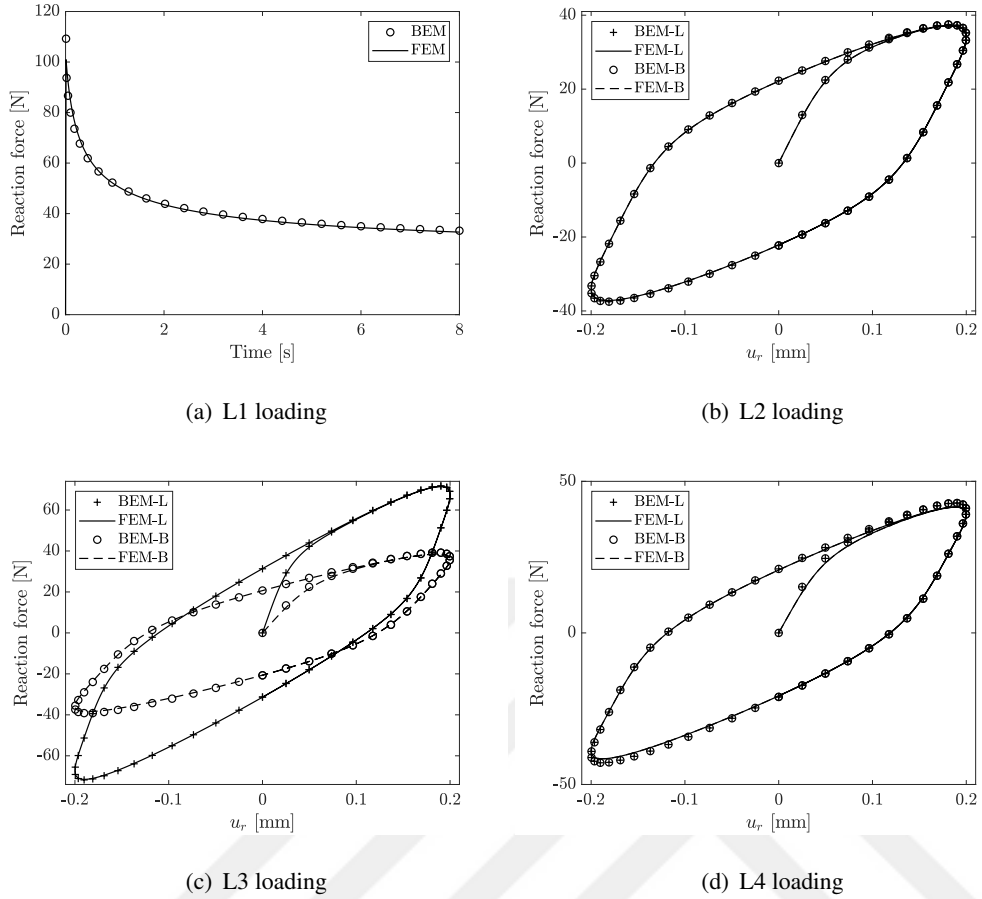
Figure 4.24(d) demonstrates the change in reaction force on the bottom and left edges when a radial displacement is applied at the bottom left corner for the L4 loading case. In the figure's legend, the capital letters "B" and "L" are used to represent the reaction forces on the bottom and left edges respectively. The prescribed radial displacement reaches the maximum at the nodes located at 45^o angle in the inner radial surface. The same reaction forces are recorded for the left and bottom edges due to the symmetry. Consistency between the FEM and BEM solutions is excellent.

Finally, in Figure 4.25, the contour plots of the norm of the viscoelastic strain for loadings L2, L3, and L4 are presented when the applied displacement reaches its maximum at 25 seconds. Since the loading L2 is constant through the circumferential direction, a uniform contour is observed in the circumferential direction. For the L3 loading case, the maximum applied displacement is at the corner of the inner and left edges, where the maximum value for the norm of viscoelastic strain is observed. The applied loading for the L4 case is minimum at two corners and reaches its maximum at a 45^o angle on the inner radial surface. Among all the contour plots, the FEM and BEM results match perfectly.

4.2.3 Concluding Remarks

In this subsection, an extension of the non-iterative algorithmic formulation of linear viscoelasticity to nonlinear power-type of viscoelasticity is presented. The domain integrals are solved using the mesh-free CTM complemented by RPIM technique. The purely elastic branch is employed for post-processing to evaluate the total strain in the model.

The performance of the proposed BEM formulation is demonstrated through the anal-



(a) L1 loading

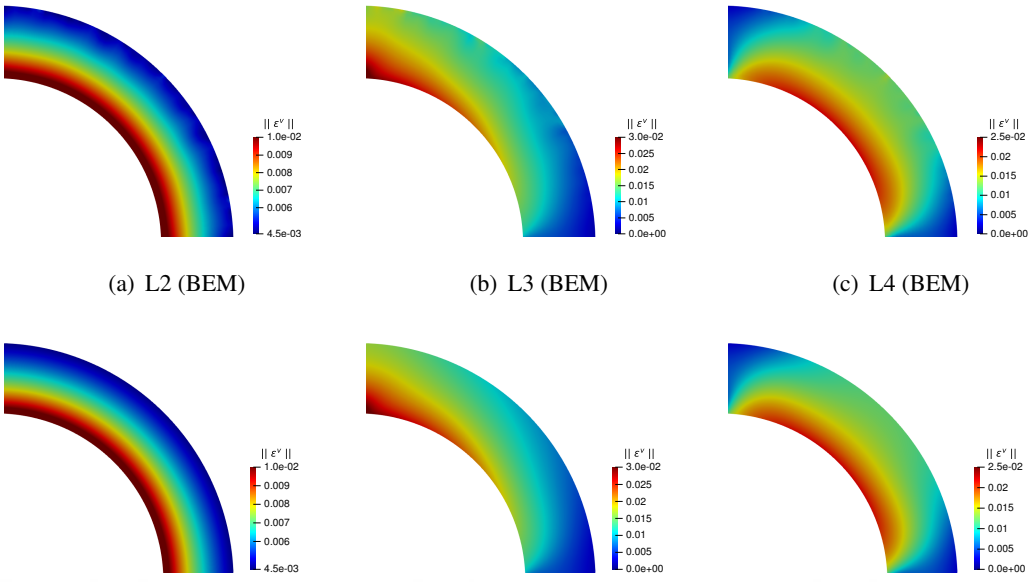
(b) L2 loading

(c) L3 loading

(d) L4 loading

Figure 4.24: Change in the reaction force with respect to the applied displacement at the node located on the bottom left corner for the investigated loadings

ysis of two widely used engineering components: the perforated plate and the flange. A comparative study is conducted with the Finite Element Method (FEM), where a fully implicit viscoelasticity model is employed. For the perforated plate model, a uniaxial sinusoidal loading is considered, and the effects of the sinusoidal loading period and the different power terms for evaluating the viscoelastic strain are investigated. For the flange model, four different radial loadings are analyzed, including three sinusoidal loadings and a relaxation-type loading applied to the inner radial surface of the flange. The global force-displacement results, as well as the contour plots obtained with the BEM approach, exhibit good agreement with the FEM results for both models. It is worth noting that as the proposed method is a semi-implicit approach, the time step affects the solution accuracy.



(a) L2 (BEM) (b) L3 (BEM) (c) L4 (BEM)

(d) L2 (FEM) (e) L3 (FEM) (f) L4 (FEM)

Figure 4.25: Contours of norm of viscoelastic strain for loadings L2 (first column), L3 (second column), and L4 (third column) obtained by the proposed BEM (first row) and FEM (second row) analyses of the flange problem at $t = 25$ s

4.3 Time-Domain BEM Formulation for nonlinear Power Type Viscoplasticity

4.3.1 Theory

In this section, the generic model of viscoplasticity is introduced, along with its constitutive equations in three-dimensional (3-D) settings. A semi-implicit integration scheme is presented for the temporal update of strain-like internal variables, including plastic strains and plastic arc length. The adoption of the viscoplasticity model to the BEM is discussed, elucidating the incorporation of the algorithmic update scheme into the BEM formulation. Furthermore, the section provides the details of a parameter identification study to determine the material parameters of the viscoplasticity model. The developed approach is verified with a BVP with a uniform strain field. Finally, in the concluding remarks, the limitations of the model are discussed.

4.3.1.1 Generic Model of Power Type Viscoplasticity

Description of Semi-Implicit Model

The viscoplasticity model utilized in this study resembles linear viscoelasticity, featuring a combination of elements. It comprises a spring with the modulus E_e, representing "ground elasticity," connected in parallel to a viscoplastic branch. This viscoplastic branch consists of an element comprising plasticity and a spring with modulus E_1 in parallel, with the entire combination connected in series to another spring with modulus E_v. The schematic representation of this rheological model is depicted in Figure 4.26.

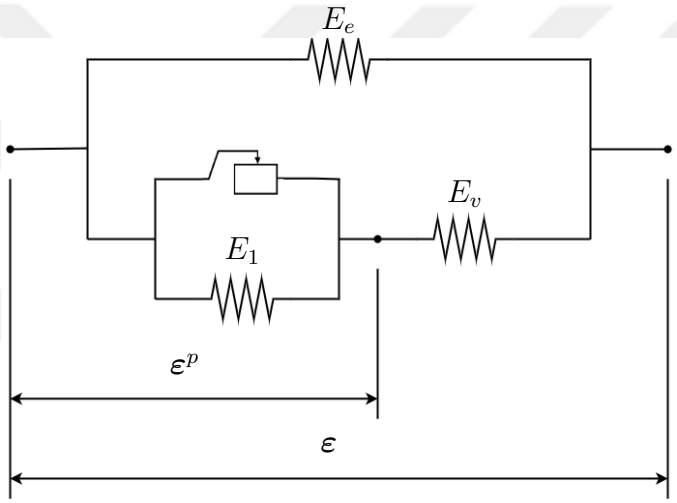


Figure 4.26: A generic rheological model of viscoplasticity

In the 3-D setting, the total stress $\boldsymbol{\sigma}$ can be expressed as the summation of the elastic stress $\boldsymbol{\sigma}^{\mathrm{e}}$ in the upper branch and the viscoplastic stress $\boldsymbol{\sigma}^{\mathrm{vp}}$ in the lower branch, as given below.

$$\boldsymbol{\sigma} = \boldsymbol{\sigma}^{\mathrm{e}} + \boldsymbol{\sigma}^{\mathrm{vp}} \tag{4.49}$$

The elastic stress can further be expressed as follows

$$\boldsymbol{\sigma}^{\mathrm{e}} = E_e \tilde{\mathbf{C}} \boldsymbol{\varepsilon}, \tag{4.50}$$

where E_e is Young's modulus of the spring element in the upper branch and $\boldsymbol{\varepsilon}$ is the total strain. The viscoplastic stress $\boldsymbol{\sigma}^{\mathrm{vp}}$ can be expressed by using the individual

spring element in the viscoplastic branch and assuming a fully deviatoric plastic strain as given in Equation 4.51

$$\begin{aligned}\boldsymbol{\sigma}^{\text{vp}} &= \kappa_v e\mathbf{1} + 2\mu_v(\boldsymbol{\varepsilon}^{'} - \boldsymbol{\varepsilon}^p) \\ &= E_v\tilde{\mathbf{C}}\boldsymbol{\varepsilon} - 2\mu_v\boldsymbol{\varepsilon}^p,\end{aligned} \tag{4.51}$$

where κ_v and μ_v are the bulk and shear moduli of the individual spring element in the viscoplastic branch, respectively. e, $\boldsymbol{\varepsilon}^{'}$, and $\boldsymbol{\varepsilon}^p$ are defined as the trace, the deviatoric part of the total strain, and the plastic strain, respectively. The non-dimensional material tensor $\tilde{\mathbf{C}}$ is introduced in Equation 4.10.

The kinematic variables $\boldsymbol{\varepsilon}$ and $\boldsymbol{\varepsilon}^p$ are defined as the total strain and the plastic strain, respectively. The evolution equation for the plastic strain reads.

$$\dot{\boldsymbol{\varepsilon}}^p := \dot{\varepsilon}^0 \frac{||\boldsymbol{\sigma}^{'}||^{m_1}}{\hat{\sigma}_0^{m_1}(\alpha)}\mathbf{n}, \text{ with } \quad \mathbf{n} := \frac{\boldsymbol{\sigma}^{'}}{||\boldsymbol{\sigma}^{'}||}. \tag{4.52}$$

In Equation 4.52, $\dot{\varepsilon}^0$ is the material parameter governing the speed of plastic flow. $\boldsymbol{\sigma}^{'}$ is the deviatoric part of the viscoplastic stress tensor $\boldsymbol{\sigma}^{\text{vp}}$, and $||\cdot||$ denotes the norm. The power term m_1 governs the order of nonlinearity of the evolution equation. The function of the yield surface $\hat{\sigma}_0(\alpha)$ can be expressed as

$$\hat{\sigma}_0(\alpha) := Y\left(1 + \frac{\alpha}{\varepsilon^0}\right)^{1/m_2}, \text{ with } \quad \dot{\alpha} = ||\dot{\boldsymbol{\varepsilon}}^p||, \tag{4.53}$$

where Y is the initial yield strength, α is the plastic arc length, and m_2 controls the saturation behavior of hardening.

The semi-implicit model, proposed in this study, starts with the linearization of $\dot{\boldsymbol{\varepsilon}}^p$ around $\boldsymbol{\sigma}_n^{'}$ and σ_{0n} as follows

$$\begin{aligned}\text{Lin}\,\dot{\boldsymbol{\varepsilon}}^p\,|_{\boldsymbol{\sigma}_n^{'},\sigma_{0n}} &= \dot{\boldsymbol{\varepsilon}}_n^p + \left(\dot{\varepsilon}^0 m_1 \frac{||\boldsymbol{\sigma}^{'}||^{m_1-1}}{\hat{\sigma}_0^{m_1}(\alpha)}\mathbf{n}\otimes\mathbf{n}\right) : \Delta\boldsymbol{\sigma}^{'} \\ &- \left(m_1\dot{\varepsilon}^0 \frac{||\boldsymbol{\sigma}^{'}||^{m_1}}{\hat{\sigma}_0^{m_1+1}(\alpha)}\mathbf{n}\right)\Delta\hat{\sigma}_0.\end{aligned} \tag{4.54}$$

The second and third expressions between brackets "$(\cdot)$" on the right side of Equation 4.54 are hereafter referred with $\mathbb{A}$ and $\mathbf{A}$ matrices, respectively. Their definitions are given as

$$\begin{aligned}\mathbb{A} &= \dot{\varepsilon}^0 m_1 \frac{||\boldsymbol{\sigma}^{'}||^{m_1-1}}{\hat{\sigma}_0^{m_1}(\alpha)}\mathbf{n}\otimes\mathbf{n} \\ \mathbf{A} &= m_1\dot{\varepsilon}^0 \frac{||\boldsymbol{\sigma}^{'}||^{m_1}}{\hat{\sigma}_0^{m_1+1}(\alpha)}\mathbf{n}.\end{aligned} \tag{4.55}$$

$\Delta\boldsymbol{\sigma}^{'}$ and $\Delta\sigma_0$ in Equation 4.54 can further be expressed as

$$\begin{aligned}\Delta\boldsymbol{\sigma}^{'} &= 2\mu(\tilde{\boldsymbol{\varepsilon}} - \boldsymbol{\varepsilon}_n^{'} - \boldsymbol{\varepsilon}^p + \boldsymbol{\varepsilon}_n^p), \text{with} \quad \tilde{\boldsymbol{\varepsilon}} = \boldsymbol{\varepsilon}_n + \Delta t\dot{\boldsymbol{\varepsilon}}_n \\ \Delta\hat{\sigma}_0 &= \hat{h}_n(\alpha - \alpha_n), \text{with} \quad \hat{h}_n = \frac{d\hat{\sigma}_0(\alpha)}{d\alpha}\Big|_{\alpha_n},\end{aligned} \tag{4.56}$$

where $\tilde{\boldsymbol{\varepsilon}}$ is called the corrected strain, which is evaluated by the explicit update of the total strain. Insertion of Equation 4.56 into Equation 4.54 gives

$$\text{Lin}\,\dot{\boldsymbol{\varepsilon}}^p\,|_{\boldsymbol{\sigma}_n^{'},\sigma_{0n}} = \mathbf{B}_n - \mathbb{A}_n : 2\mu\boldsymbol{\varepsilon}^p + \mathbf{A}_n\hat{h}_n\alpha, \tag{4.57}$$

where $\mathbf{B}_n = \dot{\boldsymbol{\varepsilon}}_n^p + \mathbb{A}_n : 2\mu(\tilde{\boldsymbol{\varepsilon}}^{'} - \boldsymbol{\varepsilon}_n^{'} + \boldsymbol{\varepsilon}_n^p) - \mathbf{A}_n\hat{h}_n\alpha_n$.

To update $\boldsymbol{\varepsilon}^p$ to time step $n+1$ by using Equation 4.57, α at the regarding time step should be determined. For this purpose, $\dot{\alpha}$ is linearized around $\dot{\boldsymbol{\varepsilon}}_n^p$ as follows

$$\begin{aligned}\text{Lin}\,\dot{\alpha}\,|_{\dot{\boldsymbol{\varepsilon}}_n^p} &= \dot{\alpha}_n + \underbrace{\left[\frac{\dot{\boldsymbol{\varepsilon}}^p}{||\dot{\boldsymbol{\varepsilon}}^p||}\right]_{\dot{\boldsymbol{\varepsilon}}_n^p}}_{\mathbf{D}_n} : (\dot{\boldsymbol{\varepsilon}}^p - \dot{\boldsymbol{\varepsilon}}_n^p) \\ &= \dot{\alpha}_n + \mathbf{D}_n : \left[\frac{1}{\Delta t}(\boldsymbol{\varepsilon}^p - \boldsymbol{\varepsilon}_n^p) - \dot{\boldsymbol{\varepsilon}}_n^p\right].\end{aligned} \tag{4.58}$$

By using Equation 4.58, α can be updated to time step $n+1$ as

$$\begin{aligned}\alpha &= \alpha_n + \Delta t\text{Lin}\,\dot{\alpha} \\ &= \alpha_n + \Delta t\dot{\alpha}_n - \Delta t\mathbf{D}_n : \dot{\boldsymbol{\varepsilon}}_n^p - \mathbf{D}_n : \boldsymbol{\varepsilon}_n^p + \mathbf{D}_n : \boldsymbol{\varepsilon}^p \\ &= \tilde{\alpha}_n + \mathbf{D}_n : \boldsymbol{\varepsilon}^p,\end{aligned} \tag{4.59}$$

where $\tilde{\alpha}_n$ is defined as the term including the values from the previous step in Equation 4.59. Then, the plastic strain $\boldsymbol{\varepsilon}^p$ in time step $n+1$ can be evaluated by using Equation 4.54.

$$\begin{aligned}\boldsymbol{\varepsilon}^p &= \boldsymbol{\varepsilon}_n^p + \Delta t \text{Lin}\, \dot{\boldsymbol{\varepsilon}}^p \\ &= \boldsymbol{\varepsilon}_n^p + \Delta t \left[\mathbf{B}_n - 2\mu \mathbb{A}_n : \boldsymbol{\varepsilon}^p + \mathbf{A}_n \hat{h}_n \alpha\right].\end{aligned} \tag{4.60}$$

Finally, insertion of Equation 4.59 in Equation 4.60 and doing the simplifications, the plastic strain $\boldsymbol{\varepsilon}^p$ in the next time step can be expressed by

$$\boldsymbol{\varepsilon}^p = \mathbb{E}_n^{-1} : \mathbf{F}_n, \tag{4.61}$$

where

$$\begin{aligned}\mathbb{E} &= \mathbb{I} + 2\mu\Delta t \mathbb{A}_n - \Delta t \hat{h}_n \mathbf{A}_n \otimes \mathbf{D}_n \\ \mathbf{F}_n &= \boldsymbol{\varepsilon}_n^p + \Delta \left[\mathbf{B}_n + \hat{h}_n \mathbf{A}_n \tilde{\alpha}_n\right].\end{aligned} \tag{4.62}$$

The constitutive law for the evolution of plastic strain is summarized in Table 4.10.

Table 4.10: Algorithmic box for constitutive law

1. Given the history variables $\{\boldsymbol{\varepsilon}_n, \dot{\boldsymbol{\varepsilon}}_n,, \boldsymbol{\varepsilon}_n^p, \alpha_n, \dot{\alpha}_n\}$.
2. Update the corrected strain $\tilde{\boldsymbol{\varepsilon}}$ through Equation 4.56.
3. Compute $\dot{\boldsymbol{\varepsilon}}_n^p$ and $\dot{\alpha}_n$ at time step t_n by using Equation 4.52 and Equation 4.53.
4. Evaluate $\mathbf{A}_n$, $\mathbb{A}_n$, $\hat{h}_n$, $\mathbf{B}_n$ and $\mathbf{D}_n$
5. Update the plastic flow α at time step t_{n+1} through Equation 4.59.
6. Calculate the plastic strain $\boldsymbol{\varepsilon}^p$ at time step t_{n+1} using Equation 4.61.

4.3.1.2 Boundary Element Formulation

Boundary Integral Equations

Recall the BEM equilibrium relation, given in Equation 4.17 of Section 4.1.1.1, adopted for viscoplasticity as follows:

$$\int_{\Gamma} u^*_{ki} t_i d\Gamma - \int_{\Omega} \varepsilon^*_{kij} \left(\sigma^e_{ij} + \sigma^{vp}_{ij}\right) d\Omega + \int_{\Omega} u^*_{ki} b_i d\Omega = 0\,. \tag{4.63}$$

Using relations introduced for the elastic and viscoplastic stresses in Equation 4.50 and Equation 4.51, the integrand of the second integral in Equation 4.63 can be re-written as

$$\begin{aligned} \varepsilon^*_{kij} \left(\sigma^e_{ij} + \sigma^{vp}_{ij}\right) &= \varepsilon^*_{kij} \left(E_e + E_v\right) \tilde{C}_{ijmn} \varepsilon_{mn} - \varepsilon^*_{kij} 2\mu_v \varepsilon^p_{ij} \\ &= \sigma^*_{kmn} \varepsilon_{mn} - \varepsilon^*_{kij} \bar{\sigma}^{vp}_{ij}\,, \end{aligned} \tag{4.64}$$

with $\sigma^*_{kmn} := \varepsilon^*_{kij} \left(E_e + E_v\right) \tilde{C}_{ijmn}$ and the new field variable $\bar{\sigma}^v$ is introduced as

$$\bar{\sigma}^{vp}_{ij} := 2\mu_v \varepsilon^p_{ij}\,, \tag{4.65}$$

where the update scheme given in Table 4.10 is used to calculate the current value of the plastic strain tensor ε^p_{ij}. Insertion of Equation 4.64 into Equation 4.63 gives the following representation

$$\int_{\Gamma} u^*_{ki} t_i d\Gamma - \int_{\Omega} \sigma^*_{kij} \varepsilon_{ij} d\Omega + \int_{\Omega} \varepsilon^*_{kij} \bar{\sigma}^{vp}_{ij} d\Omega + \int_{\Omega} u^*_{ki} b_i d\Omega = 0\,. \tag{4.66}$$

Following [71, 33, 35], the second integral expression in Equation 4.66 can be reduced to a boundary integral to recast Equation 4.66 into

$$C_{ki} u_i + \int_{\Gamma} t^*_{ki} u_i d\Gamma = \int_{\Gamma} u^*_{ki} t_i d\Gamma + \int_{\Omega} \varepsilon^*_{kij} \bar{\sigma}^{vp}_{ij} d\Omega + \int_{\Omega} u^*_{ki} b_i d\Omega\,, \tag{4.67}$$

where the term t^*_{ki} stands for Kelvin's traction solution.

The domain integral in Equation 4.67 is evaluated by the methodology presented in Section 4.1.1.2 for linear viscoelasticity.

Numerical Discretization and Post-processing

Discretizing the integral equation Equation 4.67 into N_e boundary elements with N_n nodes and utilizing CTM with N_G integration points for calculation of the domain integrals under a single summation, the discretized form of Equation 4.67 can be expressed as

$$C_{ki}u_i + \sum_{n=1}^{N_e}\sum_{\alpha=1}^{N_n} H_{ki}^{n\alpha}u_i^{n\alpha}\Gamma_n = \sum_{n=1}^{N_e}\sum_{\alpha=1}^{N_n} G_{ki}^{n\alpha}t_i^{n\alpha}\Gamma_n + \sum_{m=1}^{N_G}\left[\left(\varepsilon_{kij}^*\right)^m\left(\bar{\sigma}_{ij}^{vp}\right)^m + \left(u_{ki}^*\right)^m\left(b_i\right)^m\right] . \tag{4.68}$$

Herefter, the methodology follows the procedure given in *(Numerical Discretization and Post-processing)* subsection of Section 4.1.1.2 to obtain the system of equations for the solution.

It is important to note that the kernel expression ε_{ikj}^*, which is used in the domain integrals of Equation 4.67, introduces a weak singularity when the field point (integration point) is close to the boundary node. Treatment of these singularities is discussed by Akay et al. [129] and in Section 4.1.1.2.

The solution procedure, outlined above, for calculating the field variables at time step t_{n+1} is summarized in Table 4.11.

Table 4.11: Algorithmic box

1. Given the history variables $\{(\varepsilon_{ij})_n, (\dot{\varepsilon}_{ij})_n, (\varepsilon_{ij}^p)_n\}$

2. Update the total corrected strain through Equation 4.56.

3. Compute $(\varepsilon_{ij}^p)_{n+1}$ at time step t_{n+1} by using the semi-implicit update methodology in Table 4.10.

4. Calculate the field variable $(\bar{\sigma}_{ij}^{vp})_{n+1}$ by using Equation 4.65.

5. Solve the BEM equation given in Equation 4.68 for the current time step t_{n+1}.

6. Apply the displacement field found in Step 5 to a BEM problem considering only the auxiliary branch (upper branch) presented in Figure 4.26. Again, use Equation 4.68 for the solution by setting $\bar{\sigma}_{ij}^{vp} = 0$.

7. Calculate the total strain $(\varepsilon_{ij})_{n+1}$ by using Equation 4.25 and update the strain rate $(\dot{\varepsilon}_{ij})_{n+1}$.

8. Calculate the stresses at the upper and lower branches by using Equation 4.50 and Equation 4.51, respectively.

4.3.1.3 Identification of Material Parameters by Optimization

The material model of XCrNi 18.9 steel proposed by Haupt [11] is taken as the reference material in this study. Monotonic shear loading with different strain rates is applied to the investigated material, as presented in Figure 4.27. H1, H2, H3, H4, and H5 are the results of different strain rate loading. The bulk and the shear moduli are given as 664000 MPa and 134000 MPa, respectively. For the determination of the material parameters, which will be used for the semi-implicit BEM application, an optimization study is carried out. An implicit driver algorithm for shear loading is derived to serve as the cost function of the optimization procedure.

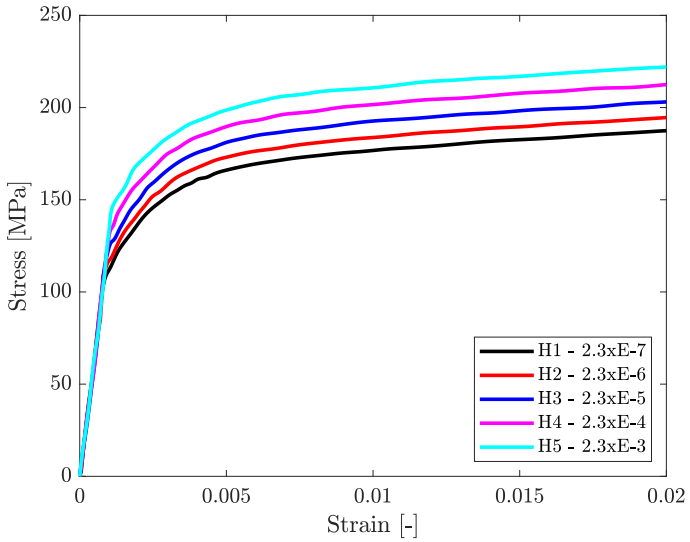


Figure 4.27: Change in shear stress with respect to shear strain for different loading rates of XCrNi 18.9 steel [11]

Nonlinear Implicit Driver Algorithm

In this sub-section, a general formulation of the driver algorithm for a uni-axial tension type of loading is presented. Extension of it to the shear loading is straightforward because it does not require an iterative loop to determine the full strain tensor.

For a uni-axial tensile loading in 3-D, the strain (ε) and the stress (σ) tensors for

isotropic materials can be written as

$$\boldsymbol{\varepsilon} = \text{diag}[\epsilon,\, \epsilon_2,\, \epsilon_2] \quad \text{and} \quad \boldsymbol{\sigma} = \text{diag}[\bar{\sigma},\, 0,\, 0], \tag{4.69}$$

where ϵ and ϵ_2 are the known ($\boldsymbol{\varepsilon}^k$) and the unknown ($\boldsymbol{\varepsilon}^u$) components of the strain tensor, respectively. For a given stress, which is a function of strain, the residue expression can be introduced as

$$\begin{aligned} r(\epsilon_2) &= \sigma_2 = \hat{\sigma}(\epsilon_2) = 0 \\ \bar{r}(\bar{\epsilon}_2) + \underbrace{\left.\frac{dr}{d\epsilon_2}\right|_{\bar{\epsilon}_2}}_{\bar{a}} (\epsilon_2 - \bar{\epsilon}_2) &= 0, \end{aligned} \tag{4.70}$$

where $\bar{\epsilon}_2$ is corrected by $\bar{\epsilon}_2 \leftarrow \bar{\epsilon}_2 - \bar{a}^{-1}\bar{r}$ until σ_2 is zero. $\bar{a}$ is determined by the material tensor, for which the derivation will be explained later in this subsection. At each update with Equation 4.70, the implicit constitutive model is used for the update of the plastic strain and $\bar{a}$. The power type plasticity model, presented in Equation 4.52 and Equation 4.53, can be expressed in residue form as

$$\begin{aligned} \mathbf{r}_1(\boldsymbol{\varepsilon}^p, \alpha) &= \boldsymbol{\varepsilon}^p - \boldsymbol{\varepsilon}^p_n - \Delta\dot{\varepsilon}_0 \frac{||\boldsymbol{\sigma}^{'}||^{m_1}}{\hat{\sigma}_0^{m_1}(\alpha)}\mathbf{n} \\ r_2(\boldsymbol{\varepsilon}^p, \alpha) &= \alpha - \alpha_n - \Delta\dot{\varepsilon}_0 \frac{||\boldsymbol{\sigma}^{'}||^{m_1}}{\hat{\sigma}_0^{m_1}(\alpha)}. \end{aligned} \tag{4.71}$$

$\mathbf{r}_1$ and r_2 can be linearized around ε^p_n and α_n as follows

$$\text{Lin}\, \mathbf{r}_1|_{\boldsymbol{\varepsilon}^p_n, \alpha_n} = \bar{\mathbf{r}}_1 + \bar{\mathbb{o}}_1 : \Delta\boldsymbol{\varepsilon}^p + \bar{\mathbf{a}}_1 \Delta\alpha = 0 \tag{4.72a}$$

$$\text{Lin}\, r_2|_{\boldsymbol{\varepsilon}^p_n, \alpha_n} = \bar{r}_2 + \bar{\mathbf{a}}_2 : \Delta\boldsymbol{\varepsilon}^p + \bar{a}_2 \Delta\alpha = 0, \tag{4.72b}$$

where

$$\bar{\mathbb{o}}_1 = \frac{\partial \mathbf{r}_1}{\partial \boldsymbol{\varepsilon}^p},\ \bar{\mathbf{a}}_1 = \frac{\partial \mathbf{r}_1}{\partial \alpha},\ \bar{\mathbf{a}}_2 = \frac{\partial \mathbf{r}_2}{\partial \boldsymbol{\varepsilon}^p} \text{ and } \bar{a}_2 = \frac{\partial r_2}{\partial \alpha}. \tag{4.73}$$

Insertion of Equation 4.72b into Equation 4.72a and performing the simplifications, the incremental updates of kinematic variables $\Delta\boldsymbol{\varepsilon}^p$ and $\Delta\alpha$ are determined as

$$\Delta\boldsymbol{\varepsilon}^p = \left(\bar{\mathbb{o}}_1 - a_2^{-1}\bar{\mathbf{a}}_1 \otimes \bar{\mathbf{a}}_2\right)^{-1} : \left(a_2^{-1}\bar{\mathbf{r}}_2\bar{\mathbf{a}}_1 - \bar{\mathbf{r}}_1\right) \tag{4.74a}$$

$$\Delta\alpha = \bar{\mathbf{a}}_2^{-1}\left(\bar{\mathbf{r}}_2 - \bar{\mathbf{a}}_2 : \Delta\boldsymbol{\varepsilon}^p\right). \tag{4.74b}$$

The material tensor ($\mathbb{C}$) can be evaluated by taking the derivative of viscoplastic stress ($\boldsymbol{\sigma}^{\text{vp}}$) in Equation 4.51 with respect to total strain ($\boldsymbol{\varepsilon}$) as follows:

$$\bar{\mathbb{C}} = \kappa \mathbf{1} \otimes \mathbf{1} + 2\mu \left(\mathbb{P} - \frac{\partial \boldsymbol{\varepsilon}^p}{\partial \boldsymbol{\varepsilon}} \right) \tag{4.75}$$

The term $\dfrac{\partial \boldsymbol{\varepsilon}^p}{\partial \boldsymbol{\varepsilon}}$ can be determined by taking the derivatives of residues $\boldsymbol{r}_1$ and r_2 in Equation 4.71 with respect to total strain ($\boldsymbol{\varepsilon}$) for frozen $\boldsymbol{\varepsilon}^p$ and α, and equating to zero. From the derivative of the second residue with respect to the total strain, an expression for $\dfrac{\partial \alpha}{\partial \boldsymbol{\varepsilon}}$ in terms of $\dfrac{\partial \boldsymbol{\varepsilon}^p}{\partial \boldsymbol{\varepsilon}}$ can be obtained. Insertion of this relation into the first derivative expression, the partial derivative of the plastic strain with respect to the elastic strain can be expressed as

$$\frac{\partial \boldsymbol{\varepsilon}^p}{\partial \boldsymbol{\varepsilon}} = \left[\bar{a}_2^{-1} \bar{\mathbf{a}}_1 \otimes \bar{\mathbf{a}}_2 - \bar{\mathbb{a}}_1 \right] : \left[\left. \frac{\partial \boldsymbol{r}_1}{d\boldsymbol{\varepsilon}} \right|_{\boldsymbol{\varepsilon}^p, \alpha} - \bar{a}_2^{-1} \bar{\mathbf{a}}_1 \otimes \left. \frac{\partial r_2}{d\boldsymbol{\varepsilon}} \right|_{\boldsymbol{\varepsilon}^p, \alpha} \right]. \tag{4.76}$$

The solution procedure of the fully implicit driver algorithm for uni-axial tension is summarized in Table 4.12.

Optimization Study

An optimization study is conducted using the developed nonlinear implicit driver algorithm as the cost function to determine the material parameters (ε0, ε.0, Y, m1, and m2) used for the nonlinear power type plasticity model. For five different strain rate loading, the material parameter set that best fits the stress-strain curve presented in Figure 4.27 is aimed. The lower and the upper bounds for the material parameters used in the optimization are given as

$$\begin{gathered} 10^{-8} < \varepsilon_0 < 4,\ 10^{-8} < \dot{\varepsilon_0} < 1,\ 10 < Y < 400 \\ 1 < m_1 < 60,\ \text{and}\ 1 < m_2 < 20. \end{gathered} \tag{4.77}$$

The built-in function *fmincon* of MATLAB is used for the optimization study. The material parameter set which is giving the best fit is obtained as

$$\begin{gathered} \varepsilon_0 = 7.73 \times 10^{-6},\ \dot{\varepsilon_0} = 0.0226,\ Y = 179.03\,\text{MPa} \\ m_1 = 50.5,\ \text{and}\ m_2 = 11.86. \end{gathered} \tag{4.78}$$

Table 4.12: Algorithmic box of nonlinear implicit driver algorithm for uni-axial tension

1. Given the history variables $\{\boldsymbol{\varepsilon}_n^p,\, \alpha_n,\, \boldsymbol{\sigma}_n^{'},\, \boldsymbol{\varepsilon}_{n+1}^k\}$

2. Set $\bar{\boldsymbol{\varepsilon}} = [\boldsymbol{\varepsilon}_{n+1}^k\, \boldsymbol{\varepsilon}_n^u]$, $\bar{\alpha} = \alpha_n$ and $\bar{\boldsymbol{\varepsilon}}^p = \boldsymbol{\varepsilon}_n^p$

3. While $\hat{\sigma}_2 - \sigma_2^k >$ tol

3.1. Initial guesses: $\bar{\boldsymbol{r}}_1 = \mathbf{1}$ and $r_2 = 1$

3.2. While $||\bar{\boldsymbol{r}}_1|| >$ tol and $r_2 = 1$

3.2.1. Determine $\bar{\mathbb{a}}_1$, $\bar{\mathbf{a}}_1$, $\bar{\mathbf{a}}_2$ and $\bar{a}_2$ using Equation 4.73.

3.2.2. Calculate $\bar{\mathbf{r}}_1$ and $\bar{r}_2$ using Equation 4.71.

3.2.3. Evaluate $\Delta\boldsymbol{\varepsilon}^p$ and $\Delta\alpha$ using Equation 4.74.

3.2.4. Update $\bar{\boldsymbol{\varepsilon}}^p \leftarrow \bar{\boldsymbol{\varepsilon}}^p + \Delta\boldsymbol{\varepsilon}^p$ and $\bar{\alpha} \leftarrow \bar{\alpha} + \Delta\alpha$.

3.2.5. Calculate:

$$\sigma_0 = Y\left(1 + \frac{\bar{\alpha}}{\varepsilon_0}\right)^{1/m_2} \text{ and } \bar{\boldsymbol{\sigma}}^{'} = 2\mu(\bar{\boldsymbol{\varepsilon}}^{'} - \bar{\boldsymbol{\varepsilon}}^p)\ .$$

3.2.6. Repeat from 3.2.1 until 3.2 is satisfied.

3.3. Determine $\dfrac{\partial\boldsymbol{\varepsilon}^p}{\partial\boldsymbol{\varepsilon}}$ and $\bar{\mathbb{C}}$ using Equation 4.76 and Equation 4.75.

3.4. Evaluate the total stress and following Equation 4.70 the unknown components of strain is evaluated as:

$$\boldsymbol{\varepsilon}_n^u = \epsilon_{2_n} = \epsilon_{2_n} - \mathbb{C}^{-1}\bar{\sigma}_2\ .$$

3.5. Repeat from 3.1 until 3 is satisfied.

In Figure 4.28, the stress-strain curves for five different shear loading rates are presented. The legends *Predicted* and *Actual* are the results obtained using the driver algorithm with the parameter set given in Equation 4.78 and in Haupt [11], respectively. Similar patterns of variation are observed between the results, which justifies the material set given in Equation 4.78 can be used to represent the XCrNi 18.9 steel.

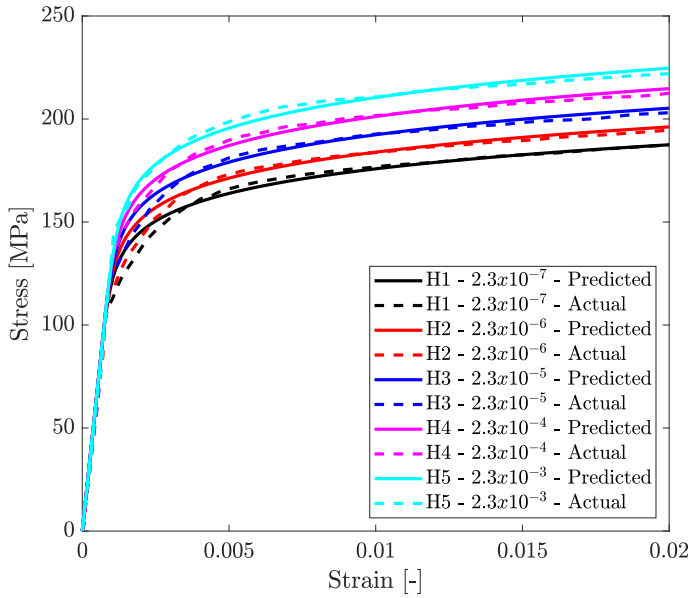


Figure 4.28: Change in shear stress with respect to shear strain for different loading rates of XCrNi 18.9 steel presented in [11] and obtained with nonlinear implicit driver algorithm

4.3.2 Numerical Example

4.3.2.1 Model Problem 1 - BVP with Uniform Strain Field

The geometry, dimensions, and boundary conditions of the numerical model are presented in Figure 4.29. A uniform ramp-type displacement loading is applied to the right boundary, while the displacements on the left boundary in the x-direction are restricted. Only the node located at the middle point of the left boundary is restricted in the y-direction to avoid rigid body displacement.

The proposed hybrid model in Figure 4.26 can be used to model complex material models of viscoplasticity. Moreover, viscoplasticity is modeled by a spring and a plasticity element connected in series. Therefore, E_e and E_1 in Figure 4.26 are set as 0.01 and 0, respectively. Since the upper branch needs to be active for post-processing purposes (see Table 4.11), instead of setting zero for E_e, a considerably smaller number than E_v is used. In Appendix E, it has been indicated that the proposed approach has no stability issues caused by very small ratios of E_e/E_v. The model parameters

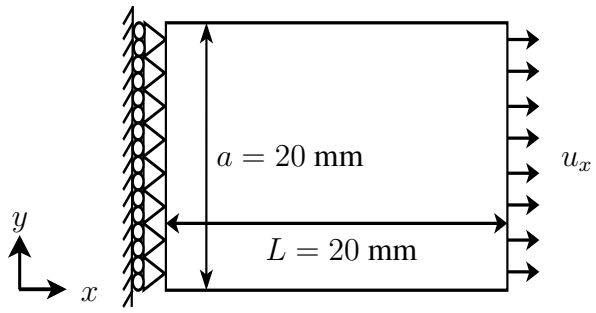


Figure 4.29: The square body subjected to displacement type ramp loading

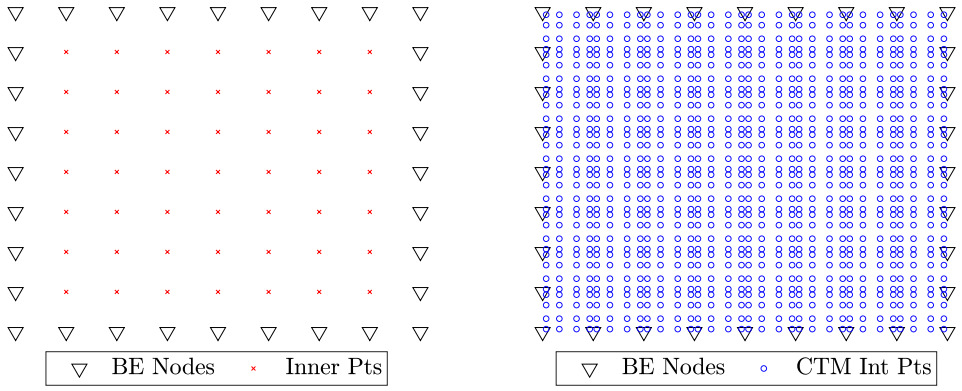
are given in Table 4.13.

Table 4.13: Model parameters used for power type plasticity with hardening

E_v [GPa]	ν [$-$]	ε_0 [$-$]	$\dot{\varepsilon}_0$ [$-$]	Y [MPa]	m_1 [$-$]	m_2 [$-$]
376.6	0.405	8×10^{-6}	0.0995	126.22	50.6	11.86

The strain loading rates H3 and H4 in Figure 4.28 are investigated in this study. The displacement type loading is gradually applied to the right edge according to the strain rate, time step, and domain length. The time steps are set to $\Delta t = 10^{-2}$ s and $\Delta t = 10^{-3}$ s for loading rates of 2.3×10^{-5} and 2.3×10^{-4}, respectively. Moreover, the special discretization used for the model is presented in Figure 4.30. The boundary is discretized with linear boundary elements of 2.5 mm in length, with downward triangles ($\triangledown$) indicating nodes. Moreover, 1024 integration points indicated by blue circles ($\bigcirc$) are used for CTM, and the post-processing is conducted through 49 inner data points shown by red crosses ($\times$) in Figure 4.30.

Figure 4.31 shows the change of viscoplastic stress in the lower branch with respect to the total axial strain under different rates of strain loading for the power-type viscoplasticity model with hardening. The BEM results are compared with the FEM solution obtained using FEAP [125]. FEM utilizes a fully implicit nonlinear viscoplasticity constitutive law, and the time steps used are selected as $\Delta t = 1$ s and $\Delta t = 0.1$ s for loading rates of 2.3×10^{-5} and 2.3×10^{-4}, respectively. The BEM results are depicted using discrete points to ensure a clearer presentation.



(a) Inner data points

(b) CTM integration points

Figure 4.30: Boundary element mesh with inner points used for interpolation and CTM integration points

Figure 4.31 shows that until the initiation of plasticity, the same behavior is observed for both loading rates. Additionally, plasticity initiates earlier at lower stress levels when the loading rate is decreased, and the end slope for both loading rates is the same. The proposed non-iterative semi-implicit BEM approach provides consistent results with the fully-implicit FEM solution. However, it is important to note that accuracy is lost for the BEM solution with coarser time discretization due to the non-iterative nature of the semi-implicit model.

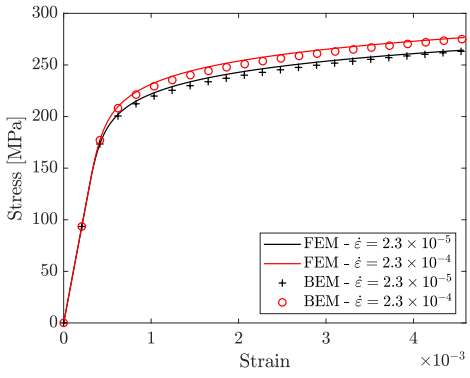


Figure 4.31: FEM and BEM result for the uniform strain loading with different rates

4.3.2.2 Model Problem 2 - Flange

The flange geometry, introduced in Section 4.2 to demonstrate the developed approach for nonlinear viscoelasticity, is utilized. Figure 4.32 provides details regarding the geometry, dimensions, and boundary conditions of the model. Nonlinear power-type viscoplasticity is modeled using the material parameters specified in Table 4.13, with values of 0.01 and 0 assigned to E_e and E_1, respectively. The spatial discretization schemes presented for nonlinear viscoelasticity in Section 4.2.2.2 are employed to model nonlinear viscoplasticity.

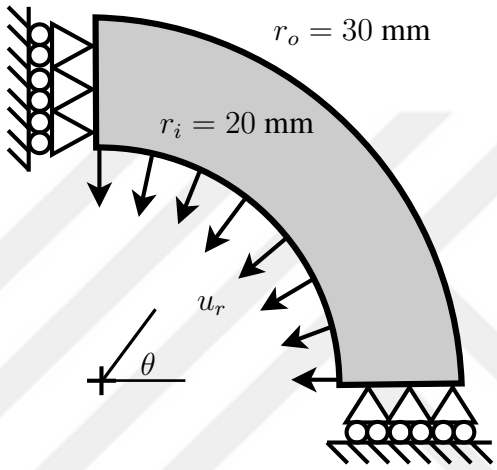


Figure 4.32: The flange body subjected to displacement type sinusoidal loading applied in radial direction

The flange experiences a radial-type loading, with prescribed displacements $u_r(t)$ applied at the inner circular edge in the radial inward direction. The radial loading function $u_r(t)$ is defined using two specific sinusoidal functions and one relaxation-type loading, as outlined in Table 4.14. The first loading type, L1, is characterized by a relaxation-type loading, while the remaining loadings exhibit sinusoidal behavior. In loadings L2 and L3, the angle θ is defined as the angle between the line connecting the nodal point on the inner surface of the flange to the origin and the horizontal x-axis.

In Figure 4.33, the variation in the reaction force concerning the applied displacement at the bottom left corner is depicted for the three loadings. Upon comparing these three loadings with the fully implicit FEM solution, inconsistencies are evident,

Table 4.14: Four different loadings investigated for the flange problem

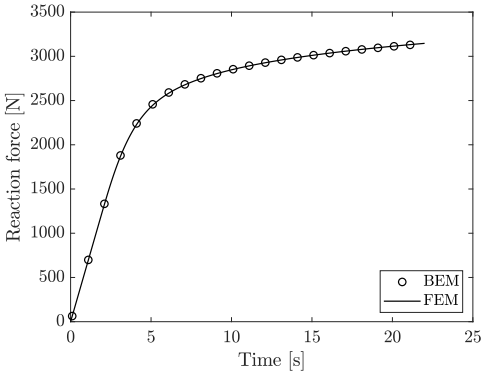
Loading	$u_r(t)$
L1	$0.2\, r_i$
L2	$(1+\theta)\ 0.2\, r_i$
L3	$\left[1+5\left(\cos(\theta-\frac{\pi}{4})-\cos(\frac{\pi}{4})\right)\right]\ 0.2\, r_i$

particularly for loadings resulting in regions with localized stresses after the softening starts. It is observed that the performance of the developed approach is limited in such examples, and potential approaches to enhance the accuracy of the developed method on these problems are discussed in the following section.

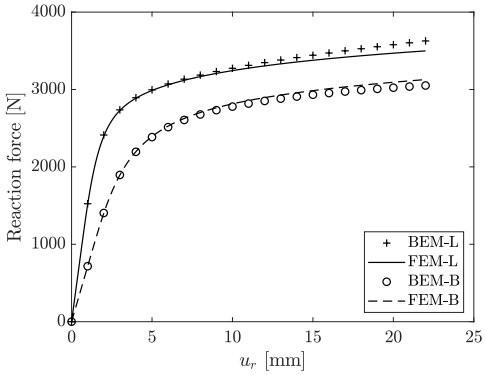
4.3.3 Concluding Remarks

In this subsection, the non-iterative algorithmic formulation for modeling power-type nonlinear viscoelasticity is extended to address nonlinear applications of viscoplasticity using the Boundary Element Method (BEM) in the time domain. The domain integrals are treated by the mesh-free integration techniques presented in this thesis study. Power-type plasticity is modeled using a spring and a plasticity element connected in series. The purely elastic branch serves as an auxiliary component, which is used only when it is needed in the physical model of viscoplasticity used in numerical examples.

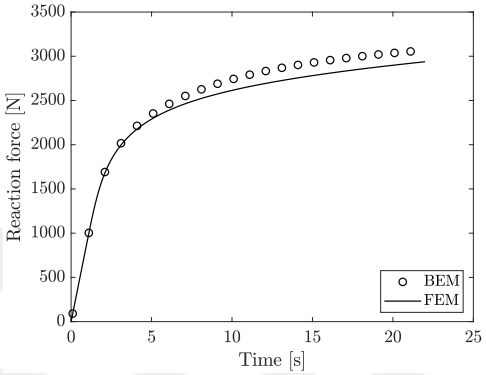
The material model proposed by Haupt [11] is utilized in the study. In order to determine the parameters of the power-type viscoplasticity model, an implicit nonlinear driver algorithm is developed. This algorithm acts as the cost function for the optimization process, where the model parameters are determined based on stress-strain



(a) L1 loading



(b) L2 loading



(c) L3 loading

Figure 4.33: Change in the reaction force with respect to the applied displacement at the node located on the bottom left corner for the investigated loadings

results obtained under different loading rates, as presented by Haupt [11].

The effectiveness of the proposed BEM formulation is demonstrated through a numerical problem involving a square domain under a uniform strain state. A comparison study is conducted with FEM, where a fully implicit plasticity model is employed. The results obtained with BEM exhibit good agreement with the FEM results. However, it should be noted that the selection of the time step can influence the solution accuracy due to the semi-implicit nature of the proposed method. To achieve a satisfactory consistency with the fully implicit FEM, a finer temporal discretization is required for the non-iterative semi-implicit approach.

While the developed approach performs satisfactorily for BVPs with uniform strain

fields, it exhibits inconsistency for more complex problems involving localized stresses, such as the flange example with non-uniform loading. In such cases, the approach predicts a slower evolution of the viscoplastic strains, particularly in regions with localized stresses. To address this issue, the developed approach can be revised by adopting a purely RPIM (Radial Point Integration Method) solution, as proposed by Kazemi et al. [130]. This modification could potentially enhance the accuracy and efficiency of the method for problems with localized stress distributions. Additionally, the adoption of adaptive meshing for the RPIM points in regions with localized stress can effectively address the observed inconsistency. By dynamically adjusting the distribution of RPIM points based on stress variations, the method can better capture the fine details of stress concentration and deformation, leading to improved accuracy and reliability in simulations of complex problems. The adaptive meshing strategy optimizes the distribution of RPIM points, concentrating them where they are needed most, and reduces computational efforts in less critical regions. This way, the method can efficiently handle problems with localized stress distributions and ensure more accurate and efficient numerical solutions.

CHAPTER 5

CONCLUSION

This thesis study mainly focuses on the solution of various elastic and inelastic engineering problems using the boundary element method (BEM) with applications to computational homogenization. Section 2 presents the 2D and 3D BEM formulations of linear elasticity and introduces homogenization methods using uniform tractions, linear displacement, and periodic displacement boundary conditions. Verification of the method is conducted on various examples from Miehe and Koch [1] and Fernandes et al. [2]. These problems include both single-inclusion/void and multi-inclusion/void cases. Homogenized stress results of the Representative Volume Elements (RVEs) and deformed shapes are compared. Overall, the macroscopic stress results of the developed algorithm are consistent with the results reported in the literature. Subsequently, the modeling of the matrix-inclusion interface is discussed, which plays a crucial role in heterogeneous materials with relatively significant differences in material properties. The interface model is adopted from the study conducted by Tan et al. [51]. Then, the implementation of an iterative bilinear traction-separation law in the boundary element method is discussed. The developed method is applied to two model problems from the literature involving single and multi-inclusion RVEs. The effects of changes in the following parameters are studied in Section 2.3:

- Inclusion diameter
- Boundary condition
- Mesh size
- Interface iteration parameters

It is observed that the developed method yields consistent results with the results presented in the literature. In Section 2.4, the viscoelastic modeling of polymer nano-composites using the Dynamic Correspondence Principle (DCP) is discussed. A concise introduction to the Dynamic Correspondence Principle is provided, and its implementation in the boundary element method is presented. Additionally, a three-phase model is introduced in this section, where the third phase, known as the *interphase*, possesses different material properties compared to the inclusion and matrix. The developed method is applied to three studies in the literature, demonstrating its effectiveness in viscoelastic modeling.

- The first application is made to the study presented by Brinson et al. [54, 3] and Fisher et al. [57]. Two-phase fully viscoelastic RVEs and three-phase RVEs with elastic inclusion are investigated. The results of the proposed model are compared with the literature and the Finite Element Method (FEM) results obtained by Guzel [56]. It is observed that the developed algorithm gives consistent results with both the literature and FEM. Moreover, the solution times for BEM are considerably faster compared to FEM.
- The second application is based on the experimental and numerical study presented by Diani et al. [4]. Six sets of specimens with various volume fractions of coated carbon-black filled styrene butadiene rubbers (SBR) in a random copolymer are investigated. Two-phase and three-phase RVEs are used in BEM to represent the materials. It is observed that three-phase RVEs yield results closer to the experimental results compared to two-phase RVEs.

In Section 3, mesh-free interpolation and integration methods are discussed, as domain integration is crucial in many engineering problems, such as linear elasticity with body force, thermal conductivity with internal heat source, transient thermal conductivity, and inelasticity problems. A truly mesh-free method called the Cartesian Transformation Method (CTM) is introduced, and its methodology and implementation in BEM are thoroughly explored. At the integration points of the CTM, the values of the integrand need to be calculated. For this purpose, local interpolation methods called Moving Least Squares (MLS) and Radial Point Integration Method (RPIM), which are offered in the literature, are implemented in the CTM. The devel-

oped mesh-free integration method is verified with mathematical examples involving singular terms in the domain in Appendix C. The effect of three different parameters on integration results is studied:

- The effect of adaptive or constant monomial order,
- The effect of integration points,
- The effect of scattered data points.

A good agreement is observed between the two interpolation methods, MLS and RPIM, for all analyses. The developed BEM algorithm, with its mesh-free domain integration capability, is applied to real engineering problems. Firstly, the solution of body force loading on the elasticity problem is discussed. Next, thermal problems are introduced to the developed BEM algorithm. The formulation and boundary integral equations of steady-state heat conduction and thermoelasticity problems are presented. In Section 3.2.3, the transient heat conduction problem is introduced to BEM, and the formulation and boundary integral equations of the problem are discussed. Furthermore, as a future work, in order to enhance the accuracy of the interpolation methods within the support domains, including the outer boundary, certain refinements suggested in the literature are planned to be integrated into the already developed methodology.

In Chapter 4, a novel non-iterative time domain formulation for the solution of inelastic problems with BEM is introduced. In Section 4.1, the application of the non-iterative algorithmic formulation for generalized models of viscoelasticity within the framework of BEM in the time domain is discussed. The proposed method is validated through BVPs with uniform and non-uniform strain fields, showcasing its robustness and accuracy in analyzing creep and relaxation types of loadings. The modular framework of the BEM approach allows for easy extension to nonlinear evolution equations of viscoelasticity, which is discussed in Section 4.2. The approach is demonstrated through the analysis of widely common engineering components, and a good agreement with iterative FEM solution results is observed. The semi-implicit nature of the method allows for achieving converged results with a similar time step to the iterative FEM approach. In Section 4.3, the developed approach is extended

to nonlinear viscoplasticity problems. A power-type viscoplasticity model is used, and the effectiveness of the proposed BEM formulation is demonstrated through numerical problems. The material parameters are determined through an optimization study. While the developed approach performs well for BVPs with uniform strain fields, it is noted that it exhibits some inconsistency in more complex problems with localized stresses. The developed approach can be revised by adopting a purely RPIM solution to address this issue, as proposed by Kazemi et al. [130]. This modification could enhance the accuracy of the method for problems with localized stress distributions. Another remedy could be the adaptive placement of the RPIM points in regions with localized stress. By dynamically adjusting the distribution of RPIM points, the method can better capture the stress concentrations, leading to improved accuracy and reliability in simulations of complex problems.

REFERENCES

[1] C. Miehe, "Computational micro-to-macro transitions for discretized microstructures of heterogeneous materials at finite strains based on the minimization of averaged incremental energy," *Computer Methods in Applied Mechanics and Engineering*, vol. 192, no. 5-6, pp. 559–591, 2003.

[2] G. R. Fernandes, G. A. Ohland, and J. F. Vieira, "A boundary element formulation to perform elastic analysis of heterogeneous microstructures," *Engineering Analysis with Boundary Elements*, vol. 87, pp. 47–65, 2018.

[3] L. Brinson and W. Lin, "Comparison of micromechanics methods for effective properties of multiphase viscoelastic composites," *Composite Structures*, vol. 41, no. 3-4, pp. 353–367, 1998.

[4] J. Diani, P. Gilormini, Y. Merckel, and F. Vion-Loisel, "Micromechanical modeling of the linear viscoelasticity of carbon-black filled styrene butadiene rubbers: The role of the filler–rubber interphase," *Mechanics of Materials*, vol. 59, pp. 65–72, 2013.

[5] D. W. Spring and G. H. Paulino, "A growing library of three-dimensional cohesive elements for use in abaqus," *Engineering Fracture Mechanics*, vol. 126, pp. 190–216, 2014.

[6] D. W. Spring and G. H. Paulino, "Computational homogenization of the debonding of particle reinforced composites: The role of interphases in interfaces," *Computational Materials Science*, vol. 109, pp. 209–224, 2015.

[7] V. Tvergaard, "Effect of fibre debonding in a whisker-reinforced metal," *Materials science and engineering: A*, vol. 125, no. 2, pp. 203–213, 1990.

[8] Z. Wu, Q. Lin, and Y. Chen, "Application of fast multipole boundary element method for two-dimensional nonlinear interface debonding of particulate com-

posites," *Engineering Analysis with Boundary Elements*, vol. 113, pp. 72–81, 2020.

[9] J.-S. Chen, C.-T. Wu, S. Yoon, and Y. You, "A stabilized conforming nodal integration for galerkin mesh-free methods," *International Journal for Numerical Methods in Engineering*, vol. 50, no. 2, pp. 435–466, 2001.

[10] G.-R. Liu and Y.-T. Gu, *An introduction to meshfree methods and their programming*, vol. 1. Springer Science & Business Media, 2005.

[11] P. Haupt, *Continuum mechanics and theory of materials*. Springer Science & Business Media, 2013.

[12] Q. Zeng, A. Yu, and G. Lu, "Multiscale modeling and simulation of polymer nanocomposites," *Progress in polymer science*, vol. 33, no. 2, pp. 191–269, 2008.

[13] G. Pal and S. Kumar, "Modeling of carbon nanotubes and carbon nanotube–polymer composites," *Progress in Aerospace Sciences*, vol. 80, pp. 33–58, 2016.

[14] P. Hohenberg and W. Kohn, "Inhomogeneous electron gas," *Physical review*, vol. 136, no. 3B, p. B864, 1964.

[15] M. G. Ahangari, A. Fereidoon, and M. D. Ganji, "Density functional theory study of epoxy polymer chains adsorbing onto single-walled carbon nanotubes: electronic and mechanical properties," *Journal of molecular modeling*, vol. 19, no. 8, pp. 3127–3134, 2013.

[16] A. Ebrahimi, H. Ehteshami, and M. Mohammadi, "Density functional calculations of response of single-walled armchair carbon nanotubes to axial tension," *Computational Materials Science*, vol. 41, no. 4, pp. 486–492, 2008.

[17] K. Panda and K. R. Chandran, "Determination of elastic constants of titanium diboride (tib2) from first principles using flapw implementation of the density functional theory," *Computational Materials Science*, vol. 35, no. 2, pp. 134–150, 2006.

[18] B. Arash, H. S. Park, and T. Rabczuk, "Mechanical properties of carbon nanotube reinforced polymer nanocomposites: A coarse-grained model," *Composites Part B: Engineering*, vol. 80, pp. 92–100, 2015.

[19] W. Voigt, *Theoretical Studies on the Elasticity of the Crystals*. Kø Society of Sciences to Göttingen, 1887.

[20] A. Reuss, "Calculation of the flow limits of mixed crystals on the basis of the plasticity of monocrystals," *Z. Angew. Math. Mech*, vol. 9, pp. 49–58, 1929.

[21] J. D. Eshelby, "The determination of the elastic field of an ellipsoidal inclusion, and related problems," *Proceedings of the Royal Society of London. Series A. Mathematical and Physical Sciences*, vol. 241, no. 1226, pp. 376–396, 1957.

[22] T. Mori and K. Tanaka, "Average stress in matrix and average elastic energy of materials with misfitting inclusions," *Acta metallurgica*, vol. 21, no. 5, pp. 571–574, 1973.

[23] M. Hori and S. Nemat-Nasser, "Double-inclusion model and overall moduli of multi-phase composites," *Mechanics of Materials*, vol. 14, no. 3, pp. 189–206, 1993.

[24] Y. Tong, Y. Li, F. Xie, and M. Ding, "Preparation and characteristics of polyimide–tio2 nanocomposite film," *Polymer international*, vol. 49, no. 11, pp. 1543–1547, 2000.

[25] G. Odegard, T. Gates, K. Wise, C. Park, and E. Siochi, "Constitutive modeling of nanotube–reinforced polymer composites," *Composites science and technology*, vol. 63, no. 11, pp. 1671–1687, 2003.

[26] S. Gajjela, V. Ramachandran, and J. Somasekharan, "Influence of interphase material and clay particle shape on the effective properties of epoxy-clay nanocomposites," *Composites Part B: Engineering*, vol. 88, pp. 11–18, 2016.

[27] D. Xie, W. Tang, Y. Wang, X. Xia, Y. Zhong, D. Zhou, D. Wang, X. Wang, and J. Tu, "Facile fabrication of integrated three-dimensional c-mose 2/reduced graphene oxide composite with enhanced performance for sodium storage," *Nano Research*, vol. 9, no. 6, pp. 1618–1629, 2016.

[28] J. Wernik and S. A. Meguid, "Coupling atomistics and continuum in solids: status, prospects, and challenges," *International Journal of Mechanics and Materials in Design*, vol. 5, no. 1, p. 79, 2009.

[29] C. Li and T.-W. Chou, "Multiscale modeling of compressive behavior of carbon nanotube/polymer composites," *Composites science and technology*, vol. 66, no. 14, pp. 2409–2414, 2006.

[30] K. Tserpes, P. Papanikos, G. Labeas, and S. G. Pantelakis, "Multi-scale modeling of tensile behavior of carbon nanotube-reinforced composites," *Theoretical and applied fracture mechanics*, vol. 49, no. 1, pp. 51–60, 2008.

[31] M. Ayatollahi, S. Shadlou, M. Shokrieh, and M. Chitsazzadeh, "Effect of multi-walled carbon nanotube aspect ratio on mechanical and electrical properties of epoxy-based nanocomposites," *Polymer Testing*, vol. 30, no. 5, pp. 548–556, 2011.

[32] M. Schanz, *Wave propagation in viscoelastic and poroelastic continua: a boundary element approach*, vol. 2. Springer Science & Business Media, 2012.

[33] A. A. Becker, *The boundary element method in engineering: a complete course*. McGraw-Hill Companies, 1992.

[34] C. Brebbia, *The boundary element method for engineers*. Pentech Press Ltd, 1980.

[35] L. C. Wrobel and M. Aliabadi, "The boundary element method: Applications in solids and structures," 2002.

[36] M. H. Aliabadi, *The boundary element method, applications in solids and structures*, vol. 2. John Wiley & Sons, 2002.

[37] L. C. Wrobel, *The boundary element method, volume 1: Applications in thermo-fluids and acoustics*, vol. 1. John Wiley & Sons, 2002.

[38] C. Brebbia and J. Dominguez, "Boundary elements: An introductory course. mcgraw-hill," *Southampton, UK*, 1992.

[39] V. Mantic, "A new formula for the c-matrix in the somigliana identity," *Journal of Elasticity*, vol. 33, no. 3, pp. 191–201, 1993.

[40] R. Hill, "On constitutive macro-variables for heterogeneous solids at finite strain," *Proceedings of the Royal Society of London. A. Mathematical and Physical Sciences*, vol. 326, no. 1565, pp. 131–147, 1972.

[41] R. Penta and A. Gerisch, "Investigation of the potential of asymptotic homogenization for elastic composites via a three-dimensional computational study," *Computing and Visualization in Science*, vol. 17, no. 4, pp. 185–201, 2015.

[42] G. I. Barenblatt *et al.*, "The mathematical theory of equilibrium cracks in brittle fracture," *Advances in applied mechanics*, vol. 7, no. 1, pp. 55–129, 1962.

[43] D. S. Dugdale, "Yielding of steel sheets containing slits," *Journal of the Mechanics and Physics of Solids*, vol. 8, no. 2, pp. 100–104, 1960.

[44] A. Needleman, "A continuum model for void nucleation by inclusion debonding," 1987.

[45] V. Tvergaard and J. W. Hutchinson, "The relation between crack growth resistance and fracture process parameters in elastic-plastic solids," *Journal of the Mechanics and Physics of Solids*, vol. 40, no. 6, pp. 1377–1397, 1992.

[46] X.-P. Xu and A. Needleman, "Numerical simulations of fast crack growth in brittle solids," *Journal of the Mechanics and Physics of Solids*, vol. 42, no. 9, pp. 1397–1434, 1994.

[47] M. Raous, L. Cangémi, and M. Cocu, "A consistent model coupling adhesion, friction, and unilateral contact," *Computer methods in applied mechanics and engineering*, vol. 177, no. 3-4, pp. 383–399, 1999.

[48] J. L. Chaboche, F. Feyel, and Y. Monerie, "Interface debonding models: a viscous regularization with a limited rate dependency," *International journal of solids and structures*, vol. 38, no. 18, pp. 3127–3160, 2001.

[49] A. C. Palmer and J. R. Rice, "The growth of slip surfaces in the progressive failure of over-consolidated clay," *Proceedings of the Royal Society of London. A. Mathematical and Physical Sciences*, vol. 332, no. 1591, pp. 527–548, 1973.

[50] M. Frémond, "Contact with adhesion," in *Nonsmooth Mechanics and Applications*, pp. 177–221, Springer, 1988.

[51] H. Tan, C. Liu, Y. Huang, and P. H. Geubelle, "The cohesive law for the particle/matrix interfaces in high explosives," *Journal of the Mechanics and Physics of Solids*, vol. 53, no. 8, pp. 1892–1917, 2005.

[52] H. Inglis, P. Geubelle, K. Matouš, H. Tan, and Y. Huang, "Cohesive modeling of dewetting in particulate composites: micromechanics vs. multiscale finite element analysis," *Mechanics of Materials*, vol. 39, no. 6, pp. 580–595, 2007.

[53] N. Ottosen and M. Ristinmaa, "Introduction to time-dependent material behavior," *The Mechanics of Constitutive Modeling. Elsevier Science*, pp. 357–378, 2005.

[54] L. C. Brinson and W. G. Knauss, "Finite Element Analysis of Multiphase Viscoelastic Solids," *Journal of Applied Mechanics*, vol. 59, pp. 730–737, 12 1992.

[55] Y. Fung, "Foundations of solid mechanics,(1965)," *Englewood Cliffs, NJ*, vol. 436, 1965.

[56] D. Güzel, "A two-level homogenization method for polymer nanocomposites with coated inclusions," Master's thesis, Middle East Technical University, 2021.

[57] F. Fisher and L. Brinson, "Viscoelastic interphases in polymer–matrix composites: theoretical models and finite-element analysis," *Composites Science and technology*, vol. 61, no. 5, pp. 731–748, 2001.

[58] A. Khosravifard and M. R. Hematiyan, "A new method for meshless integration in 2d and 3d galerkin meshfree methods," *Engineering Analysis with Boundary Elements*, vol. 34, no. 1, pp. 30–40, 2010.

[59] J. Dolbow and T. Belytschko, "Numerical integration of the galerkin weak form in meshfree methods," *Computational Mechanics*, vol. 23, no. 3, pp. 219–230, 1999.

[60] G. Liu and L. Yan, "A study on numerical integration in element-free methods," in *Proceeding of 4th Asia-Pacific Conference on Computational Mechanics, Singapore*, pp. 979–984, 1999.

[61] G.-R. Liu, *Meshfree methods: moving beyond the finite element method*. CRC Press, 2009.

[62] S. Beissel and T. Belytschko, "Nodal integration of the element-free galerkin method," *Computer Methods in Applied Mechanics and Engineering*, vol. 139, no. 1-4, pp. 49–74, 1996.

[63] M. Hematiyan, "A general method for evaluation of 2d and 3d domain integrals without domain discretization and its application in bem," *Computational Mechanics*, vol. 39, no. 4, pp. 509–520, 2007.

[64] M. Hematiyan, "Exact transformation of a wide variety of domain integrals into boundary integrals in boundary element method," *Communications in Numerical Methods in Engineering*, vol. 24, no. 11, pp. 1497–1521, 2008.

[65] M. Hematiyan, M. Mohammadi, R. Fazeli, and A. Khosravifard, "Cartesian transformation method for evaluation of regular and singular domain integrals in boundary element and other mesh reduction methods," *Advances in Boundary Element Techniques IX*, p. 93, 2008.

[66] P. Lancaster and K. Salkauskas, "Surfaces generated by moving least squares methods," *Mathematics of computation*, vol. 37, no. 155, pp. 141–158, 1981.

[67] W. S. Cleveland and E. Grosse, "Computational methods for local regression," *Statistics and computing*, vol. 1, no. 1, pp. 47–62, 1991.

[68] G.-R. Liu and M. B. Liu, *Smoothed particle hydrodynamics: a meshfree particle method*. World scientific, 2003.

[69] G. Liu and Y. Gu, "A local radial point interpolation method (lrpim) for free vibration analyses of 2-d solids," *Journal of Sound and vibration*, vol. 246, no. 1, pp. 29–46, 2001.

[70] G.-R. Liu, G. Zhang, Y. Gu, and Y. Wang, "A meshfree radial point interpolation method (rpim) for three-dimensional solids," *Computational Mechanics*, vol. 36, no. 6, pp. 421–430, 2005.

[71] C. A. Brebbia, J. C. F. Telles, and L. C. Wrobel, *Boundary element techniques: theory and applications in engineering*. Springer Science & Business Media, 2012.

[72] F. Smithies, "Conduction of heat in solids. by hs carslaw and jc jaeger pp. viii 386. 30s. 1947.(oxford, at the clarendon press).," *The Mathematical Gazette*, vol. 36, no. 316, pp. 142–143, 1952.

[73] M. Abramowitz and I. A. Stegun, *Handbook of mathematical functions with formulas, graphs, and mathematical tables*, vol. 55. US Government printing office, 1964.

[74] M. Hematiyan, M. Mohammadi, L. Marin, and A. Khosravifard, "Boundary element analysis of uncoupled transient thermo-elastic problems with time- and space-dependent heat sources," *Applied Mathematics and Computation*, vol. 218, no. 5, pp. 1862–1882, 2011.

[75] J. Swedlow and T. Cruse, "Formulation of boundary integral equations for three-dimensional elasto-plastic flow," *International Journal of Solids and Structures*, vol. 7, no. 12, pp. 1673–1683, 1971.

[76] P. C. Riccardella, *An implementation of the boundary-integral technique for planar problems of elasticity and elasto-plasticity*. Carnegie Mellon University, 1973.

[77] V. Kumar and S. Mukherjee, "A boundary-integral equation formulation for time-dependent inelastic deformation in metals," *International Journal of Mechanical Sciences*, vol. 19, no. 12, pp. 713–724, 1977.

[78] C. A. Brebbia, J. C. F. Telles, and L. C. Wrobel, *Boundary element techniques, theory and applications in engineering*. Springer-Verlag, 1984.

[79] T. JCF, *The boundary element method applied to inelastic problems*. Springer-Verlag, 1983.

[80] G. Maier and C. Polizzotto, "A galerkin approach to boundary element elastoplastic analysis," *Computer Methods in Applied Mechanics and Engineering*, vol. 60, no. 2, pp. 175–194, 1987.

[81] V. M. A. Leitao, *An improved boundary element formulation for nonlinear fracture mechanics.* PhD thesis, University of Portsmouth, 1993.

[82] H. Okada, H. Rajiyah, and S. Atluri, "A full tangent stiffness field-boundary-element formulation for geometric and material non-linear problems of solid mechanics," *International journal for numerical methods in engineering*, vol. 29, no. 1, pp. 15–35, 1990.

[83] O. Hiroshi and S. N. Atluri, "Recent developments in the field-boundary element method for finite/small strain elastoplasticity," *International journal of solids and structures*, vol. 31, no. 12-13, pp. 1737–1775, 1994.

[84] C. Chandenduang, *Boundary element analysis of time-dependent material nonlinearity*. PhD thesis, University of Nottingham, 1999.

[85] E. P. León, A. Rodríguez-Castellanos, N. Flores-Guzmán, and E. Olivera-Villaseñor, "Combined plasticity and creep analysis in 2d by means of the boundary element method," *Engineering Analysis with Boundary Elements*, vol. 37, no. 11, pp. 1436–1444, 2013.

[86] F. Rizzo and D. Shippy, "An application of the correspondence principle of linear viscoelasticity theory," *SIAM Journal on Applied Mathematics*, vol. 21, no. 2, pp. 321–330, 1971.

[87] T. Kusama and Y. Mitsui, "Boundary element method applied to linear viscoelastic analysis," *Applied Mathematical Modelling*, vol. 6, no. 4, pp. 285–290, 1982.

[88] B. Sun and C. Hsiao, "Viscoelastic boundary element method for analysing polymer quasifracture," *Computers & Structures*, vol. 30, no. 4, pp. 963–966, 1988.

[89] Y. Liu and H. Antes, "Application of visco-elastic boundary element method to creep problems in chemical engineering structures," *International Journal of Pressure Vessels and Piping*, vol. 70, no. 1, pp. 27–31, 1997.

[90] J. Perez-Gavilan and M. Aliabadi, "A symmetric galerkin boundary element method for dynamic frequency domain viscoelastic problems," *Computers & Structures*, vol. 79, no. 29-30, pp. 2621–2633, 2001.

[91] J. Wang and B. Birgisson, "A time domain boundary element method for modeling the quasi-static viscoelastic behavior of asphalt pavements," *Engineering Analysis with Boundary Elements*, vol. 31, no. 3, pp. 226–240, 2007.

[92] M. Schanz and H. Antes, "A new visco- and elastodynamic time domain boundary element formulation," *Computational Mechanics*, vol. 20, p. 452–459, 1997.

[93] M. Schanz, "A boundary element formulation in time domain for viscoelastic solids," *Communications in Numerical Methods in Engineering*, vol. 15, p. 799–809, 1999.

[94] M. Schanz, H. Antes, and T. Rüberg, "Convolution quadrature boundary element method for quasi-static visco- and poroelastic continua," *Computers and Structures*, vol. 83, no. 10, pp. 673–684, 2005.

[95] A. Mesquita and H. Coda, "A boundary element methodology for viscoelastic analysis: Part i with cells," *Applied Mathematical Modelling*, vol. 31, no. 6, pp. 1149–1170, 2007.

[96] A. Mesquita and H. Coda, "A boundary element methodology for viscoelastic analysis: Part ii without cells," *Applied Mathematical Modelling*, vol. 31, no. 6, pp. 1171–1185, 2007.

[97] D. Nardini and C. Brebbia, "Boundary element methods in engineering," in *Ch. A new approach to free vibration analysis using boundary elements*, pp. 312–326, Springer-Verlag Berlin, Heidelberg, 1982.

[98] P. Banerjee, S. Ahmad, and H. Wang, "Advanced development of bem for elastic and inelastic dynamic analysis of solids," *Developments in Boundary Element Methods: Industrial applications*, p. 75, 1989.

[99] D. P. Henry Jr and P. K. Banerjee, "A new bem formulation for tow-and three-dimensional elastoplasticity using particular integras," *International Journal for Numerical Methods in Engineering*, vol. 26, no. 9, pp. 2079–2096, 1988.

[100] R. Pollandt, "Solving nonlinear differential equations of mechanics with the boundary element method and radial basis functions," *International Journal for Numerical Methods in Engineering*, vol. 40, no. 1, pp. 61–73, 1997.

[101] B. Baranoglu and Y. Mengi, "The use of dual reciprocity boundary element method in coupled thermoviscoelasticity," *Computer Methods in Applied Mechanics and Engineering*, vol. 196, no. 1-3, pp. 379–392, 2006.

[102] Q. Zhang, S. Mukherjee, and A. Chandra, "Shape design sensitivity analysis for geometrically and materially nonlinear problems by the boundary element method," *International Journal of Solids and Structures*, vol. 29, no. 20, pp. 2503–2525, 1992.

[103] Q. Zhang, S. Mukherjee, and A. Chandra, "Design sensitivity coefficients for elasto-viscoplastic problems by boundary element methods," *International journal for numerical methods in engineering*, vol. 34, no. 3, pp. 947–966, 1992.

[104] L.-J. Leu and S. Mukherjee, "Sensitivity analysis and shape optimization in nonlinear solid mechanics," *Engineering analysis with boundary elements*, vol. 12, no. 4, pp. 251–260, 1993.

[105] L. L. J. Wei, X, S. Mukherjee, and A. Chandra, "Shape optimization in elasticity and elastoplasticity," *International journal of solids structures*, vol. 31, no. 3, pp. 553–550, 1992.

[106] H. Jin, K. Runesson, and K. Mattiasson, "Boundary element formulation in finite deformation plasticity using implicit integration," *Computers & Structures*, vol. 31, no. 1, pp. 25–34, 1989.

[107] J. Telles and J. Carrer, "Implicit procedures for the solution of elastoplastic problems by the boundary element method," *Mathematical and Computer Modelling*, vol. 15, no. 3-5, pp. 303–311, 1991.

[108] J. Telles and J. Carrer, "Static and transient dynamic nonlinear stress analysis by the boundary element method with implicit techniques," *Engineering Analysis with Boundary Elements*, vol. 14, no. 1, pp. 65–74, 1994.

[109] J. C. Simo and R. L. Taylor, "Consistent tangent operators for rate-independent elastoplasticity," *Computer methods in applied mechanics and engineering*, vol. 48, no. 1, pp. 101–118, 1985.

[110] M. Bonnet and S. Mukherjee, "Implicit bem formulations for usual and sensitivity problems in elasto-plasticity using the consistent tangent operator concept," *International Journal of Solids and Structures*, vol. 33, no. 30, pp. 4461–4480, 1996.

[111] H. Poon, S. Mukherjee, and M. Bonnet, "Numerical implementation of a cto-based implicit approach for the bem solution of usual and sensitivity problems in elasto-plasticity," *Engineering Analysis with Boundary Elements*, vol. 22, no. 4, pp. 257–269, 1998.

[112] E. D. Leonel and W. S. Venturini, "Cohesive crack propagation using a boundary element formulation with a tangent operator," *WIT Transactions on Modelling and Simulation*, vol. 49, pp. 247–255, 2009.

[113] Y. Liu, G. H. Paulino, and L. Liang, "Elasto-viscoplastic consistent tangent operator concept-based implicit boundary element methods," *Science in China Series E: Technological Sciences*, vol. 43, no. 2, pp. 154–164, 2000.

[114] G. H. Paulino and Y. Liu, "Implicit consistent and continuum tangent operators in elastoplastic boundary element formulations," *Computer methods in applied mechanics and engineering*, vol. 190, no. 15-17, pp. 2157–2179, 2001.

[115] A. Moshaiov and W. Vorus, "Elasto-plastic plate bending analysis by a boundary element method with initial plastic moments," *International journal of solids and structures*, vol. 22, no. 11, pp. 1213–1229, 1986.

[116] C. Providakis and D. Beskos, "Dynamic analysis of elasto-plastic flexural plates by the d/bem," *Engineering analysis with boundary elements*, vol. 14, no. 1, pp. 75–80, 1994.

[117] P. Fotiu, H. Irschik, and F. Ziegler, "Modal analysis of elastic-plastic plate vibrations by integral equations," *Engineering analysis with boundary elements*, vol. 14, no. 1, pp. 81–97, 1994.

[118] G. R. Fernandes and W. S. Venturini, "Non-linear boundary element analysis of plates applied to concrete slabs," *Engineering analysis with boundary elements*, vol. 26, no. 2, pp. 169–181, 2002.

[119] V. Karam and J. Telles, "The bem applied to plate bending elastoplastic analysis using reissner's theory," *Engineering Analysis with Boundary Elements*, vol. 9, no. 4, pp. 351–357, 1992.

[120] G. Ribeiro and W. Venturini, "Elastoplastic analysis of reissner's plate using the boundary element method," *Plate bending analysis with boundary elements(A 98-36576 09-39), Southampton, United Kingdom and Billerica, MA, Computational Mechanics Publications(Advances in Boundary Elements Series.*, vol. 2, pp. 101–125, 1998.

[121] M. Aliabadi *et al.*, "Boundary element method for shear deformable plates with combined geometric and material nonlinearities," *Engineering Analysis with Boundary Elements*, vol. 30, no. 1, pp. 31–42, 2006.

[122] S. Oliveira and V. Karam, "Elastoplastic analysis of reissner's plates by the boundary element method," *Engineering Analysis with Boundary Elements*, vol. 64, pp. 247–254, 2016.

[123] J. Borges and V. Karam, "Elastic-viscoplastic analysis of plate bending with reissner's theory by the boundary element method," *Engineering Analysis with Boundary Elements*, vol. 132, pp. 146–158, 2021.

[124] R. Ansys, "Academic research mechanical, release 2022 r1," *Inc.: Canonsburg, PA, USA*, 2022.

[125] R. L. Taylor, "FEAP - finite element analysis program," 2014.

[126] A. Mesquita and H. Coda, "A simple kelvin and boltzmann viscoelastic analysis of three-dimensional solids by the boundary element method," *Engineering Analysis with Boundary Elements*, vol. 27, no. 9, pp. 885–895, 2003.

[127] M. Hematiyan, A. Khosravifard, and T. Bui, "Efficient evaluation of weakly/strongly singular domain integrals in the bem using a singular nodal integration method," *Engineering Analysis with Boundary Elements*, vol. 37, no. 4, pp. 691–698, 2013.

[128] N. W. Tschoegl, *The Phenomenological Theory of Linear Viscoelastic Behavior*. Springer-Verlag Berlin Heidelberg, 1989.

[129] A. A. Akay, E. Gürses, and S. Göktepe, "A new time-domain boundary element formulation for generalized models of viscoelasticity," *Engineering Analysis with Boundary Elements*, vol. 150, pp. 30–43, 2023.

[130] Z. Kazemi, M. Hematiyan, and R. Vaghefi, "Meshfree radial point interpolation method for analysis of viscoplastic problems," *Engineering Analysis with Boundary Elements*, vol. 82, pp. 172–184, 2017.

Appendix A. 3D Homogeneous RVE

The macroscopic strain-controlled analysis is performed on a simple homogeneous 3-D cube model to check the accuracy of the developed 3-D model. The mesh consisting of 2D surface elements is shown in Figure A1. Each edge is divided into ten equal intervals. Consequently, on each face of the cube, 10×10 square elements are formed, and by dividing each square into four identical triangles, a boundary element mesh consisting of 2400 nodes in total is obtained. The dimensions of the cube are given in millimeters in Figure A1. Isotropic linear elastic material properties are defined. Young's modulus is defined as 10 MPa, and Poisson's ratio value is taken as 0.3. The model is loaded with macroscopic strain ($\bar{\varepsilon}$) under the linear displacement boundary condition. The applied strain tensor is shown in Equation A1.

$$\bar{\varepsilon} = \begin{bmatrix} \bar{\varepsilon}_{11} & \bar{\varepsilon}_{22} & \bar{\varepsilon}_{33} & 2\bar{\varepsilon}_{12} & 2\bar{\varepsilon}_{13} & 2\bar{\varepsilon}_{23} \end{bmatrix}^T = \begin{bmatrix} 0.92 & -0.39 & -0.39 & 0 & 0 & 0 \end{bmatrix}^T \tag{A1}$$

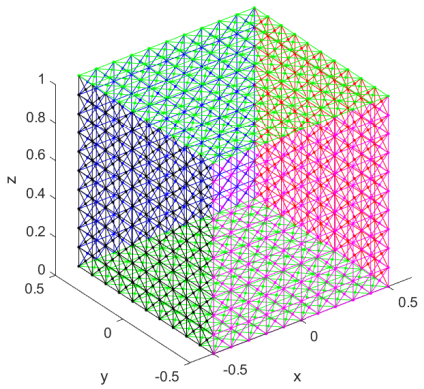


Figure A1: 3D single phase boundary element model

An analytical solution to the problem can be obtained by using the 3-D Hooke's law. In Equation A2, the stress-strain relationship is given.

$$\begin{bmatrix} \bar{\sigma}_{11} \\ \bar{\sigma}_{22} \\ \bar{\sigma}_{33} \\ \bar{\sigma}_{12} \\ \bar{\sigma}_{13} \\ \bar{\sigma}_{23} \end{bmatrix} = \frac{E}{(1+\nu)(1-2\nu)} \begin{bmatrix} (1-\nu) & \nu & \nu & 0 & 0 & 0 \\ \nu & (1-\nu) & \nu & 0 & 0 & 0 \\ \nu & \nu & (1-\nu) & 0 & 0 & 0 \\ 0 & 0 & 0 & (1-2\nu) & 0 & 0 \\ 0 & 0 & 0 & & 0 & (1-2\nu) & 0 \\ 0 & 0 & 0 & & 0 & 0 & (1-2\nu) \end{bmatrix} \begin{bmatrix} \bar{\varepsilon}_{11} \\ \bar{\varepsilon}_{22} \\ \bar{\varepsilon}_{33} \\ \bar{\varepsilon}_{12} \\ \bar{\varepsilon}_{13} \\ \bar{\varepsilon}_{23} \end{bmatrix} \tag{A2}$$

The homogenized stress tensor calculated with the boundary element method and the one with the analytical relations are compared. The results are given in Table A1. When compared with analytical solutions, it is seen that the boundary element method gives consistent results in three-dimensional homogeneous elasticity problems.

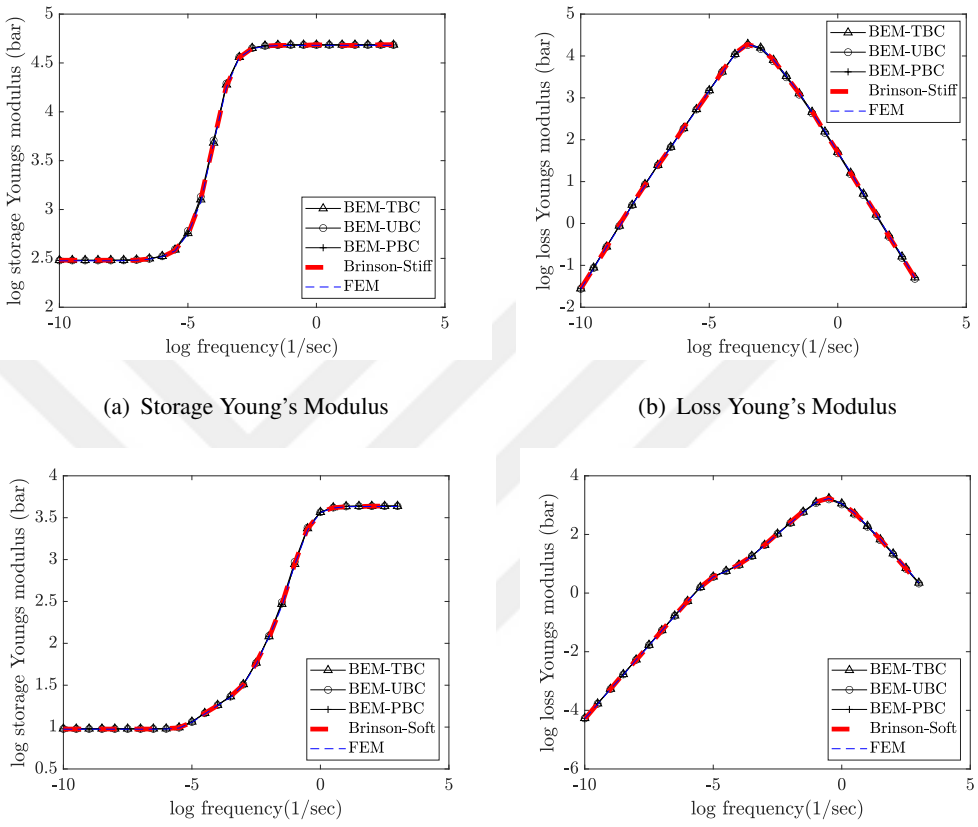
Table A1: Analytical and boundary element method stress results obtained on a simple elasticity problem under linear displacement boundary condition

	Analytical [MPa]	**BEM [MPa]**
$\overline{\sigma}_{xx}$	7.75	7.78
$\overline{\sigma}_{yy}$	-2.25	-2.23
$\overline{\sigma}_{zz}$	-2.25	-2.23

Appendix B. Two-Phase RVE with Identical Viscoelastic Material Properties on Phases

After representing the material parameters as a function of frequency, the developed algorithm is first compared with the stiff and soft material behavior presented by Brinson et al. [54]. For this purpose, a two-phase square RVE with centered circular inclusion is created. Each edge at the outer boundary is divided into 5 elements, and the inclusion boundary is divided into 20 elements. The same material properties are inserted into both phases. Storage and loss Young's modulus results concerning change in frequency are given in Figures B1 for all stiff and all soft RVEs. The results presented by Brinson et al. [54] and the finite element solution (FEM) of the same problem presented by Guzel [56] are also given in the figures. In Tables B1 and B1, the solution times of FEM and BEM are presented. It is seen that the developed BEM

algorithm gives accurate results with FEM with almost 16% of the solution time. Moreover, the agreement of the developed method with the FEM results of Brinson et al. [54] is perfect. Because the RVE is homogeneous, the three boundary conditions are presenting the same results.



(a) Storage Young's Modulus

(b) Loss Young's Modulus

(c) Storage Young's Modulus

(d) Loss Young's Modulus

Figure B1: Storage and loss Young's Modulus of viscoelastic stiff-stiff material (a)-(b) and soft-soft material (c)-(d) defined on both phases of a two-phase RVE

Table B1: Solution times of stiff and soft RVEs

Models	**Solution Time of Stiff RVE [s]**	**Solution Time of Soft RVE [s]**
TBC	8.2	7.92
UBC	8.05	7.90
PBC	7.96	8.19
FEM	48.1	48.1

Appendix C. Validation on Mathematical Examples

For the validation of the developed integration method using CTM and interpolations on the integration points using MLS and RPIM methods, the example problems presented by Hematiyan [64] are solved. A parameter study is conducted to check the effect of parameters on the performance of the developed method.

The integrands selected by Hematiyan [64] are composed of two functions, a uniform non-singular forcing function f and weakly singular kernel h, which is singular at the source point (0.25, 0.25). r is defined as the Euclidean distance from the field point to the source point, and r_i is the unit vector of r in the i direction. A square domain with $0 < x < 1$ and $0 < y < 1$ is the integration domain. In the reference study, the results of an adaptive mesh-free method and semi-analytical method offered in the article are presented. The current study uses the semi-analytical method offered in the article for comparisons. In Table C1, the integrand functions considered in this section are presented. In the parameter study part, function codes indicated in Table C1 are used for the to present results for easiness.

Table C1: Integrands of domain integral $\int_\Omega f h d\Omega$ with source point at (0.25, 0.25)

Forcing function, f	**Singular kernel,** h	**Function code**
$1 + x^2 + y^2$	$\ln\left(\frac{1}{r}\right)$	F1
$\sin(6y) + y^5 x + x^2$	$\ln\left(\frac{1}{r}\right)$	F2
$1 + y^2 + xy + x^2$	$\frac{r_1}{r^2}$	F3
$\cos(8y) + e^y x + \frac{1}{y + 0.1} x^2$	$\frac{r_1}{r^2}$	F4

This section discusses the effect of the adaptive monomial decision algorithm, integration points, scattered data points, and interpolation methods.

Effect of Adaptive Monomial Order Decision

In this section, the adaptive decision mechanism on the order of monomial depending on the number of data points in the support domain is investigated. The adaptive decision mechanism is summarized in Equation 3.19. The fine mesh shown in Figure C1 is used for the investigation of the effect of the adaptive method. In Tables C2 and C3, results for the fine mesh with adaptive monomial order (m) and with monomial order of 3 are presented for interpolation methods MLS and RPIM, respectively. Hematiyan uses only CTM without the requirement of an interpolation method and directly evaluates the values of integrand in the CTM integration points. As observed, the adaptive scheme gives more consistent results than the fixed order of monomials for both MLS and RPIM methods. For this study, MLS gives better results compared to RPIM.

Table C2: Fixed and adaptive monomial order results for MLS interpolation with fine mesh

			For constant m=3		**Adaptive m**	
F	**Exact**	**Hematiyan [64]**	**MLS**	**Error %**	**MLS**	**Error %**
F1	1.225377	1.225377	1.2287304	0.273663	1.2284658	0.252069
F2	non-exist	0.4808854	0.4770755	0.791917	0.4778198	0.637139
F3	1.661083	1.661083	1.6600196	0.064079	1.6600183	0.064157
F4	non-exist	2.357824	2.3905055	1.386517	2.3888632	1.316864

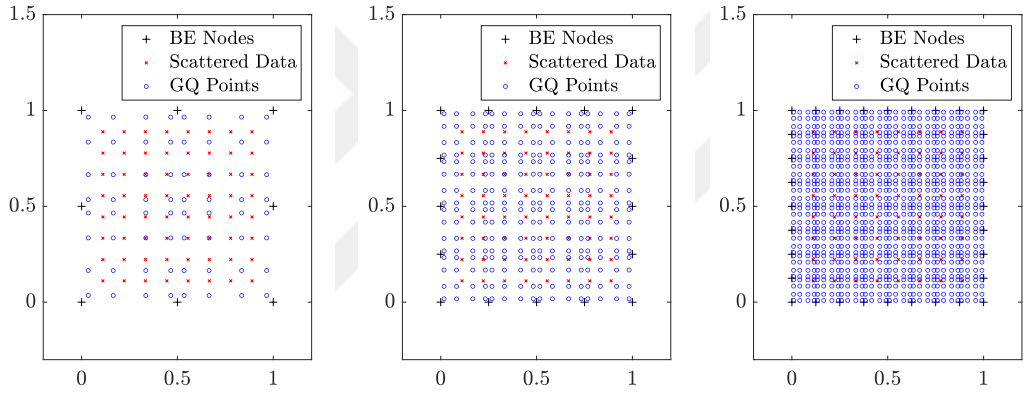
Effect of Integration Points

This section discusses the effect of several integration points used in the CTM method. The number of internal data points is kept constant at 64. An adaptive scheme for the determination of the monomial order is used in this study. Three different solution domains are created, as presented in Figure C1. Each edge of the boundary is divided into 2, 4, and 8 elements for coarse, medium, and fine models, respectively.

Table C3: Fixed and adaptive monomial order results for RPIM interpolation with fine mesh

			For constant m=3		Adaptive m	
F	**Exact**	**Hematiyan [64]**	**RPIM**	**Error %**	**RPIM**	**Error %**
F1	1.225377	1.225377	1.2320364	0.543457	1.2306449	0.4299
F2	non-exist	0.4808854	0.4709341	2.069024	0.4750133	1.220753
F3	1.661083	1.661083	1.659344	0.104751	1.6590437	0.122829
F4	non-exist	2.357824	2.3897538	1.354636	2.3857136	1.183282

Blue (◯) are the integration points and red (×) are the scattered data points, used for integration.



(a) Coarse (b) Medium (c) Fine

Figure C1: Three different integration domains used for the evaluation of the effect of integration points on the integral result

In Tables C4 and C5, the results for the three different integration meshes with adaptive monomial order (m) are presented for interpolation methods MLS and RPIM, respectively. A good convergence behavior is observed for most of the functions evaluated. There is divergent behavior for the finest mesh for some of the functions. This behavior can be explained by the number of internal data points used for the integration. Even though the number of integration points is increasing, the data point that is used for integration is kept constant. Consequently, even though the integration is finer, interpolation may not be fine anymore for those functions. The effect of the

number of inner data points is presented in the following section.

Table C4: Results for three different integration mesh for MLS interpolation

		Coarse		Medium		Fine	
F	**Hematiyan [64]**	**MLS**	**Error %**	**MLS**	**Error %**	**MLS**	**Error %**
F1	1.225377	1.2116504	1.120194	1.2284658	0.252069	1.2284123	0.24770336
F2	0.4808854	0.4740865	1.413481	0.4778198	0.637139	0.471465	1.95862326
F3	1.661083	1.6605784	0.030438	1.6600183	0.064157	1.6625358	0.087400758
F4	2.357824	2.4378294	3.393626	2.3888632	1.316864	2.3864419	1.214171262

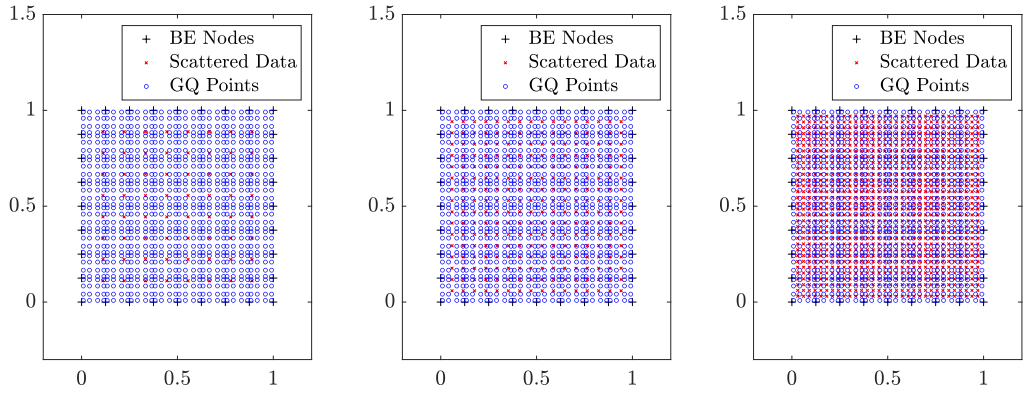
Table C5: Results for three different integration mesh for RPIM interpolation

		Coarse		Medium		Fine	
F	**Hematiyan [64]**	**RPIM**	**Error %**	**RPIM**	**Error %**	**RPIM**	**Error %**
F1	1.225377	1.2122212	1.073612	1.2306449	0.4299	1.2304544	0.414354113
F2	0.4808854	0.4726341	1.715508	0.4750133	1.220753	0.4684733	2.580748734
F3	1.661083	1.6607877	0.017838	1.6590437	0.122829	1.6668919	0.349645171
F4	2.357824	2.4351137	3.278448	2.3857136	1.183282	2.3723896	0.618182774

Effect of Scattered Data Points

In this section, the effect of several scattered data points used in the CTM method is discussed. The fine mesh discretization of the domain given in Figure .1(c) is used for the study. An adaptive scheme for the determination of monomial order is used. Three different solution domain is created, as presented in Figure C2. Models include 64, 256, and 1024 inner data points, respectively.

In Tables C6 and C7, the results for three meshes with different numbers of data points and adaptive monomial order (m) are presented for interpolation methods MLS and RPIM, respectively. A perfect convergence behavior is observed for all functions evaluated. The reason for the phenomenon observed in the previous section regarding the fine mesh is validated in these results. It is observed that as the number of data points used in the domain increases, the results of the integrals converge to a finite value. Moreover, MLS and RPIM give consistent results with each other.



(a) Coarse (b) Medium (c) Fine

Figure C2: Three domains with different numbers of inner data points used for the evaluation of the effect of data points on the integral result

Table C6: Results for three different data point mesh for MLS interpolation

		Coarse		Medium		Fine	
F	**Hematiyan [64]**	**MLS**	**Error %**	**MLS**	**Error %**	**MLS**	**Error %**
F1	1.225377	1.2311509	0.4711938	1.2270159	0.1337466	1.2257095	0.0271345
F2	0.4808854	0.4586263	4.6284372	0.4757998	1.0571995	0.4801445	0.153717
F3	1.661083	1.6657931	0.2834956	1.662476	0.0838007	1.6606596	0.0255496
F4	2.357824	2.4717644	4.8328833	2.3817464	1.0150249	2.3569125	0.0382346

Table C7: Results for three different data point mesh for RPIM interpolation

		Coarse		Medium		Fine	
F	**Hematiyan [64]**	**RPIM**	**Error %**	**RPIM**	**Error %**	**RPIM**	**Error %**
F1	1.225377	1.2334032	0.6549984	1.2276754	0.1875668	1.2258345	0.0373354
F2	0.4808854	0.4617245	3.984165	0.4765442	0.9024011	0.4806092	0.0570824
F3	1.661083	1.6660421	0.2984858	1.6616671	0.0351036	1.6604631	0.0373792
F4	2.357824	2.4675777	4.6553163	2.3851327	1.1586453	2.3541213	0.1566154

Appendix D. Analytical Solutions

The analytical solutions of creep and relaxation tests of standard linear solids shown in Figures 4.5 and 4.6 are presented in this section. The solutions are adapted from Tschoegl [128].

Analytical Solutions of SLS-K

The analytical solution for the creep of SLS-K reads

$$\varepsilon(t) = \left[\frac{1}{E_v} + \frac{1}{E_1}\left(1 - \exp\left(\frac{-t}{\tau}\right)\right)\right]\sigma_0\,, \tag{D1}$$

where $\tau = \eta_1/E_1$. The viscous strain $\varepsilon^v(t)$ can be found as $\varepsilon^v(t) = \varepsilon(t) - \sigma_0/E_v$. Similarly, the analytical solution for the relaxation of SLS-K is as follows

$$\sigma(t) = \left[\frac{E_v E_1}{E_v + E_1} + \frac{E_v^2}{E_v + E_1}\exp\left(\frac{-t}{\tau'}\right)\right]\varepsilon_0\,, \tag{D2}$$

where $\tau' = \frac{E_1\tau}{E_1+E_v}$.

Analytical Solutions of SLS-M

The analytical solution for the creep of SLS-M reads

$$\varepsilon(t) = \left[\frac{1}{E_e + E_v} + \frac{E_v}{E_e(E_e + E_v)}\left(1 - \exp\left(\frac{-t}{\tau'}\right)\right)\right]\sigma_0\,, \tag{D3}$$

where $\tau' = \frac{E_e+E_v}{E_e}\tau$ and $\tau = \eta_1/E_v$. The viscous strain $\varepsilon^v(t)$ can be obtained from $\varepsilon^v(t) = \frac{1}{E_v}[(E_e + E_v)\varepsilon(t) - \sigma_0]$. Moreover, the analytical solution for the relaxation of SLS-M reads

$$\sigma(t) = \left[E_e + E_v\exp\left(\frac{-t}{\tau}\right)\right]\varepsilon_0\,. \tag{D4}$$

The elastic stress σ^e remains constant during the relaxation test, i.e., $\sigma^e = E_e\varepsilon_0$.

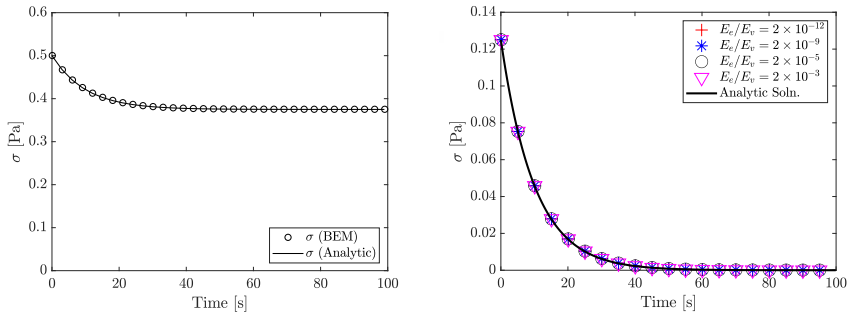
Appendix E. Comparison of SLS-Maxwell Model with Pure Maxwell Model

This section aims to supplement the explanations given in Sections 4.1.1.1 and 4.1.2.1 regarding the auxiliary use of the upper elastic branch with E_e, see Figure 4.1, for

post-processing purposes. For this purpose, we consider the SLS-Maxwell Model (SLS-M) and the pure Maxwell Model. In SLS-M, the upper elastic branch has a physical function of representing the ground elastic response in addition to its use for post-processing. In the pure Maxwell Model, however, the upper elastic branch serves as an auxiliary component solely for post-processing as the Maxwell model represents fluid-like response without any ground elasticity. These two models are compared on the basis of a relaxation-type loading in a BVP with uniform strain field analyzed through the proposed BEM approach, see Section 4.1.2.1. In the analysis, the model parameters given in Table E1 are used.

Table E1: Parameters of the SLS-Maxwell and Pure Maxwell models

	E_e [Pa]	E_v [Pa]	E_1 [Pa]	$\eta_1^\lambda = \eta_1^\mu$ [1/s]	ν [−]
SLS-M	15	5	0	10	0
Maxwell	10^{-2} to 10^{-11}	5	0	10	0



(a) Standard Linear Solid of Maxwell-Type (SLS-M)

(b) Pure Maxwell

Figure E1: Analytical and BEM results for the relaxation-type BVP with uniform strain field modeled with (a) SLS-M and (b) the Pure Maxwell Model

Comparing the relaxation response of SLS-M with that of the Maxwell Model in Figure E1, we note that while SLS-M with non-zero E_e exhibits a non-vanishing steady-state stress value, the stress in the Maxwell model converges to a vanishing steady-state value. The latter, a physically correct condition, is attained by selecting a

sufficiently small value for E_e. The value of E_e in the Maxwell Model, however, cannot be chosen exactly zero as the upper elastic branch is needed for post-processing. To illustrate the extent to which the value of E_e can be reduced without causing any numerical stability issues, we have varied the value of the ratio E_e/E_v from $2 \cdot 10^{-3}$ to $2 \cdot 10^{-12}$. The results depicted in Figure .1(b) indicate that the analytical response of the Maxwell model is successfully captured with the proposed approach for a wide range of E_e values where the selection of a value close to the machine precision has not caused any numerical instabilities.

Appendix F. Mesh and Time Step Convergence Study for the Perforated Plate

A convergence study was conducted to determine the appropriate mesh and time step for the perforated plate example. To obtain converged results, three different sets of meshes are considered. The number of elements for each mesh is provided in Table F1. In Figure F1, it is evident that the medium and fine meshed models yield consistent results, suggesting that either model can be chosen for the analysis. For computational efficiency, the medium mesh model is utilized in the analysis of the perforated plate.

Table F1: Boundary element meshes utilized in the mesh convergence study of the perforated plate

Models	# of elements on the inner/outer boundary	# of inner data points
Coarse	60/40	777
Medium	80/80	1208
Fine	100/120	1788

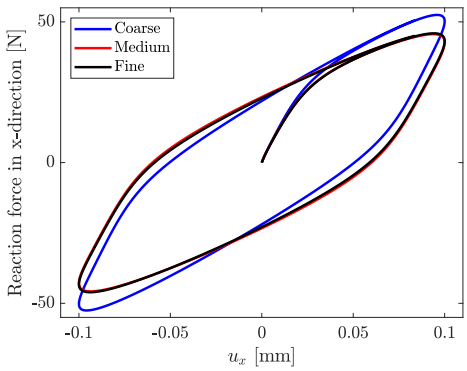
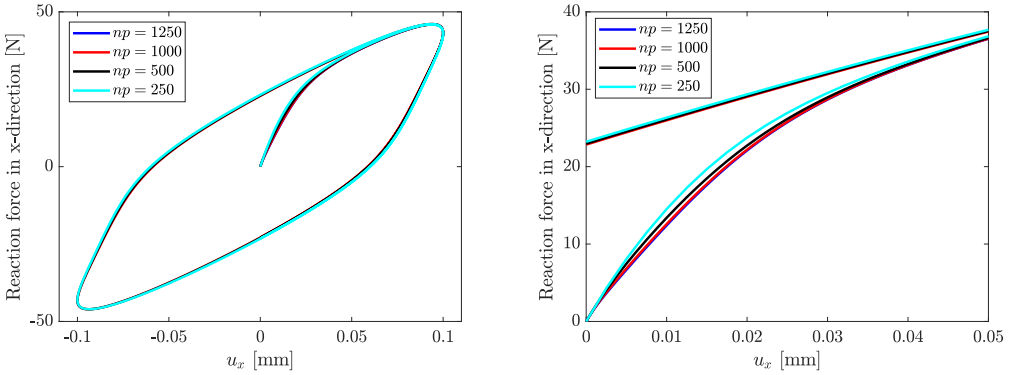


Figure F1: The change in reaction force with respect to the applied axial loading for three models with different discretizations.

The second convergence study presented here is time step convergence study. Figure F2 depicts the results of the reaction force with respect to time for different time steps. The parameter np is defined as the number of steps required to reach the end time of one loading cycle. As can be observed, particularly from the close-up view of the initial steps, the semi-implicit algorithm proposed in the study demonstrates convergent results after np values of 500. To ensure a conservative approach, np values of 1000 have been set in the analysis proposed in this study.



(a) All loading cycle

(b) Close-up view on the initial steps

Figure F2: The change in reaction force with respect to the applied axial loading for different time steps

CURRICULUM VITAE

ARDA AKAY

Structural Analyst/Researcher

ABOUT ME

I am an experienced researcher/analyst with nine years of expertise in research and teaching, specializing in theoretical and computational structural engineering within the field of Aerospace Engineering. With a strong background in computational material modeling, theoretical and experimental solid mechanics, and proficiency in computational methods like FEM and BEM, and years of experience in programming with MATLAB, I am eager to leverage my knowledge and abilities to address complex engineering challenges within a dynamic, international, and multi-disciplinary environment.

EXPERIENCE

Researcher | Aerospace Engineering, Middle East Technical University

February 2014 – June 2021 Ankara, Turkey

Scientific Project of The Scientific and Technological Research Council of Türkiye

- Developed a MATLAB-based program using finite element and boundary element methods for analyzing polymer nano-composites.
- Created linear and non-linear visco-plastic material models for solids.
- Developed a non-iterative computational approach for modeling non-linear materials.
- Investigated the properties of polymer nano-composites in structural engineering problems.
- Optimized the microstructure of nano-composite materials using the developed MATLAB program as a tool.
- Performed homogenization and interface modeling for nano-composites.
- Conducted hand calculations for stress analysis of polymer nano-composites.
- Prepared project progress reports.

Joint Research Project of Turkish Engine Industries and Turkish Ministry of Science, Industry and Technology

- Conducted finite element analysis of aerospace joints using ANSYS software and validated the results through experimental testing.
- Designed, planned, and executed mechanical experiments for various aerospace joints.
- Developed a machine learning-based design tool in MATLAB for the analysis of an aerospace engine component, addressing industry partner concerns and improving product analysis performance and speed.
- Performed hand calculations for stress analysis of aerospace joints.
- Prepared project progress and financial reports.
- Conducted research and facilitated domestic and international purchases.

Teaching Assistant | Aerospace Engineering, Middle East Technical University

June 2014 – Ongoing Ankara, Turkey

- Served as a teaching assistant for undergraduate and graduate courses in the field of solid mechanics and computational methods in Aerospace Engineering.
- Planned and set up experiments in undergraduate structural laboratories.

Internship | Mercedes-Benz Türk

June 2011 Istanbul, Turkey

- Prepared computer-aided drawings for some simple bus and truck components.

EDUCATION

Ph.D. | Aerospace Engineering, Middle East Technical University

September 2016 – August 2023 — Ankara, Turkey

- Thesis: "A New Time-Domain Boundary Element Formulation for Rate-Dependent Inelasticity with Application to Homogenization"
- GPA: 3.88/4.00

M.S. | Aerospace Engineering, Middle East Technical University

September 2013 – September 2016 — Ankara, Turkey

- Thesis: "Finite Element Analysis of Bolted Flange and Dovetail Aerospace Joints"
- GPA: 4.00/4.00

B.S. | Mechanical Engineering, Middle East Technical University

September 2008 – February 2013 — Ankara, Turkey

- GPA: 3.58/4.00

PUBLICATIONS

Journal Articles

- Under revision: A. A. Akay, E. Gürses, and S. Göktepe. "A Time-Domain Boundary Element Formulation for Nonlinear Power Type Viscoelasticity".
- A. A. Akay, E. Gürses, and S. Göktepe. "A new time-domain boundary element formulation for generalized models of viscoelasticity." Engineering Analysis with Boundary Elements 150 (2023): 30-43.

Conference/Proceedings Articles

- A. A. Akay, S. Göktepe, E. Gürses, "Determination of the Homogenized Properties of Heterogeneous Media Using the Boundary Element Method", IWCMM29 2019.
- A. A. Akay, D. Çöker, A. Kayran, E. Gürses, "Experimental Study and Finite Element Analysis of Dovetail Attachments", IMECE 2017.
- A. A. Akay, D.Çöker, A. Kayran, E. Gürses, "Implementation of the Submodelling Technique on the Dovetail Attachments", AIAC 2017.
- A. Yıldırım, A. A. Akay, H. Gülaşık, E. Gürses, D. Çöker, A. Kayran, "Development of Bolted Flange design Tool Based on Finite Element Analysis and Artificial Neural Networks", IMECE 2015.
- A. Yıldırım, A. A. Akay, H. Gülaşık, D. Çöker, E. Gürses, A. Kayran, "Parameters Correlation Study to Investigate the Effects of Geometric Variables on the Safety Bolted Flange Connections", AIAC 2015.
- A. A. Akay, H. Gülaşık, A. Yıldırım, D. Çöker, A. Kayran, E. Gürses, "Modeling of a Circular Double Flange Joint Including Contact and Friction Effects", AIAC 2015.

STRENGTHS

Engineering intuition | Interdisciplinary thinker | Collaborative team player | Resilient | Work ethic | Fast learner | Problem solver | Attentive listener

SKILLS

MATLAB | ANSYS | FEAPpv | Fortran | FEM | Nastran | Patran | GOM-Aramis | LaTeX | BEM

LANGUAGES

Turkish: Native

English: C2

German: A1

NATIONALITY

German

Turkish

REFERENCES

Ercan Gürses
Associate Professor
gurses@metu.edu.tr

Serdar Göktepe
Associate Professor
sgoktepe@metu.edu.tr

Gökhan Serhat
Assistant Professor
gokhan.serhat@kuleuven.be